UNIVERSITÉ DE NANTES
FACULTÉ DES SCIENCES ET DES TECHNIQUES

———

ÉCOLE DOCTORALE SPIGA

N° attribué par la bibliothèque

Année 2012

Impact des mélanges de minéraux à macro-échelle sur la réflectance spectrale de surfaces naturelles : étude empirique à partir de scénarios de terrain.

THÈSE DE DOCTORAT

Discipline : Science de la Terre
Spécialité : Télédétection

Présentée
et soutenue publiquement par

Ekaterina CARMINA

Le 29 mars 2012, devant le jury ci-dessous

Président	M. Richard ESCADAFAL, Directeur de Recherche, IRD/CESBIO
Rapporteurs	M. Xavier BRIOTTET, Directeur de Recherche, ONERA
	M. Philippe LAGACHERIE, Ingénieur de Recherche, INRA
Examinateurs	M. José BIOUCAS DIAS, Professeur, IST, Lisbonne

Directeur de thèse : Mme Véronique CARRERE, Maître de Conférences, Université de Nantes

Table des matières :

Liste des figures :

Liste de tableaux:

1. Introduction

La plupart des signatures spectrales qui sont enregistrées à l'échelle des capteurs aéroportés sont des mélanges de plusieurs composantes spectrales, à presque toutes les échelles d'observation (Clark, 1999). Les mélanges de minéraux dans le champ de vision des instruments de télédétection sont des phénomènes naturels, dus à la fois à la taille physique du pixel de l'image et au fait que les processus terrestres ont tendance à créer des surfaces mixtes. Les surfaces géologiques naturelles ont des compositions minéralogiques et des propriétés physiques différentes, ces paramètres peuvent être détectés avec succès en utilisant des techniques de télédétection. Ainsi, les applications de la télédétection dans le domaine du visible, du proche infrarouge, de l'infrarouge ondes courtes et de l'infrarouge thermique du rayonnement électromagnétique souffrent de problèmes d'interprétation car la nature mixte de l'information spectrale limite considérablement la précision de l'analyse spectrale (Adams et al., 1986; Atkinson et al., 1997; Gillespie, 1992; Green et al., 1998; Heinz et Chang, 2001; Keshava et Mustard, 2002; Roberts et al., 1993; Song, 2005).

Produire des démixages successifs de mélanges spectraux, définir leur constituants élémentaires et prédire leur abondance relative est un défi dans le domaine de la télédétection (Bioucas-Dias, 2009; Somers, 2011; Gillespie, 1992).

Certaines des théories supposent que les mélanges spectraux à l'échelle du terrain peuvent être résolus en utilisant des modèles linéaires (Johnson, 1983; Adams et al., 1986). Toutefois, il est bien connu que les spectres de réflectance d'un mélange sont des fonctions complexes, non linéaires, de la taille des particules, de l'abondance, de l'opacité du matériel et du type de surfaces (par exemple la poussière, le sable, la roche-mère, où les particules sont mélangées à différentes échelles) (Keshava et Mustard, 2002; Poulet et Erard, 2004).

Sur le terrain, le mélange peut être composé de différents constituants, mais également d'objets de taille différentes tels que roches et rochers, particules fines et graviers, avec des tailles de particules pouvant varier de très fines à grosses, de poussière à roches. Les objets peuvent être recouverts par des couches de poussières et des croûtes d'altération ou des patines d'épaisseur différente qui peuvent masquer ou causer des effets non linéaires dans les spectres de mélanges.

A l'échelle microscopique, un échantillon de roche se compose d'un mélange intime, non-linéaire, de minéraux qui constituent les composantes spectrales élémentaires (Singer, 1981). A cette échelle, les propriétés des minéraux, telles que la composition minéralogique, la taille de grains des minéraux, leur orientation sont importantes et peuvent créer des variations de la réflectance spectrale et des profondeurs d'absorptions (Dyar et al., 2005; Carmina et Carrère, 2009).

A l'échelle d'une image aéroportée, les mélanges sont d'ordre macroscopique, ce qui est différent. Par conséquent, les études empiriques portant sur des mélanges microscopiques de minéraux et leurs résultats ne peuvent être directement appliquées aux données macroscopiques. Les mélanges à macro-échelle (terrain) n'ont pas été aussi largement étudiés que les mélanges microscopiques. Des modèles de transfert radiatif ont été appliqués sur des mélanges simulés en laboratoire, mais n'ont pas encore été validés sur des données macroscopiques. Un grand nombre de publications proposent des traitements théoriques et des solutions analytiques, mais il est nécessaire de les compléter par plus d'études empiriques sur le terrain afin d'accroître le nombre d'observations et d'expérimentation des modèles théoriques (Longhi, 2004).

Objectifs généraux

L'objectif de cette étude est de générer des observations empiriques de macro-mélanges de roches et de minéraux dans des environnements naturels sur le terrain, de comparer des mélanges simulés et modélisés avec des données de terrain, d'observer l'influence de différents facteurs sur les mélanges et enfin, d'appliquer des algorithmes linéaires et non linéaires pour le démixage et d'évaluer leurs résultats. Les observations empiriques à l'échelle du terrain sont nécessaires pour avoir une vision complète du comportement des mélanges, pas seulement dans des conditions de laboratoire avec des mélanges simulés, mais aussi pour des scènes naturelles, telles qu'elles apparaissent sur le terrain. Par ailleurs, l'observation de mélanges contenant les mêmes constituants devraient être effectuée à différentes échelles : l'échelle du terrain, l'échelle de l'image et l'échelle microscopique, pour aider à mieux comprendre les comportements des mélanges, et améliorer les techniques de démixage.

Les principales questions scientifiques de cette étude sont les suivantes : quel est le comportement des mélanges minéraux au niveau macro-échelle? Dans quelles circonstances les macro-mélanges sont linéaires ou non linéaires? Quelle approche de démixage, linéaire ou non

linéaire, donne un meilleur résultat? Quelle est l'influence respective, au niveau macro-échelle, de différents facteurs sur le comportement des mélanges : la taille des éléments, la composition, les effets d'éclairement, l'ombre, la patine, etc.? Les mélanges en poudre sont-ils de bonnes approximations des situations naturelles sur le terrain?

La définition des composantes spectrales est un problème important dans l'analyse de mélanges, parce que cette question dépend de l'échelle d'observation. A l'échelle microscopique, les composantes spectrales sont des minéraux alors qu'à macro-échelle, les composantes spectrales sont plus complexes et peuvent correspondre à plusieurs objets, par exemple, des affleurements, des rochers ou des blocs de taille variable composés d'agrégats de minéraux, des sols, du sable composés de fines particules. Avec une échelle croissante, des structures plus complexes peuvent être considérées comme composantes spectrales, dépendant de l'unité géologique pertinente à l'échelle d'observation. Par exemple, à plus grande échelle, des roches isolées peuvent être à peine identifiées, mais font partie d'une structure plus grande, comme un plateau ou une montagne, le lit d'une rivière, ou toute autre formation géologique qui apparaît à plus grande échelle.

L'étude actuelle se concentre sur des scénarios de terrain où différents cas ont été observés. Sur la base de ces observations, les composantes spectrales ont été sélectionnées pour chaque cas. A l'échelle du terrain, un agrégat de minéraux avec une composition similaire peut être sélectionné en tant que composante spectrale homogène comme, par exemple, certains types de roches. Dans notre étude, les composantes spectrales sont sélectionnées en se basant sur des observations de terrain correspondant aux scènes mesurées.

Dans le chapitre 1, les principes de base de la télédétection sont introduits, et un aperçu théorique sur le sujet est présenté, basé sur les travaux précédents et leurs conclusions. Les méthodes de démixage existantes sont examinées. Le chapitre 2 présente la méthodologie. Cette section comprend une description de la zone d'étude, des instruments de mesure, de la stratégie d'échantillonnage, la description des échantillons et de la méthodologie de traitement des données. Dans le chapitre 3, les principaux résultats sont présentés. Ces résultats comprennent une analyse approfondie des scénarios de terrain, la modélisation linéaire (directe), la déconvolution spectrale (inverse) et l'analyse de corrélation. Le chapitre 4 contient une discussion détaillée des résultats et des conclusions générales, les avantages et les inconvénients des méthodes choisies et ouvre des perspectives d'avenir.

Mélanges de minéraux, la théorie

En général, quatre types de mélanges peuvent être définis (**Figure 1**) :

1. Mélange linéaire (mélange surfacique). Les matériels contenus dans le champ d'observation sont optiquement séparés, donc il n'y a pas de diffusion multiple entre les composants. Le signal combiné est simplement la somme des zones fractionnelles multipliées par le spectre de chaque composant.
2. Mélange intime. Un mélange intime se produit quand des matériaux différents sont en contact intime dans une surface de diffusion, tels que les grains de minéraux dans un sol ou une roche. Selon les propriétés optiques de chaque composant, le signal résultant est une combinaison fortement non linéaire des spectres de composantes spectrales.
3. Mélanges sur couches multiples («Coatings» ou couches d'altération). Ils se produisent quand un matériau recouvre l'autre. Chaque couche produit une diffusion et de la transmission (variation de la réfraction) dont l'épaisseur optique varie avec les propriétés des matériaux. Ce type de mélanges est typiquement rencontré dans les roches qui présentent des altérations de surface. Une couche appelée patine peut s'y développer. En fonction de la profondeur de pénétration, le faisceau incident peut atteindre les minéraux recouverts et interagir avec eux. Ainsi le rayonnement récupéré est le résultat de l'interaction avec la couche altérée et le constituant minéral masqué par cette couche (Clark, 1999 ; Roy, 2007).
4. Les mélanges moléculaires se produisent au niveau moléculaire, comme par exemple dans le cas de deux liquides ou d'un liquide et d'un solide mélangés. Le contact intime des composants du mélange peut causer des variations dans les bandes d'absorption (Clark, 1999).

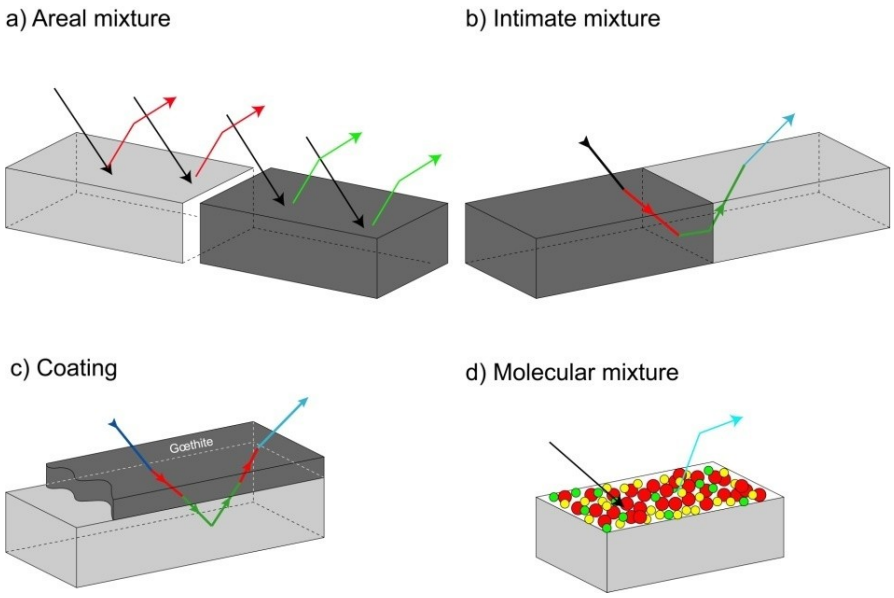

Figure 1 – Types de mélanges (Roy, 2007).

Les mélanges de minéraux ont été étudiés à l'aide de simulations de mélanges en laboratoire dont la composition et les proportions sont connues (modélisation empirique). Ces méthodes empiriques généralement utilisent des minéraux en poudre pour simuler des mélanges; avec des poudres, il est plus facile de contrôler les proportions des mélanges et les tailles de grains (Adams, 1974; Singer, 1981). Les mélanges de différente composition ont montré des comportements spectraux différents, selon les composants qui ont été mélangés, ce qui indique qu'il n'y a donc pas de règles générales qui pourraient être valables pour tous les mélanges. Les résultats des investigations empiriques à l'échelle microscopique ont été supposés valables à toutes les échelles, et plus particulièrement à l'échelle des images aéroportées (macro-échelle), et ont été utilisés pour des interprétations d'images (Singer, 1981; Adams, 1974; Combe et al., 2008; Minitti et al., 2002. Baldridge et Farmer, 2004; Farrand et al., 2006). La composition de surfaces planétaires non connues et d'astéroïdes a été déduite principalement à travers la comparaison entre les spectres acquis à distance et les mesures en laboratoire de mélanges de minéraux en poudre (Gaffey et al., 1993; Pieters et al., 1996; Pompilio, 2007).

Toutefois, des scénarios naturels sur le terrain ne peuvent généralement pas être correctement représentés par des mélanges de poudres; dans la nature, les paysages peuvent avoir des structures complexes, où les roches sont composées de minéraux jointifs qui forment un milieu continu et dont les tailles de grains et de blocs peuvent fortement différer de micro à macro échelle (Poulet, 2004; Pompilio, 2007).

Cependant, pour des raisons de simplicité, le demixage linéaire est régulière appliqué sur des mélanges à comportements non-linéaires, ce qui ne permet pas de prédire correctement les abondances des composants avec une grande précision. Le modèle linéaire peut aussi être la cause de beaucoup d'ambiguïté et d'erreurs sur l'estimation des fractions lorsqu'il est utilisé sur des mélanges non-linéaires (Mustard et Sunshine, 1999). Des algorithmes linéaires standards peuvent ajouter jusqu'à 30% d'erreur au résultat de démixage (Mustard et Sunshine, 1999; Keshava et Mustard, 2002; Combe et al, 2008). Le mécanisme de mélange spectral est encore mal compris. Donc le démixage dans le cas de terrains naturels reste encore un défi.

Le comportement spectral des mélanges dépend des propriétés optiques et physiques des médias, ainsi que de la longueur d'ondes (Nash et Conel, 1974; Singer, 1981; Clark, 1983; Johnson et al, 1992). A une longueur d'onde donnée, le mélange peut avoir un comportement hautement non-linéaire, alors qu'à d'autres le même mélange peut être linéaire. Il est connu que la diffusion et l'absorption de l'énergie dans VNIR est plus non-linéaire (Lyon, 1964; Nash et Conel, 1974; Mustard et Pieters, 1989).

La spectroscopie de laboratoire de couches de poussière démontre que même des couches de faible épaisseur (<100 μm) peuvent effectivement masquer la signature spectrale des matériaux sous-jacents dans le visible et l'infrarouge (Roush, 1982; Singer et Roush, 1983; Johnson et al, 2002). Les modèles linéaires échouent généralement à démixer la roche. De plus, l'altération des roches crée des couches concentriques de minéraux altérés autour de la roche fraîche. Au fil du temps, cette croûte d'altération se détache et est transportée, exposant la roche plus fraîche. Ainsi l'environnement rocheux peut présenter en surface des mélanges de minéraux altérés et non altérés.

Les modèles empiriques de mélanges de minéraux

Peu d'études ont vérifié le comportement des mélanges à l'échelle du terrain, où les mélanges sont supposés être plus comparables avec des mélanges à l'échelle du pixel. Les observations empiriques de mélanges de minéraux ont principalement porté sur des roches qui pourraient être représentatives des surfaces Lunaires et Martiennes. On a découvert que les phases hautement absorbantes peuvent masquer les bandes d'absorption caractéristiques d'autres phases minérales. Par exemple, le spectre d'un orthopyroxène est comparé avec des spectres de mélanges contenant du plagioclase et de la magnétite (Pieters, 1973).

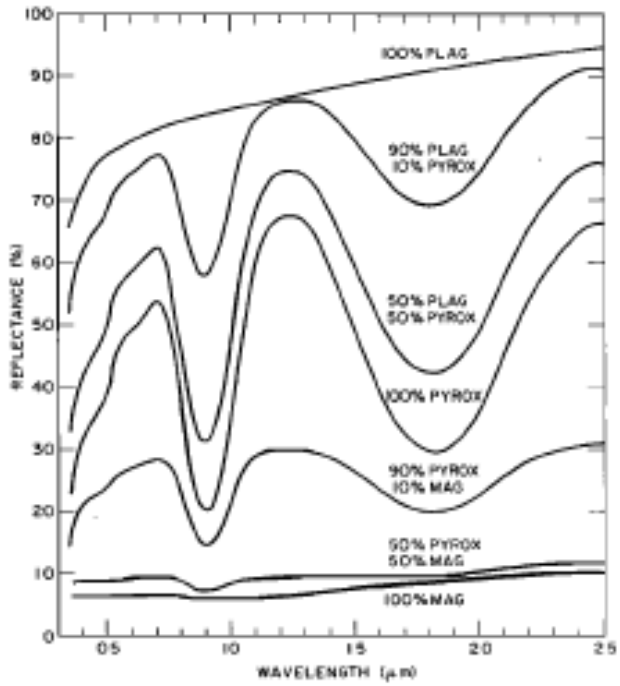

Figure 2 – Mélanges de poudres minérales de plagioclase, de pyroxène et de magnétite (Adams, 1974).

La présence de 90% de plagioclase faiblement absorbant permet encore de voir le détail complet de la bande du pyroxène, alors que 50% de magnétite, qui absorbe fortement, supprime toutes traces des bandes du pyroxène (**Figure 2**) (Nash et Conel, 1974; Adams, 1974).

Si l'on mélange pyroxènes et olivine, les spectres sont dominés par les caractéristiques du pyroxène. Avec un contenu en pyroxène de 50% ou plus, les spectres ressemblent à celui du pyroxène pur.

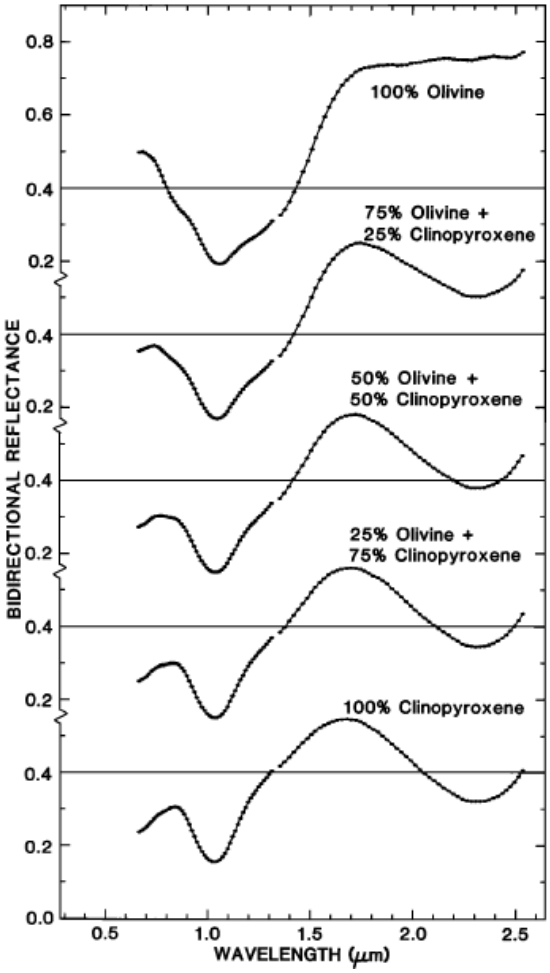

Figure 3 – Les mélanges de poudres minérales de clinopyroxène et d'olivine (Singer, 1981)

Dans les mélanges d'olivine et d'orthopyroxène, la position du minimum de la bande d'absorption pour ces mélanges n'est pas une fonction linéaire de la composition, l'orthopyroxène tend à dominer le spectre de mélange. Avec des quantités d'olivine allant jusqu'à 50%, le minimum de la bande à 1 µm survient pratiquement à la même longueur d'onde que pour l'orthopyroxène pur, et les positions des bandes à 1 et 2-µm suivent la tendance pour des pyroxènes purs. Dans les mélanges d'olivine et de limonite, aussi peu que 5% de limonite modifient considérablement le spectre de l'olivine, mais laissent la structure à trois bandes près de 1 µm reconnaissable (**Figure 4**). Avec 50% de limonite la forme du spectre est très similaire à celle de la limonite pure (Singer, 1981). La magnétite est un minéral opaque commun dans les assemblages de roches mafiques et ultramafiques. Une petite quantité de magnétite est très efficace pour réduire la réflectance spectrale d'un mélange d'olivine et de magnétite. Cet effet est

cohérent avec d'autres études utilisant des mélanges de minéraux opaques et non opaques (Johnson et Fanale, 1973; Pieters, 1973; Nash et Conel, 1974).

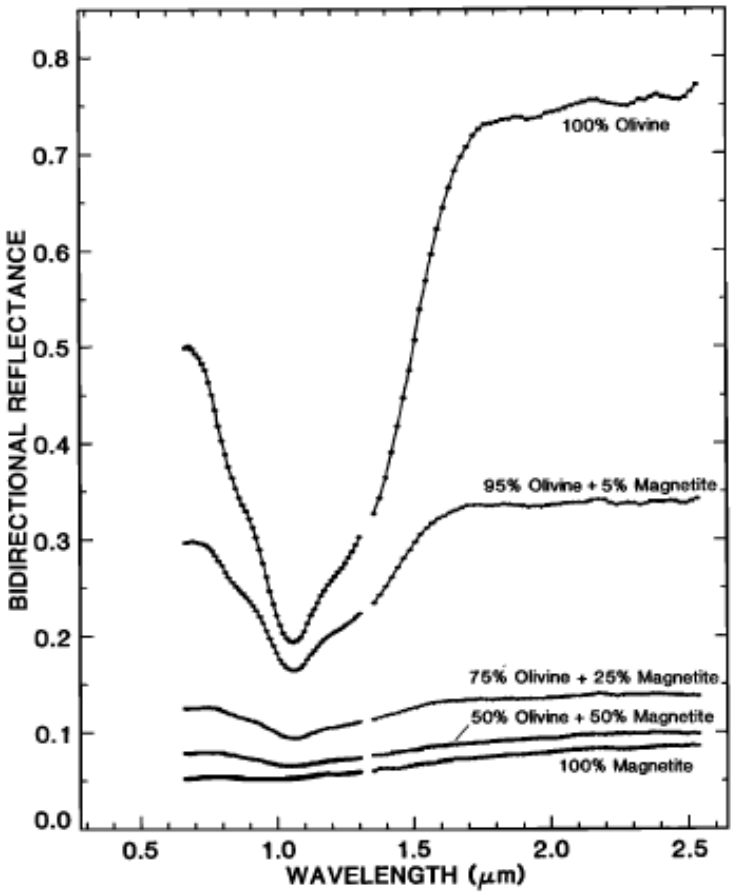

Figure 4 – Les mélanges de poudres de magnétite et d'olivine (Singer, 1981).

Les études empiriques avec mélanges de pyroxène et d'ilménite montrent que le pyroxène a une forte influence sur les bandes d'absorption alors que la présence d'ilménite tend à réduire l'albédo. En d'autres termes, le pyroxène produit l'absorption et d'ilménite réduit l'albédo dans des proportions non-linéaires (Nash et Conel, 1974). L'ilménite est un minerai d'oxyde de titane et de fer caractérisé par une faible albédo. Dans un mélange de plagioclase et d'ilménite, la courbe du plagioclase est abaissée et la bande à 1,3 µm est effacée dès que la quantité d'ilménite dépasse 25%. Également dans un mélange à trois phases, l'ilménite opaque est l'élément dominant qui réduit l'albédo, aplatit le spectre et réduit la profondeur des bandes d'absorption du pyroxène. Cependant la bande à 0,9 µm du pyroxène persiste sur une large gamme de contenus en pyroxène et sa profondeur est directement proportionnelle à l'abondance du pyroxène (**Figure 5**). Par conséquent les minéraux opaques provoquent une déformation minimale des bandes

d'absorption, mais un maximum d'assombrissement du mélange, tandis que le verre non-opaque provoque une déformation maximale des bandes d'absorption, mais un assombrissement minimum (Nash et Conel, 1974). L'assombrissement est produit par de très petites inclusions de fer réduit comme démontré par Pieters et al. (2000). Il est connu que les absorptions causées par les transferts de charges sont beaucoup plus fortes que celles dues aux transitions de champ cristallin (Clark, 1999; Hunt, 1977). Ces types d'absorption sont communs pour les minéraux contenant du fer.

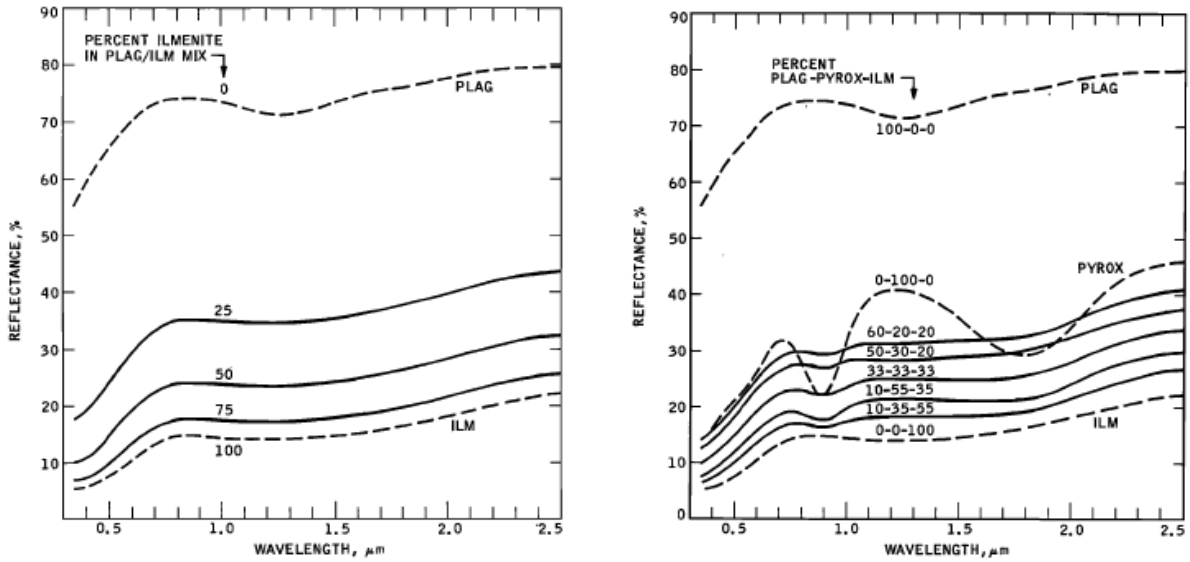

Figure 5 - Les spectres des mélanges ternaires de poudre de plagioclase-pyroxène-ilménite (à gauche) et de plagioclase-ilménite (à droite) (Nash et Conel, 1974).

Dans les mélanges multi-composants, la présence d'une phase spectralement neutre mène à une sous-estimation de la composante ayant la bande d'absorption la plus faible. Plus la différence de contraste entre les bandes est grande, plus grande est l'erreur systématique. Une composante noire domine toujours la réflectance d'un mélange, même lorsque la taille des particules des deux membres est égale. Toutefois, les bandes d'absorption situées à des grandes longueurs d'onde sont moins influencées par le contraste entre les matériaux sombres et clairs (Moroz et Arnold, 1999).

Toutes ces observations ont été produites à l'échelle microscopique, mais il n'a pas été vérifié si à l'échelle macroscopique ces effets avaient des mécanismes similaires.

L'effet de la taille des grains

La prédiction réussie de la composition exige une certaine connaissance de la distribution granulométrique. La taille de grains des minéraux a une influence significative sur la réflectance, la forme spectrale et les profondeurs d'absorption d'un mélange. Un agrégat de particules non-triées présente des propriétés de réflexion très semblables à celles des plus petites tailles de particules dans des poudres, si l'on se base sur l'observation de spectres de poudres de roches silicatées avec différentes tailles de grains (Adams et Filice, 1967). Plus les particules de roches silicatées sont petites moins elles sont absorbantes. Il en résulte une augmentation de la lumière réfléchie. De plus, plus les grains sont petits, plus des absorptions sont faibles. Et *a contrario*, plus les grains sont gros plus les absorptions sont prononcées. Les mélanges composés de minéraux de tailles différentes présentent des phénomènes complexes dus à la diffusion volumique, dans laquelle les propriétés spectrales des matériaux les plus gros prédominent généralement (Clark et Kierein, 1988).

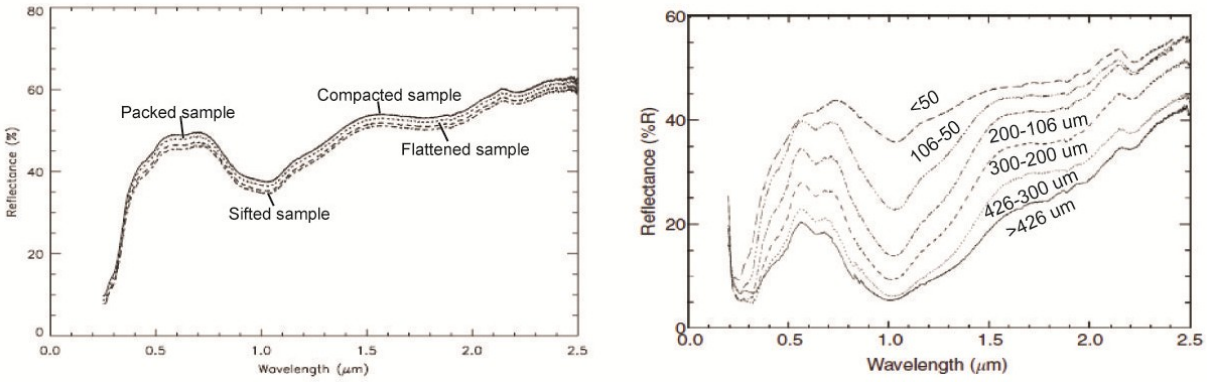

Figure 6 – Spectres de particules de taille comprise entre 50 et 426 µm, obtenus avec des techniques de préparation différentes : particules compactées, tassées, aplaties, échantillons tamisés (à gauche) et spectres de particules de différentes granulométries dont la surface a été lissée (à droite) (Orofino et al, 2006).

Un exemple de spectres (**Figure 6**, à gauche) montre des particules de poudre d'olivine dans la gamme de taille allant de 50 à 106 µm dans le cas d'un échantillon tamisé compacté, échantillon tassé, et d'une surface lissée. Ce graphique montre que non seulement la taille des grains, mais aussi la manière dont l'échantillon est préparé influencent la réflectance. La **Figure 6** (à droite) montre l'exemple des spectres de particules avec des granulométries différentes (Orofino et al., 2006).

Il est généralement observé que la réflectance diminue lorsque la taille des grains augmente, jusqu'à un certain point (appelé granulométrie efficace), après quoi un processus inverse se produit (Hapke, 1993; Moroz, 1999). Les variations dans la taille des particules de l'échantillon de poudre et les variations de rugosité de surface produisent les mêmes effets spectraux : plus la surface est rugueuse, plus la réflectance est basse.

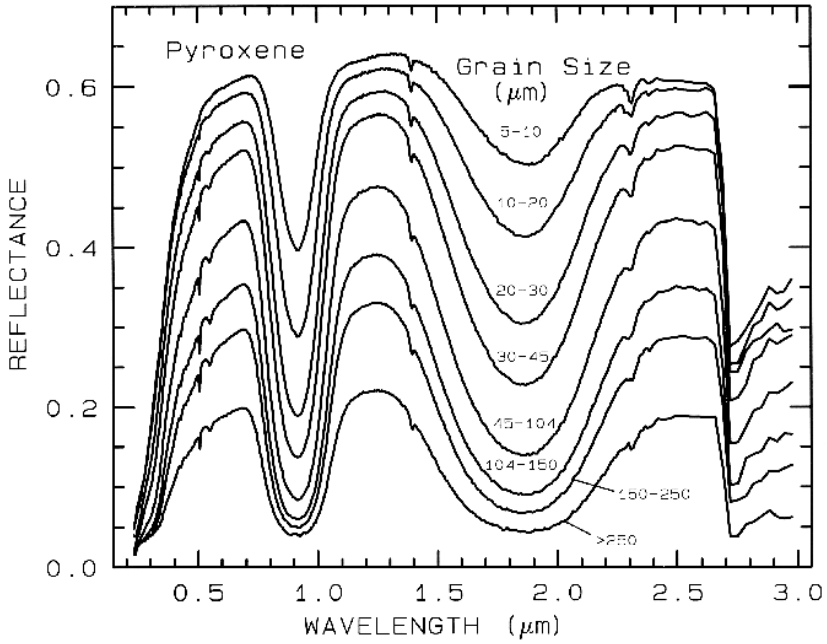

Figure 7 – Spectres de poudre de pyroxène en fonction de la taille des grains (Clark, 1999)

Si l'on se base sur la comparaison des propriétés de diffusion d'échantillons de basaltes avec celles de poudres, des spectres d'échantillons de roches sont caractérisés par des bandes d'absorption profondes et un continuum présentant une pente vers le bleu (Clenet, 2011). L'histoire de la diffusion d'un photon dans une telle texture est similaire dans son principe à son comportement dans un mélange intime. Dans une étude sur du pyroxène et des mélanges d'oxydes de fer par Poulet et Erard (2004), il a été démontré que les différences de réflectance entre la poudre et l'échantillon de roche venaient de la taille des grains de pyroxène et de la teneur en oxyde de fer. Dans le cas de l'échantillon de roche, la petite taille des grains produit des bandes d'absorption plus faibles tandis que le contenu plus important en oxydes de fer diminue les bandes d'absorption. Ce dernier effet est qualitativement cohérent avec l'interprétation de l'effet de maturation dans les régolites, où l'assombrissement est produit par de très petites inclusions de fer réduit (Pieters et al., 2000).

Le régolite est généralement considéré comme représentatif de la composition du substratum rocheux (Pompilio, 2007). L'examen détaillé des spectres de roche est encore dans une phase de développement (Longhi et al., 2000; Harloff et Arnold, 2001; Longhi et al., 2001; Pompilio, 2005). Des questions restent toujours ouvertes concernant principalement : 1) la reproductibilité des spectres de roche par des spectres de mélanges de minéraux en poudre, 2) l'effet de la texture de la roche sur la position et la forme des absorptions diagnostiques des minéraux purs, et 3) la capacité d'un modèle mathématique pour sans ambiguïté résoudre les composantes spectrales dans les spectres de roche.

L'effet de la taille des grains sur les spectres est connue pour des mélanges microscopiques, cependant l'effet de la taille à l'échelle macroscopique peut être associé à la taille de blocs, si les composants du mélange sont des roches (minéraux agrégés). L'influence de la taille des constituants dans des mélanges à macro-échelle n'a pas encore été bien étudiée.

Algorithmes de démixage

Le démixage spectral est la procédure par laquelle le spectre mesuré d'un pixel mixte est décomposé en une collection de spectres de constituants, ou composants, et un ensemble de fractions correspondantes, ou abondance, qui indiquent la proportion de chaque composante spectrale présente dans le pixel (Keshava et Mustard, 2002). La première étape dans une analyse de mélange est de définir un ensemble de composantes spectrales de l'image. Une composante spectrale d'image est contenue dans une scène et a l'abondance physique definitif. Les signaux de pixels mixtes sont généralement modélisés en utilisant soit un modèle linéaire (LMM) ou non-linéaire (NLMM). Un modèle de mélange convertit les comptes numériques de l'image en fractions de quelques composantes spectrales (Adams et Gillespie, 2006). La question de savoir si les processus linéaires ou non linéaires dominent les signatures spectrales des pixels mixtes est une question souvent non résolue (Somers et al., 2011).

Modélisation linéaire

L'hypothèse physique de base d'une LMM est que chaque photon incident interagit avec un seul des composants du pixel. Le prémisse de base de la modélisation de mélange est que dans une scène donnée, la surface est dominée par un petit nombre de matériaux distincts qui ont des propriétés spectrales relativement constantes. Dans la **Figure 8**, la surface réfléchissante est

présentée comme un mélange en forme de damier, et une portion donnée du rayonnement incident interagit avec un seul composant (i.e., pas de diffusion multiple entre les composants). Si la surface totale est considérée comme étant répartie proportionnellement en fonction de l'abondance fractionnelle des composantes spectrales, le rayonnement réfléchi va véhiculer les caractéristiques des médias associés dans les mêmes proportions. En ce sens, il existe dans le rayonnement réfléchi, une relation linéaire entre l'abondance fractionnelle des substances présentes dans la zone observée et les spectres (Keshava et Mustard, 2002).

Un signal de pixel mixte (r) en tant que tel peut donc être décrit comme une combinaison linéaire de signatures spectrales pures de ses éléments constitutifs, pondérées par leur fraction sub-pixellaire (Adams et al., 1986) :

$$r = Mf + \varepsilon \qquad (1.1)$$

Dans l'équation. (1,1) M est une matrice dans laquelle chaque colonne correspond au signal spectral d'une des composantes spectrales spécifiques. f est un vecteur colonne $[f_1,\ldots,f_m]^T$ désignant le pourcentage de couverture occupé par chacune des composantes spectrales m dans le pixel. ε est la partie du spectre qui ne peut pas être modélisée en utilisant ces composantes spectrales (Somers, 2011).

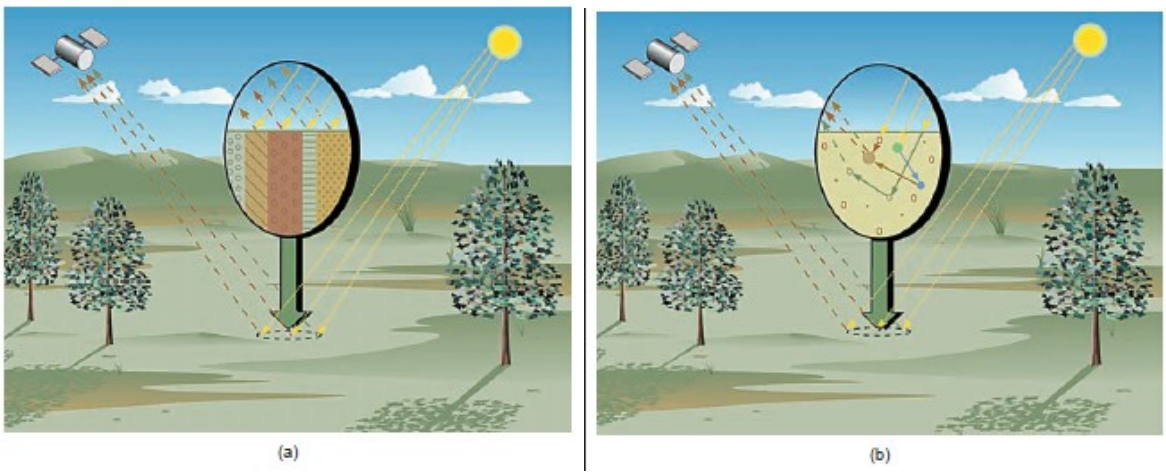

Figure 8 - Schéma de mélange linéaire (a), schéma de mélange non-linéaire (b) (Keshava et Mustard, 2002).

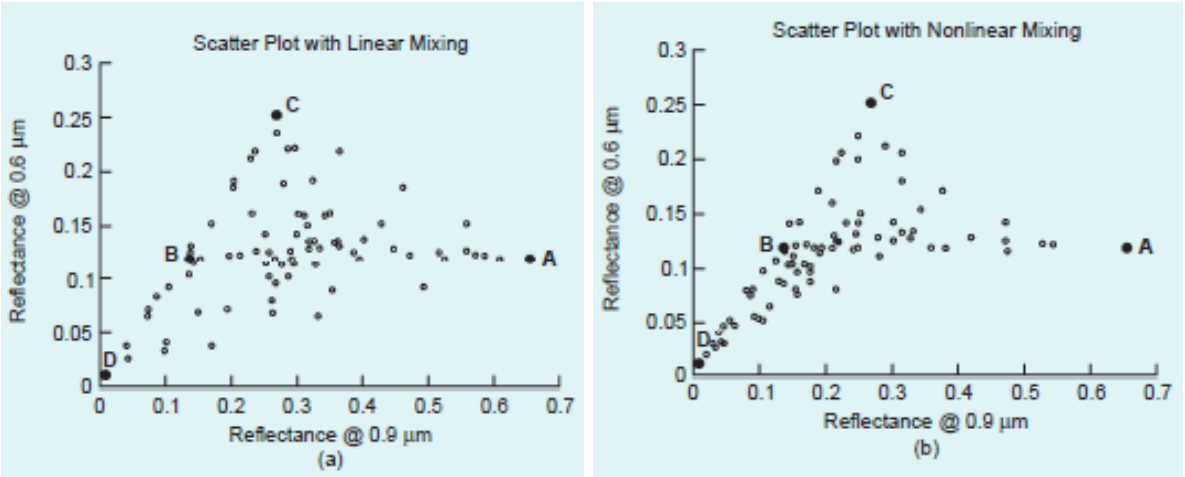

Figure 9 - Diagramme de dispersion avec des mélanges linéaires (a), diagramme de dispersion avec des mélanges non-linéaires (b) (Keshava et Mustard, 2002).

Une approche souvent utilisée pour des modèles linéaires est le SMA (Analyse des Mélanges Spectraux). C'est un modèle à base physique qui transforme des valeurs de luminance ou de réflectance en variables physiques, qui sont liées à l'abondance sub-pixellaire de composantes spectrales dans chaque pixel. Il fournit des résultats quantitatifs qui peuvent à leur tour être incorporés dans des modèles de processus régissant la distribution des matériaux dans l'image (Tompkins et al., 1997).

L'hypothèse du SMA est que le mélange est systématiquement linéaire, c'est-à-dire que chaque pixel est un mélange de plusieurs composants pondérés par une certaine abondance de surface, et le spectre du mélange est une combinaison linéaire des spectres de réflectance des composantes spectrales. Pour être physiquement réalisable, les coefficients d'abondance doivent être non négatifs et leur somme égale à 1 (Keshava, 2003).

Au cours des dernières décennies, un certain nombre de techniques d'analyse d'images pouvant prendre en compte les problèmes de mélange ont été proposées, et le démixage est devenu l'une des techniques plus couramment utilisées dans de nombreuses applications (e.g., Atkinson et Tatnall, 1997; Brown et al., 1999; Carpenter et al., 1999; Guilfoyle et al., 2001; Nascimento et Bioucas-Dias, 2005a; Wang, 1990).

Pour de nombreux problèmes, le modèle linéaire est considéré offrir une précision suffisante pour cartographier les abondances sub-pixellaires dans les données de télédétection (Elmore et

al., 2000), d'autant plus que l'analyse linéaire est mathématiquement plus simple que l'analyse non-linéaire, qui est souvent complexe (Adams et Gillespie, 2006).

Modélisation non linéaire

Les modèles non-linéaires de mélange prennent en compte un processus non linéaire, qui est le produit de la diffusion multiple entre au moins deux matériaux dans le champ de vision. Si, toutefois, les éléments d'intérêt sont dans une association intime (les matériaux des composantes spectrales sont mélangés à des échelles spatiales plus petites que la longueur du trajet des photons dans le mélange), comme illustré dans la **Figure 8**, comme des grains de sable de composition différente dans un dépôt de plage, la lumière interagit généralement avec plus d'un composant, et le mélange systématique entre ces différentes composantes est non-linéaire.

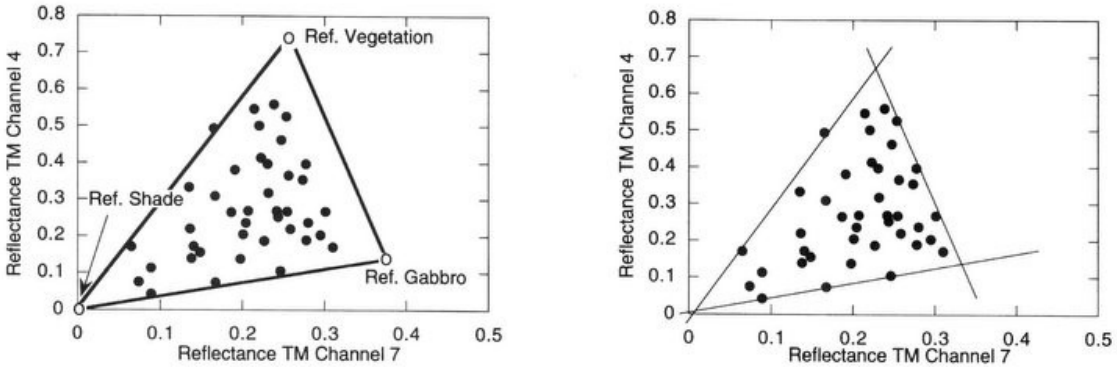

Figure 10 – Diagrammes illustrant le concept de base de l'analyse spectrale de mélanges : à gauche – les composantes spectrales sont tracées et l'espace de mélange défini, (composantes spectrales d'image représentée par des cercles ouverts); droit - techniques automatisées pour l'identification des composantes spectrales qui utilisent l'enveloppe convexe sur le nuage de données pour définir les composantes spectrales (Adams, 1993).

Les modèles non-linéaires de mélanges spectraux (NLMM) tiennent compte de la présence d'interactions multiples des photons par l'introduction d'un terme d'«interaction» dans le modèle de mélange spectral linéaire. Chaque terme compte les interactions multiples entre les composantes spectrales et est représenté par le produit croisé des composantes spectrales interactives (Borel et Gerstl, 1994; Chen et Vierling, 2006; Ray et Murray, 1996).

En utilisant une série de données d'entraînement, les relations mathématiques entre données spectrales d'entrée et données de sortie (classes d'intérêt) peuvent également être automatiquement calculées en utilisant la modélisation informatique avancée, avec des méthodes

comme les réseaux de neurones artificiels (**Figure 10**) (Atkinson et Tatnall, 1997; Carpenter *et al*., 1999; Guilfoyle *et al*., 2001; Mercier *et al*., 2005;). L'existence de mélanges non-lineaires a été clairement établie pour les minéraux dans les sols (e.g., Mustard et Pieters, 1987, 1989; Nash et Conel, 1974; Shipman et Adams, 1987). Cependant les effets quantitatifs de mélange non-linéaire sur la précision des estimations de la couverture fractionnaire restent mal compris.

2. Matériaux et méthodes

La zone d'étude

Le site d'étude choisi pour l'acquisition de données se situe dans la région de Makhtesh Ramon, dans le sud d'Israël. Cette zone a été choisie parce que : 1) elle est dépourvue de végétation, et les affleurements rocheux sont nombreux; 2) Makhtesh est un environnement généralement sans nuages, aride, et donc c'est un site idéal pour acquérir des mesures spectrales en raison des conditions météorologiques, 3) le site contient une grande variété de constituants minéralogiques, notamment des roches sédimentaires, ce qui est particulièrement intéressant pour nous, différents scénarios peuvant y être choisis.

Différents scénarios de mélanges de roches naturelles ont donc été sélectionnés sur le terrain afin de représenter plusieurs situations différentes de mélanges.

Makhtesh Ramon se situe au centre du Néguev, dans le sud d'Israël (**Figure 11**). La région est considérée comme une région extrêmement aride et est presque sans nuages, avec une pluviométrie moyenne annuelle d'environ 85 mm pour la rive nord et d'environ 56 mm dans sa partie centrale. La température moyenne quotidienne en Juillet est de 34 ° C, et tombe à 12,5 ° C en Janvier, alors que la température moyenne annuelle est de 17 à 19 ° C.

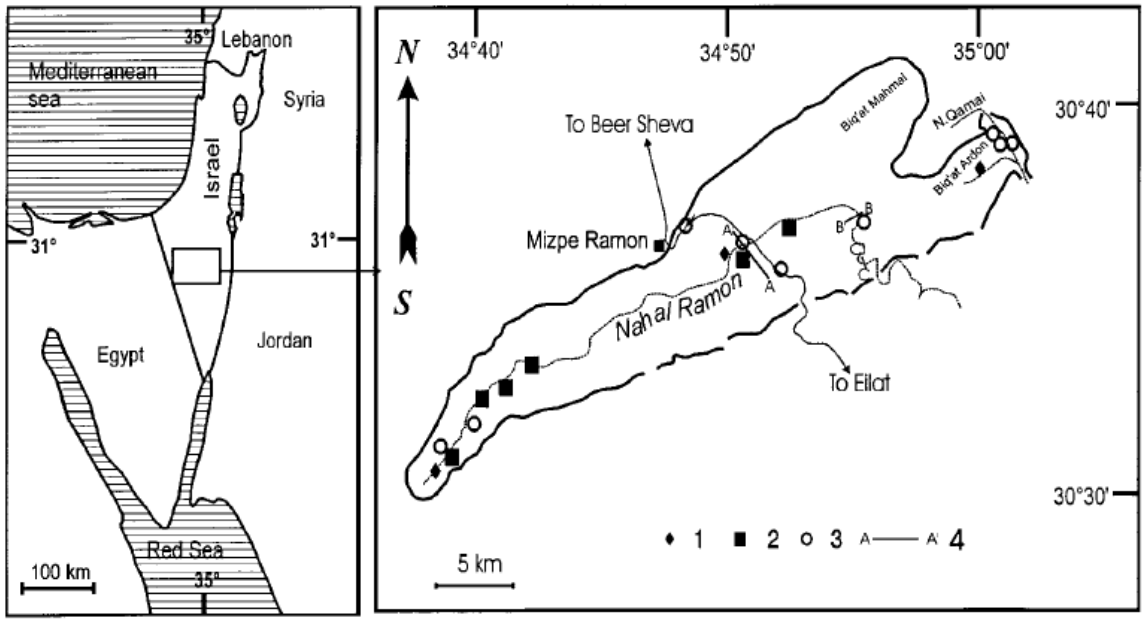

Figure 11 – La zone d'étude, carte de Makhtesh Ramon (Plakht, 1999).

Acquisition des données

Les mesures spectrales sur le terrain ont été obtenues avec un spectromètre portable de type ASD FieldSpec FR2. Cet appareil a 2151 bandes spectrales dans VIS-NIR-SWIR de 0,4 à 2,5 µm avec une résolution spectrale de 1 nm, après ré-échantillonnage. Il permet d'acquérir directement un spectre de la cible et d'exécuter les mesures en réflectance, en luminance ou d'éclairement.

Les mesures spectrales ont été acquises sur le terrain pendant quatre jours, du 12/10/09 au 15/10/09. Ces mesures étaient effectuées aux alentours du midi solaire (plus / moins une heure) pour obtenir un éclairement solaire optimal, un minimum d'effets directionnels, et un minimum d'ombre. Afin de convertir les données en réflectance, une mesure du panneau blanc de référence en Spectralon ® (Labsphere) était effectuée toutes les 5 mesures. Les mesures ont été effectuées avec une visée verticale (nadir, perpendiculaire à la surface), à une hauteur d'environ 80 cm. L'angle de vision (FOV) de l'appareil est de 25 °, par conséquent le champ de vision des scènes mesurées forme un cercle avec un diamètre d'environ 0,35 mètre (**Figure 12**). Un appareil photo numérique (Casio) placé directement sous la poignée du pistolet a permis d'enregistrer les scènes mesurées dans leur état au moment de l'acquisition spectrale.

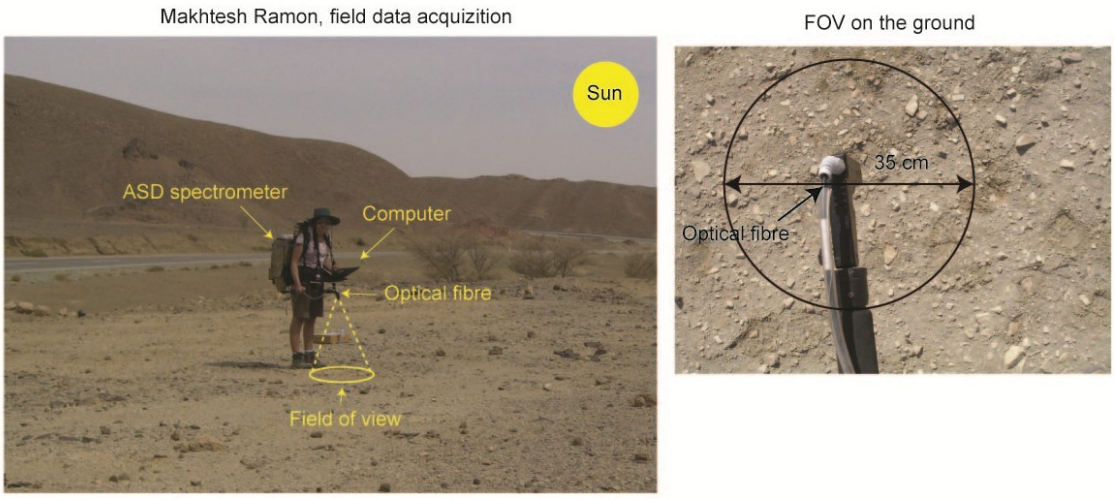

Figure 12 - Collecte de spectres sur le terrain avec le spectromètre portable FieldSpec d'ASD FieldSpec (à gauche), FOV d'une scène sur le terrain (à droite).

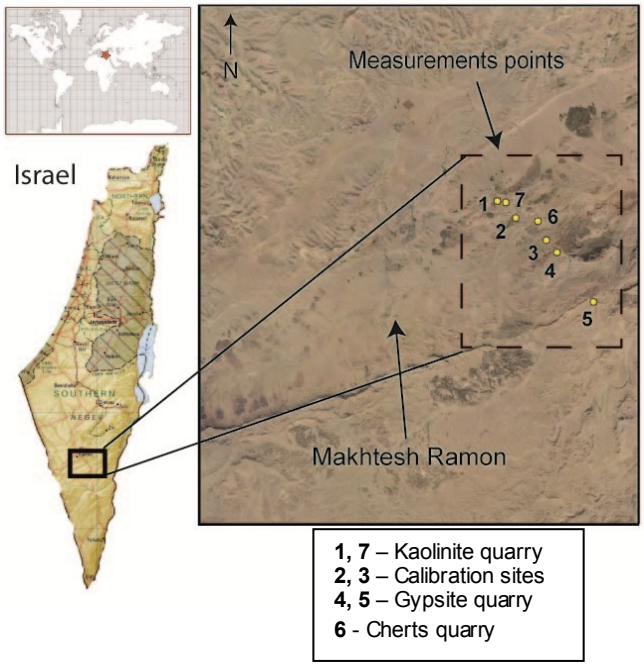

Figure 13 – La zone d'étude de Machtesh Ramon et les sites mesurés.

Le traitement d'échantillons

Des échantillons représentatifs des roches et des sols ont été prélevés sur chaque site dans l'état où ils se trouvaient sur le terrain. Ils ont été emballés avec soin afin d'arriver au laboratoire avec leur condition initiale aussi bien préservée que possible et donc de mieux représenter les mélanges de terrain. Puis au laboratoire, les échantillons ont été identifiés et analysés : type de roche, composition minéralogique, taille de grains, etc.

Les échantillons collectés ont été mesurés avec un spectromètre ASD au laboratoire. Les échantillons recueillis sur les lieux mesurés ont été analysés au microscope pour évaluer la taille des grains et la composition minéralogique. A cet effet des lames minces ont été préparées, ainsi que des poudres pour reproduire des mélanges dans des proportions similaires aux roches qui ont été mesurées sur le terrain, mais à l'état de poudre, et comparer les spectres de terrain et de laboratoire. Les mélanges en poudre sont intimes et vont directement pointer sur les différences entre les mélanges intimes et les mélanges surfaciques, composés de composantes spectrales similaires.

De nombreuses études de mélanges spectraux de minéraux utilisent des poudres, ce qui permet de contrôler facilement les proportions de minéraux dans un mélange, et la distribution granulométrique. Cependant il n'est pas évident que la poudre puisse pleinement représenter des situations de terrain et des pixels mixtes d'environnements naturels.

Des échantillons prélevés sur le terrain ont été broyés puis tamisés afin d'obtenir trois principaux groupes de taille de grain : 100-500 µm, 500 µm-0,7mm, > 0,7 mm-1 mm. La proportion relative de chaque composante a été adaptée en fonction de ce qui avait été observé sur le terrain. Puis les mélanges en poudre ont été mesurés avec la source lumineuse fournie par ASD.

Les échantillons du site 1 collectés sur le terrain sont présentés dans **Figure 14**. Pour chaque type de roche, une lame mince a été préparée, pour identifier les minéraux la composant.

Les spectres des composantes spectrales qui ont été mesurées avec un spectromètre ASD au laboratoire sont illustrés par la **Figure 15**. On observe des variations résultant des hétérogénéités des échantillons, telles que la couverture par une patine, la rugosité de surface, etc. Ces variations sont indiquées en pointillés pour chaque composante spectrale.

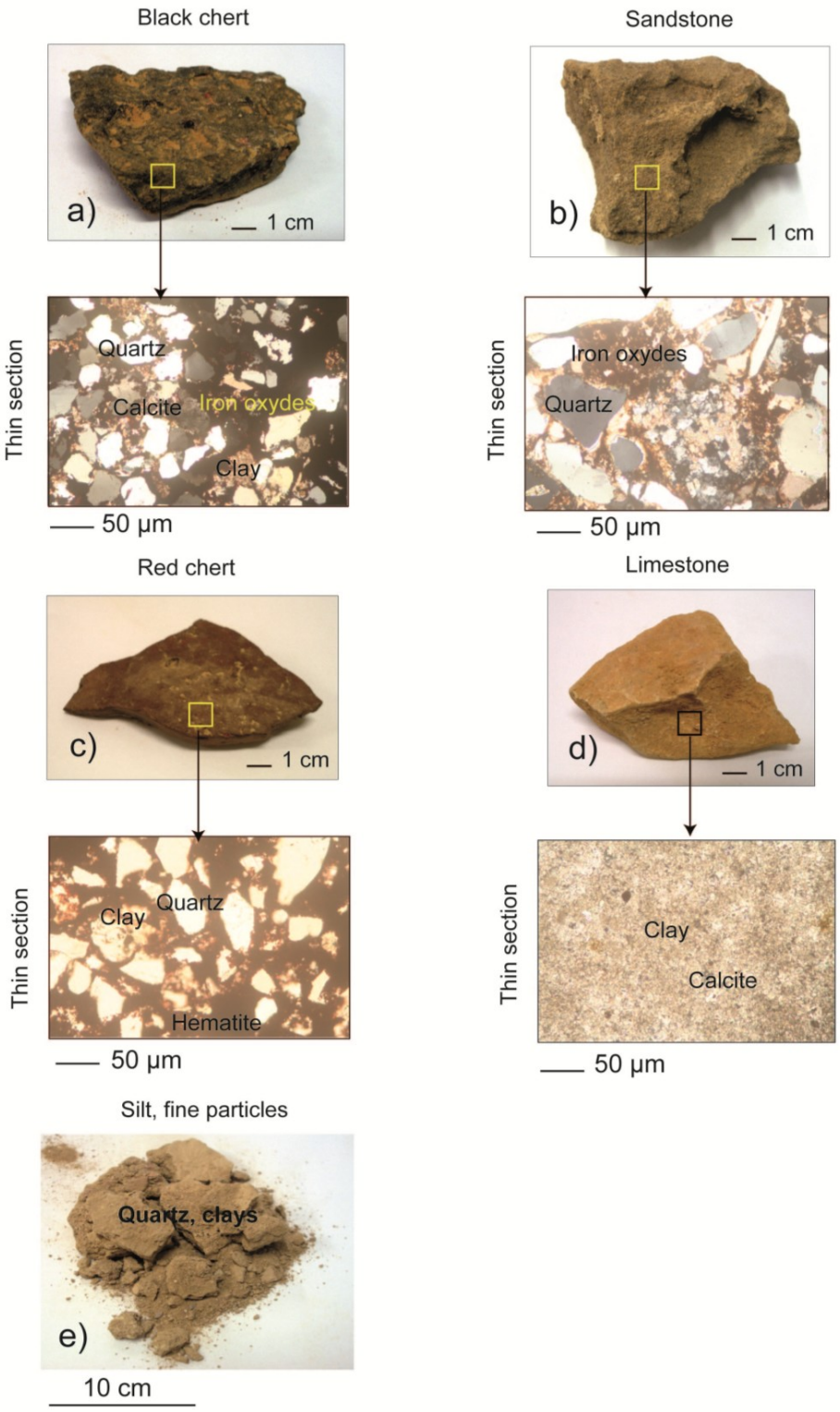

Figure 14 – Echantillons du site 1 et lames minces de chaque échantillon.

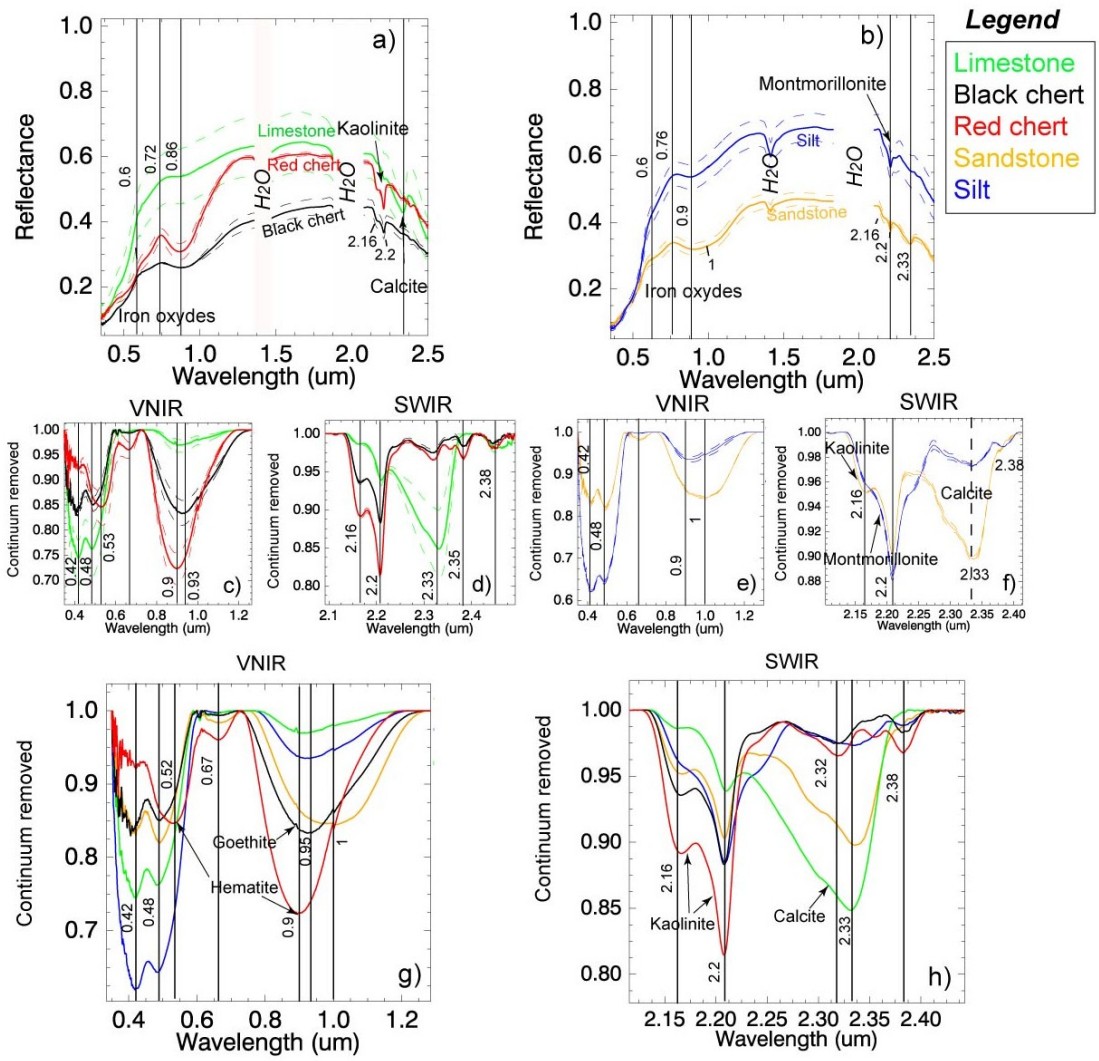

Figure 15 - Spectres des échantillons du site 1 : a, b) gamme complète de spectres; c, e) continuum VNIR enlevé; d, f) continuum SWIR enlevé, les spectres + / - écart type sont représentés en pointillés; g, h) la comparaison des absorptions des composantes spectrales après retrait du continuum.

Le traitement des données

La proportion de chaque composante spectrale qui contribue au mélange a été estimée en appliquant une classification supervisée aux photographies numériques qui ont été prises sur le terrain simultanément aux mesures spectrales. Le résultat des classifications a été validé avec une technique de validation croisée pour estimer la précision et la proportion de mauvaise classification.

Après que les composantes spectrales ont été triées par classes, les images ont été converties en format vectoriel, en utilisant le logiciel ArcGIS.

La distribution de taille des composantes spectrales par scène (en cm^2) a ainsi été obtenue. Ensuite, les paramètres statistiques de tailles par scène ont été calculés : moyenne, minimum,

maximum, écart-type, asymétrie, kurtosis, ont été obtenus pour chaque classe de composantes spectrales en utilisant un logiciel statistique (Origine 8).

Cela permet de comprendre comment la taille des éléments sur le terrain, comme la fraction fine, les graviers, les blocs rocheux, etc., peut influencer les signatures spectrales des mélanges, si leur influence est importante dans l'analyse de mélange à macro-échelle, ou si seule la contribution surfacique des composantes est importante à l'échelle du terrain. Ce paramètre (taille des éléments) n'est pas pris en compte par la modélisation de mélange linéaire, puisque le modèle linéaire prend seulement en compte la contribution surfacique des composantes spectrales. Toutefois, les environnements naturels sont plus sophistiqués que la prédiction du modèle linéaire simple et comprennent des éléments de différentes tailles, qui peuvent également avoir une influence sur la réponse spectrale, et devraient être pris en compte dans la modélisation du mélange.

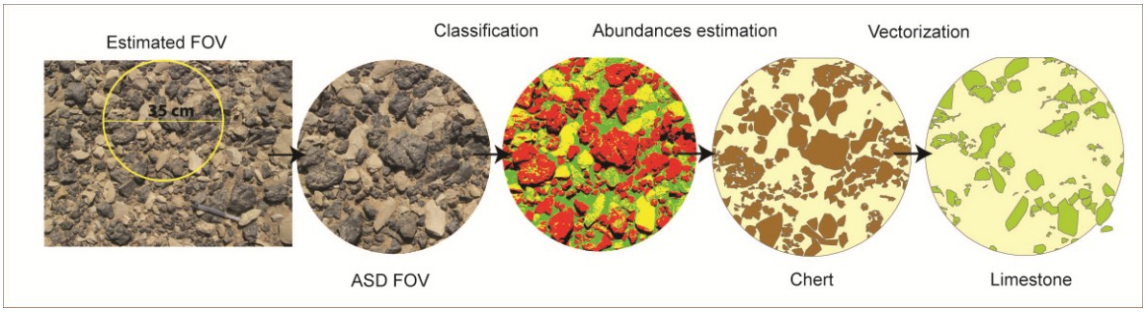

Figure 16 – Étapes du traitement d'image, de l'acquisition de spectres de terrain à l'estimation de l'abondance et la classification.

Le traitement des données spectrales

Chaque spectre de mélange combine les caractéristiques spectrales de ses composantes spectrales. Ainsi les indicateurs spectraux comme la position des absorptions, la profondeur d'absorption, l'intensité de la réflexion et la forme spectrale doivent correspondre à la composition des constituants du mélange.

Si le mélange est une combinaison linéaire des composantes spectrales, les caractéristiques spectrales doivent aussi être combinées proportionnellement. Si le mélange est non-linéaire, nous constatons que les caractéristiques spectrales ne correspondent pas à la combinaison proportionnelle des composantes spectrales. Un certain nombre de paramètres spectraux ont été choisis comme indicateurs des caractéristiques spectrales du mélange. Les paramètres spectraux étudiés sont : la profondeur d'absorption, la surface de l'absorption, la symétrie de l'absorption (**Figure 17**), la pente spectrale, et la différence spectrale normalisée entre le spectre mesuré et le spectre simulé.

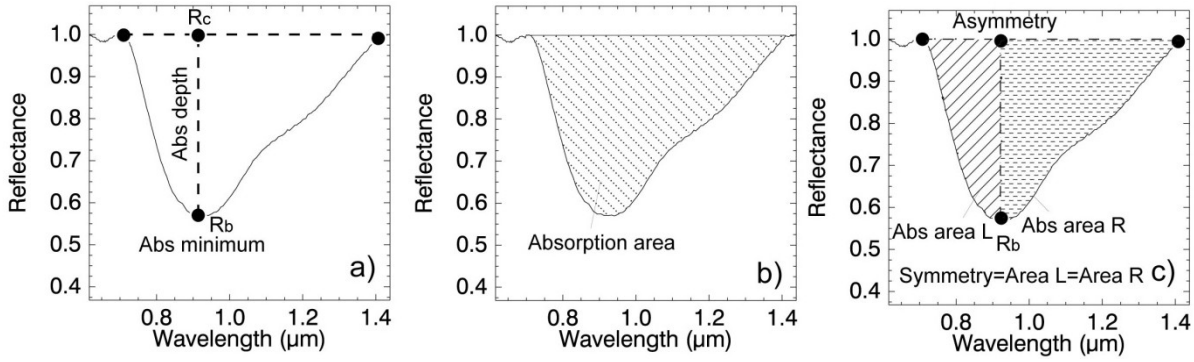

Figure 17 – Caractéristiques d'absorption : profondeur d'absorption (a); surface d'absorption (b); symétrie d'absorption (c).

Ces paramètres sont les indicateurs principaux de la composition du mélange et de la quantité (proportion) de ses minéraux constitutifs. Si un mélange a un comportement non-linéaire et que certains paramètres (caractéristiques d'absorption ou albédo) d'une des composantes spectrales sont masqués par d'autres composantes, l'interprétation spectrale en fonction de ces paramètres pourrait être faussée.

Il sera impossible de détecter une des composantes spectrales dont la réponse spectrale est masquée par d'autres constituants, ou sa contribution pourra être mésestimée. Les paramètres spectraux mentionnés ci-dessus seront donc observés à la fois pour les spectres des composantes et pour les spectres du mélange, étant considérés comme des indicateurs de certaines règles optiques (comportement linéaire ou non linéaire) dans les mélanges.

Patine et la roche fraîche

Les mesures spectrales des échantillons en laboratoire ont été acquises en essayant de préserver l'état naturel de l'échantillon. C'est particulièrement important pour représenter les composantes spectrales de terrain de manière plus précise. Toutefois, des différences significatives entre les spectres des roches patinées et fraiches peuvent être observées. La **Figure 18** montre des spectres de roches patinées et fraîches. La profondeur des absorptions est plus prononcée dans le cas de roches fraîches que de roches présentant une patine. Cette patine couvre une roche suite à des phénomènes d'érosion chimique (oxydation) et de désagrégation physique. Par conséquent le spectre de patine est moins absorbant que celui de roche fraîche. Les caractéristiques d'absorption de roches étant causées par les minéraux qui la composent, si les minéraux sont altérés, l'absorption sera moins prononcée.

La surface fraîche de l'échantillon de chert noir réfléchit davantage que sa surface patinée, les absorptions dues aux oxydes de fer et à la kaolinite sont également plus marquées. Pour le grès, la surface fraîche a une réflectance plus élevée et une absorption plus forte que la roche patinée. Le spectre de la surface fraîche du chert rouge présente également une absorption plus marquée que la surface patinée. De ce fait, si un spectre de roche fraîche est utilisé lors du démixage ou pour la modélisation, il en résultera une surestimation des composantes spectrales correspondantes dans le cas où les roches patinées composent le mélange.

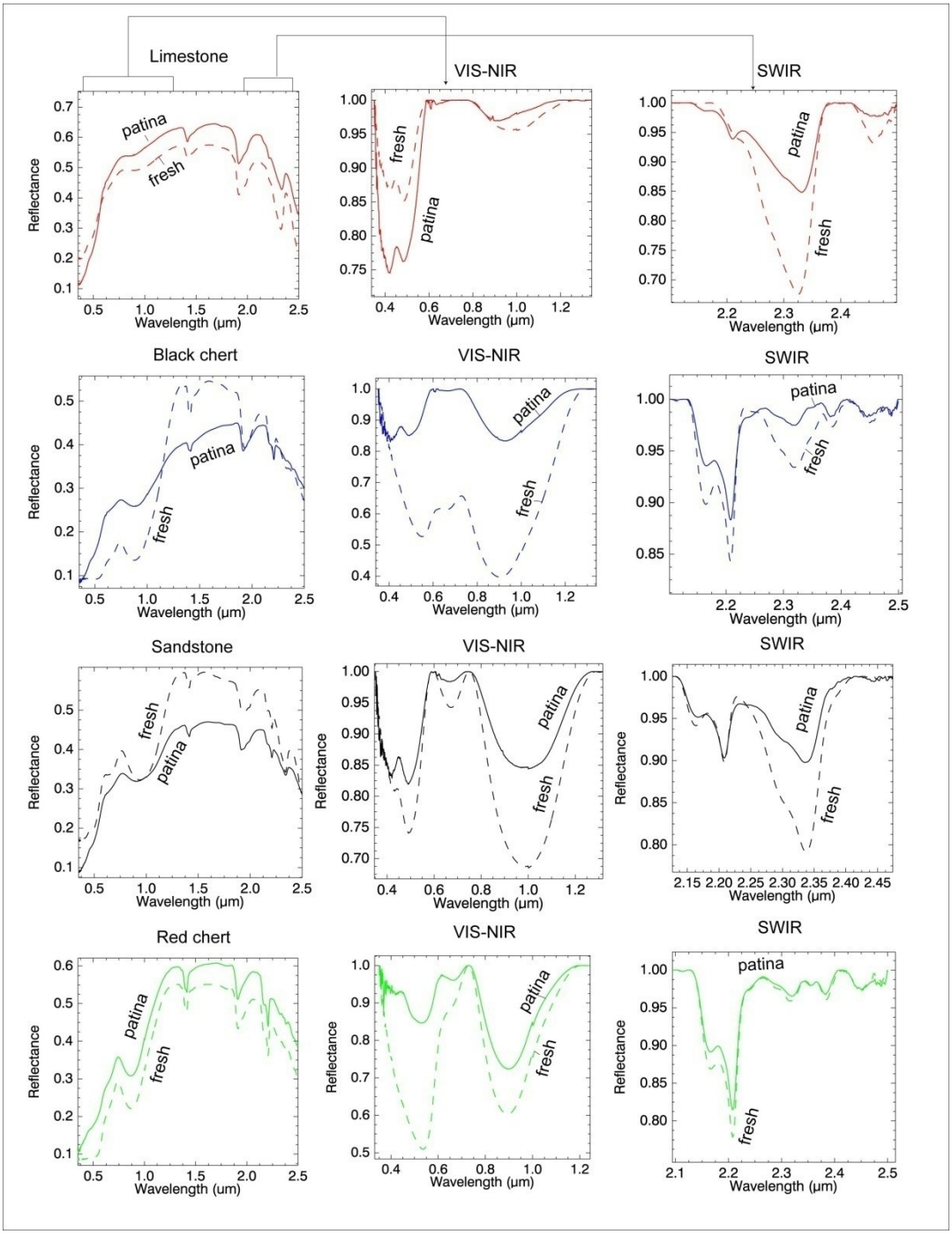

Figure 18 - Comparaison des spectres de la roche avec patine et de la roche fraîche pour différents échantillons, mesurés en laboratoire avec le spectromètre ASD FS3.

Modélisation directe de mélanges linéaires.

Le mélange spectral linéaire est une méthode pour la modélisation de mélanges spectraux à partir de spectres de composantes dont les proportions dans le mélange sont connues. L'objectif de la modélisation directe est de tenter de simuler le spectre FieldSpec ASD des mélanges mesurés sur le terrain. Les fractions qui ont été utilisées sont celles dérivées des classifications des photographies numériques. Les composantes spectrales sont les spectres de laboratoire de chaque composant de base de la scène, et sont utilisées pour créer un spectre synthétique et le comparer à celui mesuré sur le terrain.

Les incertitudes dans les spectres de simulation peuvent avoir plusieurs sources. Les échantillons recueillis sur le terrain peuvent ne pas correspondre exactement aux composantes spectrales qui contribuent au mélange observé (patine différente, croûte d'altération, etc.). L'idée était de collecter des échantillons qui correspondent exactement aux composantes spectrales sur le terrain, mais ce n'était pas toujours facile en raison de l'hétérogénéité des constituants.

Elles peuvent également provenir du positionnement du champ de vision du FieldSpec sur les photographies numériquesqui peut être légèrement décalé au cas par cas. On introduit ainsi un biais dans l'estimation des pourcentages de constituants. Enfin, le pourcentage de couverture pour chaque composant peut être mal estimé à cause d'erreurs d'identification, en particulier si leurs couleurs sont similaires.

Différence spectrale normalisée

La différence normalisée entre les spectres a été calculée et a servi à localiser et à estimer quantitativement les différences entre les deux spectres, le spectre simulé et le spectre mesuré, à chaque longueur d'ondes. L'importance de la différence peut varier selon la longueur d'ondes, et peut être liée à des éléments du mélange et à leurs propriétés. En d'autres termes la différence normalisée contient des informations sur les caractéristiques spectrales qui sont dissemblables dans les deux spectres.

Démixage spectral - modélisation inverse

Démixage linéaire

Dans les surfaces étudiées, les signatures spectrales acquises sur le terrain devraient être bien modélisées par des mélanges linéaires des signatures des composantes spectrales, puisque à l'échelle macroscopique la lumière incidente interagit principalement avec un seul matériau.
Formellement, nous avons :

(1.2) $Y=M\ X+N$

où Y est une matrice $L\ x\ n$ contenant n vecteurs spectraux de taille L, M est une matrice de mélange contenant $l\ x\ p$ signatures spectrales des composantes spectrales de taille L, X est une matrice d'abondance $p\ x\ n$ fractions contenant n vecteurs, une par vecteur spectral acquis, N – une matrice $L\ x\ n$ des erreurs additives et les erreurs de modélisation.
L'algorithme de la classe de volume minimal, appelé SUNSAL a été utilisé pour le démixage linéaire (Bioucas Dias, 2009). La régression éparse est une direction qui a récemment été explorée pour le démixage hyperspectral. Elle utilise à la fois la statistique et les cadres géométriques. Dans cette approche, des vecteurs mixtes sont appliqués à des mélanges linéaires des signatures spectrales d'une bibliothèque spectrale disponible *a priori*. L'estimation des composantes spectrales n'est donc pas nécessaire dans ce type de méthode. La somme des abondances fractionnées est égale à un et celles-ci sont non négatives (contraintes de régression éparses).

Démixage non-linéaire

Une des difficultés dans l'utilisation d'un simple algorithme de démixage linéaire est que les signatures spectrales que nous avons ont été acquises en laboratoire dans des conditions différentes de celles présentes sur le terrain (l'éclairement, la taille des grains, la patine). Afin de pallier cette difficulté, nous avons supposé que les signatures sur le terrain sont liées non linéairement avec celles obtenue au laboratoire via l'expression :

(1.3) $m_f = a_0+a_1\ m_l + a_2\ m_l^b$

Où m_f et m_l sont les réflectances de terrain et de laboratoire des composantes spectrales à une longueur d'onde donnée, et a_0, a_1, a_2, et b sont des paramètres indépendants du modèle.
La justification de la relation ci-dessus provient de la relation non linéaire existant entre l'albédo de diffusion simple et la réflectance dans le cas de mélanges intimes.

Dans ce travail, les deux démixages linéaire et non linéaire ont été appliqués et les résultats obtenus ont été comparés.

3. Résultats principaux

Les résultats des scénarios sur le terrain sont présentés dans le travail en partant des cas les plus simples ayant le plus petit nombre de composantes spectrales aux plus compliqués, avec un grand nombre de composantes spectrales et de paramètres. Les principaux paramètres des mélanges sont : le nombre de composantes spectrales, le type de composantes spectrales, la taille des éléments, l'effet d'ombre, la présence d'une croûte d'altération. Chacun de ces paramètres influe sur la signature spectrale d'un mélange.

Quelques études de cas seront présentées dans cette brève introduction, les principales conclusions seront discutées plus loin.

3.1 Exemples d'analyse de cas de terrain.

Mélanges de deux composantes spectralement très contrastées (Site 6, groupe A).

Pour ce groupe, les mélanges sont des combinaisons d'un constituant sombre (chert noir), contenant une grande quantité d'oxydes de fer sur un substrat clair (silt) composé de quartz (spectralement neutre) et d'argiles. Le contenu en hématite et en goethite dans les cherts peut varier d'un caillou à l'autre en raison de degrés d'altération différents. To facilate nommer des groupes dans le texte, par exemple pour le groupe A à partir du site 6, sera appelé 6-A.

Présentation des cas

		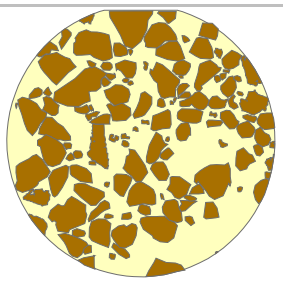	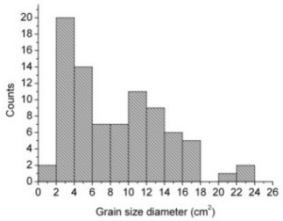
2184	Carte de classification	Chert	Distribution de la taille des éléments

	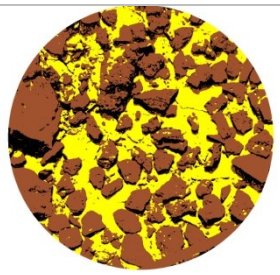	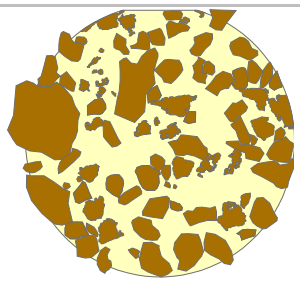	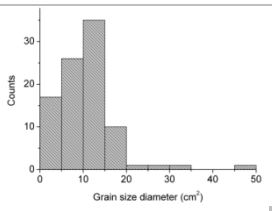
2185	Carte de classification	Chert	Distribution de la taille des éléments
	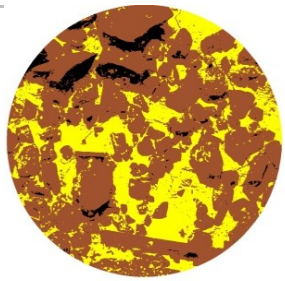	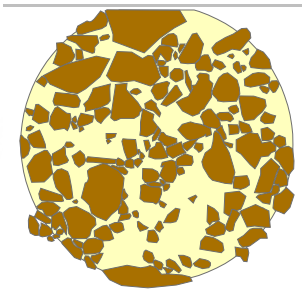	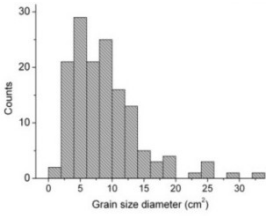
2187	Carte de classification	Chert	Distribution de la taille des éléments
	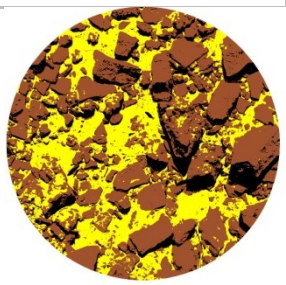	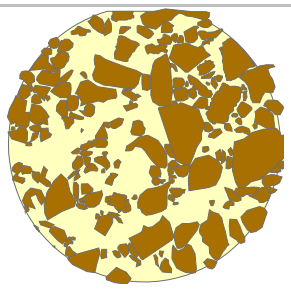	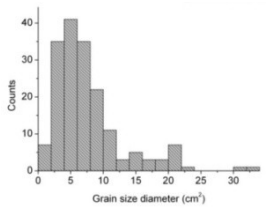
2188	Carte de classification	Chert	Distribution de la taille des éléments
		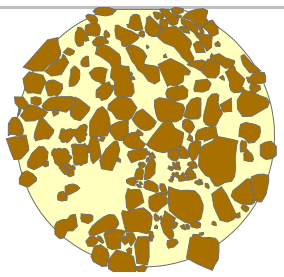	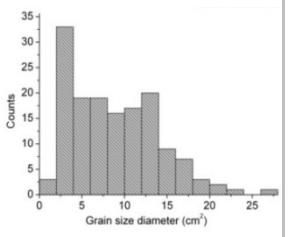
2189	Carte de classification	Chert	Distribution de la taille des éléments

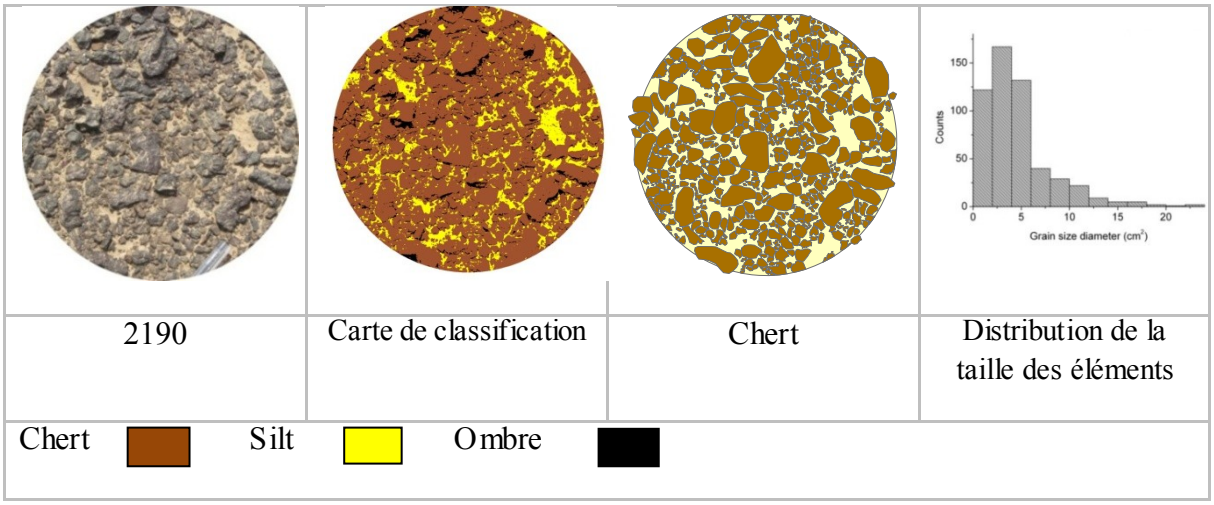

Figure 19 – Mélanges de terrain, cartes de classification et de distribution de la taille d'éléments du site 6, groupe A.

La proportion de chert dans ce groupe de mélanges varie au cas par cas, de faible dans le cas 2185 et 2188 à élevé dans les cas 2187, 2189 et 2190 (**Table 1**).

Table 1 - Abondances de composantes spectrales, mélanges du site 6, groupe A.

ID	Silt%	Ombre%	Chert%	Précision de classification %
2184	34.98	12.50	52.52	99.00
2185	37.68	15.52	55.20	96.00
2187	36.24	5.19	58.56	99.00
2188	31.68	17.47	50.85	98.00
2189	29.99	12.64	57.36	98.00
2190	25.04	5.50	69.45	98.00

Les estimations de pourcentage de couverture prennent en compte l'abondance de tous les constituants, y compris l'ombre, et la précision de la classification est élevée.

Les résultats de classification et la distribution des tailles des éléments pour chaque scène est fournie sur la **Figure 19**, des statistiques complètes sur la taille des éléments se trouvent dans l'annexe.

Pour le cas **2184,** l'abondance de chert est élevée (52,5%), la taille des éléments est d'environ 8 cm^2 en moyenne. Ce n'est pas une taille très grossière par rapport aux autres cas. Un écart-type élevé indique la variabilité des tailles de blocs, qui varient de petits graviers à gros blocs. L'abondance de silt est de 35%..

Pour le cas **2185,** l'abondance de chert est de 55,2%, de silt de 38%. Dans ce mélange, les éléments de chert sont plus grossiers que dans le cas précédent, avec une taille moyenne de 10 cm^2. Les blocs les plus gros sont observés dans cette scène, atteignant 45,35 cm^2.

Dans le cas **2187,** il y a une grande quantité de chert (59%), l'abondance de silt atteint 36%, la taille des éléments de chert est de 9 cm^2 en moyenne, avec des éléments grossiers, mais la quantité de petits éléments est plus élevée. L'écart type des tailles d'élément est de 7,73 cm^2.

Dans le cas **2188,** le contenu en chert est de 51%, en silt de 32%, la taille moyenne des éléments de chert est de 7,6 cm^2. C'est la plus petite moyenne par rapport aux autres, et l'écart type est de 6,13 ; les éléments ont environ la même taille, comme on peut le voir sur la photographie.

Le cas **2189** est composé de chert (57%) et de silt (30%), la taille des blocs de chert est d'environ 9 cm^2 en moyenne, l'écart type est de 8,24, ce qui signifie qu'il y a des variations de taille dans cette scène.

Dans le cas **2190,** le chert couvre presque tout le champ de vision (70%), tandis que la proportion de silt est d'environ 25%. Toutefois, la taille des éléments pour le chert est plus petite, 4,6 cm^2 en moyenne. L'écart-type de la taille des éléments est le plus faible (3,65) par rapport aux autres cas ; cela signifie que la distribution des tailles est assez homogène.

Les caractéristiques spectrales

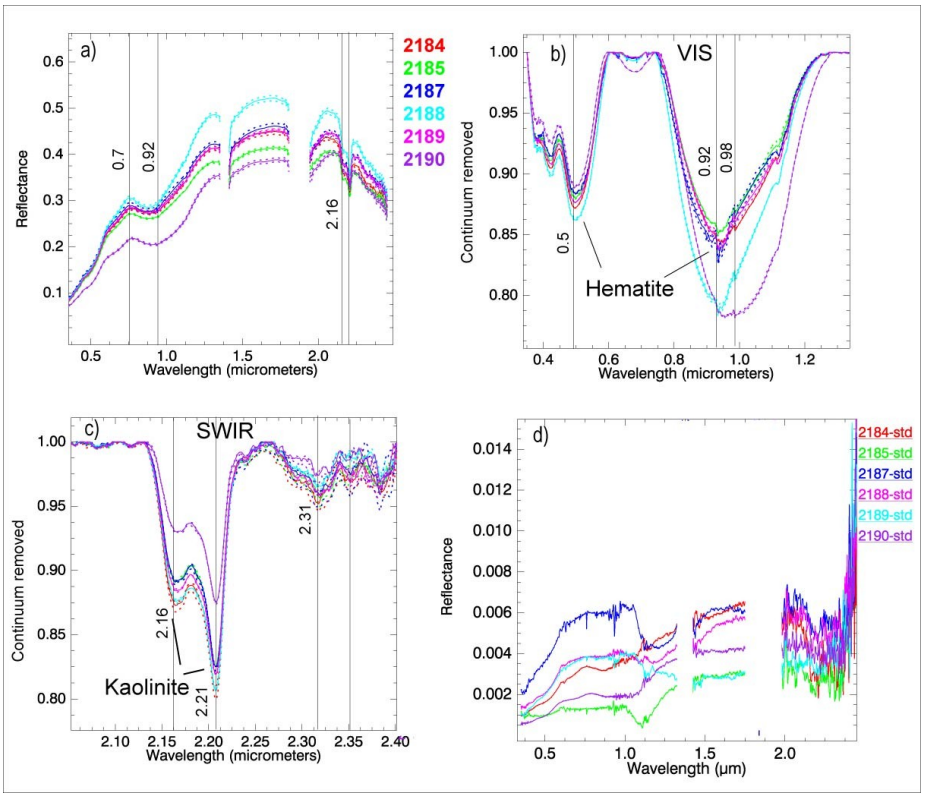

Figure 20 – Spectres de terrain de mélanges, le site 6, groupe A : a) spectres des scènes; b) VNIR continuum enlevé; c) SWIR continuum enlevé; d) Ecart type des spectres de terrain.

Les spectres du groupe A sont présentés sur la **Figure 20**, avec (a) la gamme spectrale complète, (b) le VNIR continuum enlevé, (c) le SWIR continuum enlevé, et (d) l'écart type des mesures sur le terrain: les valeurs d'écart type sont faibles, moins de 0,1%, les spectres deviennent plus bruités à la fin du SWIR.

À partir des mélanges observés, le plus haut niveau de réflexion relève du cas 2188. Dans ce cas, l'abondance du silt est relativement élevée (51%), et le contenu de chert est relativement faible (32%), comparativement à d'autres mélanges. L'absorption de l'hématite, située à 0,92 µm, avec une asymétrie négative, et elle est bien marquée. La taille des éléments de cherts est relativement petite (taille moyenne de 7,6 ± 6,13 cm^2), de nombreux petits graviers peuvent être observés dans la scène. La réflectance la plus basse a été acquise pour le cas 2090. Dans ce cas, le chert est une composante spectrale dominante, il couvre presque la totalité du champ de vision (70%), tandis que la quantité de silt est d'environ 25%. L'absorption des oxydes de fer, autour de 0,96 µm, est le plus marquée dans ce cas. Les cherts dans cette scène sont riches en oxydes de fer de type goethite, qui est identifiable grâce à son absorption située à 0,96 µm. Pour le cas 2188, l'absorption des oxydes de fer a son minimum à 0.95 µm, elle est bien prononcée et asymétrique; le minimum est déplacé vers les longueurs d'ondes plus courtes, ce qui indique l'hématite (**Figure**

20 b). L'absorption de 0,4 à 0,6 µm est également asymétrique, avec un minimum à 0,5 µm qui est également un indicateur de l'hématite. Pour les cas 2184, 2185, 2187 et 2189, les profondeurs d'absorptions des oxydes de fer sont dans la même gamme. Ces mélanges ont les mêmes proportions de chert.

La double absorption de la kaolinite à 2.16 - 2.20 µm a la même intensité dans tous les cas sauf pour le cas 2190. L'absorption à 2,2 µm est relativement faible dans le cas 2190 par rapport à d'autres scènes. Ce mélange contient moins de silt, donc moins de kaolinite. L'absorption à 2,31 µm est due à la dolomite présente dans les cherts ; dans les mélanges avec un contenu plus élevé de chert, elle devient plus profonde, mais cette absorption n'est pas très prononcée pour tous les cas observés.

Table 2 - Caractéristiques d'absorption des scènes de terrain, le site 6, groupe A

Cas ID	Min wvl 0.44-0.61	Min wvl 0.73-0.99	Abs area 0.95	Abs area 2.2	Asymmetry 0.95	Abs. depth			
						0.42	0.48	0.95	2.2
2184	0.497	0.942	0.043	0.010	-0.011	0.095	0.118	0.156	0.162
2185	0.498	0.934	0.040	0.009	-0.011	0.089	0.110	0.146	0.142
2187	0.499	0.935	0.043	0.009	-0.009	0.085	0.106	0.160	0.141
2188	0.498	0.935	0.058	0.010	-0.012	0.100	0.127	0.208	0.157
2189	0.498	0.935	0.043	0.009	-0.012	0.091	0.114	0.158	0.147
2190	0.498	0.960	0.067	0.006	-0.017	0.074	0.100	0.217	0.098

Mélange linéaire (modélisation directe)

La modélisation directe est une combinaison linéaire (surfacique) des composantes spectrales en utilisant les abondances qui ont été dérivées à partir des cartes de classification. Dans ce groupe, les fractions de deux composantes spectrales ont été prises en compte, à l'exclusion de l'ombre et d'autres effets non-linéaires. Les spectres des composantes spectrales utilisées pour la modélisation sont présentés sur la **Figure 21**, avec la gamme spectrale complète et le continuum retiré du VIS et du SWIR.

Le modèle linéaire montre de bons résultats pour les cas prédits. Les niveaux d'albédo correspondent bien aux mélanges de terrain. Toutefois pour la plupart des cas, le modèle prédit une albédo plus élevée que ce qui a été mesuré sur le terrain. L'estimation de la forme spectrale dans le VIS est meilleure que dans le NIR.

Dans le NIR, le modèle prédit des pentes plus élevées pour les spectres des cas 2184, 2185, 2187, 2189 et 2190. La différence entre le modèle et les spectres de terrain est plus faible pour

les cas 2184, 2185 et 2187, et plus élevée pour les cas 2189 et 2190. L'absorption dans le visible liée aux oxydes de fer est surestimée dans tous les cas, sauf pour 2188, pour lequel le modèle a prédit une meilleure absorption de l'hématite avec un minimum à 0,90 µm (**Figure 22**).

Les cas 2189 et 2190 sont des mélanges avec une dominante de chert ; la réflectance de terrain de ces mélanges est plus faible que celle estimée par la modélisation linéaire. Pour ces cas, les constituants sombres ont une influence supérieure à leurs abondances. L'absorption des oxydes de fer dans les spectres modélisés est plus influencée par l'hématite (asymétrie d'absorption à gauche), leur profondeur est légèrement surestimée.

Dans le cas 2188, la prédiction du modèle est proche de la forme spectrale des données de terrain et les réflectance sont très similaires, l'absorption dans le VIS correspond bien mais un petit décalage vers les longueurs d'ondes plus longues est observé. Dans le SWIR une très bonne absorption de la kaolinite est observée. Dans ce cas, le contenu en chert est plus faible que dans les autres cas.

Les spectres des composantes spectrales utilisées pour le modèle, + / - écart type, sont illustrés en pointillés.

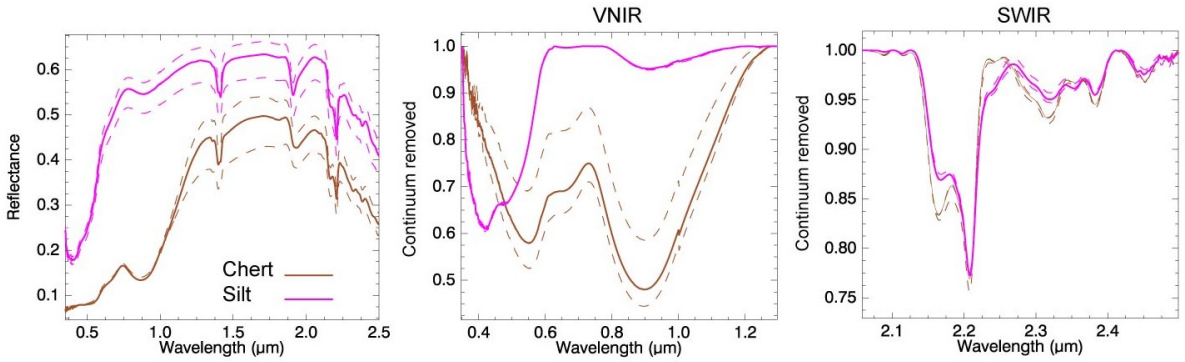

Figure 21 – Spectres des composantes spectrales des mélanges.

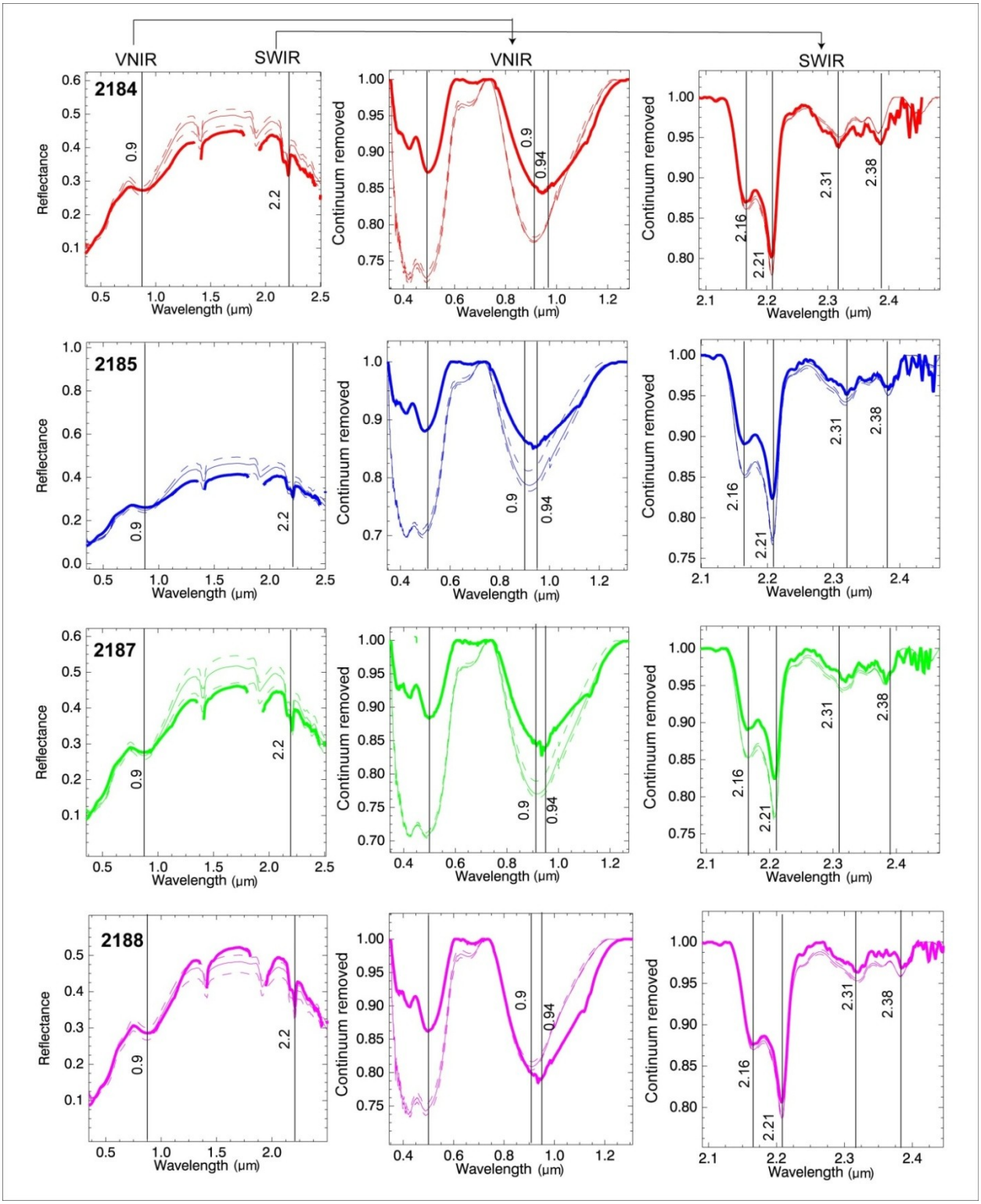
VNIR
SWIR
VNIR
SWIR
2184
2185
2187
2188
Reflectance
Continuum removed
Wavelength (μm)
0.9
0.94
2.16
2.21
2.31
2.38
2.2

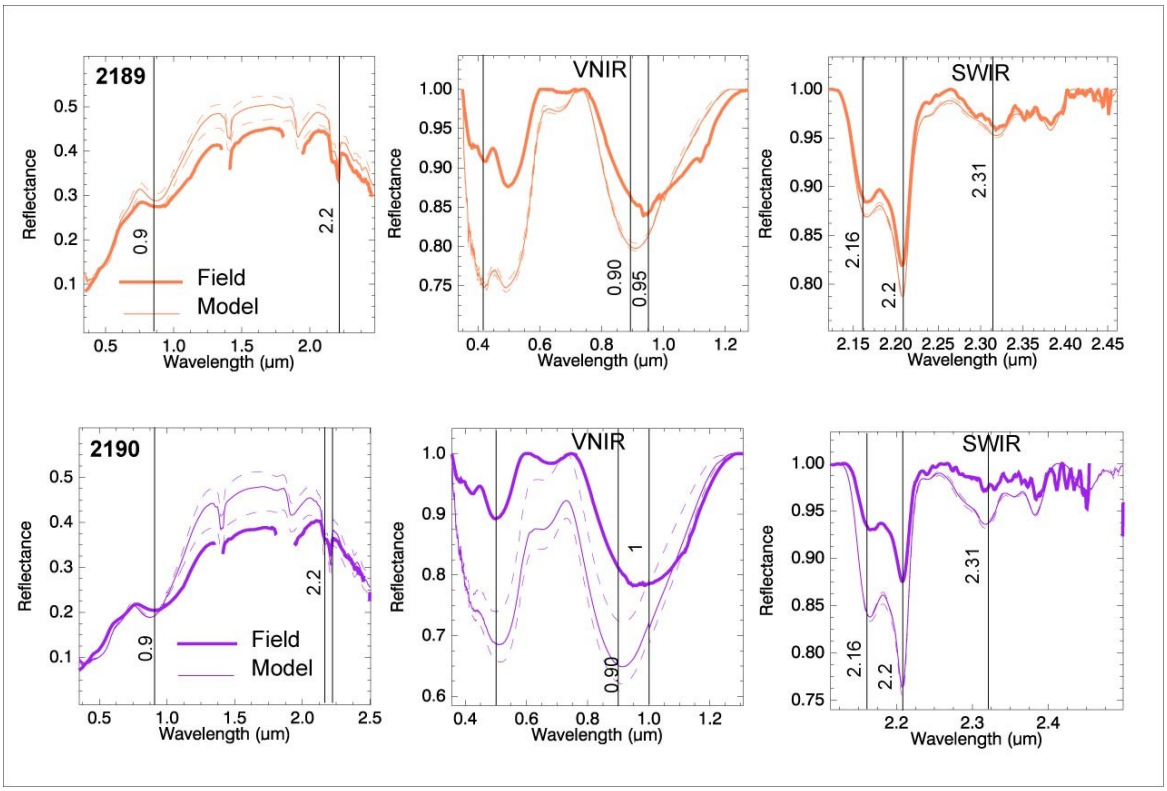

Figure 22 - Spectres modélisés par rapport aux spectres de terrain, les lignes en pointillés indiquent les spectres modélisés + / - écart type des mélanges du site 6, groupe A.

Formules utilisées pour les mélanges linéaires (modélisation directe) :

2184 = *(0.3498 * Sp $_{Silt}$) + (0.5252 * Sp $_{Chert}$)*

2185 = *(0.3768 * Sp $_{Silt}$) + (0.5520 * Sp $_{Chert}$)*

2187 = *(0.3624 * Sp $_{Silt}$) + (0.5856 * Sp $_{Chert}$)*

2188 = *(0.3168 * Sp $_{Silt}$) + (0.5085 * Sp $_{Chert}$)*

2189 = *(0.2999 * Sp $_{Silt}$) + (0.5736 * Sp $_{Chert}$)*

2190 = *(0.2504 * Sp $_{Silt}$) + (0.6945 * Sp $_{Chert}$)*

Différence Normalisée

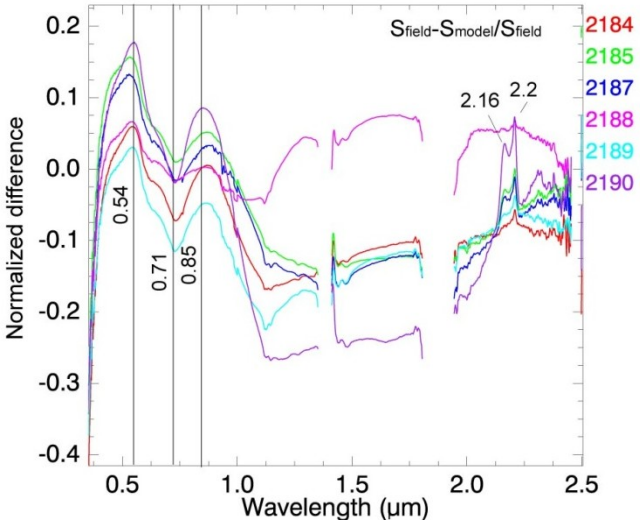

Figure 23 – Différence normalisée entre spectres de terrain et spectres modélisés.

La différence entre les spectres modélisés et de terrain est représentée sur la **Figure 23**. La différence est positive dans le VIS et négative dans le NIR. Dans le SWIR, la différence est relativement faible, et ses valeurs sont proches de 0. Les pics ou les creux à 0,54, 0,71 et 0,85 µm résultent de différences dans le contenu prédit en oxydes de fer : l'estimation du type d'oxyde de fer et de leur quantité ne correspond pas à la réalité. La différence dans le NIR est négative dans tous les cas, sauf pour le cas 2188, pour lequel la prévision par le modèle linéaire dans le NIR a été plus élevée que ce qui était observé sur le terrain. Les pentes des spectres modélisés dans le NIR sont plus élevées que sur le terrain. Le continuum et les pentes des spectres de mélanges dans le NIR sont plus bas que la prédiction du modèle linéaire. Le chert « assombrit » donc les spectres plus que ne le laisse prévoir sa proportion. Cet effet est mis en évidence dans le cas 2190, où le chert couvre presque toute la scène, avec comme résultat une réflectance faible ; dans le spectre de différence normalisée, des valeurs négatives dans le NIR indiquent la plus grande différence entre modèle et spectre de terrain. Par ailleurs, les différences de position de l'absorption du fer entre le modèle et les spectres de terrain peut résulter du fait que l'échantillon de chert collecté sur le terrain est riche en hématite, alors que sur le terrain, nous observons des cas avec l'absorption de la goethite (2189 et 2190).

Démixage spectral - modélisation inverse

Les spectres des composantes spectrales ont été utilisés comme entrées de l'algorithme de déconvolution. Les proportions résultantes ont été comparées à celles estimées à partir des photographies. Les deux démixages, linéaire et non linéaire ont été appliqués, le résultat est montré sur la **Figure 24**.

Le démixage linéaire prédit des abondances qui correspondent mieux au terrain que le démixage non-linéaire. L'algorithme non-linéaire a légèrement surestimé le contenu de silt dans les mélanges. Dans ce cas, l'algorithme non-linéaire a été moins efficace que le linéaire.

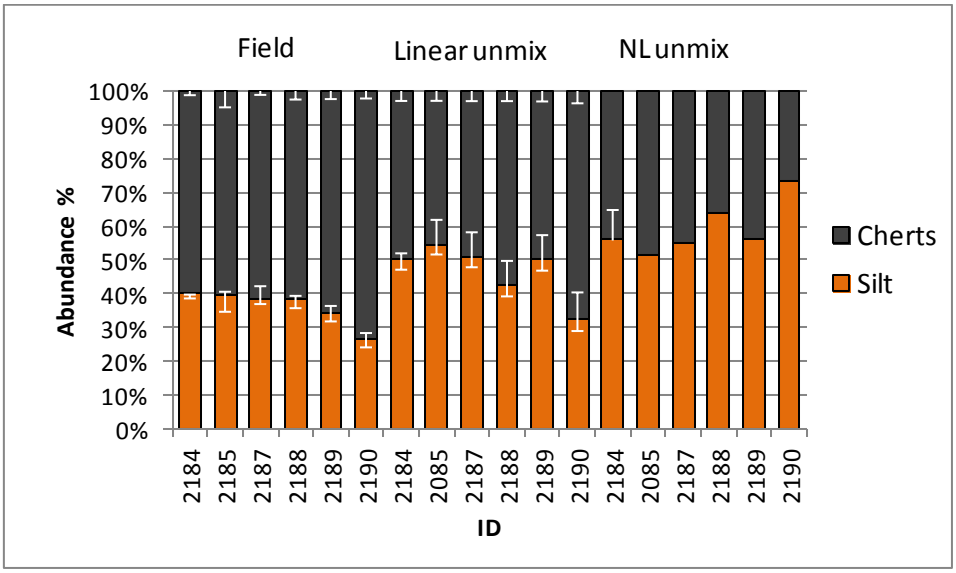

Figure 24 – Résultats de démixage pour le site 6, group A : resultats du démixage linéaire et non linéaire par rapport à l'abondance de terrain.

Table 3 –Erreurs de demixage (RMSE).

Linear un-mixing all spectra					
2184	**2085**	**2187**	**2188**	**2189**	**2190**
0.0089	0.0115	0.0126	0.0101	0.0136	0.0236
Non-linear un-mixing					
2184	**2085**	**2187**	**2188**	**2189**	**2190**
0.0086	0.0085	0.0099	0.012	0.0112	0.021

L'observation de ce groupe de cas a montré que le modèle linéaire peut être utilisé pour représenter ces mélanges de terrain. Cependant il y a certains facteurs, qui dérivent de conditions de mesure différentes, comme la non homogénéité des éléments, leur différence de taille des éléments, et l'ombre qui introduisent des effets non linéaires dans le mélange. Dans les cas où ces

facteurs sont minimes, le modèle linéaire donne le meilleur ajustement. Mais dans les cas où ces effets non linéaires sont élevés, le modèle non-linéaire devrait être utilisé. Pour ce groupe de mélanges 6-A, les effets non linéaires ne sont pas élevés, donc la démixage linéaire a donné un meilleur résultat dans l'estimation de l'abondance que le démixage non-linéaire.

Mélanges de trois composantes spectralement contrastées (Site 1, Groupe B).

Ce groupe de mélanges est composé de trois composantes spectrales : des blocs de chert noir et de calcaire, et du silt. Dans ces cas, les constituants les plus abondants sont les calcaires et les cherts noirs et la fraction de silt est mineure.

	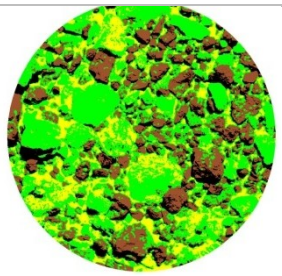 Carte de classification	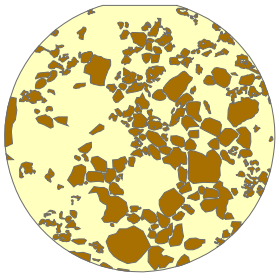 Chert noir	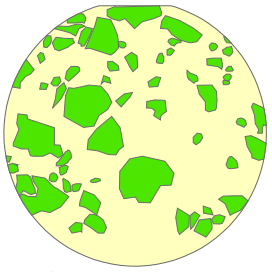 Calcaires
2049		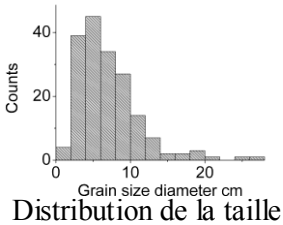 Distribution de la taille des éléments	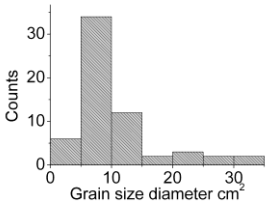 Distribution de la taille des éléments
	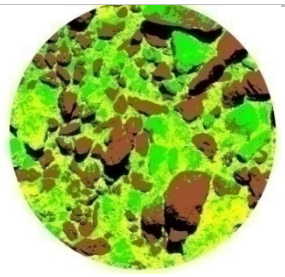 Carte de classification	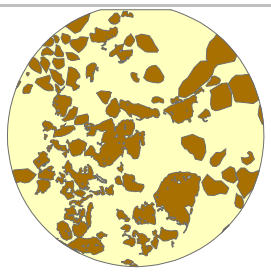 Chert noir	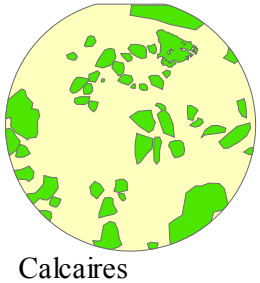 Calcaires
2050		Distribution de la taille	Distribution de la taille

		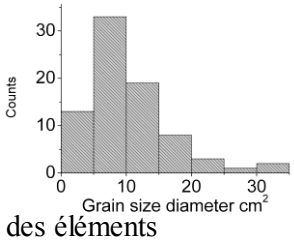 des éléments	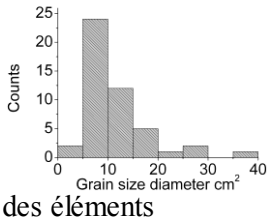 des éléments
	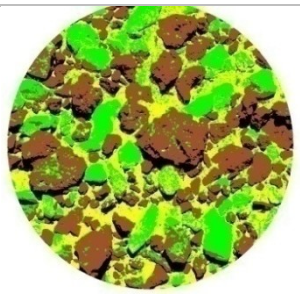 Carte de classification	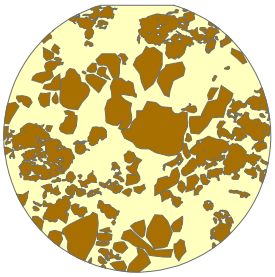 Chert noir	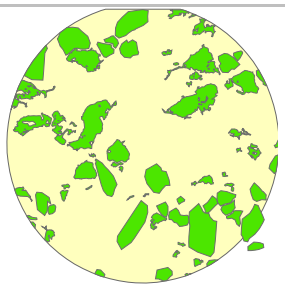 Calcaires
2051		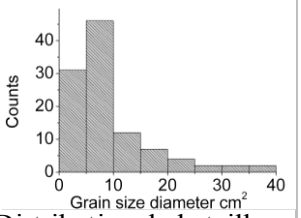 Distribution de la taille des éléments	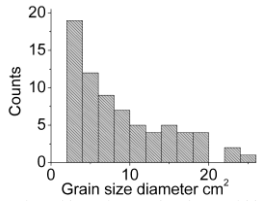 Distribution de la taille des éléments
	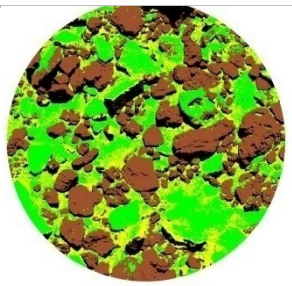 Carte de classification	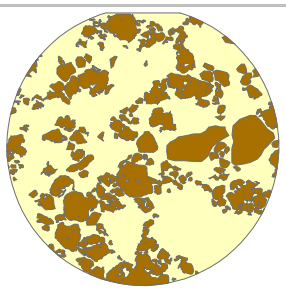 Chert noir	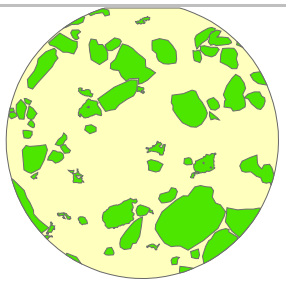 Calcaires
2052		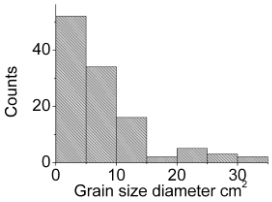 Distribution de la taille des éléments	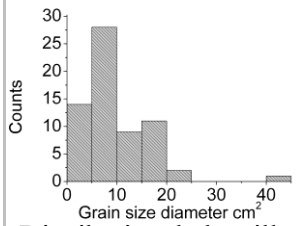 Distribution de la taille des éléments

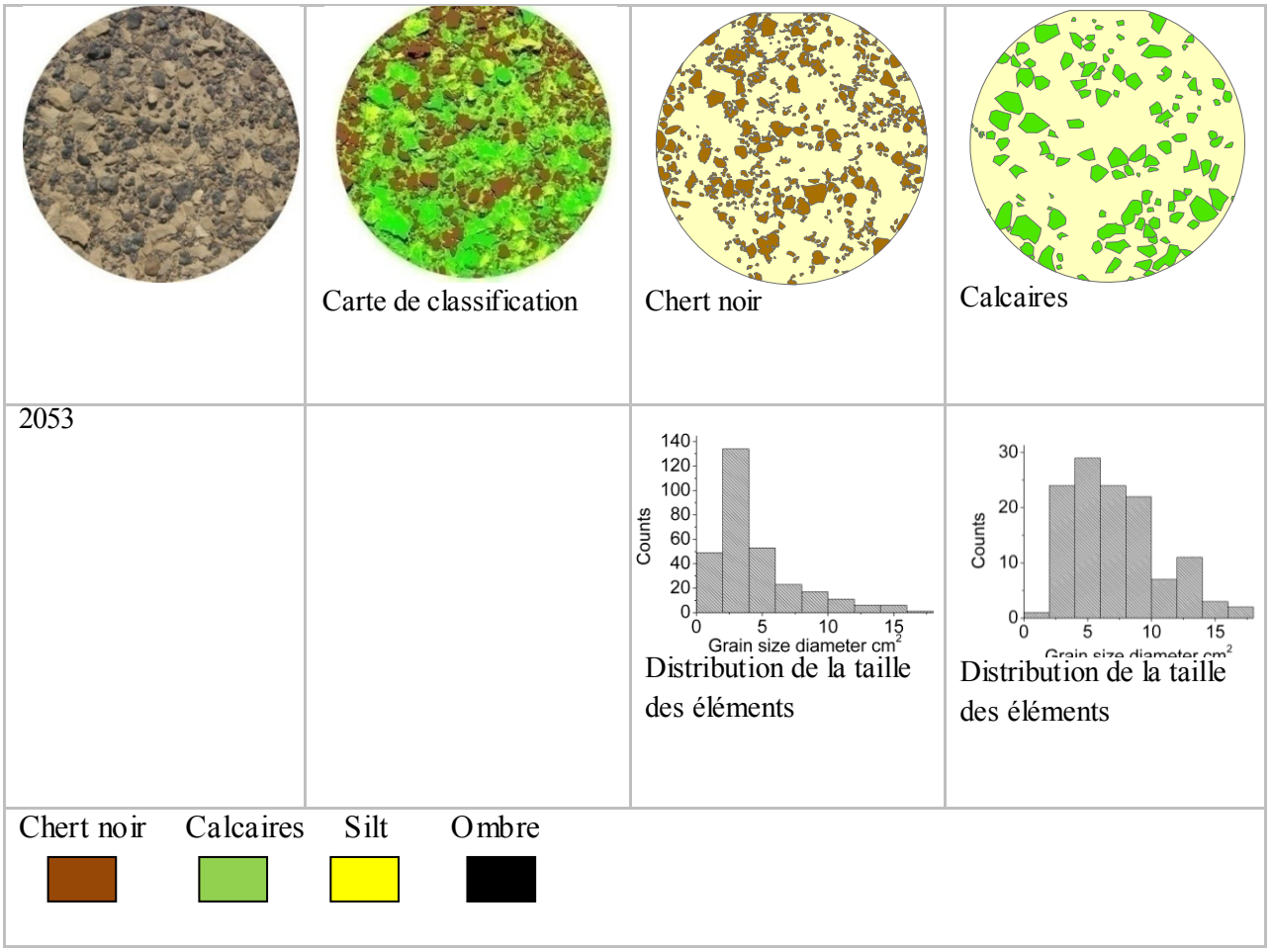

Figure 25 - Mélanges de terrain et cartes de classification des composantes spectrales, le site 1, groupe B.

Présentation des cas

Le cas **2049** - la composante spectrale dominante est le chert noir (40%), la taille moyenne du chert est de 7 cm^2, l'écart type est de 4 cm^2 (relativement élevé), la taille maximale est de 26 cm^2. La distribution des tailles n'est pas normale (l'asymétrie est supérieure à 1,5), le nombre de gros blocs est supérieur à celui des petits. On peut observer sur l'image que la taille de bloc de cherts est plus petite et leur quantité est plus élevée que pour les autres cas. L'abondance de calcaire est de 27%, leur taille est relativement grossière, en moyenne 10,5 cm^2, avec une taille maximale de 34,2 cm^2. L'abondance de silt est de 26% (**Table 4**).

Le Cas **2050** est composé de chert noir (33%), avec une taille moyenne de 10 cm^2, et une taille maximale de 33 cm^2, qui est plus grossière que dans le cas précédent. Le calcaire constitue 29%, la taille des blocs est relativement grossière, 11 cm^2 en moyenne, avec un maximum à 37 cm^2. Le silt constitue 26% du mélange.

Le cas **2051** est composé de 42% de chert, la taille moyenne des cherts est de 9,3 cm^2, celle de l'élément maximum est de 38,3 cm^2. Le calcaire constitue 32% du mélange et 24% est constitué de silt. La taille de calcaire est relativement grossière, en moyenne 8,8 cm^2, taille de l'élément maximal atteint 25 cm^2.

Le cas **2052** est composé de 36% de chert noir, la taille moyenne de l'élément de chert noir est de 7,8 cm^2, avec un maximum de 30 cm^2, 29% de calcaires, dont la taille moyenne des éléments est 9,9 cm^2, maximum 41,3 cm^2. Le silt constitue 19% du mélange.

Le cas **2053** est composé des mêmes composantes, mais leur taille est relativement petite comparée à d'autres scénarios. La taille moyenne du chert est de 4,5 cm^2, la taille moyenne des calcaires est 7cm^2. L'abondance de chert noir est 27%, de calcaire 34%, le silt constituant 20%.

Table 4 - Abondances des composantes spectrales des mélanges sur le terrain, le site 1, groupe B.

Id	Black chert %	Limestone %	Silt %	Shadow %	Accuracy %
2049	33	27	29	11	92
2050	32	29	26	13	80
2051	42	22	24	12	90
2052	36	29	19	16	85
2053	27	34	20	19	80

Les caractéristiques spectrales

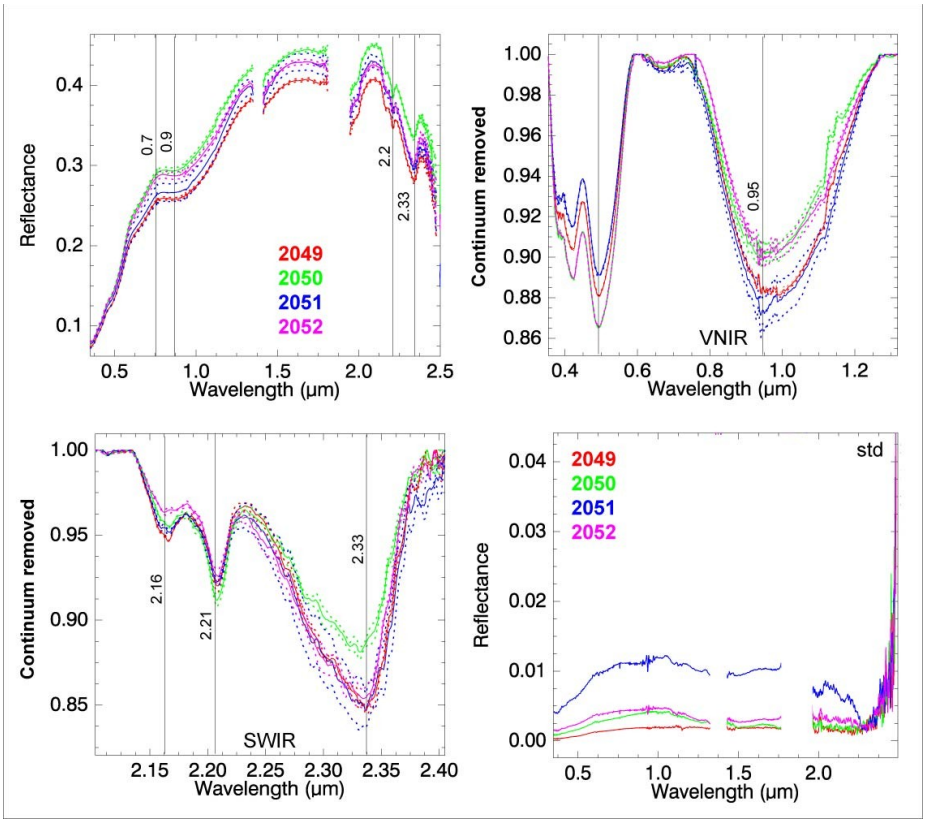

Figure 26 – Spectres de terrain des mélanges du site 1, groupe B : a) gamme spectrale complète; b) VNIR continuum enlevé; c) SWIR continuum enlevé; d) écart type des mesures sur le terrain

Le mélange 2053 est celui qui présente l'albédo la plus élevée. Dans ce mélange, la taille des éléments est relativement fine. Le cas 2053 a des abondances à peu près similaire des composantes spectrales que les cas 2050 et 2052, mais avec une taille plus fine des éléments. Ceci est la raison principale pour l'augmentation de sa réflectance dans le VIS, NIR et SWIR. Dans ce groupe de mélanges, les albédos les plus basses sont observées pour les mélanges 2049 et 2051. Dans ces mélanges, la quantité de chert noir est plus élevée, et la taille des éléments est plus grossière que pour les cas 2050 et 2052.

Après retrait du continuum dans le VIS, les cas 2049, 2051 et 2053 ont des profondeurs d'absorption similaires pour les oxydes de fer, autour de 0,95 µm (**Figure 26** b). L'absorption est moins prononcée pour les cas 2050 et 2052 ; pour ces cas le contenu en chert est plus faible. L'absorption d'argile dans le SWIR à 2,16 et 2,21 µm semble avoir la même profondeur dans tous les cas. L'absorption de la calcite à 2,33 µm est plus forte pour les cas 2049 et 2051 et plus faible pour les cas 2050 et 2053 (**Figure 26** c). La raison en est la quantité de calcaire dans le mélange. L'abondance de calcite était censée être élevée pour le cas 2050. Probablement

quelques uns des calcaires de la scène ont été confondus avec du grès. L'absorption à 2,33 µm est plus faible comparée à d'autres scènes.

Pour les cas 2049 et 2053, la longueur d'onde du maximum d'absorption des oxydes du fer entre 0,73 et 0,99 µm est décalée vers les plus grandes longueurs d'onde et se situe à 0,98 µm, à cause du contenu élevé en goethite. Dans les cas 2050, 2051 et 2052, le maximum de cette absorption est décalé vers les longueurs d'onde plus courtes (0,94 µm) avec une asymétrie négative. Cela indique un contenu en goethite supérieur (**Table 5**). La surface de l'absorption à 0,95 µm augmente proportionnellement à l'augmentation du contenu en chert dans les mélanges. La plus grande surface d'absorption (1,856) est observée dans le cas 2051 et la plus petite (1,405) est observée dans le cas 2050. La superficie d'absorption à 2,33 µm est la plus élevée dans le cas 2049, où l'abondance de la calcite est plus élevée.

Table 5 - Caractéristiques d'absorption des spectres des mélanges de site 1, groupe B.

ID	Min wvl 0.73-0.99	Abs area 0.95	Abs area 2.2	Abs area 2.33	Asymmetry 0.95	0.4	0.48	0.95	2.2	2.33
2049	0.989	1.731	0.102	0.51	0.009	0.091	0.115	0.117	0.057	0.146
2050	0.94	1.405	0.107	0.36	-0.027	0.104	0.131	0.098	0.064	0.118
2051	0.94	1.856	0.089	0.45	-0.036	0.082	0.105	0.128	0.055	0.135
2052	0.935	1.413	0.076	0.46	-0.048	0.105	0.131	0.1	0.054	0.139
2053	0.986	1.768	0.072	0.34	0.001	0.104	0.131	0.122	0.055	0.106

Mélange linéaire - modélisation directe

Les spectres modélisés et les spectres de terrain sont représentés sur la **Figure 28**, ainsi que les différences entre les spectres prédits et les spectres de terrain. La plus grande différence est observée pour le cas 2049. Ce mélange est composé de chert noir, de calcaire et de silt. L'absorption des oxydes de fer à 0,92 µm est sous-estimée par le modèle. Le minimum de l'absorption dans le spectre modélisé est situé à 0,92 µm, quand sur le terrain le minimum se situe proche de 1 µm, ce qui correspond plus à du grès. L'absorption de la calcite à 2,33 µm est profonde et correspond à une forte teneur en calcaire. Dans ce cas, les deux absorptions des oxydes de fer et de la calcite obtenus avec le modèle linéaire ne correspondent pas aux absorptions du spectre sur le terrain. Sur la photographie, le calcaire semble sombre, et parfois peut être confondu avec le grès.

Dans le cas 2050, les absorptions d'oxydes de fer autour de 0.95 µm et l'absorption de la calcite à 2,33 µm ont été sous-estimées par la modélisation linéaire (**Figure 28**). Le minimum d'absorption

des oxydes de fer dans le spectre de terrain est situé à environ 1 µm. Dans le spectre modélisé le minimum est plus proche de 0.95µm, qui correspond à l'hématite.

Dans le cas 2051 le modèle linéaire a également sous-estimé toutes les profondeurs d'absorption (**Figure 28**). L'absorption des oxydes de fer à 0,95 µm est sous-estimée et son minimum est déplacé plus près de 0,92 µm. Dans le spectre modélisé cette absorption est asymétrique, ce qui correspond à l'hématite alors que dans le spectre de terrain, cette absorption est symétrique. Dans ce cas, c'est l'absorption de la calcite à 2,33 µm qui présente la différence la plus grande avec les spectres modélisés. Dans les cas 2052 et 2053, les mêmes caractéristiques sont observées : la réflectance du spectre de terrain est inférieure à celle modélisée. L'absorption des oxydes de fer dans le VIS est sous-estimée de manière similaire au cas précédent, l'absorption de la calcite à 2,33 µm est également sous-estimée. Cependant, l'absorption de la kaolinite est du même ordre de grandeur.

Il y a quelques explications possibles pour les différences observées entre le terrain et les spectres modélisés. Tout d'abord, les composantes spectrales utilisées pour les mélanges ne correspondent pas exactement à celles sur le terrain. Même si les composantes spectrales correspondent à des échantillons représentatifs recueillis sur le terrain, les roches peuvent avoir des différences de rugosités de surface, de croûtes d'altération, de composition. En conséquence le modèle linéaire aura de la difficulté à prédire le spectre correct. Le second problème peut être une mauvaise identification des composantes spectrales. Par exemple, le calcaire peut être visuellement confondu avec le grès, avec comme résultat des différences entre les spectres modélisés et observés. Une autre raison possible pour les différences sont les conditions de mesure : le spectre modélisé est calculé en utilisant les spectres acquis en laboratoire d'échantillons recueillis sur le terrain, tandis le spectre de terrain est acquis directement à partir de mélanges dans les conditions de terrain, avec un éclairement solaire particulier, des angles de mesure spécifiques, etc.

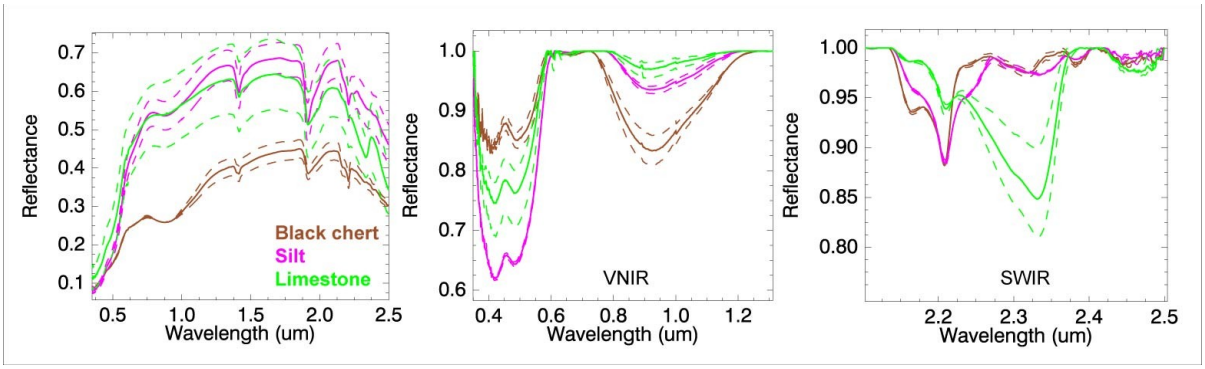

Figure 27- Spectres des composantes spectrales de mélanges de site 1, groupe B

Formules utlisées pour la modélisation linéaire :

$$\textbf{2049} = (0.33 * Sp_{B.chert}) + (0.27 * Sp_{Limestone}) + (0.29 * Sp_{Silt})$$

$$\textbf{2050} = (0.32 * Sp_{B.chert}) + (0.29 * Sp_{Limestone}) + (0.26 * Sp_{Silt})$$

$$\textbf{2051} = (0.42 * Sp_{B.chert}) + (0.22 * Sp_{Limestone}) + (0.24 * Sp_{Silt})$$

$$\textbf{2052} = (0.36 * Sp_{B.chert}) + (0.29 * Sp_{Limestone}) + (0.19 * Sp_{Silt})$$

$$\textbf{2053} = (0.27 * Sp_{B.chert}) + (0.34 * Sp_{Limestone}) + (0.20 * Sp_{Silt})$$

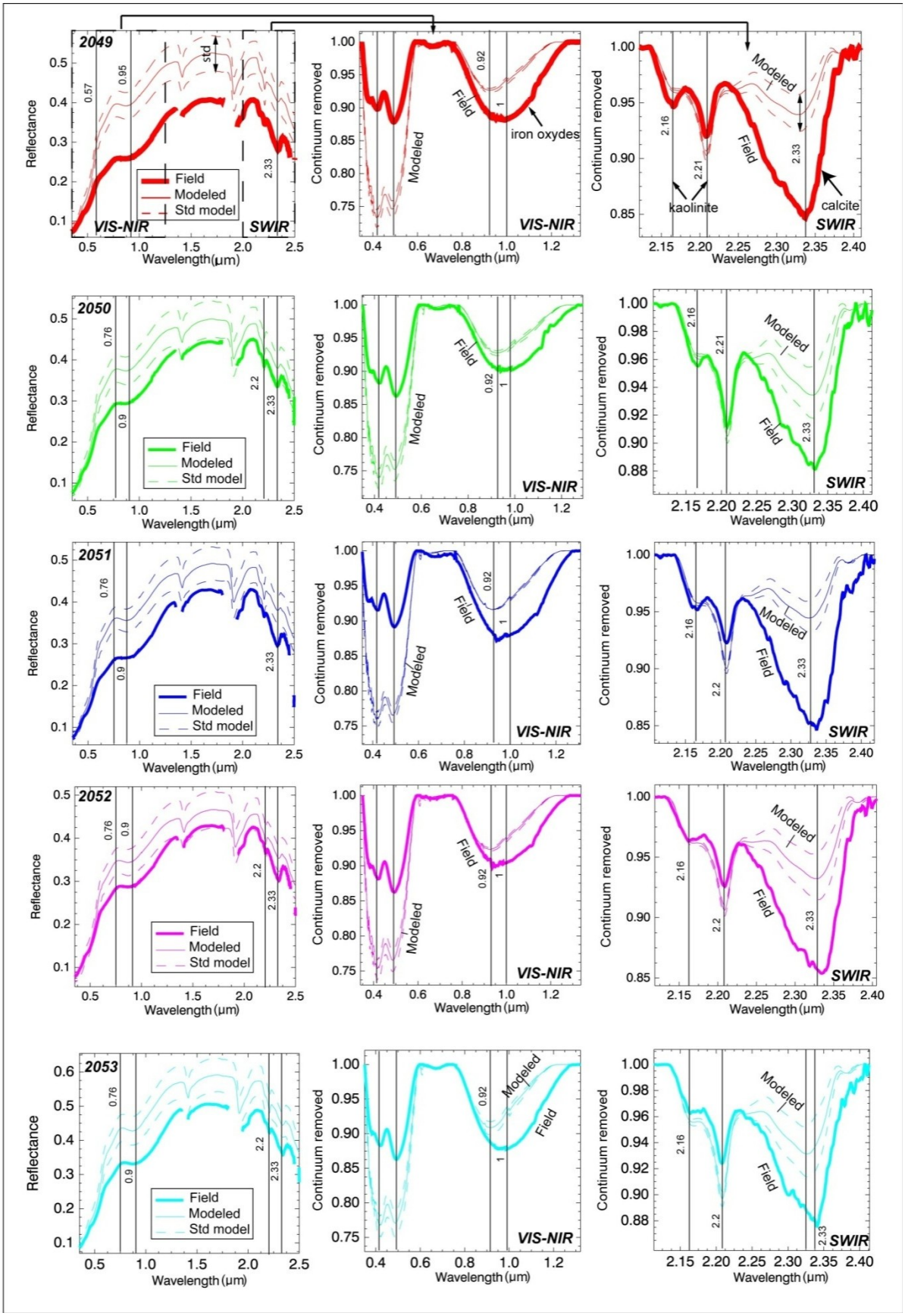

Figure 28 – Spectres modélisés de terrain, mélanges du, site 1, groupe B.

Différence Normalisée

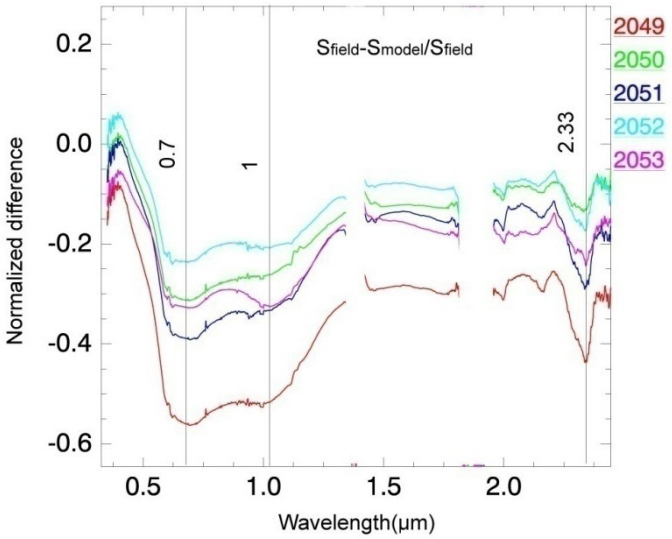

Figure 29 – Différence normalisée entre des spectres de terrain et des spectres modélisés.

Les différences normalisées entre spectres de terrain et spectres modélisés sont indiquées sur la **Figure 29**. Les valeurs négatives pour la différence sont dues à une plus forte réflectance pour le terrain que pour le spectre modélisé. La plus grande différence est observée dans le VIS, alors que dans le NIR et SWIR les valeurs sont plus proches de 0. Dans le SWIR, il y a une sous-estimation du calcaire.

Déconvolution spectrale

Les proportions des composantes spectrales obtenues par démixage sont indiquées sur la **Figure 30**. De meilleurs résultats ont été obtenus en utilisant la gamme spectrale complète que seulement la partie visible des spectres. Lorsque seul le visible a été utilisé, le démixage a mal estimé le silt et l'a remplacé par du calcaire. Aussi les erreurs sont plus faibles lorsque toute la gamme spectrale est utilisée. C'est pourquoi il est important d'utiliser la gamme spectrale complète pour obtenir des résultats plus véridiques.

Les estimations des modèles linéaires et non linéaires sont très proches, il est donc difficile de définir quel modèle fait une meilleure prédiction. Le démixage non-linéaire prédit mieux la teneur en silt, mais la teneur en calcaire est sous-estimée, et celle en chert est surestimée (**Figure 30**). Les barres d'erreur sont plus faibles pour le démixage linéaire de toute la gamme spectrale, que pour le démixage non-linéaire.

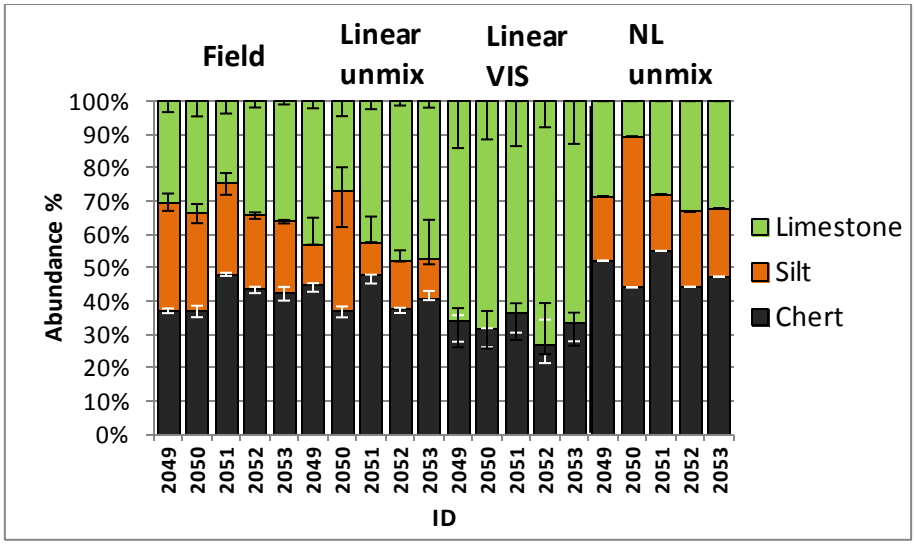

Figure 30 – Résultats de déconvolution par rapport à l'abondance de terrain.

Table 6 - RMSE du démixage.

Linear un-mixing all specta					Linear un-mixing VIS				
2049	**2050**	**2051**	**2052**	**2053**	**2049**	**2050**	**2051**	**2052**	**2053**
0.0138	0.0158	0.015	0.0135	0.0126	0.0051	0.0042	0.0057	0.0048	0.0052
Non-linear un-mixing all spectra									
2049	**2050**	**2051**	**2052**	**2053**					
0.0109	0.011	0.0123	0.0099	0.0089					

L'observation de ce groupe a montré que les spectres de terrain de ces mélanges ne sont pas mieux représentés par la modélisation linéaire (en utilisant un modèle direct). Les absorptions des spectres de mélange ont été sous-estimées et les niveaux de réflectance sur le terrain sont plus faibles en comparaison avec les spectres modélisés. Dans ces mélanges, la taille des éléments était plus grossière. Dans les cas où il y a une non-conformité entre les composantes spectrales d'un mélange ou lorsqu'il y a une grande hétérogénéité des composantes spectrales, un modèle non-linéaire devrait minimiser ces différences (en forçant les spectres de laboratoire à s'adapter aux spectres de terrain).

3.2 Les mélanges de poudres

Des mélanges de poudres ont été préparés a partir des échantillons collectés sur le terrain avec des proportions équivalentes à celles des composantes spectrales sur le terrain. Nous avons sélectionnés le cas des mélanges 2049, 2050, 2051 et 2052, appartenant au groupe B du site 1. Les spectres des mélanges de terrain et les spectres de poudre sont indiqués sur la **Figure 31**. Les

constituants de ces mélanges sont : chert noir, silt et calcaire. Les proportions de chaque composant sont indiquées dans la la

Table 7.

Table 7 – Abondances des composantes spectrales dans les mélanges du site 1,group A.

Id	Black chert %	Limestone %	Silt %	Shadow %	Accuracy %
2049	33	27	29	11	92
2050	32	29	26	13	80
2051	42	22	24	12	90
2052	36	29	19	16	85

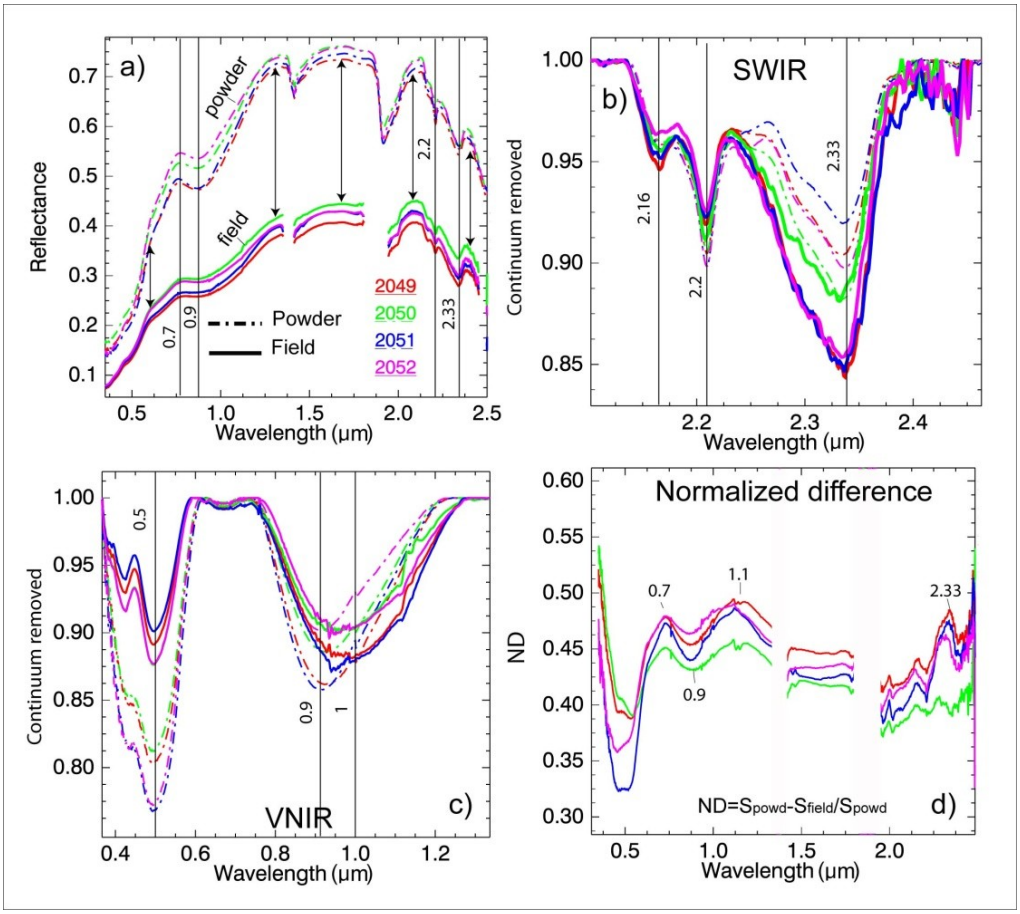

Figure 31 – Les spectres des mélanges de poudres (granulométrie 100-500 µm) et les spectres de terrain à partir des mélanges avec les abondances correspondantes (a, b, c), la différence normalisée entre les spectres de poudre et les spectres de terrain (d).

La réflectance des poudres est significativement plus élevée que la réflectance obtenue à partir des mélanges de terrain et leurs formes spectrales sont différentes. Les différences entre la réflectance de terrain et la réflectance des poudres peuvent atteindre 40-50% en raison de la diffusion volumique (d). La diffusion est plus élevée lorsque la taille des grains est plus petite, en conséquence, elle est plus élevée pour les poudres. La plus petite différence est observée dans le VIS (entre 0,48 et 0,6 µm), où sont situées les absorptions spécifiques des oxydes de fer, et donc où la lumière est moins diffusée puisque la plupart de la lumière est absorbée par les oxydes de fer. Les différences augmentent vers la fin du VIS ; dans le NIR la différence atteint un maximum à 1,1 µm et reste élevée dans le SWIR.

Les absorptions dans les poudres dans le VNIR sont principalement causées par de l'hématite, l'absorption de fer est asymétrique, avec un minimum de 0,9 déplacé vers 0,92 µm. Pour les mélanges de terrain, l'absorption des oxydes du fer est située à environ 1 µm, qui est correspond à la goethite. Ce résultat est dû à l'altération de surface. Sur le terrain, les cherts noirs sont altérés et recouverts d'une croûte, alors que les poudres ont été préparées à partir de roche entière, et non seulement de la croûte, donc contenant à la fois des minéraux frais et altérés.

Les profondeurs des absorptions sont du même ordre de grandeur pour les poudres et les spectres de terrain. Il n'y a pas de grande différence dans les profondeurs de l'absorption de la kaolinite à 2,2 µm dans le SWIR. L'absorption de la calcite à 2,33 µm est plus prononcée dans les mélanges de terrain que dans les poudres.

Il est connu par la théorie que la taille des grains des poudres doit être équivalente à celle des minéraux dans la roche. Toutefois, dans certains cas, la taille des grains de minéraux dans un échantillon peut être différente, ou est parfois difficile à définir. Par exemple, la taille des grains de calcite dans les calcaires du site 1 a été difficile à définir, parce que dans la lame mince de l'échantillon regardé, elle semble homogène. Nos résultats ont montré que la taille des grains (100-500 µm) de calcite dans la poudre n'était pas assez importante pour former un mélange avec les bonnes profondeurs d'absorption, correspondant à celles du terrain.

3.3 L'analyse de corrélation

Le but de cette section est de trouver les paramètres qui correspondent aux composantes spectrales spécifiques en utilisant l'analyse de corrélation, ce qui permet d'examiner la relation entre les propriétés physiques / chimiques des matériaux et les spectres. La composition du mélange, la taille des éléments, la rugosité, l'abondance des composantes spectrales sera corrélée à des caractéristiques spectrales. Chaque composante spectrale est responsable de certaines

caractéristiques dans le mélange, et influence une partie spécifique de la région spectrale. Les caractéristiques des absorptions ont été décrites par des paramètres tels que la position en longueur d'onde du minimum, la superficie de l'absorption, la symétrie / asymétrie, la profondeur d'absorption. Le continuum et la forme ont été caractérisés par des niveaux de réflectance moyenne et les pentes spectrales.

Les mélanges (35 cas) du site 1 et du site 6 ont été sélectionnés pour l'analyse de corrélation, car ils sont composés de composants semblables : chert noir, silt, calcaire et grès. Les absorptions spécifiques des spectres de ces mélanges sont similaires (même composition), donc les mêmes absorptions spécifiques peuvent être examinées à chaque fois.

Le résultat de l'analyse de corrélation pour les paramètres de l'albédo de spectres des mélanges est présenté. La **Table 8** montre les coefficients de corrélation entre les albédos moyennes du VIS-NIR-SWIR, représentées par des limites de 0,61 à 0,73 µm, 1,42 à 1,79 µm et 2,03 à 2,15 µm et des pentes spectrales entre 0,35 et 0,78 µm, et 0,89 et 1,3 µm et les abondances des composantes.

Table 8 - Coefficients de corrélation entre les propriétés d'albédo et l'abondance des composantes spectrales.

	Average reflectance level				Spectral slope	
	0.61-0.73	**1.42-1.79**	**2.03-2.15**		**0.35-0.78**	**0.89-1.3**
Black chert	**-0.40**	**-0.39**	**-0.38**		**-0.41**	**-0.21**
Silt	**0.86**	0.37	0.49		**0.85**	-0.20
Red Chert	**0.40**	**0.73**	**0.69**		0.08	**0.83**
Sandstone	-0.53	**-0.73**	**-0.71**		-0.22	-0.78
Shadow	-0.34	-0.45	-0.44		-0.24	-0.25

Chaque composante spectrale devrait influencer une partie spécifique du spectre. Le chert noir est une matière sombre, donc il abaisse les niveaux de réflectance, avec comme résultat une corrélation négative avec les reflectance dans le VIS-NIR-SWIR et les pentes spectrales (**Table 8**).

Le silt a une forte corrélation positive avec la région spectrale dans le début du VIS (0,61 à 0,73 µm). La pente entre 0,35 et 0,78 µm est plus élevée avec une teneur élevée en silt (R = 0,85). Le silt est une composante spectrale claire et se compose de fines particules ce qui augmente la

diffusion et la réflexion des mélanges. Il a une grande influence dans le VIS, et moins dans le NIR et le SWIR. Il existe une corrélation positive entre la quantité de silt et la pente de la réflectance dans le VIS, mais une faible corrélation dans le NIR. La diffusion étant fonction de la taille des grains, à courtes longueurs d'onde, la diffusion est plus élevé qu'à des longueurs d'onde plus longues.

Le chert rouge a plus de corrélation avec les spectres dans le proche infrarouge et le SWIR (R = 0,7) ; cette corrélation est positive, ce qui signifie que le chert augmente la réflectance dans ces régions. Cependant, au début du VIS (R = 0,4), son influence est faible. Le grès a une corrélation négative avec les niveaux de réflectance et les pentes des spectres du mélange, cela signifie que le grès est un constituant sombre, relativement aux autres et diminue les niveaux de réflectance.

L'ombre est négativement corrélée avec les niveaux de réflectance et les pentes spectrales, elle abaisse la réflectance dans le VIS-NIR et le SWIR. La corrélation la plus élevée a été observée dans le NIR et le SWIR (R =- 0,45). L'ombre n'est pas un constituant, mais il réduit le niveau de rayonnement (réflectance) provenant de l'ensemble des constituants. L'ombre n'a pas d'influence significative sur les caractéristiques d'absorption, mais son influence sur l'albédo est perceptible.

Ce type d'analyse a permis de relier les spectres des mélanges aux paramètres et de montrer la façon dont les différents constituants influencent chaque paramètre spectral.

Taille des éléments

L'influence de la taille des éléments sur les spectres de réflectance des mélanges à macro-échelle a également été examinée avec l'analyse de corrélation sur l'exemple des cherts. Les paramètres de taille des cherts ont été sélectionnés : le nombre de blocs, de taille moyenne, l'écart-type, l'asymétrie, la taille minimum, maximum et la médiane. Ces caractéristiques ont été corrélées aux caractéristiques spectrales : profondeur d'absorption à 0,42 µm, 0,48 et 0,95 µm, niveau moyen de la réflectance et les pentes des spectres. Le résultat est montré dans la **Table 9**. Pour les plus petits éléments, la diffusion multiple doit augmenter la réflectance, alors que pour des éléments grossiers, la réflectance va diminuer, et les absorptions seront plus prononcées.

La taille des éléments de cherts a été corrélée (corrélation négative moyenne) avec des niveaux de réflectance moyenne dans le VIS, entre 1,42 et 1,79 µm et dans le SWIR, entre 2,03 et 2,15 µm. La pente spectrale dans le proche infrarouge à 0,89 et 1,3 µm est aussi négativement corrélée à la taille moyenne des éléments de chert. Avec une taille croissante des éléments de chert, la réflectance est plus basse et la pente est inférieure, et à l'inverse, plus petite est la taille des

éléments de chert, plus élevée est la réflectance et la pente dans le NIR est plus forte. Il y a une influence de la taille des éléments sur les profondeurs d'absorption.

Table 9 - Statistiques sur la taille des éléments par rapport aux propriétés spectrales d'albédo, coefficients de corrélation (R), sites 1 et 6.

	Abs. depths			Refl. Mean			Slope	
Size	0.4	0.48	0.95	0.61-0.73	1.42-1.79	2.03-2.15	0.35-0.78	0.89-1.3
N total	-0.16	-0.16	0.19	-0.17	-0.04	-0.06	-0.17	0.09
Mean	0.03	-0.19	**-0.36**	-0.11	**-0.31**	-0.27	-0.08	**-0.38**
STD	0.00	-0.06	-0.15	-0.29	**-0.31**	-0.29	-0.22	-0.22
Skewness	-0.12	0.11	0.34	-0.21	0.05	0.01	-0.19	0.28
Minimum	0.02	0.04	-0.16	-0.15	-0.15	-0.11	-0.09	-0.14
Median	0.04	-0.23	-0.41	-0.03	-0.29	-0.25	-0.03	**-0.42**
Maximum	-0.10	-0.09	0.02	**-0.39**	**-0.31**	**-0.31**	**-0.33**	-0.11

Le chert est un constituant sombre donc son influence sur les spectres d'un mélange est négative, une forte teneur en chert diminue la réflectance. Toutefois, les coefficients de corrélation ne sont pas très élevés. La taille de l'élément influe sur les paramètres spectraux, mais pas de manière significative, comme l'abondance relative. L'influence de plusieurs constituants qui composent un mélange doit être prise en compte, puisque chacun des constituants peut influer sur une partie spécifique d'un spectre. Le chert constitue un seul paramètre, mais il y a d'autres constituants : silt, grès, calcaire. La taille de l'élément est une propriété d'un constituant et elle est responsable de la diffusion, qui change quand la taille augmente ou diminue. A macro-échelle, cet effet n'est pas linéaire, car il était supposé que la taille des éléments est une partie de la contribution surfacique des constituants. A partir de nos résultats, nous avons observé qu'à macro-échelle, la taille des éléments d'un mélange joue un rôle important.

4. Discussion et conclusions

L'objectif principal de ce travail était d'effectuer une étude empirique des mélanges de minéraux à l'échelle macroscopique (l'échelle du terrain), afin d'observer des scénarios de mélanges naturels dans des environnements réels. La plupart des études empiriques sur des mélanges de minéraux sont basées sur des mesures en laboratoire à l'échelle microscopique. Il y a un manque d'observations de mélanges sur le terrain, à partir d'environnements naturels. Des spectres de réflectance couvrant différents scénarios naturels ont été acquis sur le terrain avec un

spectromètre ASD dans la région de Makhtesh Ramon, Israël, une région riche en mélanges de minéraux clairement exposés. Des mélanges de constituants et de propriétés différentes ont été choisis : composés de composantes à fort ou faible contraste spectral, mélanges avec des proportions différentes de constituants et des tailles d'éléments différentes.

Tous les mélanges ont été classés en groupes selon leurs propriétés, puis leurs spectres ont été analysés. Les spectres des mélanges ont été modélisés avec un modèle surfacique (linéaire) en utilisant les spectres des constituants recueillis sur le terrain. La contribution surfacique des composantes a ainsi pu être caractérisée et estimée.

L'analyse de la différence normalisée (DA) a permis de comparer les spectres modélisés et les spectres de terrain, de voir les différences en fonction de la longueur d'ondes. Les spectres des mélanges acquis à partir d'images hyperspectrales ont été comparés avec les données de terrain et les mélanges de minéraux en poudre, en conservant pour les différents constituants des proportions équivalentes. Ceci a permis une comparaison directe des spectres de mélanges à différentes échelles. De plus le démixage linéaire et non-linéaire a été appliqué sur les scènes observées, et les résultats ont été comparés.

Non-linéarité des mélanges

Les spectres des mélanges de terrain devaient correspondre à des modèles linéaires dans le cas où la contribution de leurs composantes est surfacique. Cependant, si la contribution est non-linéaire, les spectres peuvent être différents de ceux du modèle linéaire. Comme notre étude l'a montré, les spectres de mélanges de terrain et ceux obtenus par des modèles linéaires sont différents, tant par la forme spectrale que par l'albédo.

Dans certains cas, les profondeurs d'absorption des spectres modélisés et des spectres de terrain correspondent les unes aux autres, en particulier dans les cas où la taille des éléments n'est pas très importante.

Quant aux mélanges à fort contraste, où la taille des éléments de chert était grossière à très grossière et le chert moins altéré, le modèle linéaire a sous-estimé l'influence du chert. Sur le terrain, les absorptions spécifiques du fer étaient plus prononcées.

Il existe quelques raisons pour la non-correspondance entre le modèle linéaire et les mélanges de terrain :

1. L'ombre réduit les niveaux de réflectance. Notre étude a montré que l'ombre réduit la réflectance spectrale dans le VIS-NIR-SWIR. Une corrélation négative a été trouvée entre la

quantité d'ombre et la réflectance. Le modèle linéaire ne prend pas en compte l'effet de l'ombre dans le mélange, cependant sur le terrain il est bien évident que l'ombre a une influence sur la réflectance. L'ombre est fonction de l'illumination et de la taille des éléments, la quantité d'ombre étant censée être plus importante quand les éléments sont plus grossiers.

2. Les conditions d'acquisition. Les conditions de mesure sur le terrain et en laboratoire sont différentes. Sur le terrain, les spectres sont influencés par les effets atmosphériques, l'angle de visée (BRDF) et la source lumineuse, qui est différente de la source de lumière artificielle. Par conséquent, les spectres provenant de différentes sources incluent déjà une partie des différences. Donc la comparaison des spectres microscopiques avec des spectres à macro-échelle présente des incertitudes provenant de conditions de mesure différentes.
3. Le modèle de mélange linéaire ne tient pas compte de la distribution de tailles des éléments, seulement de leur contribution surfacique. Il a été trouvé dans cette étude que la taille des blocs de chert était corrélée avec les niveaux et les pentes de réflectance spectrale pour les mélanges de terrain. Comme la taille des blocs a été réduite, la réflectance est plus élevée et la pente est moins forte. A l'échelle du terrain, la taille de blocs est un facteur important qui habituellement n'est pas pris en compte par les algorithmes linéaires de démixage. A l'échelle microscopique, la gamme de tailles des éléments est différente de celle à macro-échelle. A l'échelle microscopique, les spectres sont plus sensibles aux variations de taille des grains, l'effet de la diffusion est plus fort. A macro-échelle, la taille des constituants est également importante, mais la diffusion par les macro-constituants sera plus faible.
4. Les roches sur le terrain ne sont pas homogènes, elles peuvent varier en rugosité, par la présence de patine ou de croûte d'altération. Il en résulte que les spectres d'un même type de roche peuvent varier en fonction de ces facteurs. Comme cela a été observé à partir des spectres d'une roche fraîche et patinée, il y a des différences importantes entre les spectres. Pour des échantillons altérés, les absorptions spécifiques sont plus faibles, et la forme spectrale est différente. Dans les cas que nous avons observés, les roches sur le terrain étaient pour la plupart couvertes par de la patine, nous avons donc utilisé des échantillons patinés pour notre analyse. Cependant dans le cas où l'accès sur le terrain est limité, ainsi que la connaissance *a priori*, l'état d'altération des roches peut être la cause de grandes incertitudes.
5. Il pourrait y avoir une contribution non-linéaire de certaines composantes spectrales. Par exemple, certains des constituants pourraient influer davantage sur certaines parties du spectre que sur les autres. Lorsque nous procédons à la modélisation de mélange linéaire, nous supposons que l'influence de chaque constituant du mélange est égale sur l'ensemble des

spectres et à toutes les longueurs d'ondes et correspond à leur proportion dans le mélange. De nos résultats, il est à remarquer que la contribution de certaines composantes spectrales est supérieure à leurs proportions surfaciques. On a constaté que dans les mélanges qui contiennent une grande quantité de chert rouge, les spectres dans le VIS sont fortement influencés par les absorptions des oxydes de fer qui proviennent du chert. En particulier, l'influence des autres constituants sur l'absorption est ignorée dans le VIS où celle des oxydes de fer est très fortes et masque les caractéristiques spectrales des autres constituants. Dans tous les cas observés, l'absorption de la calcite des spectres de terrain ne correspond pas aux absorptions modélisées. Dans les spectres de terrain l'absorption de la calcite est plus profonde que dans les spectres modélisés, pour des proportions de composantes spectrales correspondant à la proportion surfacique.

Analyse des différences

Le spectre de différence normalisé (ND) contient de l'information, il peut avoir différentes formes et intensités. Plus les mélanges sont différents plus leur différence sera grande, et inversement, si les mélanges sont égaux, leur spectre de différence sera proche de 0. Il a été constaté que dans une partie des cas étudiés, la ND avait des valeurs élevées dans le visible et plus faibles dans le SWIR. Ces mélanges étaient composés de composantes spectrales contrastées. La différence dans le VIS provient de proportions différentes de constituants clairs et foncés. Par conséquent les spectres de mélanges ayant des composantes spectrales très contrastées sont plus influencés dans le VIS. Pour des mélanges avec des constituants peu contrastés, la différence dans le VIS est plus petite, les différences les plus grandes ayant dans ce cas été observées dans le NIR et le SWIR. Ces différences proviennent des différences de composition et de tailles d'éléments des mélanges. Des différences avec les spectres de formes similaires mais d'intensité différente ont également été observées dans les mélanges avec la même proportion de constituants, mais des éléments de tailles différentes.

Les mélanges de poudres ont été comparés à des mélanges de terrain avec des proportions équivalentes à celles des minéraux les composant. En raison d'effet de la diffusion entre les grains de la poudre, la réflectance des poudres est plus élevée que la réflectance de terrain. Toutefois, les profondeurs d'absorption des poudres et des mélanges de terrain sont pratiquement identiques, pour des poudres dont la taille de grains ne dépasse pas 500 µm. La taille des éléments dans les poudres influe non seulement sur les niveaux de réflectance, mais aussi sur les absorptions. Il est très important de trouver une taille de grain optimale de poudre pour

représenter un mélange macroscopique (simulation de mélanges de terrain par des poudres), ce qui, dans certains cas, est assez difficile. Il est généralement considéré que la taille des grains de la poudre doit correspondre à la taille des grains des minéraux qui composent la roche. Toutefois, dans certains cas, un minéral dans une roche peut avoir différentes tailles ou sa taille est difficile à définir. A partir de nos observations, la taille des grains de chert de 100-500 µm a été une assez bonne approximation pour représenter les absorptions du chert dans le mélange, mais dans le cas des calcaires, cette taille de grains n'était pas suffisante pour représenter les absorptions de la calcite. Les spectres des poudres sont différents des spectres de terrain, par conséquent, leurs niveaux de réflectance (albédo) ne peuvent pas être comparés. De plus, à micro-échelle, les facteurs physiques et environnementaux sont différents, donc des scènes à macro et à micro-échelle ne peuvent pas être comparées directement. On a cependant trouvé une bonne adéquation entre les pixels de l'image et les spectres de terrain, dans le cas de mélanges équivalents.

Déconvolution

Le démixage linéaire est une méthode communément utilisée pour produire le démixage de macro-mélanges. Cependant, nos résultats ont montré que la méthode de démixage linéaire n'est pas efficace dans certains cas où elle a donné des résultats avec des erreurs de prédiction élevées. Nos résultats ont montré que l'utilisation d'une gamme spectrale complète est plus efficace que seulement le visible, même si dans certains cas le visible est suffisant pour prédire des abondances correctes. Les composantes spectrales pourraient avoir des spectres similaires dans le visible, auquel cas il est impossible de les différencier. Par conséquent, il est recommandé d'utiliser la gamme spectrale complète du VIS-NIR-SWIR. Le démixage non-linéaire, dans certains cas, améliore le résultat, cependant il n'a pas toujours été pleinement efficace.

Cette méthode est efficace dans le cas où les spectres des composantes spectrales ne correspondent pas parfaitement aux spectres des constituants de terrain. Parfois, des effets non linéaires peuvent modifier la réponse spectrale des composantes spectrales : présence de patine, croûte d'altération, ombre, la réponse spectrale d'un même composant variant en fonction de différents facteurs. Nos résultats ont montré que l'utilisation de spectres d'un même échantillon peuvent ajouter / supprimer jusqu'à 30% de l'abondance des composantes spectrales prédites dans certains cas. Le domaine visible est plus sensible à ces variations. Donc l'algorithme non-linéaire peut améliorer le résultat en ajustant le spectre des composantes en fonction du spectre de mélange de terrain. Selon nos résultats, il n'y a pas de problème significatif lors du démixage entre composantes spectrales sombres et composantes spectrales de contraste élevé. Les

meilleurs résultats de démixage ont été obtenus pour les mélanges binaires de silt et chert. Plus le nombre de composantes était petit, meilleur était le résultat de démixage. Le pire résultat a été obtenu dans le cas où les spectres des composantes se ressemblaient (pour des composantes spectralement similaires), tels que chert rouge et grès. Par conséquent, la technique utilisée dans ce travail pourrait être améliorée.

L'ajustement non-linéaire des composantes spectrales est utile surtout pour le démixage de macro-mélanges, les macro-mélanges correspondant aux pixels des images aéroportées. Et généralement, les effets non linéaires ne sont pas pris en compte par les algorithmes conventionnels de démixage linéaire, et ces effets non linéaires pourraient se présenter en particulier dans les cas où les spectres de bibliothèques spectrales sont pris comme composantes spectrales. Des effets tels que la patine, les croûtes, la rugosité différente, l'ombre sont communs à cette échelle, donc ils seront une source d'erreur dans le résultat des prédictions.

Perspectives d'avenir

Cette étude a analysée des mélanges à macro-échelle, et a observé des mélanges de minéraux sur le terrain en environnements naturels. Un nombre limité de cas a été observé et constitue une première étape pour ce type de recherche. Cette étude est importante car les macro-mélanges sont représentatifs des pixels mixtes des images hyperspectrales aéroportées et satellitaires. Dans l'avenir, il est fortement recommandé d'observer plus de situations naturelles, avec différents types de surfaces : régolite, sols, etc.

Il est également fortement recommandé d'effectuer des simulations de mélanges à macro-échelle, avec une proportion contrôlée de constituants et de tailles d'éléments, à l'instar des observations empiriques en laboratoire, mais dans des conditions naturelles de terrain. Ces simulations permettront de séparer les différents paramètres d'un mélange, tels que l'influence de l'abondance, la taille des éléments, l'ombre, la croûte d'altération, etc.

Cette technique pourrait être appliquée à une image hyperspectrale pour mieux comprendre les comportements des mélanges à l'échelle du sous-pixel. A cet effet, une connaissance exacte de la localisation des pixels est requise, afin que le pixel puisse être divisé en sous-domaines. Ce type d'analyse manque dans notre étude. Parce que notre campagne de terrain n'était pas prévue pour cela, mais davantage axée sur les scenarios de terrain. Les surfaces planétaires étant en général composées de mélanges et pas d'un matériau unique, plus d'attention devrait être accordée à l'analyse de mélanges au niveau macroscopique.

La définition du nombre de composantes spectrales est un problème pour les algorithmes de déconvolution aujourd'hui. Avec l'augmentation du nombre de composantes spectrales, l'exactitude du démixage est réduite. En démixage, une attention particulière devrait être accordée aux composantes spectralement similaires, qui correspondent aux erreurs les plus élevées. De plus, la majorité des algorithmes linéaires ne prennent pas en compte les effets importants qui se produisent sur le terrain, et résultent en une classification erronée. Donc les algorithmes non-linéaires ont un grand potentiel pour améliorer la déconvolution si on est dans des conditions telles que la présence d'ombre, ou des effets de tailles d'éléments.

Les modèles physiques ont un fort potentiel en SMA. Dans certains cas, ils ont donné de très bonnes interprétations. Mais comme pour la modélisation empirique, ces modèles sont basés sur des mélanges de poudre mesurées dans des conditions de laboratoire. Logiquement, il est prévu de tester ces modèles physiques (Hapke, Shkuratov, etc.) sur des scénarios de terrain naturels, pour d'autres applications de ces modèles sur des données spatiales. Des essais sur le terrain permettraient d'évaluer la capacité de ces techniques pour analyser des mélanges dans des environnements réels, et d'estimer l'ampleur des erreurs.

Le facteur d'échelle dans l'analyse de mélanges est également une question importante, les caractéristiques spectrales peuvent être différentes à différentes échelles. Par exemple, à l'échelle macro certaines propriétés de mélange qui existent à micro-échelle peuvent ne pas avoir d'effet. Un effet de masquage par le fer a été observé dans les mélanges microscopiques, les spectres de minéraux «fortement absorbants » peuvent masquer d'autres constituants. Par conséquent, il serait difficile d'identifier et d'estimer les fractions mineures de «constituants faibles», si le fer masque leurs caractéristiques. Un autre effet est l'orientation des minéraux, qui est observée à micro-échelle, mais à l'échelle du terrain cet effet semble moins pertinent.

L'analyse des mélanges spectraux n'a pas de solution unique, ce sujet est aussi complexe que la complexité des mélanges des matériaux dans la nature.

UNIVERSITÉ DE NANTES
FACULTÉ DES SCIENCES ET DES TECHNIQUES

———

ÉCOLE DOCTORALE SPIGA

N° attribué par la bibliothèque

Année 2012

Impact of mineral mixtures at macro-scale on surface spectral reflectance: empirical study of natural field scenarios.

THÈSE DE DOCTORAT
Discipline : Science de la Terre
Spécialité : Télédétection

Présentée
et soutenue publiquement par

Ekaterina CARMINA

Le 29 mars 2012, devant le jury ci-dessous

Président	M. Richard ESCADAFAL, Directeur de Recherche, IRD/CESBIO
Rapporteurs	M. Xavier BRIOTTET, Directeur de Recherche, ONERA
	M. Philippe LAGACHERIE, Ingénieur de Recherche, INRA
Examinateurs	M. José BIOUCAS DIAS, Professeur, IST, Lisbonne

Directeur de thèse : Mme Véronique CARRERE, Maître de Conférences, Université de Nantes

Table of contents (English full version of the thesis)

List of figures:

Chapter I

Chapter III

List of tables

Ch. 1

Ch 2

Ch. 3

Annex:

Acknowledgements:

This research was funded by Marie Curie fellowship and CNRS being a part of European project “HYPER-I-NET”. I would like to thank to all the people, who supported me and helped during this work, my main supervisor Dr. Véronique Carrère for review and consistent remarks and to my second supervisor Dr. Jose Bioucas-Dias, who introduced me the un-mixing techniques. Thank you very much for your support and help!

My best regards to the people from laboratory of Planetologie et Geodynamique in Nantes, France, where I spent most of the time of my PhD. Without your support and assistance this work couldn’t be possible. Also, here I learned many interesting things being attended to the courses and seminars. My grateful thanks to the people from Instituto Superior Technique in Lisbon, Portugal, there I spent the last period of my PhD. Thanks for your warm assistance.

I would like also to thank also professor Eyal Ben-Dor for support in organization of the field campaign in Israel.

And finally, I would like to thank to members of my family that were available and supported at any moment.

Chapter I

1. Introduction

Most spectral signatures that are recorded at the scale of airborne sensors are mixtures of several end-members, at just about any scale at which we view it (Clark, 1999). Mixtures of minerals within the field of view of remote sensing instruments is a natural phenomenon, due both to the physical size of image pixel and because earth processes tend to create mixed surfaces. Natural geological surfaces have various mineralogical compositions and physical properties, these parameters may be successfully detected using remote sensing techniques. Thus, remote sensing applications in visible, near-infrared, short-wave infrared and thermal infrared regions of the electromagnetic radiation, suffer from image interpretation issues as the mixed nature of the spectral information considerably constrains the accuracy of spectral analysis (Adams et al., 1986; Atkinson et al., 1997; Gillespie, 1992; Green et al., 1998; Heinz and Chang, 2001; Keshava and Mustard, 2002; Roberts et al., 1993; Song, 2005). Producing successful un-mixing of mixture constituents and predicting their relative abundance is a challenge in the field of remote sensing (Bioucas-Dias, 2009; Somers, 2011; Gillespie, 1992).

Some of the theories claim that mixtures at the field scale can be approximately resolved using linear mixtures models. It was usually supposed that if mixture end-members at field scale do not lie in intimate contact with each other, the probability for a photon for being spread among the representatives of a mixture is dependent only on contribution area of each constituent specimen (Johnson, 1983; Adams et al., 1986). However it is known that reflectance spectra of a mixture are complex nonlinear functions of particle size, abundance, material opacity and type of surfaces (e.g. dust, sand, bedrock, where particles are mixed at different scales) (Keshava and Mustard, 2002; Poulet and Erard, 2004).

In the field, mixture may be composed of various end-members, in one scene there might be rocks and boulders, fine particles and grains, while particle sizes can vary from very fine to coarse, from dust to rocks or boulders. Coatings and crusts may overlay the constituents with a layer of different thickness and may mask or cause non-linear effects to mixture spectra.

At microscopic scale, a rock sample is composed of an intimate, non-linear, mixture of minerals which constitute the end-members (Singer, 1981). At this scale single mineral properties such as mineral composition, mineral grain size, mineral orientation are significant and may add variations to the spectral reflectance and absorption depths (Dyar et al., 2005; Carmina and

Carrère, 2009). In a rock, the relative abundance of the components may vary, depending on several causes: variations in composition may generate during mineral and rock genesis and subsequent alteration, according to well defined geochemical process in specific geological settings, or may occur through unpredictable contamination or mixing in various geological environments. The composition of a single mineral may vary owing to ionic substitution and the presence of impurities (Longhi, 2004).

At the scale of an airborne image, mixtures have macroscopic behavior, which is different. Therefore microscopic empirical studies of mineral mixtures and their results cannot be directly applied to the airborne data. The macro (field) scale mixtures have not been studied as widely as microscopic mixtures. Radiative transfer models have been applied on simulated mixtures in the laboratory, but have not yet been validated on macro-scale (real field) data. A large number of papers provide theoretical treatments and the necessary analytical solutions, but more laboratory and field measurements are needed to increase the number of observational and experimental inputs for theoretical models (Longhi, 2004).

1.1 General objectives

The aim of this study is to produce empirical observations of macro-mixtures of rocks and minerals in natural outcrops in the field, to compare simulated and modeled mixtures with real field data, to observe the influence of different factors on mixtures at macro-scale and finally, to apply linear and non-linear un-mixing algorithms and to evaluate their results. Empirical observations at the field scale are necessary to have a full vision of mixtures behavior, not only in laboratory conditions with simulated mixtures, but also in natural scenes, as they appear in the real field environments. Furthermore, observation of mixtures containing the same end-members should be produced at different scales: field scale and microscopic scale, to help better understand mixture behaviors, to obtain versatile vision on mixtures. This will help to improve existing un-mixing techniques. In contrast to radiative transfer models empirial study refers to real data, where different environmental factor may take place, in different field conditions, all these factors are usually not encountered by models. However are important for analysis of airborne data. Aim of this study to define various factors that influence reflectance of mixtures at macro-scale, in real field conditions.

The main scientific questions of this study are: what is the behavior of mineral mixtures at macro-scale? Under which circumstances macro mixtures are linear or non-linear? How different factors at macro-scale influence mixture: element size, composition, illumination effects,

shadow, coatings etc. What is the magnitude of the influence of each factor on mixture spectra? Which un-mixing approach, linear or non-linear, gives better result in the field scenarios and why? Which factors influence on un-mixing and cause to prediction errors? Is possible to improve current un-mixing techniques reliying on the knowledge of mixture behavior? Are powder mixtures good approximations of natural field situations?

The definition of end-members is an important issue in mixture analysis, because this issue is scale-dependent. At microscopic scale the end-members are single minerals, at macro-scale end-members are more complex and may be compiled from different formations, for example, boulders, rocks – aggregates of minerals, soils, sand composed of fine particles, etc. With increasing scale, more complex structures may be encountered into end-members, dependent on geological unit relevant at current scale. For example, at larger scale single rocks may be hardly identified, however they are encountered as a part of a larger structure, such as, plateau or mountain, river bed, or other geological formation.

In current study, focusing on field scenarios, various field cases will be observed. Based on the observations, end-members are selected for each unique scene. At the field scale end-members may vary from scene to scene and may be dependent on type of the surface, site or specific place. Current study refers to geological surface mostly devoid of vegetation. For such surface an aggregate of minerals with similar composition (properties) may be selected as an end-member, for example, rocks of specific types of various sizes, fine particles fraction (sand or silt), etc.

In chapter 1, basical principles of remote sensing are introduced, and a theoretical overview on the subject is presented, based on previous works and their findings. The existing un-mixing methods are overviewed. Chapter 2 presents the methodology, including a description of the study area, the instrumentation and measurement setup, the sampling strategy and samples description and the methodology followed for data processing. In chapter 3, the main results are presented, including an extended analysis of the various field scenarios, linear modeling, spectral un-mixing and correlation analysis. Chapter 4 contains a detailed discussion on the results and some general conclusions, advantages and disadvantages of the selected methods and an overwiew on future prospectives.

1.2 Remote Sensing

1.2.1 Principles of remote sensing

Remote sensing enables collection of information about an object without making physical contact with it (Rees, 2001). The method, that allows deriving information from an object using its electromagnetic spectrum, is called spectroscopy. Spectroscopy is the study of light as a function of wavelength that has been emitted, reflected, or scattered from a solid, liquid or gas (Clark, 1999). The radiation emitted, reflected, or scattered from a body generates a radiant flux density in the surrounding space that contains information about the body's properties. To measure the properties of this radiation, a collector is used, followed by a detector.

Passive remote sensing detects radiation emitted by the sun (this radiation consists mostly of ultra-violet, visible light and near-infrared radiation). The sensor detects electromagnetic radiation after it has interacted with or been emitted by the "target" material. Electromagnetic radiation (EMR) is a form of energy exhibiting wave-like behavior as it travels through space (Fig 1.1). EMR has both electric and magnetic field components, which oscillate in phase perpendicular to each other and perpendicular to the direction of energy propagation.

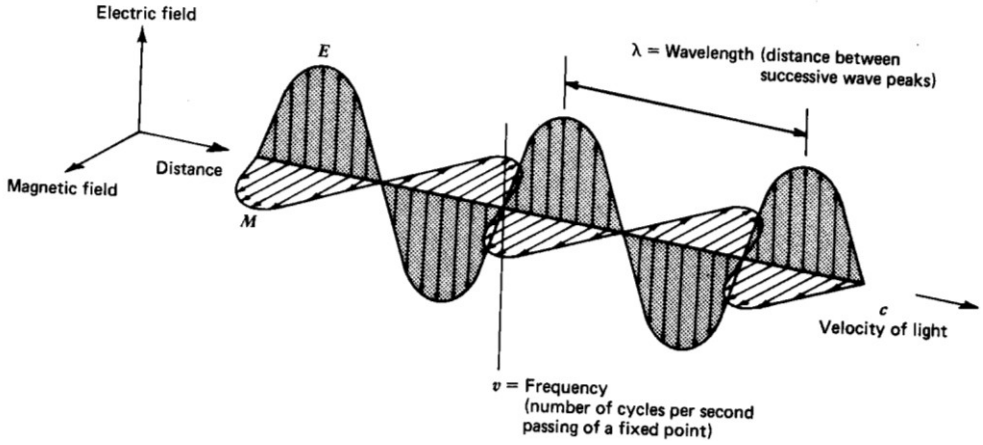

Figure 1.1 – An electromagnetic wave. Components include a sinusoidal electric wave (E) and similar magnetic wave (M) at right angles, both being perpendicular to the direction of propagation (Lillesand et al., 2004).

Electromagnetic radiation is classified according to the frequency of its wave. In order of increasing frequency and decreasing wavelength these are radio waves, microwaves, infrared radiation, visible light, ultraviolet radiation, X-rays and gamma rays (Fig. 1.2). The photon is the quantum of the electromagnetic interaction and the basic "unit" of light and all other forms of electromagnetic radiation.

The visible spectrum is the portion of the electromagnetic spectrum that is visible to the human eye. It corresponds to the wavelengths from 0.39 to 0.75 µm, with a maximum sensitivity at around 0.55 µm. Infrared range of electromagnetic radiation, with a wavelength longer than that of visible light, starts from the edge of the visible red light at 0.7 µm and extends conventionally up to 50 µm. The infrared range can be subdivided into sub-regions: near-infrared (NIR) from 0.78 to 1.5 µm, Short Wave Infrared (SWIR) from 1.5 to 3 µm, and Thermal Infrared (TIR) from 3 to 50 µm. Finally, the Microwave portion of the spectrum extends from 1 mm to 1 m.

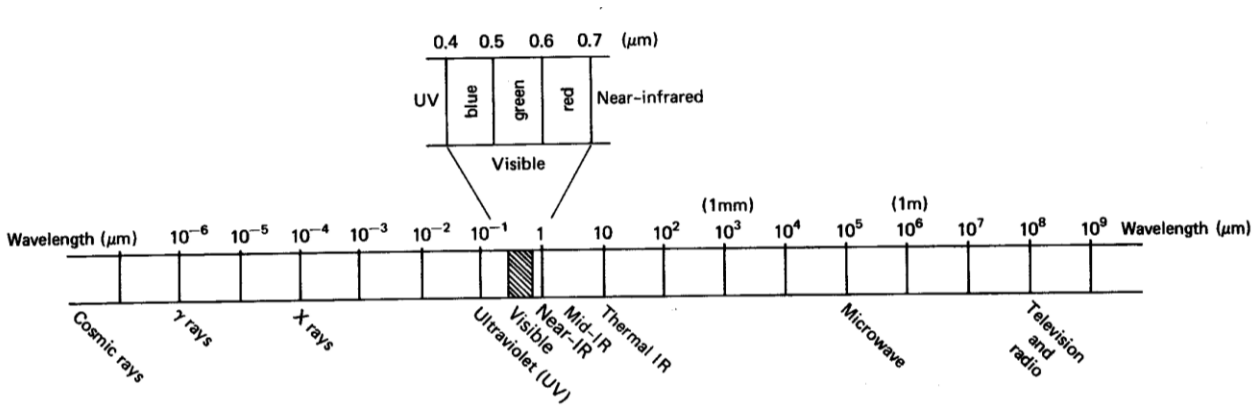

Figure 1.2 – The Electromagnetic spectrum (Lillesand et al., 2004)

The practical theory suggests that electromagnetic radiation is composed of many discrete units called photons. As photons enter a mineral, some are reflected from grain surfaces, some pass through the grain, and some are absorbed. Those photons that are reflected from grain surfaces or refracted through a particle are said to be scattered. Scattered photons may encounter another grain or be scattered away from the surface so they may be detected and measured. Photons may also originate from a surface, a process called emission. All natural surfaces emit photons when they are above absolute zero. However, we are focusing here on reflected solar energy.

Photons are absorbed by minerals through several processes. The variety of absorption processes and their wavelength dependence allows us to derive information about the chemistry of a mineral from its reflected or emitted light. There are two main processes, electronic and vibrational, that cause absorption bands in the spectra of materials.

1.2.1.1 Energy interaction with the surface

When electromagnetic energy is incident on any given earth surface feature, three fundamental energy interactions with the feature are possible (Fig 1.3). Various fractions of the energy incident on the element are *reflected*, *absorbed*, and/or *transmitted*. Applying the principle of conservation of energy, we can state the interrelationship among these three energy interactions as

$$E_I(\lambda) = E_R(\lambda)+E_A(\lambda)+E_T(\lambda) \quad (1.1)$$

Where

E_I = incident energy

E_R = reflected energy

E_A = absorbed energy

E_T = transmitted energy

with all energy components being a function of wavelength λ.

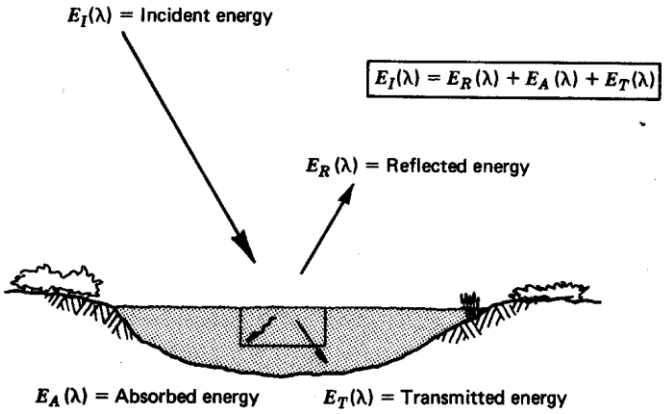

Figure 1.3 – Basic interactions between electromagnetic energy and earth surface feature (Lillesand et al., 2004).

The geometric manner in which an object reflects energy is also an important consideration. This factor is primarily a function of the surface roughness of the object. Reflectance received from the surface can be specular or diffuse. Specular reflectance is observed in cases when surface reflects light in one direction, these surfaces are mirror-like. One example of specular reflectance is reflection of light on water (sunglint). Diffuse reflectance (a lambertian surface is a perfect diffuser-equal intensity in all directions) is produced when the object surface is rough, in this

case light is scattered in different directions (Fig. 1.4). However, roughness is relative to the wavelength of observation, something can be considered smooth in the IR and be rough in the visible. Most natural surfaces are neither perfectly specular nor lambertian.

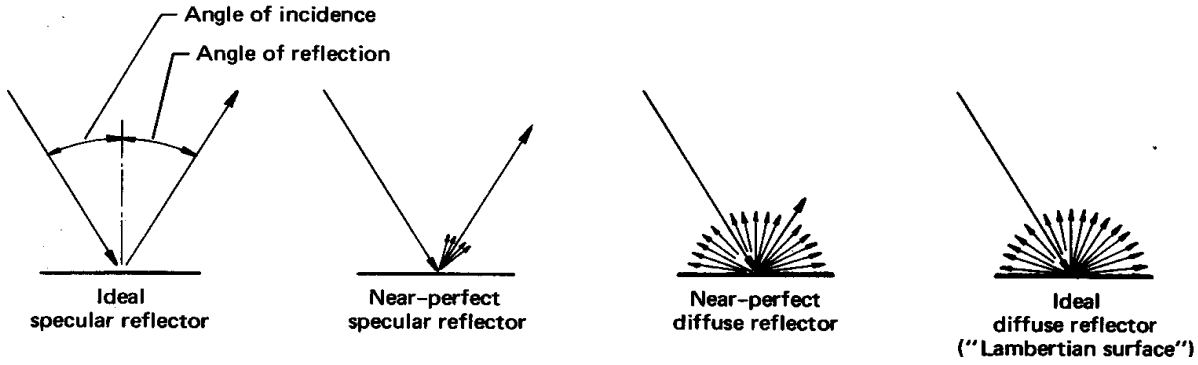

Figure 1.4 – Specular versus diffuse reflectance (Lillesand et al., 2004).

1.2.1.2 Causes of absorptions

1.2.1.2.1 Electronic Processes

The VNIR region spans an energy range sufficiently wide to encounter effects due to several different electronic processes (Hunt, 1977). Isolated atoms and ions have discrete energy states. Absorption of photons of a specific wavelength causes a change from one energy state to a higher one. Emission of a photon occurs as a result of a change in an energy state to a lower one (Fig. 1.5). When a photon is absorbed it is usually not emitted at the same wavelength. For example, it can cause heating of the material, resulting in grey-body emission at longer wavelengths (Clark, 1999).

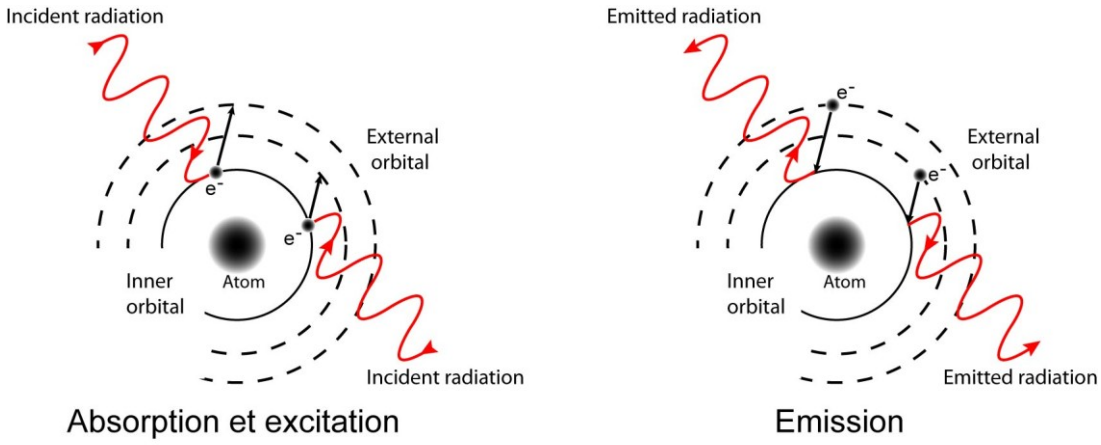

Figure 1.5 – Electronic processes in absorption (a) and emission (b) (modified after Roy, 2007).

In a solid, electrons may be shared between individual atoms. The energy level of shared electrons may become smeared over a range of values called "energy bands." However, bound electrons will still have quantized energy states (e.g. see Burns, 1970, 1993).

The most frequently encountered electronic features in the VNIR spectra of minerals (in rocks and soils) are due to the presence of iron in some form.

1.2.1.2.2 Crystal Field Effects

The most common electronic process revealed in the spectra of minerals is due to unfilled electron shells of transition elements (Ni, Cr, Co, Fe, etc.). Iron is the most common transition element in minerals. For all transition elements, *d* orbitals have identical energies in an isolated ion, but the energy levels split when the atom is located in a crystal field (e.g. see Burns, 1970, 1993). This splitting of the orbital energy states enables an electron to be moved from a lower level into a higher one by absorption of a photon having an energy matching the energy difference between the states (Fig 1.6). The energy levels are determined by the valence state of the atom (e.g. Fe^{2+}, Fe^{3+}), its coordination number, and the symmetry of the site it occupies. The levels are also influenced by the type of ligands formed, the extent of distortion of the site, and the value of the metal-ligand interatomic distance (e.g. Burns, 1993). The crystal field varies with crystal structure from mineral to mineral, thus the amount of splitting varies and the same ion (like Fe^{2+}) produces obviously different absorptions, making specific mineral identification possible from spectroscopy (Clark, 1999).

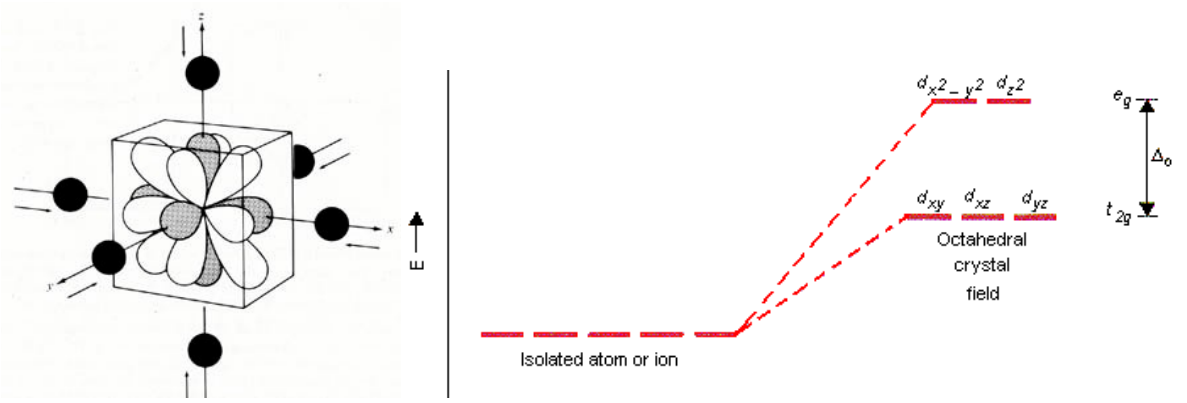

Figure 1.6 – Crystal field effects: a) octahedral crystal field; b) energy levels, the difference between the energies of the t2g and eg orbitals in an octahedral complex is represented by the symbol 0. This splitting of the energy of the d orbitals is not trivial (http://chemed.chem.purdue.edu).

1.2.1.2.3 Charge Transfer Absorptions

Absorption bands can also be caused by charge transfers, or inter-element transitions where the absorption of a photon causes an electron to move between ions or between ions and ligands. The transition can also occur between the same metal in different valence states, such as between Fe^{2+} and Fe^{3+}. In general, absorption bands caused by charge transfers are diagnostic of mineralogy. Their strengths are typically hundreds to thousands of times stronger than crystal field transitions (Burns, 1970; Hunt, 1977). The band centers usually occur in the ultraviolet with the wings of the absorption extending into the visible. Charge transfer absorptions are the main cause of the red color of iron oxides and hydroxides. Morris *et al.* (1985) studied the details of sub-micron iron oxides where it was found that the absorption bands rapidly decrease in intensity. This occurs because of the increased surface to volume ratio at small grain size which results in a greater proportion of grain boundaries where crystal field effects are different, resulting in lower magnetic coupling and reduced absorption strength. Other iron oxides probably show similar effects. Reflectance spectra of iron oxides have such strong absorption bands that the shape changes significantly with grain size. Small shifts in absorption band position are also observed due to substitution of other elements, like aluminum for iron in hematite (e.g. Morris *et al.*, 1985, Clark, 1999).

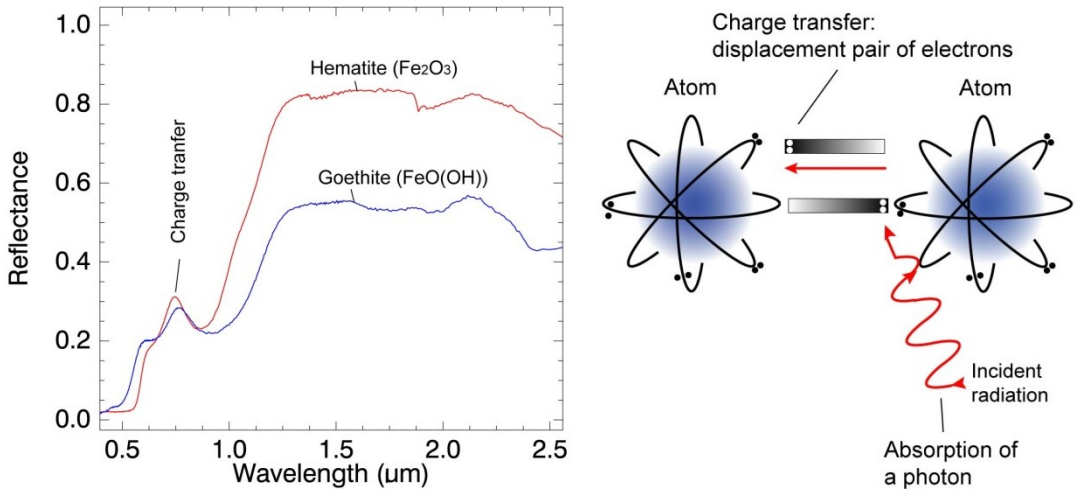

Figure 1.7 – A schematic view of charge transfer (right) (modified after Roy, 2007); spectra of Hematite and Goethite from USGS spectral library shows iron oxides absorptions in the VIS caused by charge transfer.

1.2.1.2.4 Color Centers

A few minerals show color due to absorption by "color centers." A color center is caused by irradiation (e.g. by solar UV radiation) of an imperfect crystal. Crystals in nature have lattice defects that disturb the periodicity of the crystal. For example, defects might be caused by impurities (Hunt, 1977).

1.2.1.2.5 Vibrational Processes

The bonds in a molecule or crystal lattice are like springs with attached weights: the whole system can vibrate. The frequency of vibration depends on the strength of each spring (the bond in a molecule) and their masses (the mass of each element in a molecule). For a molecule with N atoms, there are 3N-6 normal modes of vibrations called fundamentals. Each vibration can also occur at roughly multiples of the original fundamental frequency. The additional vibrations are called overtones when they involve multiples of a single fundamental mode, and combinations when they involve different modes of vibrations (Hunt, 1977; Clark, 1999).

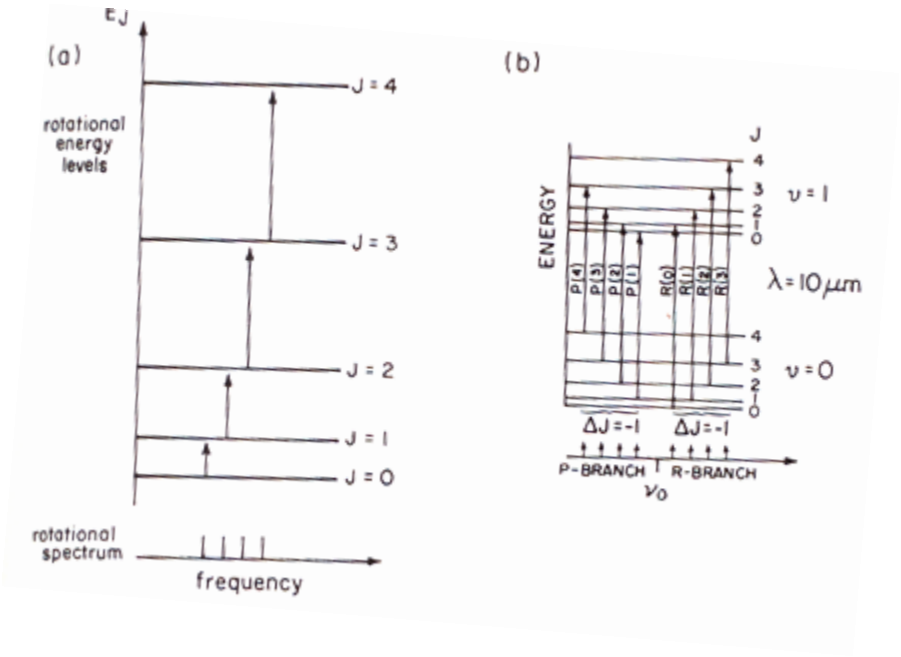

Figure 1.8 - Energy levels and the resulting spectrum of molecular rotation (a), vibrational-rotational transitions between the lowest vibrational and rotational levels (b) (Burns, 1970).

A vibrational absorption will be seen in the infrared spectrum only if the molecule responsible shows a dipole moment (it is said to be infrared active). A symmetric molecule, like N2 is not normally infrared active unless it is distorted (for example, when under high pressure). Vibrations from two or more modes can occur at the same frequency, and because they can't be distinguished, are said to be degenerate. An isolated molecule with degenerate modes may show the modes at slightly different frequencies in a crystal because of the non-symmetric influences of the crystal field.

A free molecule can rotate and move translationally, but even in a solid partial rotation and slight translation can occur. These motions are called lattice modes and typically occur at very low energies (longer mid-infrared wavelengths), beyond about 20 μm.

Traditionally, the frequencies of fundamental vibrations are labeled with the Greek letter nu (ν) and a subscript (Herzberg, 1945). If a molecule has vibration fundamentals ν_1, ν_2, ν_3, then it can have overtones at approximately $2\nu_1$, $3\nu_1$, $2\nu_2$ and combinations at approximately $\nu_1+\nu_2$, $\nu_2+\nu_3$, $\nu_1+\nu_2+\nu_3$, and so on. These examples used summations of modes, but subtractions are also possible (e.g. $\nu_1+\nu_3-\nu_2$). Each higher overtone or combination is typically 30

to 100 times weaker than the last. Consequently, the spectrum of a mineral can be quite complex. In reflectance spectroscopy, these weak absorptions can be measured easily and diagnostic information routinely gained from 2nd and 3rd overtones and combinations.

Figure 1.9 summarizes specific absorptions of common minerals resulting from different processes (Hunt, 1977).

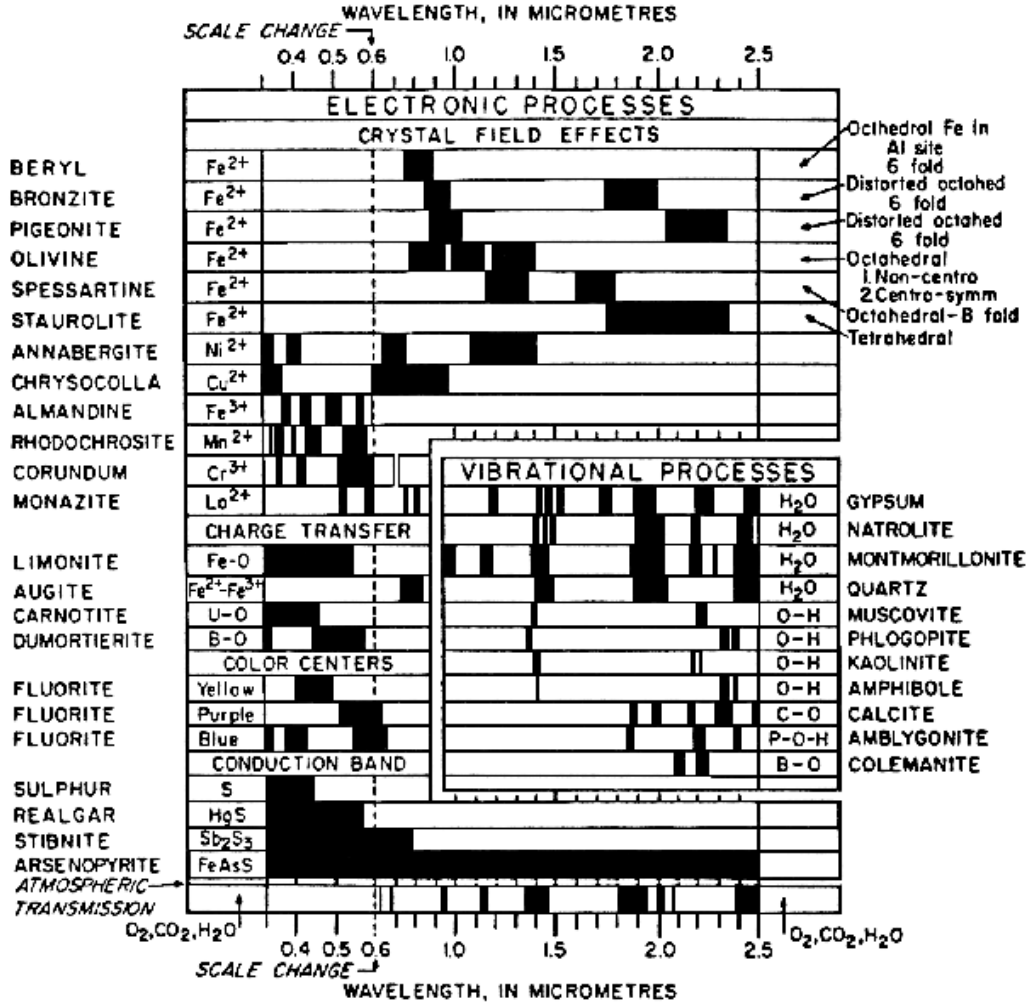

Figure 1.9- Spectral signature diagram, specific absorptions of common minerals (Hunt, 1977)

1.2.2 Imaging spectroscopy

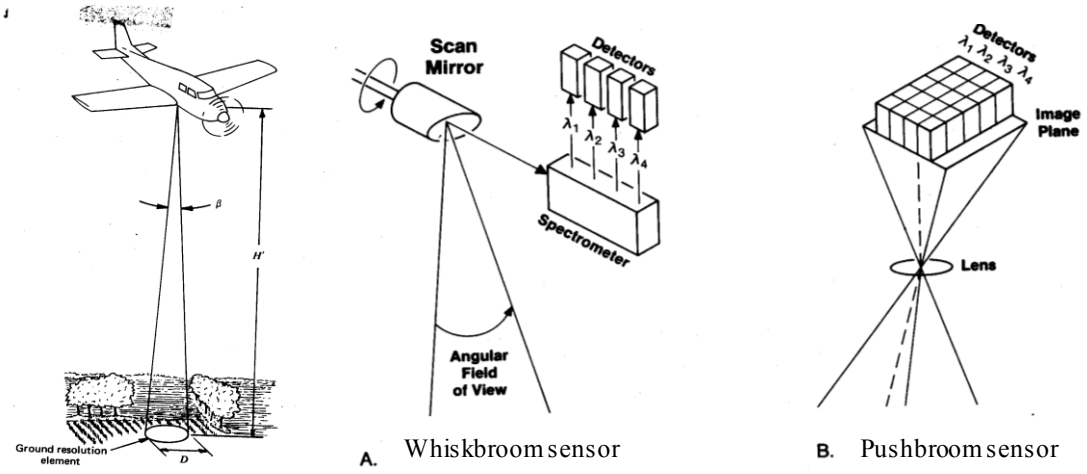

Figure 1.10 – Hyperspectral scanning systems: a) whiskbroom sensor b) pushbroom sensor; (Lillesand, 2004).

Imaging spectroscopy is a technique which enables to acquire image pixels which have spectral signatures. Accordingly, each pixel of a spectral image has three dimensions: spatial (x, y) and spectral (z). As the result, a data cube is acquired, where at each layer of this cube reflectance values are recorded at specific wavelength. In other words, it is the simultaneous acquisition of spatially coregistered images in many spectrally contiguous bands (Fig. 1.11).

Each pixel (the smallest unit of the image) has an associated continuous spectrum that can be used to identify the surface materials. Hyperspectral sensors usually acquire images in many, very narrow, contiguous spectral bands: these systems collect about 100 or more bands of data (depending on sensor configuration).

There are two types of spectrometers: whiskbroom and pushbroom (Fig. 1.10 a,b). Whiskbroom sensors (Fig. 1.10.a) scan the terrain using a rotating mirror, along scan lines. This allows the scanner to repeatedly measure the energy from one side of the aircraft to the other. Successive scan lines are covered as the platform moves forward, yielding a series of contiguous, narrow strips comprising a two dimensional image of rows and columns (Rees, 2001; Kerekes, 2009).

In pushbroom sensors (Fig. 1.10.b) a linear array of detectors is used. Linear array consist of numerous charge-coupled devices (CCDs) positioned end to end in a line. Each detector element is dedicated to sensing the energy in a single column of data. Pushbroom enables one row of an

image to be collected at once, while the platform motion provides the down track sampling or columns of the image. An advantage here is the significantly longer dwell time for the detectors and as a result higher signal-to-noise ratio (Kerekes, 2009) (Fig. 1.10 a).

1.2.2.1 Energy detection

The detection of electromagnetic energy at each wavelength is done by electronic sensors that generate an electrical signal that corresponds to the energy variations in the original scene. The intensity of each pixel corresponds to the average brightness or Digital Number (DN) measured electronically over the ground area corresponding to each pixel. DN values are acquired for each pixel of an image at specific wavelengths, in a defined spectral range, resulting in a continuous spectrum for each pixel. Sensor signals are recorded in terms of an electrical voltage value, then values are converted to DN. The DN output values are integers, DN range for actual sensors is 10 to 12 bits, that is 2^{10} to 2^{12} values.

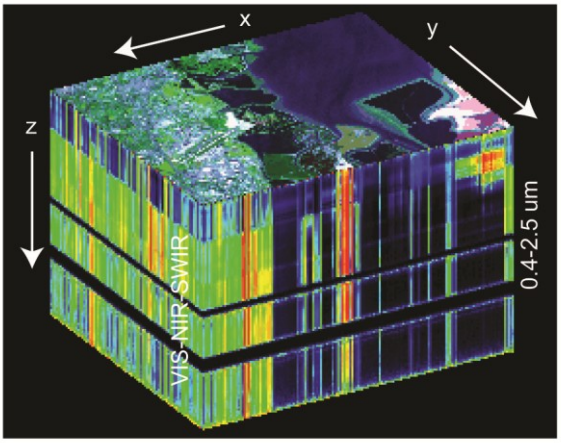

Figure 1.11- Hyperspectral data cube.

1.2.2.2 Noise effects

The quality of an image can be stated by the signal-to-noise ratio (or the Noise Equivalent Delta Radiance, NeΔR) recorded by the sensor. Another noise effects may appear in the image as a result of instrument defects: dead pixels, boreside effect, smile effect, etc. Since noise effects are present in the image they should be removed (or at least attenuated) in order to make a correct interpretation of the data, otherwise data may present false results.

1.2.2.3 Atmospheric effects

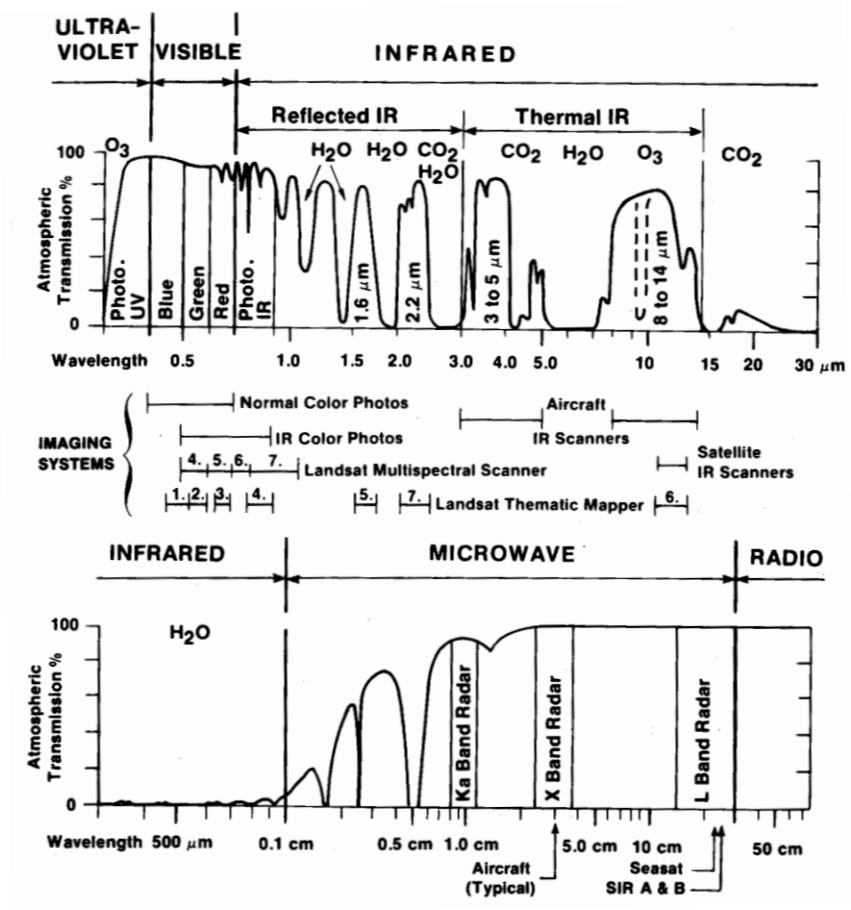

Figure 1.12 – Expanded diagrams of the visible and infrared regions (upper) and the microwave region (lower) showing atmospheric windows. Wavelength bands of commonly used remote sensing systems are indicated. Gases responsible for atmospheric absorptions are shown (Lillesand and Kiefer, 1994)

Atmospheric scattering is the diffusion of radiation by particles in the atmosphere. *Rayleigh* scattering is common when radiation interacts with atmospheric molecules and other tiny particles that are much smaller in diameter than the wavelength of the interacting radiation. There is a much stronger tendency for short wavelengths to be scattered by this mechanism than long wavelengths. *Mie* scattering exists when atmospheric particle diameters essentially equal the wavelengths of the energy being sensed. Water vapor and dust are major causes of Mie scattering (white appearence of the clouds is due to Mie scattering). This type of scatter tends to influence longer wavelengths compared to Rayleigh scattering.

Atmospheric absorption, in contrast to scattering, results in the effective loss of energy to atmospheric constituents. This normally involves absorption of energy at given wavelengths. The most efficient absorbers of solar radiation in this regard are water vapor, carbon dioxide, and ozone. Because these gases tend to absorb electromagnetic energy in specific wavelength bands,

they strongly influence “where we look” spectrally with any given remote sensing system. The wavelength ranges in which the atmosphere is particularly transitive of energy are referred to as *atmospheric windows* (Fig.1.12).

In order to access information relevant to surface properties, atmospheric effects have to be removed from the data. Atmospheric correction removes atmospheric effects and enables interpretation of data coming from the surface. This is particularly important for imaging spectrometer data which are covering the 400-2500 nm wavelength range continuously. However, saturation of the 1.4 and 1.9 μm atmospheric water vapor absorption bands prevents from “seeing” the surface and cannot be corrected for. Therefore these wavelength regions are often avoided for Earth surface observation.

1.3 Mineral mixtures

In general, four types of mixtures can be defined (Fig 1.13):

1. Linear mixture (areal mixture). The materials in the field of view are optically separated, so there is no multiple scattering between components. The combined signal is simply the sum of the fractional area times the spectrum of each component.
2. Intimate mixture. An intimate mixture occurs when different materials are in intimate contact in a scattering surface, such as the mineral grains in a soil or rock. Depending on the optical properties of each component, the resulting signal is a highly non-linear combination of the end-member spectra.
3. Coatings occur when one material coats another. Each coating is a scattering-transmitting layer whose optical thickness varies with material properties and wavelength. At geological sites this type of mixtures is usual for surfaces covered by dust or for altered or weathered surfaces, when weathered minerals produce a layer over a fresh rock. This weathered layer, depending on its depth may mask spectral signal coming of rock surface.
4. Molecular mixtures occur on a molecular level, such as two liquids or a liquid and a solid mixed together. The close contact of the mixture components can cause band shifts (Clark, 1999).

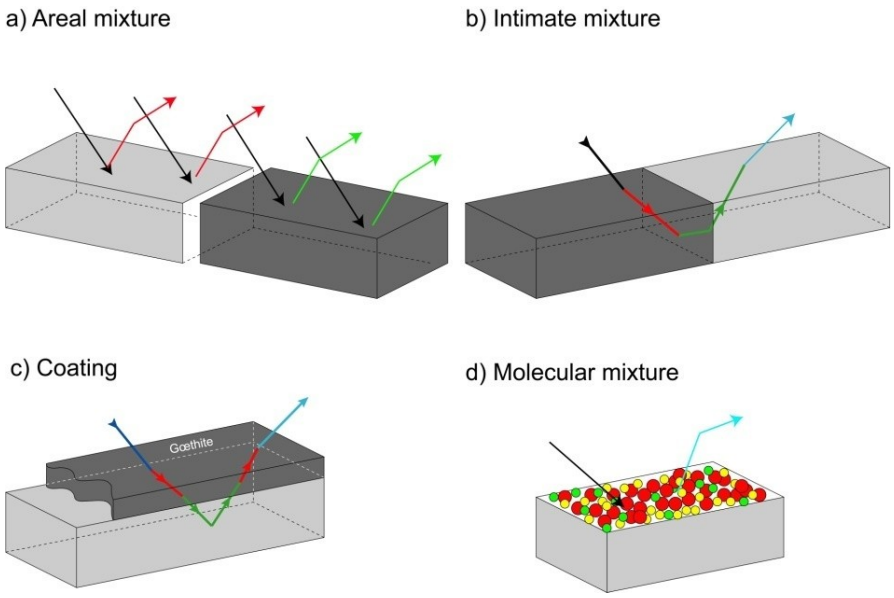

Figure 1.13 – General types of mixtures (modified after Roy, 2007)

One of the ways in which mineral mixtures were studied is mixture simulations in the laboratory, with known composition and proportions of components (empirical modeling). Usually empirical methods use powdered minerals to simulate mixtures; with powders it is easy to control mixtures proportions and grain sizes (Adams, 1974; Singer, 1981). Mixtures of different components showed different behaviors, depending on which end-members were mixed; therefore there are no general rules which could be valid for all mixtures, or even for some of them. Results of microscopic empirical investigations were assumed to be valid at all scales, and particularly at the scale of airborne images (at macro-scale), and were used for image interpretations (Singer, 1981; Adams, 1974; Combe et al., 2008; Minitti et al., 2002; Baldridge and Farmer, 2004; Farrand et al., 2006). Composition of un-known planetary surfaces and asteroids has been inferred mainly through comparison between remotely acquired spectra and laboratory measurements of powdered minerals and mixtures (Gaffey et al., 1993; Pieters et al., 1996; Pompilio, 2007).

However, usually, natural field scenarios cannot properly be represented by mixtures of powders; in nature landscapes might have complex structures, where rocks are composed of minerals, which are continually connected to each other and grain and boulder sizes in the field can highly differ from micro to macro scale (Poulet, 2004; Pompilio, 2007)

However it is known that regular linear un-mixing applied on mixtures with non-linear behavior cannot predict correct abundances of end-members with high accuracy if their combination in the mixture is non-linear. The linear model can cause considerable ambiguity and false fractions

when used on non-linear mixtures (Mustard and Sunshine, 1999). Standard linear un-mixing algorithms are expected to add up to 30% error to un-mixing results (Mustard and Sunshine, 1999; Keshava and Mustard, 2002; Combe et al., 2008). The mixture problem is complex, because in some cases, mixtures might be highly non-linear, though in some cases components within a mixture appear in an areal proportion (Nash and Conel, 1974). The mechanism of spectral mixing is still not well understood.

Therefore un-mixing of natural outcrops is a challenge, which does not have a unique solution. Mixture behavior depends on optical and physical properties of the media, while there is also wavelength dependence of mixture linearity (Nash and Conel, 1974; Singer, 1981; Clark, 1983; Johnson et al., 1992). At one wavelength, mixture might have a highly non-linear behavior, while at others the same mixture may be linear. It is known that scattering and absorption of energy in the VNIR results in the spectral nonlinearity of mineral mixtures (Lyon, 1964; Nash and Conel, 1974; Mustard and Pieters, 1989). The scattering is caused by the geometric optics of the particles with respect to wavelength together with the absorption coefficient of the minerals (Hapke, 1981; Johnson et al., 1983; Moersch and Christensen, 1995). If minerals have small absorption coefficient, a photon path length is larger, therefore photons undergo significantly greater volume scattering at these shorter wavelengths (Eastes, 1989; Wald and Salisbury, 1995). Volume scattering occurs where a photon passes through one or more grains of a mixture and is incoherently scattered at every particle interface and grain asperity. The large probability that photons will survive passage through several transparent grains, even where those grains are much larger than the wavelength of the photon, causes weakly absorbing materials to have larger degrees of nonlinear volumetric scattering.

In geological sites, rocks may have various sizes from outcrops, to boulders, from grains of sand to dust particles. Sometimes dust particles may coat boulders, resulting in intimate mixtures (Johnson et al., 2002). For example, interpretations of surface composition of Mars using both *in situ* and remote reflectance often are hindered by the masking effect of atmospherically deposited dust coatings (Arvidson et al, 1989; Mustard and Sunshine, 1995; Feldman et al., 2002). Laboratory spectroscopy of dust coatings demonstrate that thin (<100 μm) layers can effectively obscure the spectral signature of underlying materials in the visible and the infrared (Roush, 1982; Singer and Roush, 1983; Johnson et al., 2002). Linear models typically fail to un-mix coating from rock. Additionally, weathering of rocks creates rings of altered minerals surrounding fresher rock. Over time the ring breaks off and is transported away, exposing more

fresh rock. Thus rock outcrops may contain mixtures of altered and unaltered minerals at the surface.

1.3.1 Mineral mixture models.

1.3.1.1 Empirical models

Many mixture simulations at microscopic scale were produced in laboratory conditions. There, mixture components proportions and grain sizes could be controlled, and then their spectral behavior was studied. Microscopic mixtures (intimate mixtures) are usually fabricated from powdered minerals, with controlled proportions and known grain size (Adams, 1974; Singer, 1981; Le Bras and Erard, 2003; Harloff and Arnold, 2001; Adams and Filice, 1967; Rendon and Serna, 1981; Orofino et al., 2006). But not many studies checked mixtures behavior at field scale, where mixtures are supposed to be more comparable to pixel mixture. Empirical observations of mineral mixtures studied mainly rocks that could represent lunar and Martian surfaces.

It was found that highly absorbing phases may mask the characteristics absorption bands that are contributed by other phases. For example, the "strong" spectrum of an orthopyroxene is compared with the curves of mixtures with plagioclase and with magnetite (Pieters, 1973).

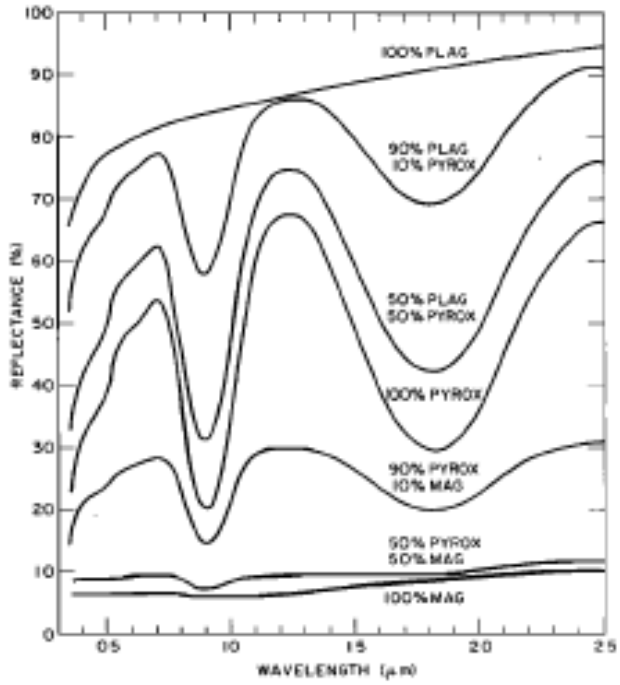

Figure 1.14 – Mineral mixtures of plagioclase, pyroxene and magnetite powders (Adams, 1974).

The presence of 90% of the weakly absorbing plagioclase still allows the full detail of the pyroxene bands to be seen, whereas 50% of the strongly absorbing magnetite removes all but the last vestiges of the pyroxene bands from the combined spectrum (Fig. 1.14) (Nash and Conel, 1974; Adams, 1974).

In two-component mixtures of pyroxenes and olivine, mixtures are dominated by pyroxene characteristics, pyroxene is opaque. With pyroxene contents of 50% or greater the spectra look similar to that of pure pyroxene (Fig. 1.15).

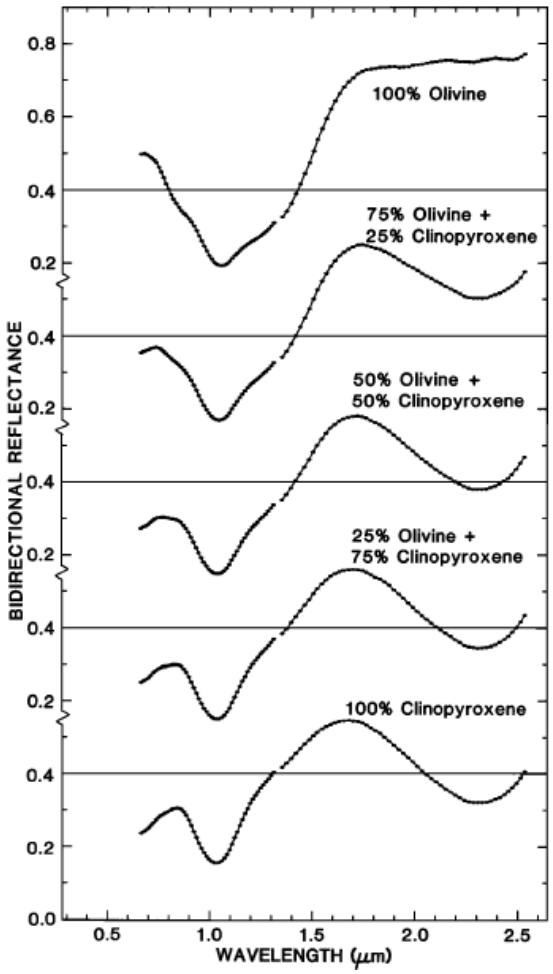

Figure 1.15 – Mineral mixtures of clinopyroxene and olivine powders (Singer, 1981)

In mixtures of olivine and orthopyroxene the band minimum position for these mixtures is not a linear function of composition, orthopyroxene tends to dominate the mixture spectra. With quantities of olivine up to 50% the minimum of the 1 μm band occurs at virtually the same wavelength as for pure orthopyroxene, and the 1- and 2-μm band positions fall on the trend for

pure pyroxenes. In mixtures of olivine and limonite, as little as 5% limonite, significantly alters the olivine spectrum but leaves the three-band structure near 1 μm recognizable. With 50% limonite the spectrum shape looks very similar to that of pure limonite (Singer, 1981). Magnetite is a common opaque mineral in mafic and ultramafic assemblages. Small amounts of magnetite are very effective at reducing the reflectance and spectral contrast of a mixture of olivine and magnetite. This effect is consistent with other studies of opaque + non opaque mineral assemblages (Johnson and Fanale, 1973; Pieters, 1973; Nash and Conel, 1974). Fifty percent magnetite content reduces the reflectance of the mixtures to less than 0.1 but does not entirely eliminate the olivine absorptions (Fig. 1.3).

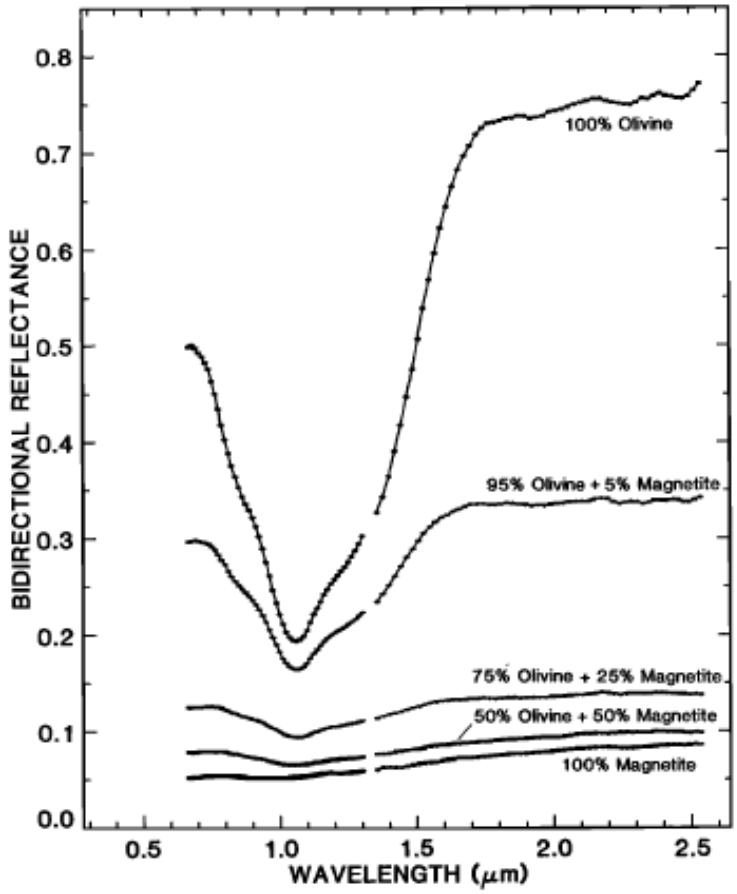

Figure 1.16- Mixtures of magnetite and olivine powders (Singer, 1981)

Empirical studies of pyroxene/ilmenite mixtures show that there is a strong band-producing property of pyroxene and a strong albedo-reducing property of ilmenite (Nash and Conel, 1974).

Ilmenite is a titanium-iron oxide mineral characterized by a low albedo. In mixture of plagioclase/ilmenite, the plagioclase curve was depressed and the 1.3 μm band was erased by

25% or more of ilmenite. Also in three-phase mixtures opaque ilmenite is the dominant component that lowers albedo, flattens the spectrum and reduces the depth of pyroxene absorption bands. However the 0.9 μm pyroxene band persists over a wide range of pyroxene contents and its depth is directly proportional to pyroxene abundance. Therefore opaque minerals will cause minimum band distortion, but maximum darkening of a mixture, while non-opaque glass will cause maximum band distortion, but minimum darkening of a mixture (Nash and Conel, 1974). Darkening is produced by very small inclusions of reduced iron as demonstrated by Pieters et al. (2000). It is known that absorptions caused by charge transfer are much stronger than crystal field transitions (Clark, 1999; Hunt, 1977). These types of absorption are common for minerals containing iron (iron is a transition element).

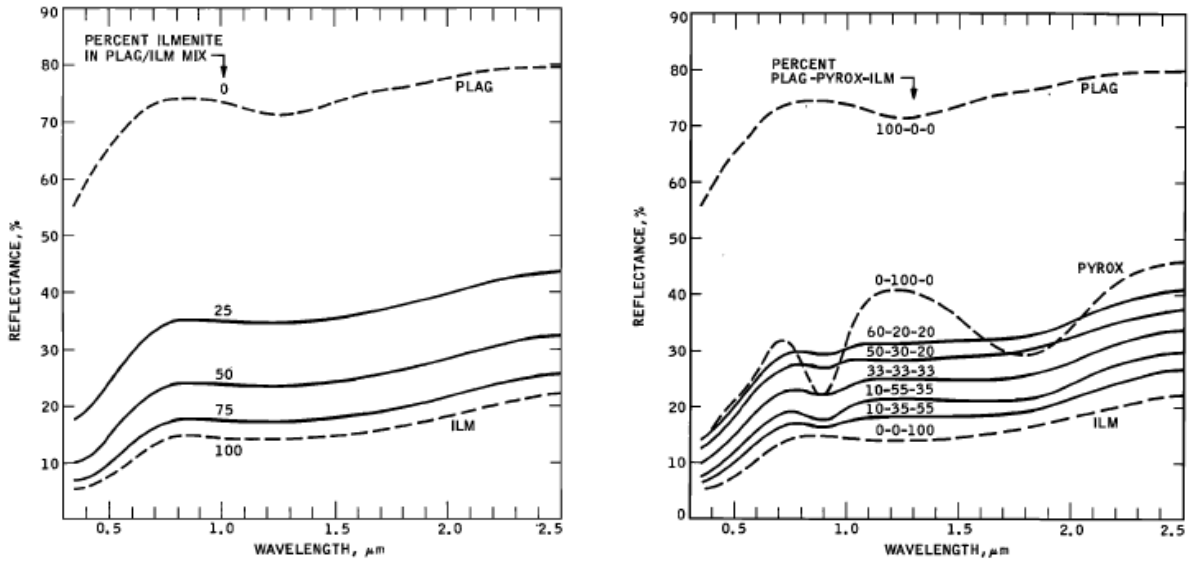

Figure 1.17 – Spectra of powder ternary mixtures of plagioclase-pyroxene-ilmenite (left) and plagioclase-ilmenite (right) (Nash and Conel, 1974).

In multicomponent mixtures the presence of a spectrally neutral phase leads to underestimation of the component with a weaker band. The larger the difference in contrasts between the bands, the larger is the systematic error. A dark component always dominates the reflectance of a mixture, even when the particle sizes of both end-members are equal. Absorption bands located at longer wavelengths should be less influenced by contrast between bright and dark materials (Moroz and Arnold, 1999).

These observations were produced at microscopic scale, however it was not checked if at macro scale these effects have similar mechanisms.

1.3.1.1.1 Effect of grain size

Successful prediction of end-member composition requires some knowledge of grain size distribution. Grain sizes of minerals have a significant influence on reflectance, spectral shape and absorption depths of a mixture. An aggregate of un-sorted particles closely matches the reflectance properties of smallest particle sizes in powders, based on observation of spectra of powders with different grain sizes of silicate rocks (Adams and Filice, 1967). Individual particles of silicate rocks become less absorbing as they are made smaller. Because the drop in absorption is the dominant effect as particle size is diminished, the net result is an increase in reflected light. For smaller grain size absorptions are smaller. Coarser samples commonly show more pronounced absorption bands. Mixtures involving minerals having different particle sizes exhibit complex volume-scattering phenomena, in which the spectral properties of the coarser material typically predominate (Clark and Kierein, 1988).

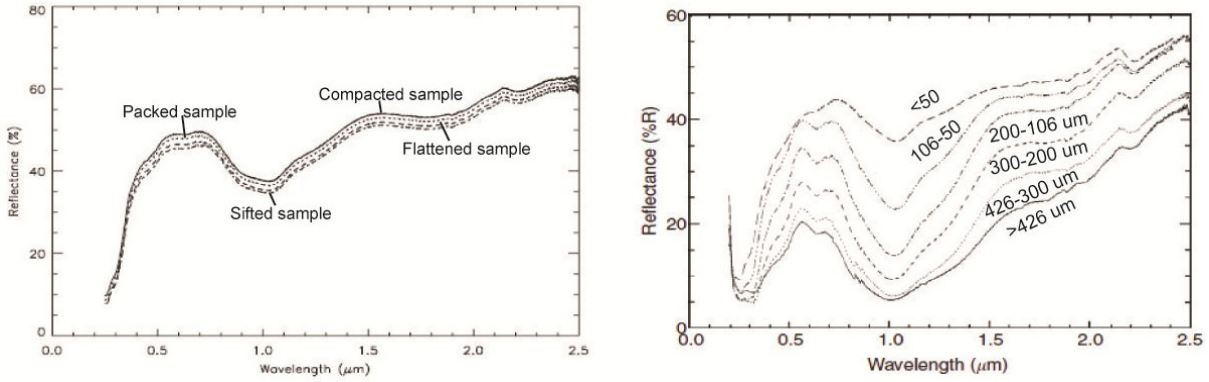

Figure 1.18- Spectra of particles in size range (106-50µm) in different preparation techniques: packed, flattened, sifted samples (left) and spectra of flattened particles of different grain sizes (right) (Orofino et al., 2006).

An example of fig.1.18 shows spectra of powdered particles of olivine in the size range 106-50 µm in compacted sample, packed sample, flattened sample and sifted sample. This graph proves that not only grain size, but also the way a sample is prepared influences reflectance. Fig 1.18 (right) shows an example of spectra of particles of different grain sizes (Orofino et al., 2006). With increasing grain size, reflectance decreases.

It is generally observed that reflectance decreases when grain size is increasing, up to a certain point (called effective grain size), after which an opposite process occurs (Hapke, 1993; Moroz, 1999). Variations in particle size of powder sample and variations in roughness for bulk sample

produce the same spectral effects: the rougher is the surface, the lower the reflectance. The NIR continuum slope also becomes bluer with increasing roughness. However more examinations should take place to help explaining the processes occurring for a bulk sample. If multiple scattering dominates in a mixture, as is usually the case in the visible and near-infrared, the reflectance decreases as the grain size increases (Fig 1.19). In the mid-infrared absorption coefficients are much higher, the first surface reflection is a larger or even dominant component of the scattered signal. In these cases the grain size effects are more complex, even reversing trends commonly seen at shorter wavelengths (Clark, 1999).

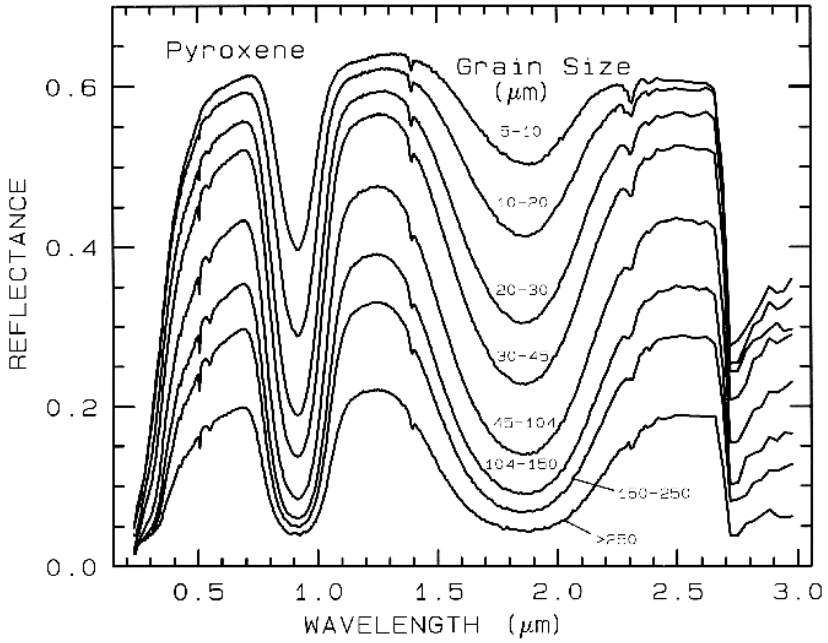

Figure 1.19 – Spectra of powdered pyroxene as a function of grain size (Clark, 1999).

According to comparison of scattering properties of bulk and powdered samples of basalts, spectra of bulk samples are characterized by shallower bands and a usually bluer sloped continuum (Clenet, 2011). The scattering history of a photon in such a texture is similar in principle to its behavior in an intimate mixture. In a study on pyroxene and iron oxides mixtures by Poulet and Erard (2004), it was found that differences between powder and bulk sample reflectance came from the derived grain size of pyroxene and the iron oxide content. In the case of bulk rock, the smaller grain size reproduces the weaker absorption bands, while the larger iron oxide content diminishes the absorption bands. This last effect is qualitatively consistent with the interpretation of maturation effect in regoliths, where darkening is produced by very small inclusions of reduced iron (Pieters et al., 2000).

The regolith is generally considered as representative of the bedrock composition (Pompilio, 2007). The mineral association in the regolith is the result of: 1) excavation and fragmentation of buried rocks due to impact processes, which often involve rocks from various stratigraphic levels in the crust; 2) sedimentary processes responsible for selective deposition and mixing of materials from different provenances. The detailed examination of solid rock spectra is still in a developmental stage (Longhi et al., 2000; Harloff and Arnold, 2001; Longhi et al., 2001; Pompilio, 2005). Open questions still exist and mainly relate to: 1) the reproducibility of solid rock spectra with mineral mixture spectra, 2) the effect of rock texture on position and shape of diagnostic absorptions of pure minerals, and 3) the capability of a mathematical model to unambiguously resolve the spectral components within solid rock spectra.

Fig.1.20 shows an example of spectra of solid rock and powders with the same constituents.

The rock spectrum (1) is closer to that of powder (C), which has the coarser grain size.

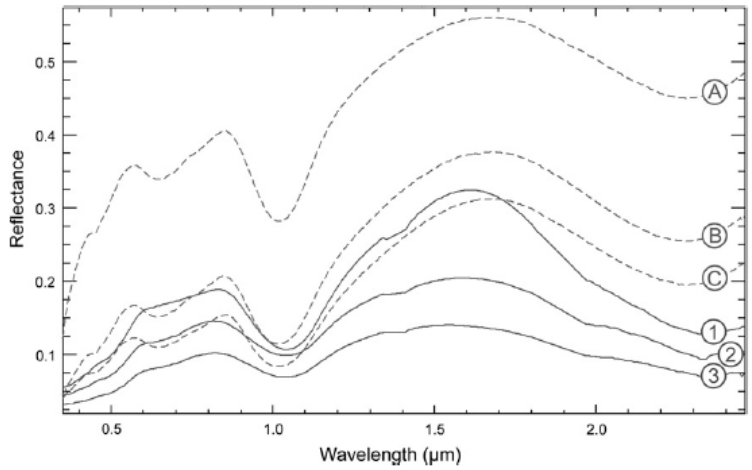

Figure 1.20 – Difference between powder clinopyroxene spectra A (< 45 µm), B(45-75µm), C(75-125µm) and natural rocks spectra (1, 2, 3), (Clenet et al., 2011).

The effect of grain size on spectra is known for microscopic mixtures, however the effect of size at macroscopic scale can be associated with boulder size, if mixture composers are rocks (aggregated minerals). Influence of size of macro constituents in mixtures has not been well studied yet.

1.3.1.2 Physical models

Physical models can estimate mixture composition from spectra using optical constants of its components. For this some *a priori* knowledge of constituents is required: optical constants and grain size distribution. Grain size can be estimated with physical models, but composition has to be known (Hapke 1981, 1984, 1986; Hapke and Wells, 1981; Lumme and Bowell, 1981; Shkuratov, 1999). Using Hapke (1981, 1993) radiative transfer theory and optical constants of minerals, reflectance spectra of pure minerals at a single grain size, spectra of a pure mineral with a known grain size distribution, and mineral mixtures with varying grain size components can all be computed (Clark, 1999). The inversion of reflectance to quantitative abundances has been tested in the case of laboratory mixtures (Johnson et al., 1983, 1992; Clark, 1983; Mustard and Pieters, 1987, 1989; Shipman and Adams, 1987; Sunshine and Pieters, 1990, 1991). Exact solutions to Hapke's model require multiple viewing geometries which are not commonly obtained by imaging spectrometers.

1.3.1.2.1 Hapke bidirectional reflectance model (Hapke, 1981)

The reflectance r (i, e, α, ω) of a semi-infinite medium of regolith particles or scatterers, which are large compared to the wavelength λ, can be computed from Hapke's (1981) Eq. (1.2), where i is the angle of incident light, e is the angle of emergent light, α is the phase angle, and ω is the average particle single scattering albedo. The albedo is calculated independently of the method used to solve the radiative transfer equation. Bidirectional reflectance $r=\bar{I}/J$ of a surface consisting of particles of arbitrary shape in close proximity to one another, is given with a good approximation by:

$$r(\mu_o,\mu,g) = \frac{w}{4\pi}\frac{\mu_o}{\mu_o+\mu}\{[1+B(g)]P(g)+H(\mu_o)H(\mu)-1\} \quad (1.2)$$

Where $B(g)$ is the backscattering function given by (1.3), $H(\mu)$ is a multiple-scattering function given by (1.4), and ω is the average single-scattering albedo and is computed from (1.5)

$$B(g) = B_o\left[1-\frac{\tan|g|}{2h}\left(3-e^{-\frac{h}{\tan|g|}}\right)(1-e^{-h/\tan|g|})\right] \quad |g| \le \frac{\pi}{2} \quad (1.3)$$

$$B(g) = 0 \qquad |g| \ge \pi/2$$

$$For\,|g| \ll 1, B(g) \cong B_o(1-\frac{3|g|}{2h})$$

(1.4) $$H(\mu) = \frac{1+2\mu}{1+2\gamma\mu}$$

(1.5) $$w = S/E$$

E is the extinction coefficient, S, the scattering coefficient of the medium.

The parameter B_0 describes the magnitude of the opposition effect. For a low-albedo surface, such as the Moon or Mercury, $B_0 \cong 1$. This quantity is hard to measure uniquely in the laboratory because the experimental results depend on the degree of collimation of the incident light and angular size of the detector, as well as the properties of the surface.

From the recent study of Shepard and Helfenstein (2007), in its current stage of development, the Hapke model does not treat optical interactions in particulate samples with sufficient fidelity to be utilized as a reliable remote sensing tool for estimating unique and meaningful physical properties of planetary surfaces. Retrieved values of the Hapke model parameters generally do not accurately represent the properties of the particulates alone, but rather some complex combination of particulate properties, surface roughness, and packing state.

Another geometrical optics model for spectral albedo dependence of regolith-like surfaces, presented by Shkuratov (1999) has some advantages relatively to Hapke models. This simple model is also based on geometrical-optics approximation and has an important advantage — it is analytically invertible, i.e., the wavelength behavior of average absorption coefficient of regolith material can be estimated from spectral albedo data. The model is applicable to surfaces of different structure and composition and uses spectra of optical constants of the components of the surface material. This model includes dependence on porosity, and is analytically invertible; i.e., explicit formulas are derived to calculate the imaginary part of the refractive index using albedo value, if some *a priori* information about the real part of the refractive index and surface porosity is used (Shkuratov, 1999).

Using Shkuratov model, Poulet and Cuzzi (2002) provided the first good fit of the entire UV/near-IR spectrum of Saturn's ring, which is typical of spectra of high-albedo surfaces. This indicates that Shkuratov model is applicable to surfaces of different nature (as expressed by significantly different grain sizes and roughness) and composition (as expressed by significantly different albedos).

In nature, mineral composition of rocks is extremely variable as well as grain size. Models show successful predictions for a limited number of simulated mixtures allowing retrieving their

components, their abundances and grain sizes. Moreover not all mineral constants are known, in some cases they might be unavailable, therefore there is a limitation on the implementation of physical models.

1.3.2 Un-mixing algorithms

Spectral un-mixing is the procedure by which the measured spectrum of a mixed pixel is decomposed into a collection of constituent spectra, or *end-members*, and a set of corresponding fractions, or *abundances*, that indicate the proportion of each end-member present in the pixel (Keshava and Mustard, 2002).

The first stage in a mixture analysis is to define a suite of image end members. An image end member is one that is contained within a scene and has a maximum abundance of the physical end member it is mostly composed of.

Mixed pixel signals are generally modeled using either a linear (LMM) or nonlinear mixture model (NLMM). A mixture model converts the image DNs to numerical fractions of a few end-members (Adams and Gillespie, 2006). The question whether linear or non-linear processes dominate spectral signatures of mixed pixels is still an unresolved matter (Somers et al., 2011).

1.3.2.1 Linear mixture modeling

The underlying physical assumption of a LMM is that each incident photon interacts with a single pixel component only. The basic premise of mixture modeling is that within a given scene, the surface is dominated by a small number of distinct materials that have relatively constant spectral properties. In Fig. 1.21 (a), the reflecting surface is portrayed as a *checkerboard* mixture, and any given package of incident radiation only interacts with one component (i.e., no multiple scattering between components). If the total surface area is considered to be divided proportionally according to the fractional abundances of the end-members, then the reflected radiation will convey the characteristics of the associated media with the same proportions. In this sense, there exists a linear relationship between the fractional abundance of the substances comprising the area being imaged and the spectra in the reflected radiation (Keshava and Mustard, 2002).

A mixed pixel signal (r) can as such be described as a linear combination of pure spectral signatures of its constituent components (i.e., end-members), weighted by their sub-pixel fractional cover (Adams et al., 1986):

$$r = Mf + \varepsilon \quad (1.6)$$

In Eq. (1.6) M is a matrix in which each column corresponds to the spectral signal of a specific end-member. f is a column vector $[f_1,\ldots,f_m]^T$ denoting the cover fractions occupied by each of the m end-members in the pixel. ε is the portion of the spectrum that cannot be modeled using these end-members.

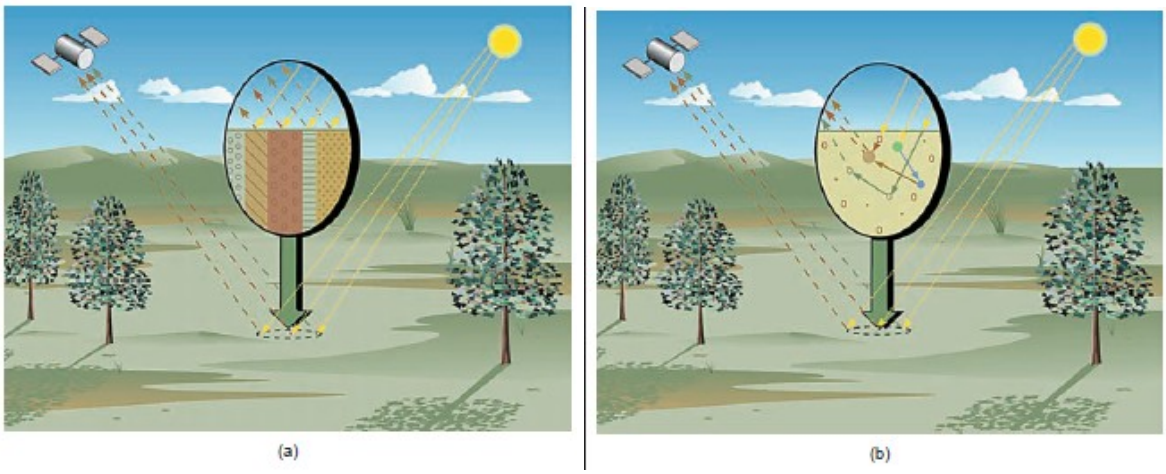

Figure 1.21 – Linear mixing scheme (a), non-linear mixing scheme (b) (Keshava and Mustard, 2002).

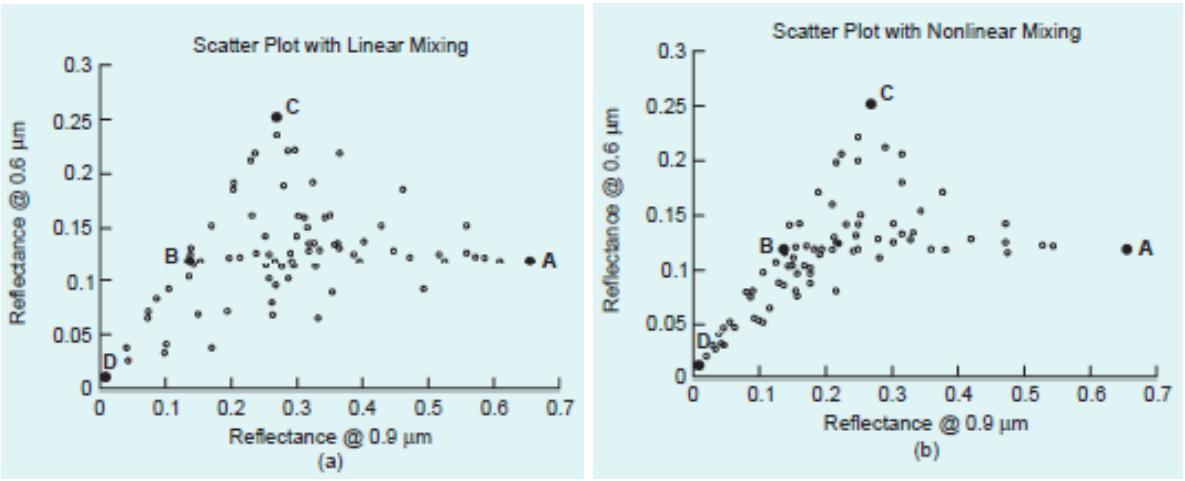

Figure 1.22 – Scatter plot with linear mixing (a), scatter plot with nonlinear mixing (b) (Keshava and Mustard, 2002).

A linear approach that is often used by linear models is SMA (Spectral Mixture Analysis). It is a physically based model that transforms radiance or reflectance values into physical variables, which are linked to the sub-pixel abundances of end-members within each pixel. It provides quantitative results that can in turn be incorporated into models of the processes governing the distribution of materials within the image scene (Tompkins et al., 1997). Assumption of SMA is linear mixing systematic, that is each pixel is a mixture of multiple components weighted by some surface abundance, and the spectrum of the mixture is a linear combination of the end-members reflectance spectra. To be physically realizable, the abundance coefficients should be non negative and should sum to one (Keshava, 2003).

Over the past decades, a number of image analysis techniques accommodating mixing problems have been proposed (e.g., Atkinson and Tatnall, 1997; Brown et al., 1999; Carpenter et al., 1999; Guilfoyle et al., 2001; Nascimento and Bioucas-Dias, 2005a; Wang, 1990) with SMA (Adams et al., 1986; Keshava and Mustard, 2002) being one of the most common techniques utilized in many applications.

For many problems, the linear model is thought to provide sufficient accuracy to map sub-pixel abundances in remotely sensed data (Elmore et al., 2000), so much the more because the linear analysis is computationally simpler compared to the often complex NLMM's (Adams and Gillespie, 2006).

1.3.2.2 Non-linear mixing modeling

Non-linear mixing models account for a nonlinear mixing process, which is a product of multiple scattering between at least two materials in the field of view. If, however, the components of interest are in an intimate association (the end-member materials are mixed on spatial scales smaller than the path length of photons in the mixture), as illustrated in Fig. 1.21 (b), like sand grains of different composition in a beach deposit, light typically interacts with more than one component as it is multiply scattered, and the mixing systematic between these different components is non-linear.

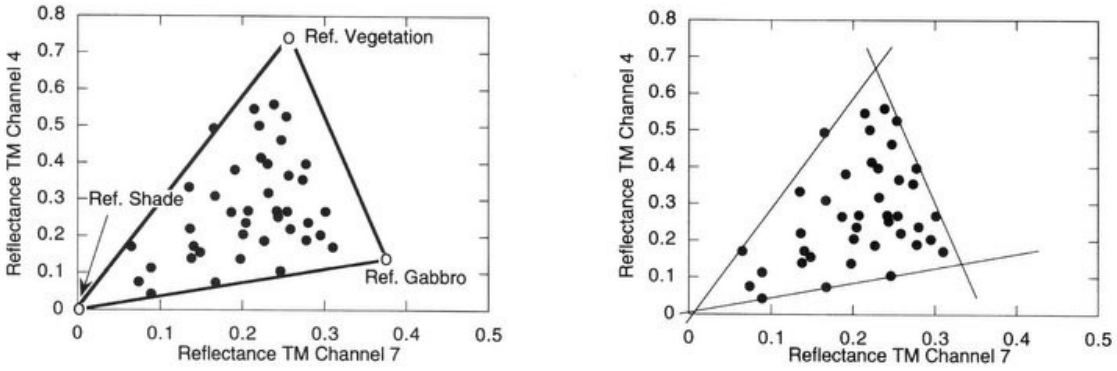

Figure 1.23– Conceptual diagrams illustrating the basic concept and terms of spectral mixture analysis: left- reference end-members plotted and proper mixing space defined, image end-members represented by open circles; right- automated techniques for the identification of mixing end-members can use the convex hull of the data cloud to define the vertices of the intersection where the reference end-member should be (Adams, 1993).

Nonlinear Spectral Mixture Models (NLMM) account for the presence of multiple photon interactions by introducing additional 'interaction' terms in linear spectral mixture model (Eq. (1.6)). Each term accounts for multiple interactions between end-members and is represented by the cross-product of the interacting end-members (Borel and Gerstl, 1994; Chen and Vierling, 2006; Ray and Murray, 1996).

For tree–soil mixtures the simplest nonlinear mixture model, defined in Eqs. (1.7) and (1.9), includes the first order mixture (linear) effect (R_t, R_s) and the interaction mixture (multiple scattering influences) effect (R_t R_s) (Ray and Murray, 1996).

$$R_i = c_1 R_{i,t} + c_2 R_{i,s} + c_3 R_{i,t} R_{i,s} + \varepsilon_i \quad (1.7)$$

$$where\ c_1, c_2, c_3 \geq 0, and\ \sum_{j=1}^{3} c_j = K \quad (1.8)$$

$$f_j = \frac{c_j}{K}\ and\ \sum_{j=1}^{3} f_j = 1 \quad (1.9)$$

c_1, c_2, c_3, f_1, f_2, f_3 are the contribution factors and fractions of the tree, soil, and tree and soil end-members, respectively. Similar to LSMA, fraction estimates are applied by model inversion (Eq. (1.7)) using approaches such as LSE regression (Chen and Vierling, 2006). In Eq. (1.6) f_3 can be considered as a 'virtual' fraction as it only has a physical meaning at the spectral level. The fraction, which accounts for the relative contribution of the tree–soil interaction to the integrated pixel signal, can, however, not be interpreted as an actual physical part of the ground cover. The sum to one constraint (Eq. (1.9)) as such induces significant underestimation of the actual ground

cover (i.e., f_1, f_2). Therefore, despite the fact that NLMMs improve the modeling of mixed pixel spectra its applicability for the estimation of ground cover is limited. (Somers *et al.*, 2009).
Using a training data set, the mathematical relationships between input (spectral data) and output data (classes of interest) can also be automatically calculated using advanced computer modeling approaches such as Artificial Neural Networks (Atkinson and Tatnall, 1997; Carpenter *et al.*, 1999; Guilfoyle *et al.*, 2001; Mercier *et al.*, 2005;) and decision tree classifiers (i.e., Vegetation Continuous Fields, Morton et al., 2005) (1.23). Nonlinear mixing has been firmly established for mineral soils (e.g., Mustard and Pieters, 1987, 1989; Nash and Conel, 1974; Shipman and Adams, 1987). Nevertheless, the quantitative effects of nonlinear mixing on the accuracy of fractional cover estimates remains poorly understood.

1.3.2.3 End-members selection

The choice of representing end-members of a mixture is not a convenient process. If composing end-members of mixture are known, their spectra can be used as input for un-mixing algorithm. Spectra can be derived directly from the image cube. In this case, the cube's spectral variance is best taken into account using a constrained, least-squares mixing model (Adams et al., 1993; Gillespie et al., 1990). Also end-member spectra can be measured in the laboratory from samples collected in the field or in cases when field samples are not available being taken from spectral libraries. Usually, spectral libraries are composed of spectra of powdered minerals (Clark et al., 2007). End-members taken from the field are measured in the laboratory with a spectrometer (Asner and Lobell, 2000; Roberts et al., 1998). Yet, end-member reference spectra can also be derived directly from the image data themselves (e.g. Bateson et al., 2000; Goodwin, 2005; Somers et al., 2011) or simulated using radiative transfer models (Collins et al., 2001; Dennison et al., 2006; Eckmann et al., 2008; Painter et al., 2003; Peddle et al., 1999; Sonnetag et al., 2007). However, one sample can be non homogeneous, sometimes covered by patina or dust, and as a result produces spectral variety, which will cause variations of un-mixing results, not all species in the field being exactly the same.

One of the attempts to address end-member variability was made by Roberts et al. (1998). These authors introduced the use of iterative mixture analysis cycles. In their Multiple End-member Spectral Mixture Analysis (MESMA) technique, end-members are allowed to vary on a per pixel basis. MESMA as such permits multiple end-members for each component and thereby refutes the fixed end-member restriction made in SMA. In an iterative procedure, based on a spectral

library of hundreds of spectra, accounting for each plausible end-member condition, the best-fit model (i.e., lowest RMSE) is assigned to each pixel. Today, this approach is by far the most widely used SMA technique. MESMA has been successfully tested in natural (e.g., Bedini et al., 2009; Eckmann et al., 2008, 2009; Fitzgerald et al., 2005; Li et al., 2005; Okin et al., 2001; Roberts et al., 1998; Sonnetag et al., 2007) and extraterrestrial environments (e.g., Combe et al., 2008; Li and Mustard, 2003) as well as hyperspectral optical imagery (e.g., Chabrillat et al., 2000; Chen and Vierling, 2006; Dennison and Roberts, 2003a;Somers, 2011).

Optimally, SMA requires that the spectral variability of the image pixels is described with a minimum number of end-members (Sabol et al., 1992). Too many end-members, or end-members that are spectrally similar, lead to end-member fraction images that are physically inaccurate as judged, for example, against field assessments (Song, 2005).

1.3.2.4 Accuracy

The accuracy of spectral un-mixing is often quantified based on the fit between the modeled and observed mixed spectral signals. Model fit can be assessed by an error metric such as the residual term ε (Rogge et al., 2006) or the Root Mean Square error (RMSE; Roberts et al., 1998). In cases where accurate ground reference data are available, the suitability of the selected end-members and the quality of the subpixel abundance estimates can be assessed more reliably by checking the discrepancy between the estimated and real end-member fractions (Plaza et al., 2004). The fraction abundance error (Rogge et al., 2006; Somers et al., 2009d) and the coefficient of determination (Elmore et al., 2000; McGwire et al., 2000; Zhang et al., 2004) are widely used discrepancy measures (Somers, 2011).

Another example for one of the variations of SMA is multiple end-member linear spectral un-mixing model (MELSUM). This algorithm selects the best linear combination of spectra among the families of minerals available in a spectral library. The best fit of the observed spectrum on each pixel is calculated by the same un-mixing equation used in SMA (Combe et al., 2008). However because mixtures in the field have complex non-linear behavior, differences between mineral abundances and inverted coefficients by the linear spectral un-mixing may reach 30% (checked on ternary mixtures of two pyroxenes and olivine) (Mustard and Sunshine, 1999; Keshava and Mustard, 2002). One drawback of linear mixture models is that they do not account for certain factors such as multiple reflections, which can result in complex nonlinearities in the

spectral mixing process. In this situation, a more sophisticated nonlinear spectral mixture model may be required (Borel and Gestl, 1994).

1.3.2.5 Un-mixing algorithms problematic

The sources in hyperspectral un-mixing exhibit statistical dependency. This characteristic, together with high dimensionality of the data, places hyperspectral un-mixing beyond the reach of most standard source separation algorithms (Bioucas-Dias and Figueiredo, 2006). The theoretical limit to the number of end-members is defined by the dimensionality of the data and constraints of the mixture inversion. This results in a total number of possible end-members equal to the number of spectral channels in the data set plus 1.The theoretical limit requires that the spectral channels be independent variables and that the spectral end-members be linearly independent. Channel-to-channel variance in spectral data sets is highly correlated. In addition, materials of different physical components may exhibit similar spectral properties over a given wavelength range or have spectral properties that can be defined mathematically by linear combination of other components.

1.3.2.6 Alternative techniques for SMA.

1.3.2.6.1 PCA

One of the methods used in mixture analysis is Principal Component Analysis PCA (Johnson et al, 1985). This is a method to extract the end-member information from the data itself, and is a straightforward statistical approach. Principal component analysis (PCA) identifies orthogonal axes for dimension reduction by performing an eigen decomposition of the sample covariance matrix of the data. The PCA can be used to identify the type of mixing (macroscopic versus intimate) and to estimate the relative proportion of end-members (Chevrel et al., 1999; Pieters et al, 2001).

The spectra can be converted to the relevant dimensionality by a linear transformation with the significant eigenvectors computed from PCA. The eigenvectors are analogous to optimum bandpass filters, that when convolved with spectra, transform the spectra into fewer data points. They correspond to the principal independent sources of spectral variations. Maximum or minimum values of the elements of each eigenvector define those wavelengths most significant

to each independent axes of variation. The shape of the eigenvector elements with wavelength is determined by the suite of mineral end-members contributing to the spectra (Smith et al., 1985).

PCA enclose the cloud of pixel spectra within a solid geometric figure whose number of vertex is equal to the dimensionality of the basis space (Fig. 1.23, 1.24) (White and Drake, 1993; Bryant, 1996). However, despite the fact that these methods guarantee the feasibility of the outcoming fractions, they assume that the true end-members are contained within a dataset. In practice, it is difficult to find pure targets, fully covered by unique material at the spatial resolution of satellite sensors (Garcia-Haro et al., 1999). Quantitative determination of end-member abundances with this technique is complex for mixtures containing two or more components (Poulet et al., 2004).

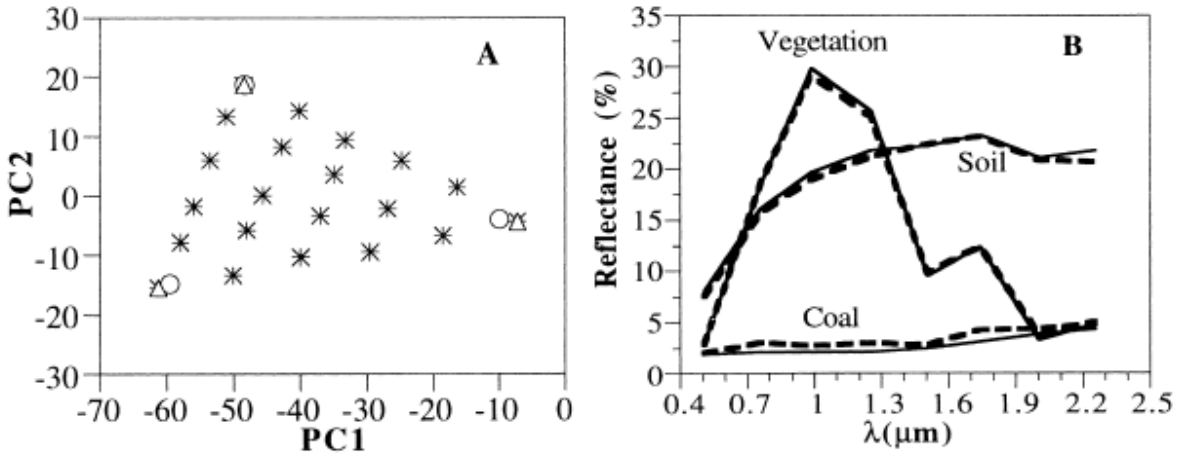

Figure 1.24 – Data cloud transformed by PCA (a), spectra of end-members (b) (Garcia-Haro et al., 1999).

Convex geometry applications (Xu and Greeley, 1992) have some utility in determining the number of end-members that are possible in a data set and to estimate the spectral properties of those end-members. In this approach the raw radiance or reflectance data are first transformed into ordered principal components using a minimum noise fraction (MNF) algorithm (Green et al., 1988). This determines the number of valid dimensions of the data sets. A simplex is fit to the convex hull of the n-dimensional reduced data cloud. The faces of this simplex are regions void in one or more end members and the vertices of the simplex define the spectral properties of the end-members. This method is repeatable and has distinct advantages for objective analysis of a data set to assess the general dimensionality and to define end members. The primary disadvantage of this method is that it is fundamentally a statistical approach dependent on the specific spectral variance of the scene and its components. Thus the resulting end members are mathematical constructed and may not be physically realistic.

1.3.2.6.2 Modified Gaussian Model (MGM)

The pioneering work by Sunshine et al. (1990) relies on the fact that spectrum variations in visible and near-infrared are caused by absorption features that can be described by means of Gaussians (Clark and Roush, 1984). Sunshine et al. (1990) used modified Gaussians to obtain a mathematical solution closer to the physical reality. Each Gaussian is parameterized by a band center, band width and band strength (Fig. 1.25).

As described in Sunshine and Pieters (1999), at first order, in the case of simple mineralogies, MGM is thus able to retrieve modal and/or chemical composition from an un-known spectrum. Successive studies have shown the interest of the MGM approach for planetary surface characterization (e.g., Mustard and Sunshine, 1995; Mustard et al., 1997; Noble et al., 2006; Kanner et al., 2007). However, one should note that for the reference studies, all the spectra used were acquired on controlled laboratory powder samples, with grain size between 24 and 250 µm. Kanner et al. (2007) have also pointed out that the MGM returned solutions were sensitive to some extent to the band centers initialization. So far, more complex situations addressing complex mineralogies, (i.e. olivine and pyroxene(s) and/or different pyroxene composition and/or rock samples (e.g., Pompilio et al., 2007) have been little explored by the MGM approach at the exception of a few recent works (e.g., Pompilio et al., 2006, 2009; Parente and Bishop, 2006; Pinet et al., 2006, 2007, 2009; Clenet et al., 2008, 2009).

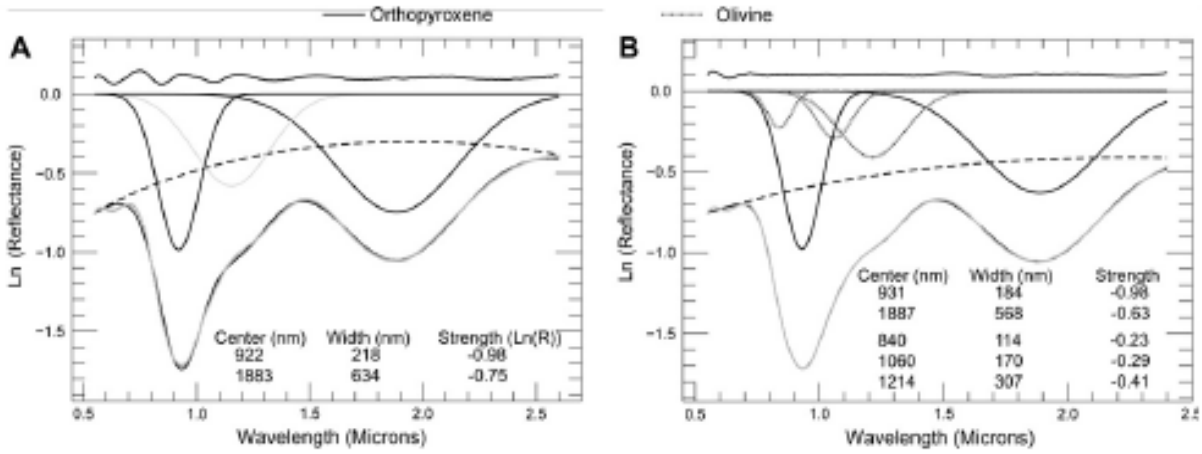

Figure 1.25 – An example of MGM analysis of orthopyroxene spectrum, Gaussians represent band position, depth and strength (Clenet et al., 2003).

Using MGM information, relative abundances has been derived for some types of surfaces (Sunshine and Pieters, 1993, 1998; Mustard et al., 1993, 1997; Cooper and Mustard, 2002).

The MGM method or its derivates are subject to large errors in the derivation of the quantitative analysis of multicomponent mixtures when part of the components is spectrally featureless (Moroz and Arnold, 1999). Automated band detection of spectra can be produced based on wavelet filtering (Gendrin and Erard, 2003). Consequently, the MGM approach is in essence able to achieve a direct detection and quantification of minerals which make up the observed surface. The strength of PCA and MGM methods is to aid in determining appropriate end-members with limited *a priori* knowledge.

1.3.2.6.3 Other techniques

There are series of non-linear un-mixing algorithms based on Fuzzy logic (Zadeh, 1965) that have an ability to mix combinatorial operations with imprecise plain English statements, based on Fuzzy sets (Kwan et al., 2006; Bovolo et al., 2010). FS are initially implemented as a series of production relationships, i.e. if-than-else rules. To reduce uncertainty, the posterior probability of each end member is determined first by means of fuzzy logic and only the highly probable end members are being unmixed for each grid element.

Genetic adaptive algorithms are non-linear un-mixing algorithms that present information as a "gene" string or a chromosome consisting of genes with values of "1" or "0", e.g. 1001101 (Holland, 1962). The chromosomes are then sorted based on closeness to the solution or "fitness". The chromosomes with the best values are chosen to go to the next cycle. Neural networks were also used for un-mixing (Barnard and Casasent, 1989).

Simulated annealing (SA) was adapted to be used for non-linear un-mixing (Kirkpatrick et al., 1983). The implementation of SA involves normalizing a random combination of initial end-member vectors and calculating the Euclidian distance between them and the target vector.

Foreground/background analysis (FBA) - In this technique, spectral measurements are divided in two groups of foreground and background spectra that comprise a selected subset of spectra which emphasizes the presence of a signature of interest.

Table 1-1 presents end-member variability reduction techniques in SMA (Somers, 2011).

Table 1-1 - Overview of the implementation modalities of different end-member variability reduction techniques. Panel (a) lists the spectral transformations needed to be performed on the end-member libraries prior to SMA. Panel (b) highlights the operations needed to be performed on the image prior to SMA; (c) summarized the different SMA operations and how the output is presented; (d) indicates possible application caveats for the different techniques (Somers, 2011).

(a)

	Spectral transformations performed on endmember libraries* prior to SMA		
	*Operation(s) should only be applied once on the endmember library		
Multiple endmember SMA	–	–	–
Monte Carlo unmixing	–	–	–
Endmember bundles	–	–	–
Bayesian SMA	Assessing endmember population distribution		
PCA-based SMA	Principal component analysis	Spectral feature selection	–
Stable Zone unmixing	Instability index (ISI) calculation	ISI based feature selection	–
Derivative Spectral Unmixing	Derivative analysis	(Spectral feature selection)	–
Wavelet-based SMA	Wavelet tranformations	(Spectral feature selection)	–
Weighted SMA	Spectral normalization	ISI calculation	Spectral weighting
Soil Modeling Mixture Analysis	–	–	–
Integrated SMA	Derivative analysis	ISI calculation	ISI based feature selection

(b)

	Spectral transformations performed on image data*prior to SMA	
	*Operation should be applied on each image pixel, i.e. iterative process	
Multiple endmember SMA	–	–
Monte Carlo unmixing	–	–
Endmember bundles	–	–
Bayesian SMA	–	–
PCA-based SMA	Principal component analysis	–
Stable zone unmixing	–	–
Derivative spectral unmixing	Derivative analysis	–
Wavelet-based SMA	Wavelet tranformations	–
Weighted SMA	Spectral normalization	ISI based spectral weighting
Soil Modeling Mixture Analysis	Soil endmember modeling based on reflectance model and SMC inputs	–
AutoSWIR	Tying transformation	–
Integrated SMA	Derivative analysis	–

(c)

	Spectral Mixture Analysis			
	No of spectral features in analysis	Iterative mixture cycles	Endmember selection	*Output*
	(F=full spectral range; S=spectral subset)	*(i.e. multiple SMA cycles per pixel)*	*(R=random; S=standard*; P=based on endmember probility density function)*	*(cover fractions)*
Multiple endmember SMA	F	X	R	from iteration with best model fit
Monte Carlo unmixing	F	X	R	mean output of all iterations
Endmember bundles	F	X	R	mean, maximum and minimum
Bayesian SMA	F	X	P	From iteration with best model fit
PCA-based SMA	S	–	S	output of the single cycle
Stable zone unmixing	S	–	S	output of the single cycle
Derivative spectral unmixing	(S)	–	S	output of the single cycle
Wavelet-based SMA	(S)	–	S	output of the single cycle
Weighted SMA	F	–	S	output of the single cycle
Soil Modeling Mixture Analysis	F	–	S	output of the single cycle
AutoSWIR	S	X	R	mean output of all iterations
Integrated SMA	S	–	S	output of the single cycle

*Commonly standard endmembers are defined as the mean of the endmember libraries

(d)

	Cavaets and remarks
Multiple endmember SMA	Iterative mixture procedure, can be a CPU efficiency burden when applied on hyperspectral data
Monte Carlo unmixing	Iterative mixture procedure, can be a CPU efficiency burden when applied on hyperspectral data
Endmember bundles	Iterative mixture procedure, can be a CPU efficiency burden when applied on hyperspectral data
Bayesian SMA	Iterative mixture procedure, can be a CPU efficiency burden when applied on hyperspectral data
PCA-based SMA	Operational applicability not yet fully explored; literature reports contrasting results
Stable Zone unmixing	Designed for simple environments with a fixed number of limited endmember classes; for complex environments the algorithm should be used in combination with a segmentation approach (e.g., Rogge et al., 2006)
Derivative spectral unmixing	A careful calibration/validation is required as derivatives tend to increase high-frequency noise
Wavelet-based SMA	Operational applicability not yet fully explored
Weighted SMA	Designed for simple environments with a fixed number of limited endmember classes; for complex environments the algorithm should be used in combination with a segmentation approach (e.g., Rogge et al., 2006)

Chapter II

2. Materials and Methods

2.1 Site description

The test site for field data acquisition was selected in Makhtesh Ramon, in southern Israel. In general, this site has very rich geological history, but in particular for our study this area was selected because: 1) it is devoid of vegetation, and rock outcrops are extensive; 2) Makhtesh area is a cloud free arid environment making it, with respect to weather conditions, an ideal site to acquire spectral measurements; 3) the site contains a variety of mineralogical constituents, mainly sedimentary rocks, particularly interesting for us, thus different scenarios could be selected; 4) airborne data from the site were available, since the site represents a potential interest as a calibration site for space-borne imaging systems.

Various scenarios of natural rock mixtures were selected in the field.

2.1.1 Study area

The location of Makhtesh Ramon is in central Negev, southern Israel (Fig. 2.1). The region is considered arid to extremely arid and is nearly cloud free, with a mean annual rainfall of about 85 mm at the northern rim and about 56 mm in the central part. Mean daily temperature in July is 34° C, which drops to 12.5° C in January, whereas the mean annual temperature is 17-19°C.

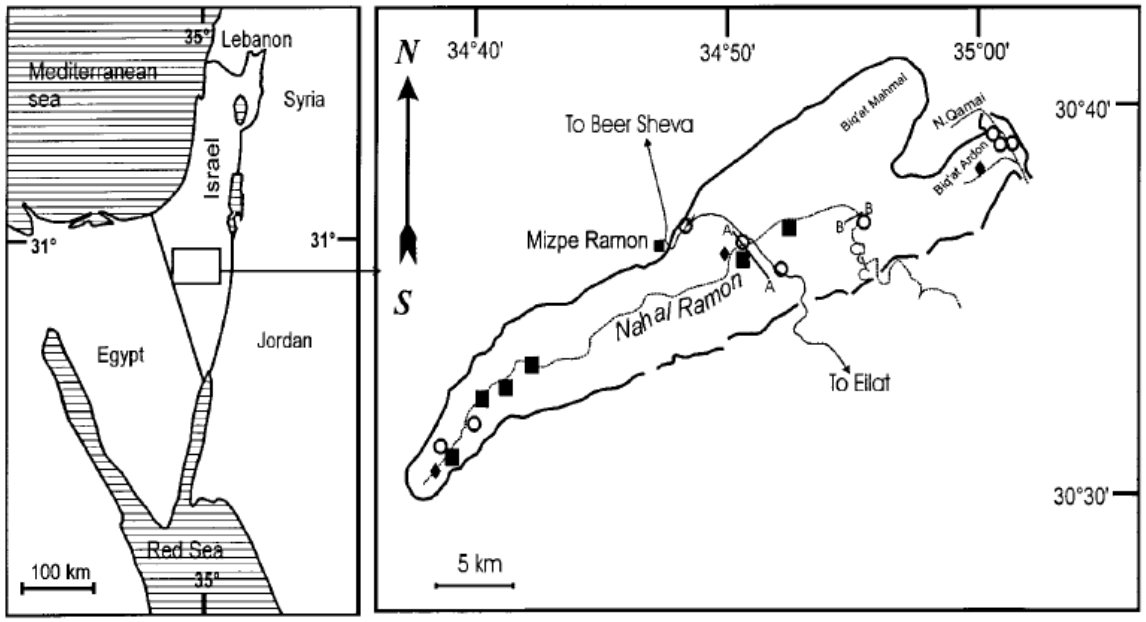

Figure 2.1 – Study area, map of Makhtesh Ramon (Plakht, 1999).

2.1.1.1 Geological setting

The Makhtesh is located along the axis of an anticline and its N-E part has evolved into two sub-valleys following the split of the anticline axis (Fig. 2.1). Makhtesh Ramon is situated at the top of the Ramon Anticline on the eastern margin of the Negev-Sinai sub-plate, overlooking the landscape channel of the local Great Rift Valley section, into which it is drained (Fig. 2.2). The Ramon erosion 'cirque' is 40 km long and 12 km wide, its area is 241 km^2. Altitudes range from 1020 m on the western rim to 420 m above sea level, near the outlet of the main wadi, Nahal Ramon. This ephemeral stream is 39 km long within the Makhtesh and drains most of it.

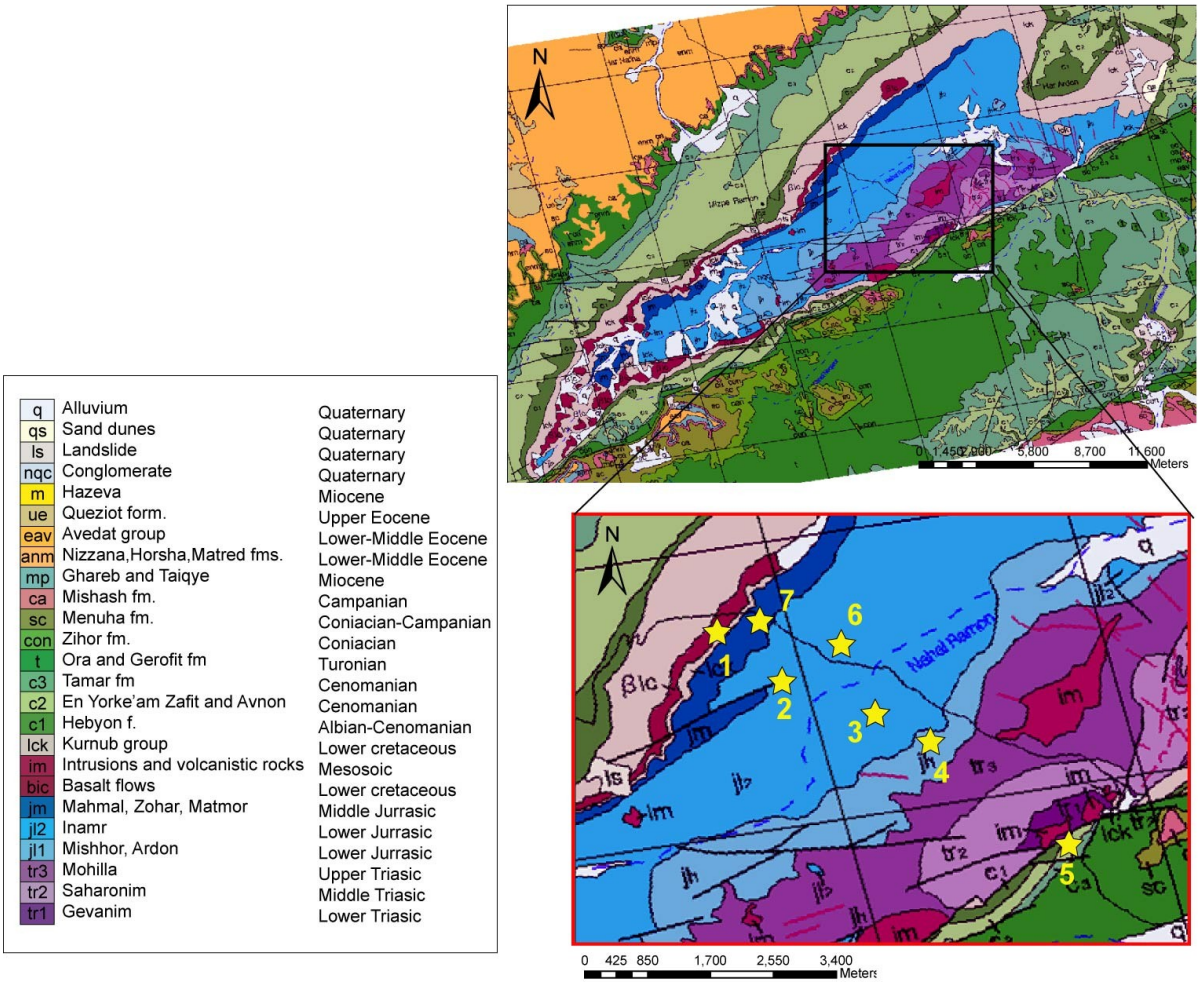

q	Alluvium	Quaternary
qs	Sand dunes	Quaternary
ls	Landslide	Quaternary
nqc	Conglomerate	Quaternary
m	Hazeva	Miocene
ue	Queziot form.	Upper Eocene
eav	Avedat group	Lower-Middle Eocene
anm	Nizzana,Horsha,Matred fms.	Lower-Middle Eocene
mp	Ghareb and Taiqye	Miocene
ca	Mishash fm.	Campanian
sc	Menuha fm.	Coniacian-Campanian
con	Zihor fm.	Coniacian
t	Ora and Gerofit fm	Turonian
c3	Tamar fm	Cenomanian
c2	En Yorke'am Zafit and Avnon	Cenomanian
c1	Hebyon f.	Albian-Cenomanian
lck	Kurnub group	Lower cretaceous
im	Intrusions and volcanistic rocks	Mesosoic
bic	Basalt flows	Lower cretaceous
im	Mahmal, Zohar, Matmor	Middle Jurrasic
jl2	Inamr	Lower Jurrasic
jl1	Mishhor, Ardon	Lower Jurrasic
tr3	Mohilla	Upper Triasic
tr2	Saharonim	Middle Triasic
tr1	Gevanim	Lower Triasic

Figure 2.2 – Geological map of Makhtesh Ramon, and measurements points (Israel Geological Survey, 1998).

The geological map of Makhtesh Ramon (Fig. 2.2) reveals a concentric structure of an outer Cenomanian ring, and in inward direction rings of Lower Cretaceous and Jurassic, and a Triassic core. The structure discloses that the Makhtesh has been excavated along the axis of an

asymmetric anticline. The Triassic-Cenomanian rock sequence is made up of conform rock strata that disclose accumulation in a flat landscape, frequented by sea invasions and retreats. When the Eocene sea retreated, the whole set of the Makhteshim Country anticline was exposed on land, where they were truncated by erosion. This truncation exposed in some anticlines the inner core of Lower Cretaceous sandstones, but the whole region was still a low flatland and the exposed sandstone remained in place.

2.1.1.1.1 Evolution of Makhtesh Ramon

The initial formation of Makhtesh started about at 110 Ma, with the deposition of the Hatira sandstone. Abundant plant fossils indicate continental to shallow marine environment (Fig. 2.3-a). Deposits of more than 500 m of massive marine carbonates are remnants of the Judea group (100-90 Ma) (b). Menuha chalk deposits on the Judea group sequence indicate the formation of the Ramon asymmetric anticline along the Ramon fault in the early Senonian. Conglomerate found at the top of the Menuha formation indicates uplifting above the sea level and erosive truncation of the top of the structure (80 Ma) (c). The Mishash and Ghareb formation deposits indicate further development of the structure. Conglomerate and sand derived from the Hatira formation found within the Ghareb formation indicate the development of an embryonic Makhtesh on the sandstone core of the structure (60-70 Ma) (d). The Avedat group limestone observed near the top of the western Ramon anticline indicates burial of the erosive relief by the sea (40-50 Ma) (e). Remnants of truncated hills around the Ramon indicate the development of a peneplain in the region. The Ramon structure was deeply truncated, exposing a large sandstone outcrop along the core of the structure (30 Ma) (f). Remnants of the conglomerate and sandstone found above the peneplain indicate the deposition of the Hazeva formation continental sediments on the flat relief. The elevation of the region exceeds few tens of meters (10-20 Ma) (g). Remnants of the uplifted and tilted Avedat plateau around the Ramon indicate a regional uplifting to the present day elevation and regional tilting to the North-East. The tectonic activity was followed by intensive incision into the sandstone core of the eroded anticline that excavated the present Makhtesh (Avni, 2001).

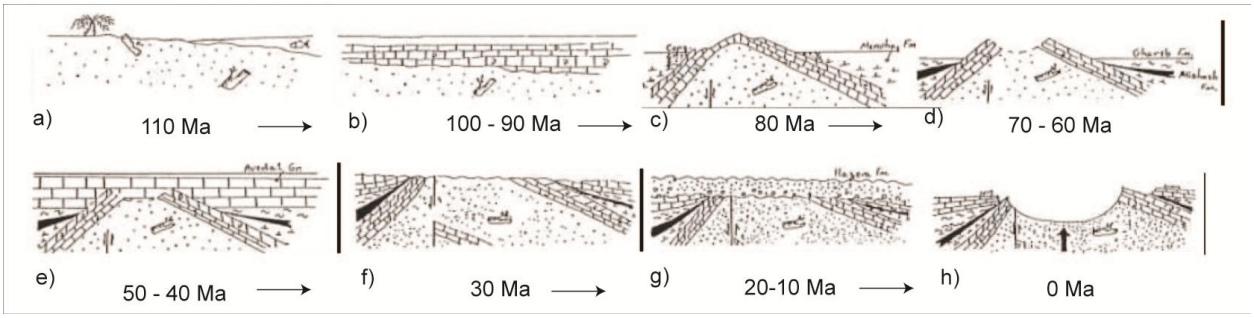

2.2 – Inferred stages of the evolution of the Ramon anticline and the carving out of Makhtesh (Avni, 2001).

2.2.1.1 Stratigraphic sequence

The lithological sequence exposed in Makhtesh Ramon ranges from Triassic to Cretaceous. Triassic rocks, which are about 500 m thick (Zak, 1963), are composed of carbonate, sulphate, shale and sandstone lithofacies (Fig. 2.4). The Jurassic section, about 400 m thick (Nevo, 1963) is composed mainly of friable sandstones of the Inmar Formation (Goldberg, 1970) with a subordinated representation of carbonate rocks, siltstones and clays. The Early Cretaceous Hatira Formation is divided into three members: the lower and upper members are composed of loose sandstones 5±40 m and 80±120 m thick, respectively. Sandstone members are separated by a basanite unit 100 m thick in the western part of Makhtesh Ramon (Eyal et al., 1996), and 0± 30 m in its central part. The cliffs surrounding the Makhtesh are built of 300 m thick hard limestones and dolomites of the Middle Cretaceous Hazera Formation (Fig. 2.4).

The lower landforms are younger because of the higher topographic position of Makhtesh Ramon in relation to its base level in the Dead Sea basin. An interrupted incision of the Makhtesh Ramon drainage system occurred since the Pliocene (Ben-David et al., 1992; Zilberman, 1991).

The environment was drastically changed when the adjacent Great Rift Valley segment subsided at the Miocene and the rim of the westward moving sub-plate was uplifted, forming the present Makhteshim Country Highland. Thus, a deep drainage basin was formed, the sandstone interior of the anticline was washed away and the Makhtesh summit valley was formed (Ben-Dor et al., 2009). All of our measured sites are located in the Jurasic sequence, with the exception of site 4, which is located in the Triassic sequence.

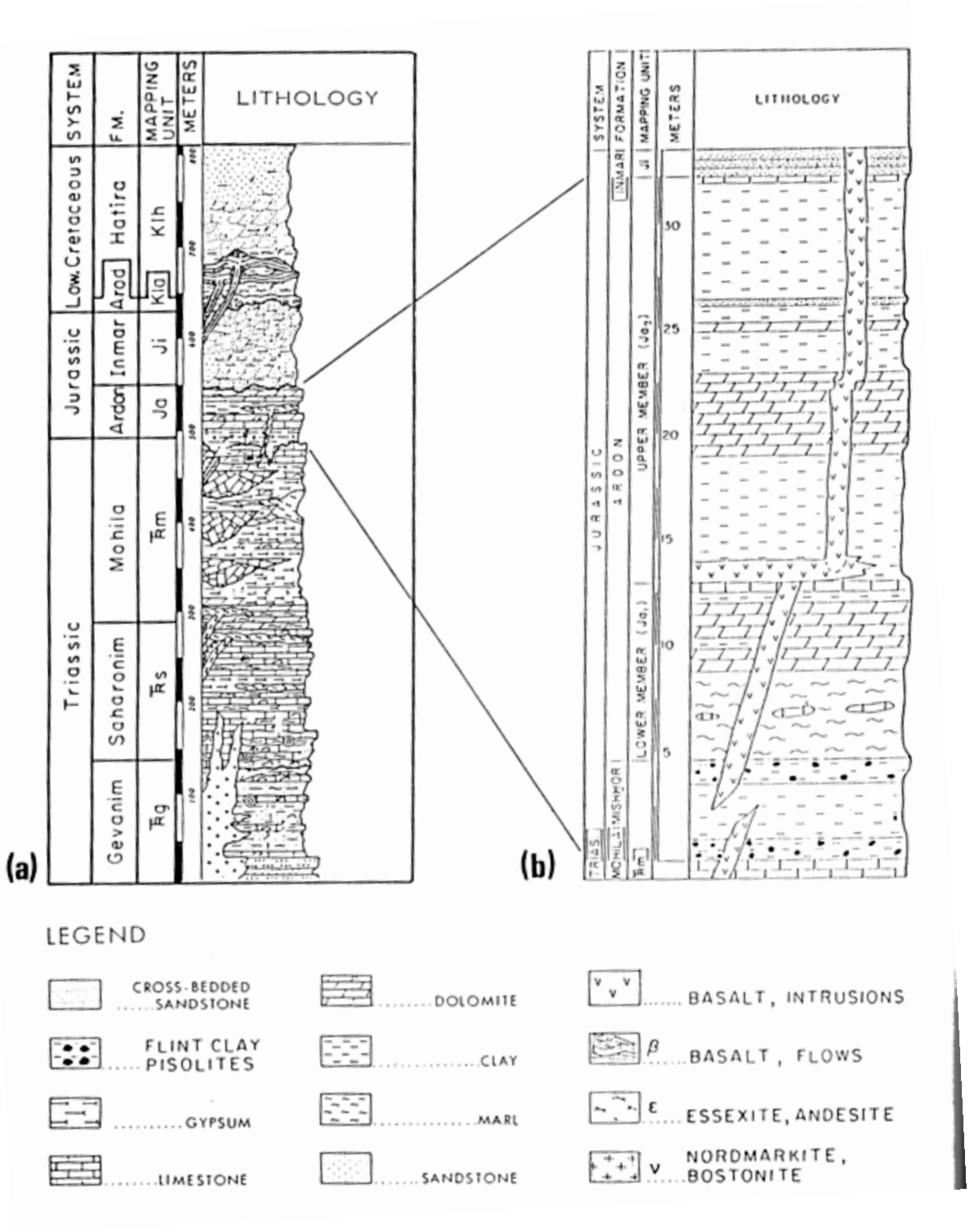

Figure 2.4 – Stratigraphic sequence or log of Makhtesh Ramon valley (Israel Geological Survey 1998).

2.2.1.2 Morphology

Nahal Neqarot, which flows east of the Ramon anticline towards the Dead Sea, serves as the local erosion base level of the Ramon valley (Plakht et al., 2000).

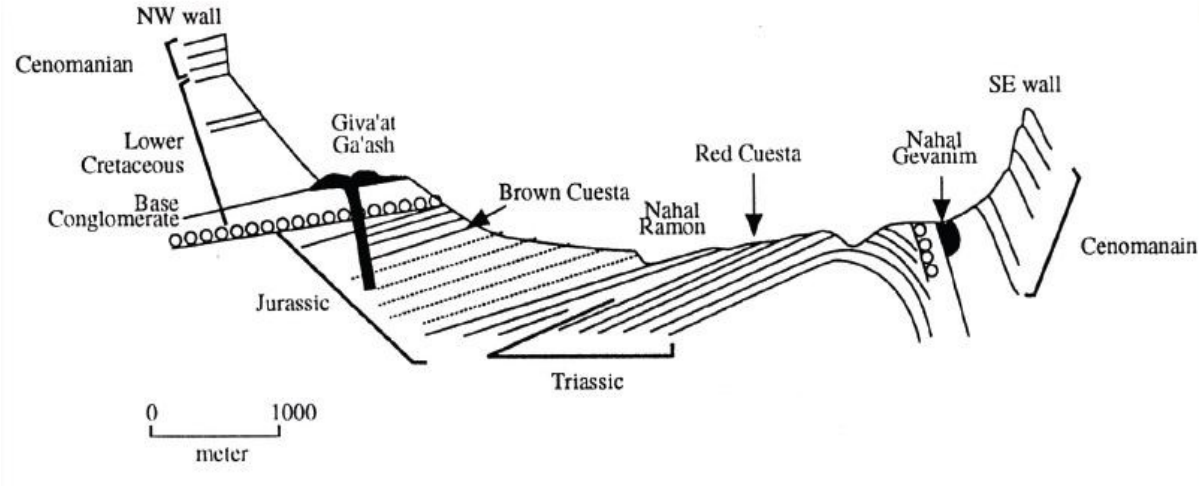

Figure 2.5 – A geological cross section of Makhtesh Ramon valley along the main road (Plakht et al., 2000).

The Quaternary development of Makhtesh Ramon can be generalized as the alternation of periods of erosion and stability, caused by periodic lowering of the base level. The first stage of base-level lowering began with erosion activity, associated with the deformation along the Dead Sea and Arava Rift Valley (Zilberman, 1991). Erosion destroyed the regional Oligocene erosion surface and exposed the Ramon anticline structure. Pediment cover occupies 29% and 23% respectively of the total area (241,5sq. km). Different types of slopes, eolian forms and alluvial fans occupy 17% of the total area (Fig. 2.5) (Placht, 1996).

2.3 Data acquisition

2.3.1 Field work

2.3.1.1 Instrumentation

Field spectral measurements were obtained with an ASD portable FieldSpec FR2 (FS) spectrometer. This device has 2151 spectral bands in VIS-NIR-SWIR from 0.4 to 2.5 μm with a spectral resolution of 1 nm after resampling. It enables to produce direct spectral measurement from the target and to perform solar spectral reflectance, radiance and irradiance measurements.

Table 2-1 summarizes technical characteristics of the ASD portable spectrometer used in the field.

Table 2-1 – ASD FieldSpec FR2 technical characteristics (ASD Inc.).

Spectral Range	350-2500 nm
Spectral Resolution	3 nm @ 700 nm
	10 nm @ 1400/2100 nm
Sampling Interval	1.4 nm @ 350-1050 nm
	2 nm @ 1000-2500 nm
Scanning Time	100 milliseconds
Detectors	One 512 element Si photodiode array 350-1000 nm
	Two separate, TE cooled, graded index InGaAs photodiodes 1000-2500 nm
Input	1.5 m fiber optic (25º field of view)
	Optional foreoptics available
Noise Equivalent Radiance (NEdL)	UV/VNIR 1.1 x 10^{-9} W/cm^2/nm/sr @700 nm
	NIR 2.4 x 10^{-9} W/cm^2/nm/sr @ 1400 nm
	NIR 4.7 x 10^{-9} W/cm^2/nm/sr @ 2100 nm
Weight	12 lbs (5.2 kg)

2.3.1.2 Spectral measurements procedure

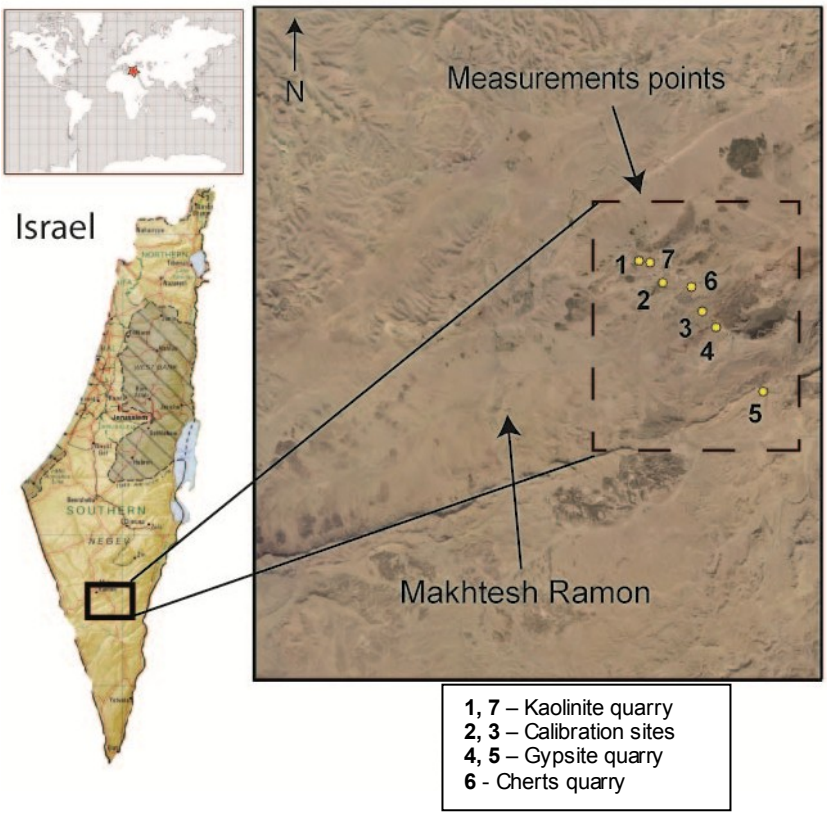

Figure 2.6 – The study area, Makhtesh Ramon, Israel and measurements points.

Field spectral measurements were acquired during four days from 12.10.09 to 15.10.09. Measurements time during the day was around midday (plus/minus one hour) to obtain optimal sun illumination position and minimum shadow. Prior to each 5 measurements the ASD spectrometer was calibrated to a white reference Spectralon® panel (Labsphere). Dark current was recorded systematically before each acquisition and subtracted to the signal to remove instrument noise. It is the signal that is present when the instrument is running with the shutter closed (no light) and is mostly due to electronic noise. The optimization is performed over the brightest target, which is Spectralon ®, to adjust the gains of the instrument, avoid saturation and balance the signal between spectrometers.

2.3.1.2.1 Field scenes measurement setup

For each surface scan (as well as white reference scan) the ASD FS pistol grip was directed nadir (90°, perpendicular to the surface) at a height of approximately 80 cm above the surface. The angle of view of the device is 25°, consequently the field of view (FOV) of the measured scenes formed a circle with a diameter of about 0.35 meter (Fig.2.7). All spectral scans were conducted facing the sun, which enables to minimize directional effects and to stay in the same observation geometry. To reduce instrument noise, 10 x 10 spectra were averaged (average of 10 spectra per measurement and 10 measurements per stop). A digital camera (Casio) placed directly under the pistol grip registered measured scenes in their condition at the moment of spectral acquisition. Since the height of the pistol grip remained fixed during the measurements, approximately the same field of view was acquired for all scenes. A portable GPS was attached to the spectrometer and registered the location coordinates of the measured points.

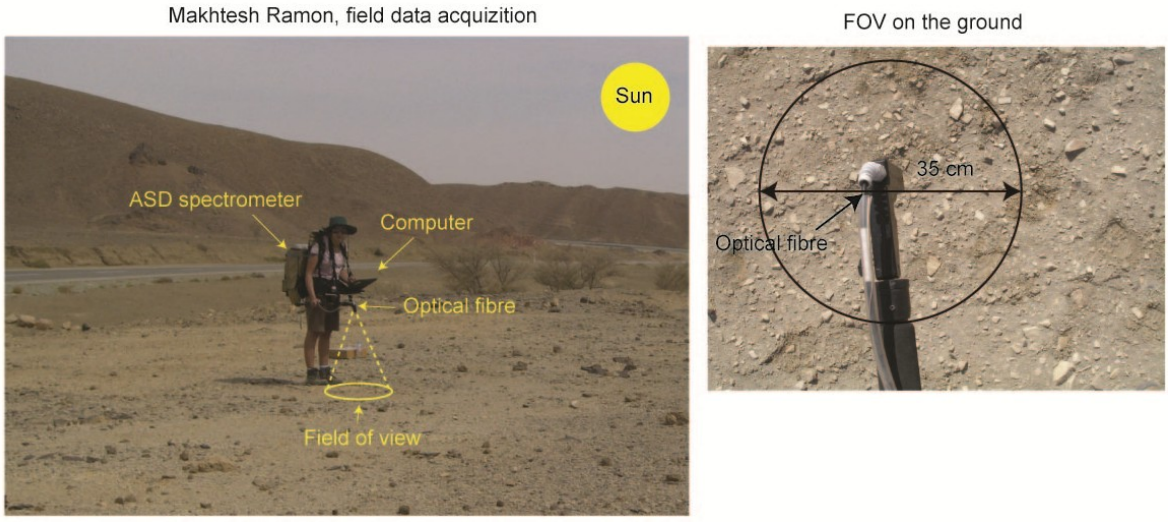

Figure 2.7 – Spectral data collection in the field achieved with ASD FieldSpec portable spectrometer (left), FOV of a scene on the ground (right), Makhtesh Ramon, 2009.

FOV of measured scene:

$$G = 2 * D * \tan(\alpha/2) \quad (2.1)$$

Where d – distance, α – FOV (25° in the case of the ASD FS2)

The surface measured by the FieldSpec was estimated from the digital photographs using formula 2.1, a pen was placed on the ground for scale. Part of the picture corresponding to the FieldSpec FOV (circle of 35 cm in diameter) was extracted.

2.3.1.3 Sample collection

Representative samples of rocks and soils were collected from each site as they were found in the field. For each scene, composing end-members were defined to give a full representation of the mixture. At field scale, end-members are units that are visually separated. In our case,they consist of rocks, gravels, boulders, fine particles fraction or sand.

Samples were carefully packed in order to arrive in the laboratory with their initial condition preserved as well as possible and therefore best represent the field mixtures. Then in the laboratory, the samples were identified and analyzed: type of rock, composing minerals, grain size, etc.

2.3.2 Laboratory work

2.3.2.1 Spectral reflectance measurements

An ASD spectrometer FieldSpec FR3 (FS3) was used for laboratory spectral measurements. It has similar characteristics as the field spectrometer (see table 2-1). In contrast to the field measurements, where natural sun radiation can be used as the light source, in the laboratory an artificial illumination source, a halogen lamp, was used, placed inside a contact probe (Fig. 2.8). During a measurement, the contact probe is positioned on the sample (diameter of the probe is 17 mm) and the light reflected from a sample collected through an optical fiber to the detector.

Prior to each measurement, the ASD FieldSpec was calibrated to a white reference (Spectralon ®). Ten scans were produced for each measurement, and their average spectrum was calculated, as well as its standard deviation. Each sample was measured from different sides with the aim to acquire full representation. Usually samples are not homogeneous; they have different surface roughness, coatings and weathering stage.

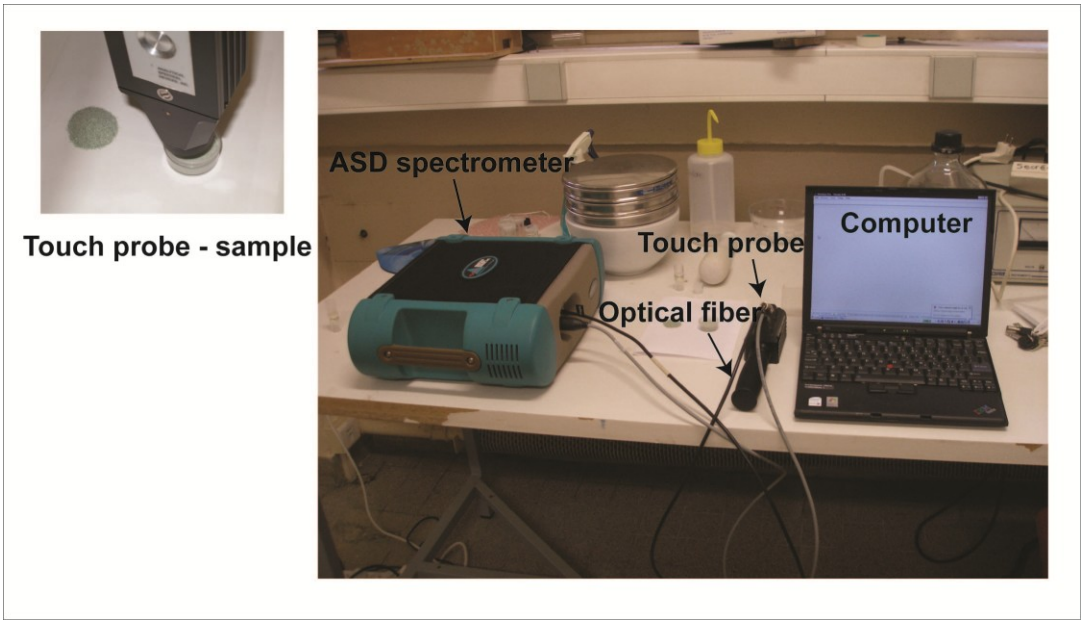

Figure 2.8 – Laboratory setup for spectral reflectance measurements.

2.3.2.2 Sample preparation

2.3.2.2.1 Preparation of thin sections

Samples collected from measured scenes were analyzed under the microscope to assess grain size and mineralogical composition; for that purpose, thin sections were prepared.

Generally, the preparation of a thin section from a rock sample involves several steps: first, a piece of rock is lapped flat in a conditioning ring under a pressure block and a 3.5 load on a grooved, cast iron lapping plate. Then the sample is mounted on a piece of glass and is lapped till its thickness reaches 30-40 μm. With this thickness, thin sections of rocks and their composing minerals can be observed with a polarizing microscope under transmitted plain and cross-polarized light. Minerals can be identified, using their optical properties: refraction index, cleavages, shape, etc. In addition to spectral information, petrological observations are necessary to identify rock composing minerals and define their proportions.

2.3.2.2.2 Preparation of powders

Powders were prepared from samples collected in the field for the following reasons:

1) To produce mixtures with similar proportions of rocks as were measured in the field, but in powdered state, and to compare field and laboratory spectra. Powdered mixtures are intimate and will directly point to differences between intimate and areal mixtures of the similar end-members.
2) Powdered mixtures are microscopic mixtures, and compared to field mixtures and image mixed pixels represent small scale, this comparison will enable to check the influence of scale factor on mixtures behavior.

Many studies of spectral mineral mixtures used powders, which enabled easily to control proportions of minerals in a mixture, and grain size distribution, however it is not obvious that powder can fully represent field scenes and mixed pixels of natural outcrops.

Samples from the field were grounded into powders and then were sieved into 3 main grain size groups: 100-500 μm, 500 μm- 0.7mm, > 0.7 mm-1 mm. Relative proportion of each end-member was adjusted accordingly to its appearance in the field scenes. Then powdered mixtures were measured with the ASD FS3 contact probe.

2.4 Data processing

2.4.1 Field data processing

2.4.1.1 End-member proportions estimation

The proportion of each end-member contributing to the mixture was estimated by applying a supervised classification to the digital photographs that were taken in the field concurrently to the spectral measurements. A Support Vector Machine (SVM) algorithm (ENVI ITT Visual Software) was applied. After each end-member was classified its proportional abundance was estimated (with classification analysis tools in ENVI, fig 2.9). The classification result was validated with cross-validation technique to estimate the accuracy and miss-classifications. For this procedure areas on the image with known end-members are selected manually, than these areas are compared to the result achieved from classification. The percent of miss-estimated areas is calculated for each end-member and the average accuracy of the scene was estimated.

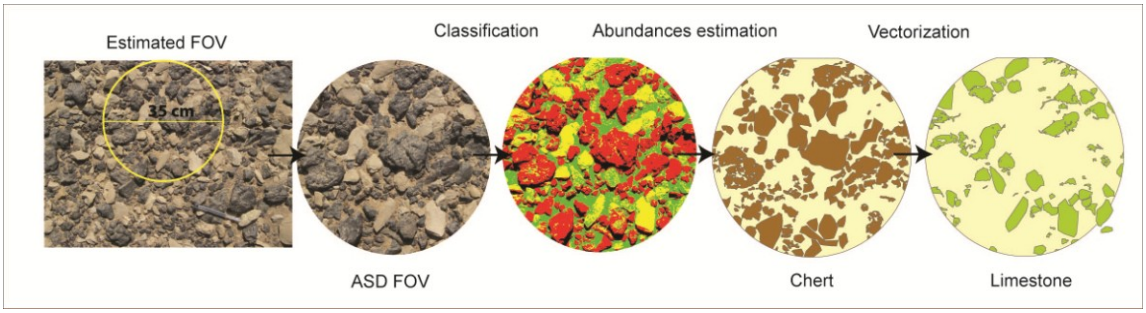

Figure 2.9 – Field image processing steps.

Considering the fact that in our case classification is based only on three bands (RGB), there is a probability for misclassification, especially for rocks (or land cover) with similar colors. For example, in some cases limestone and sandstones have identical colors. Thus it is difficult for the algorithm to distinguish between them. In such cases manual editing was required. RGB images processing steps are shown schematically on the Figure 2.10.

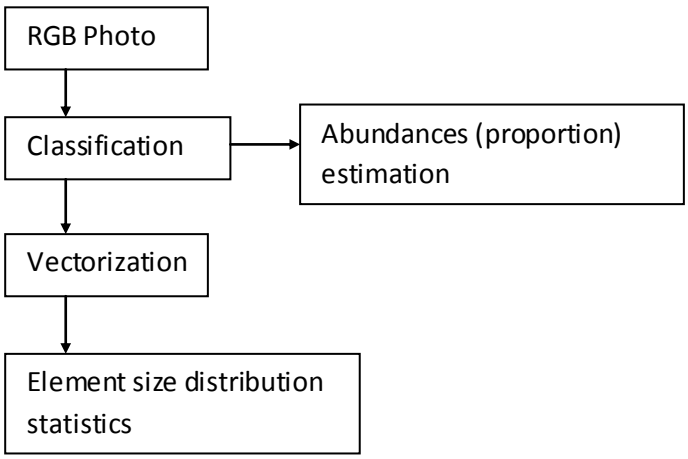

Figure 2.10 - Chart flow of pictures processing.

2.4.1.2 Element size estimation

After the composing end-members were sorted into classes, images were converted to vector format, using ArcGIS software. Vector format enables to edit classes in a more straightforward way, to calculate proportions for each class and to perform other mathematical manipulations. Each vectorized object is an independent issue, consequently the size can be estimated in more straightforward way. Size distribution of composing end-members per scene (in cm^2) was

acquired. Afterwards, the size statistical parameters per scene: mean, minimum, maximum, standard deviation, squewness, kurtosis were calculated for each end-member class using statistical software (Origin 8).

The area of each vector object (rock, gravel) extracted from the field scene was calculated. Using a pen, placed at each scene for scaling, an estimated pixel size for the digital photography was about 0.025 cm, and was a basis for the following calculations.

D_0, the equivalent disk diameter was calculated following eq. 2.2.

$$D_0 = 2 * \sqrt{\frac{area}{\pi}} \qquad (2.2)$$

D_0 was estimated for each object in the scene, and statistics were calculated for each end-member. D_0 is widely used for grain/element size analysis. This parameter presents several advantages: it normalizes non-regular shapes of objects, the acquired equivalent values have a normal distribution and scale and are therefore more robust for analysis. To separate areal contribution of end-members in the scene from size contribution with respect to spectral signal, it was decided to use D_0, this parameter being related to the size of elements in the scene and not to their proportion.

This is done to understand how size of elements in the field, such as gravels, rocks, boulders may influence spectral signatures of the mixtures, if their influence is significant in mixture analysis at macro-scale or only areal contribution of end-members is important at the field scale. This parameter (size of elements) is not taken into account by linear mixture modeling, since linear model only takes into account areal contribution of end-members. However, natural outcrops are more sophisticated than simple linear model prediction and comprise elements of different sizes that also may have an influence on spectral response and should be taken into account in mixture modeling.

2.4.2 Spectral data processing

Spectral data was processed following steps, which will be described in details in the current section. Different spectral parameters were extracted from the data, furthermore direct and inverse mixing models were applied.

Each mixture spectrum combines spectral features of its composing end-members. Hence spectral indicators like: absorptions position, absorption depth, reflectance intensity and spectral shape are expected to correspond to the sequence of composing constituents of the mixture. However, from number of experiments mentioned in the theoretical overview, in non linear, intimate mixtures masking effect of some end-members by others can take place. Linear mixture supposes that all spectral features should be combined linearly, e.g. absorptions and shapes, reflectance and slopes. If the mixture is a linear combination of composing end-members, spectral features should be combined proportionally (see eq. 2.8). If the mixture is non-linear, we will find that spectral features do not correspond to proportional combination of the end-members. Non-linearity of mixtures may derive from physical effects, like multiple scattering of the grains or from chemical properties of the composers, like presence of transitional elements, such as iron oxides, that have quite strong absorption features and mask other constituents.

The spectral parameters under study are: absorption depth, absorption area, absorption symmetry, spectral slope, normalized spectral difference. These parameters are main indicators of mixture composition and quantity (proportion) of its composing minerals. If a mixture has a non-linear behavior and some of the parameters (absorption features or albedo) of one end-member are masked by other end-members, then spectral interpretation based on these parameters might be wrong. It will be impossible to detect an end-member whose spectral feature is masked by other constituent, or its quantity identification may be inconsistent. Therefore spectral parameters mentioned above will be observed either for spectra of end-members or for mixture spectra, as being the indicators of some rules (linear or non-linear behavior) in the mixtures. That will help to explain the source of non-linearity. The detailed description of the calculation of these spectral parameters appears in the next sections.

2.4.2.1 Absorption depth

Depth of absorption is a spectral feature that is related to concentration: the deeper is the absorption, the higher is the concentration of the corresponding element (mineral) in a mixture. For non-normalized spectrum (if continuum is not removed), the depth of absorption is calculated using the following formula:

$$D_{abs} = \frac{(R_c(\lambda) - R_b(\lambda))}{R_c \Delta\, \rho(\lambda)} \quad (2.3)$$

Where R_c is reflectance at center of absorption maximum, R_b is reflectance at absorption minimum (Fig 2.11 a).

Continuum removal of a spectrum enables to estimate absorption depth without influence of albedo, and factors such as scattering, and to focus on selected absorption. In our study continuum of a spectrum was removed following the approach of Clark and Roush (1984). After the removal of continuum R_c is equal to 1, so the depth of the absorption can be simply calculated by:

$$D_{abs} = 1 - R_b. \quad (2.4)$$

where R_b is reflectance at absorption minimum.

2.4.2.2 Absorption area

Absorption area (A_{abs}) is actually a sum of absorption depths at each wavelength of absorption, or in other words it is the integration of the reflectance over wavelength (Fig 2.11 b).

$$A_{abs} = \int_y \frac{[R_c(\lambda) - R_b(\lambda)]}{R_c(\lambda)} \quad (2.5)$$

The absorption area varies as a function of constituent concentration, but also as a function of grain size. Absorption area will be bigger with a higher concentration of the constituent. In fact, this parameter is more informative compared to absorption depth, because it contains information about the entire area of absorption, both at the center, and at the shoulders which may be very informative in some cases. Also it allows to "smooth" the effect of instrument noise, to which simple absorption depth is sensitive.

2.4.2.3 Absorption symmetry

To estimate absorption symmetry, the area of the absorption is calculated before its minimum and after its minimum (R_b).

$$\text{Symmetry} = A_{abs}\,L - A_{abs}\,R \quad (2.6)$$

If the two areas are equal, symmetry is equal to 0, the absorption is symmetric; if one of the areas is larger than the other then the absorption is asymmetric. If the left area (Area L) is larger than

the right (Area *R*) then the absorption is asymmetric with a positive asymmetry. If the right area *R* is larger than the left area *L*, the asymmetry is negative (Fig 2.11 c).

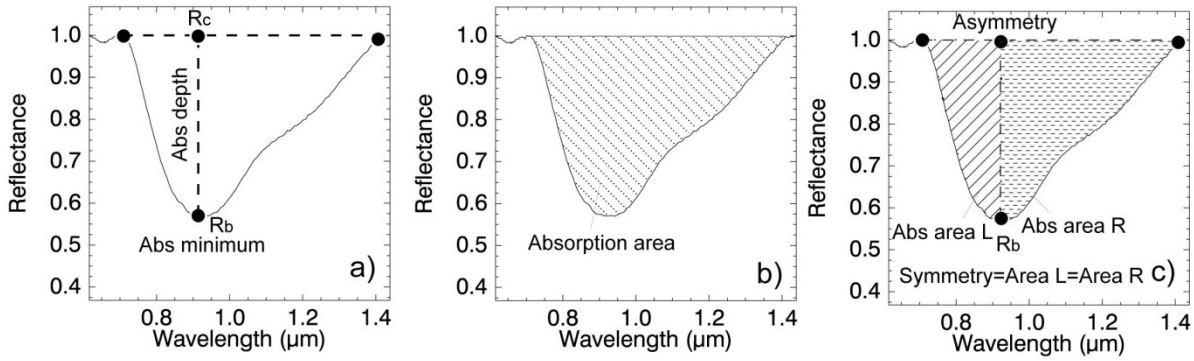

Figure 2.11 – Absorption characteristics: absorption depth (a); absorption area (b); absorption symmetry (c).

The symmetry parameter gives information about end-members composition: when absorption positions of different constituents are very close (such as for hematite and goethite, for example), absorption symmetry enables to distinguish between them. In the case of hematite absorption symmetry will be more positive, while for goethite absorption symmetry will be more negative.

2.4.2.4 Spectral slope

Spectral slope is calculated using the following formula:

$$Slope = \frac{\rho(\lambda_1)-\rho(\lambda_2)}{\Delta\lambda} \quad (2.7)$$

Slope is calculated between selected wavelengths of the spectra, the wavelengths selection depends on the objective. For example, spectral slope between VIS and NIR can be an indicator of volume scattering effects. It is known that with decreasing grain size, volume scattering increases, and elevate the reflectance especially in the VIS-NIR range (Clark, 1999). This is true for powders of single minerals, however for mixtures a t field scale this is obviously not the same. Nevertheless, volume scattering may also occur at the field scale, as a result of multiple scattering between elements that are present in the field: rocks, gravels, fine particles. Multiple scattering will influence spectral reflectance, consequently, spectral slope between VIS and NIR can be one of the indicators for this effect, and indirectly for element size distribution. It is

expected that slope will increase if element size will increase, and the opposite, slope will decrease if element size will decrease.

Spectral slope is also an albedo feature, which corresponds to the presence of bright or dark materials in the mixture. However field mixtures have sophisticated character and contain complex contribution of different effects, either multiple scattering effects, or albedo controlling features, the observation of different elements will help to describe field mixture in a full manner. It is important to detect the influence of each effect on the spectral signature of a mixture, it will help to understand complex mixture behavior. Spectral slopes boundaries were selected from the beginning of the VIS at 0.35 µm to 0.78 µm. This spectral range is sensitive to volume scattering; at shorter wavelengths usually scattering of light is stronger. In the NIR, the spectral range between 0.89 µm and 1.3 µm was selected, as an indicator for volume scattering resulting from grain size variations (Clark, 1999).

2.4.2.5 Spectral difference

Normalized difference between spectra was calculated to locate and quantitatively estimate the differences between two spectra at each wavelength. The magnitude of the difference may be wavelength dependant, and may be related to the mixture elements and their properties. In other words normalized difference contains information of spectral features that are dissimilar in two spectra. For example, spectral difference can be calculated between spectra of two scenes with different properties, or between simulated and measured spectra using the following formula:

$$ND = (S_1 - S_2)/S_1 \quad (2.8)$$

If *ND* is close to 0, there is no difference between the spectra. Differences can be positive or negative, and may arise from variation in albedo, strength or shape of absorption features, and their magnitude can be wavelength dependent.

2.4.3 Spectral linear mixing-direct modeling

Spectral linear mixing is a method for modeling spectral mixtures from spectra of end-members while their proportions in the mixture are known:

$$\rho_\lambda = f_1\rho_{\lambda,1} + f_2\rho_{\lambda,2} + \cdots + f_n\rho_{\lambda,n} + E_\lambda \quad (2.9)$$

where ρ_λ is the reflectance observed in band λ, f_1,...,f_n represent the fraction of each of n possible end-members contained in a pixel, $\rho_{\lambda,1}$,...$\rho_{\lambda,n}$ is reflectance, that would be observed if a pixel was completely covered by the corresponding end-member; and E_λ is the error term. Consequently, in mixture spectra the contribution of the end-members is according to their fractional abundance.

The objective for the direct modeling is to attempt to simulate the ASD FieldSpec spectrum of the mixtures measured in the field. The fractions that were used are those derived from classifications of the digital photographs. End-members are laboratory spectra of each basic component of the scene (fractions (f) are estimated from classification), used to create a synthetic spectrum and compare it to the one measured in the field.

2.4.3.1 Sources of uncertainties

Sources of uncertainty in the simulation spectra may derive from several factors: samples collected in the field do not exactly match the end-member in the mixture (different patina, coating, etc.). The idea was to collect samples which exactly match end-members in the field, however it was not always possible due to heterogeneity of the constituents of the mixtures. Another uncertainty may derive from the location of FieldSpec field of view on the digital pictures, it may be slightly shifted from case to case. And finally, the estimation of percent coverage for each end-member might have some identification errors of the end-members, especially if their colors are similar.

2.4.4 Spectral un-mixing – inverse modeling

2.4.4.1 Linear un-mixing

In the studied surfaces, the spectral signatures acquired in the field are well modeled by linear mixtures of end-member signatures, since the mixing scale is macroscopic and the incident light interacts with just one material. Formally, we have:

$$Y = M\,X + N \quad (2.10)$$

where Y is an L x n matrix containing n acquired spectral vectors of size L, M is an L x p mixing matrix containing p end-member spectral signatures of size L, X is a p x n fractional abundance

matrix containing n vectors, one per acquired spectral vector, $N - L \; x \; n$ perturbation matrix modeling additive errors and modeling errors.

The algorithm of the minimum volume class, termed SUNSAL (Sparse UN-mixing via variable Splitting and Augmented Lagrangian methods) (Bioucas Dias, 2009), was used for linear un-mixing. Sparse regression is another direction recently explored for hyperspectral un-mixing, which has connections with both the statistical and the geometrical frameworks. In this approach, the problem is formulated as that of fitting the observed (mixed) hyperspectral vectors with sparse (*i.e.,* containing a small number of terms) linear mixtures of spectral signatures from a large dictionary available *a priori*. Estimating the end-members is thus not necessary in this type of methods. Notice that the sparse regression problems in this context are not standard, as the unknown coefficients (the fractional abundances) sum to one (the so-called *abundance sum constraint* – ASC) and are nonnegative (*abundance non-negativity constraint* – ANC). These problems are thus referred to as *constrained sparse regression* (CSR).

Hyperspectral linear un-mixing amounts to finding the minimum volume simplex containing the hyperspectral vectors. This is a non-convex optimization problem with convex constraints. In the proposed approach, the positivity constraints, forcing the spectral vectors to belong to the convex hull of the end-member signatures, are replaced by soft constraints. The obtained problem is solved by a sequence of augmented Lagrangian optimizations. The resulting algorithm is very fast and able to solve problems far beyond the reach of the current state-of-the art algorithms. Compared to linear un-mixing algorithm LSU in ENVI (Boardman, 1999), that is widely used, the SUNSAL is more precise and does not output negative fractions as LSU can do.

2.4.4.2 Non-linear un-mixing

One of the difficulties in using simple linear un-mixing algorithm is that the spectral signatures we have were acquired in the laboratory under conditions that were different from those present in the field (light, grain sizes, patina). In order to mitigate this difficulty, we have assumed that the signatures in the field are nonlinearly related with those in the laboratory via the expression

$$m_f = a_0 + a_1 m_l + a_2 m_l^b \qquad (2.11)$$

where m_f and m_l are reflectance of the field and of the lab end-members at a given wavelength, and a_0, a_1, a_2, and b are wavelength independent model parameter to be inferred.

The justification for the above relation stems from the nonlinear relation existing between single-scattering albedo and reflectance in the case of intimate mixtures.

In order to infer the model parameters and the fractional abundances, we implemented the Nonlinear Block iterative scheme in Matlab code solved with the SUNSAL algorithm (Bioucas Dias, 2009).

2.4.5 Correlation coefficient

In statistics, the correlation coefficient is typically denoted by (r) and is a measure of the correlation (linear dependence) between two variables X and Y, giving a value between +1 and −1 inclusive. It is widely used as a measure of the strength of linear dependence between two variables:

$$(2.12) \qquad Correl\,(X,Y) = \frac{\sum(x-\bar{x})(y-\bar{y})}{\sqrt{\sum(x-\bar{x})^2\,\sum(y-\bar{y})^2}}$$

where x and y are the sample means, in visual basic code are (AVERAGE(array1) and AVERAGE(array2).

The correlation coefficient ranges from −1 to +1. A value of +1 implies that a linear equation describes the relationship between X and Y perfectly, with all data points lying on a line for which Y increases as X increases. A value of −1 implies that all data points lie on a line for which Y decreases as X increases. A value of 0 implies that there is no linear correlation between the variables.

In our study correlation coefficients were calculated between spectral properties of the mixtures: absorption depths, reflectace levels, spectral slopes and physical parameters: abundance of the constituents, element size of mixture composers, shadow coverage.

2.5 Sites description

2.5.1 Site 1: Kaolinite quarry

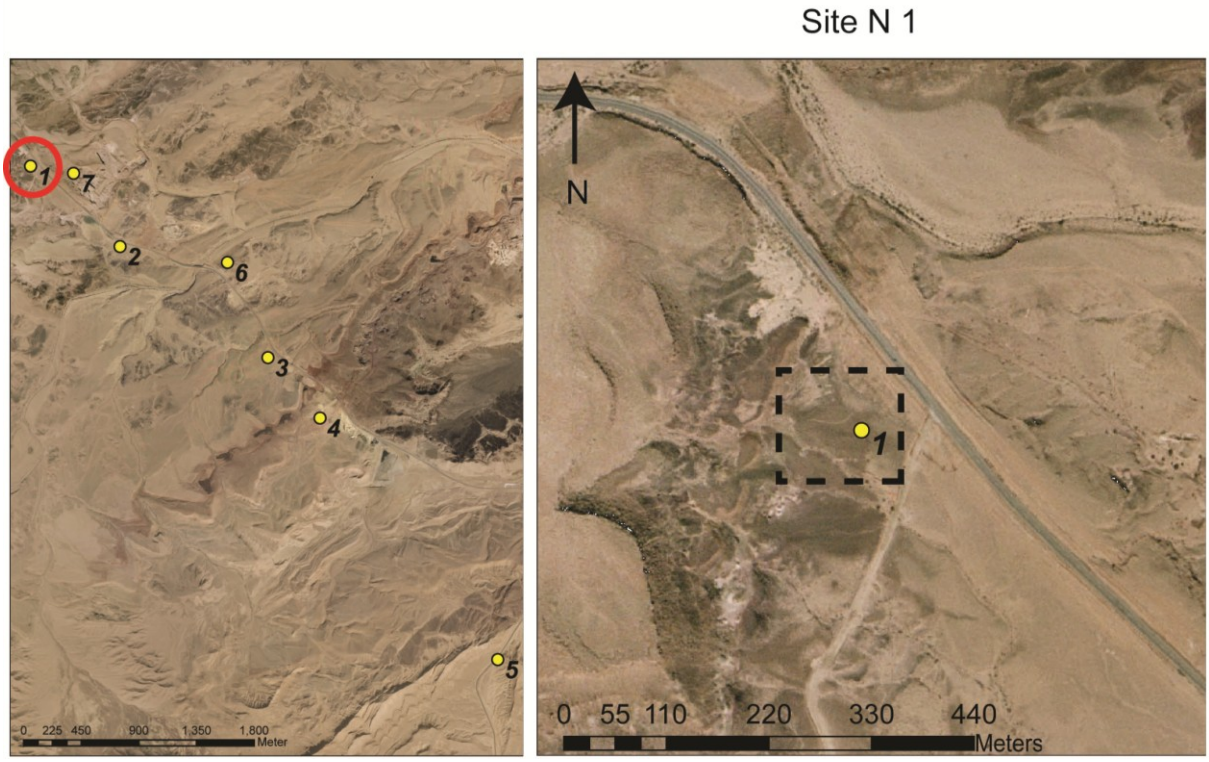

Figure 2.12 - Site N1, location on the map and zoom on the area on high resolution orthophotography.

Kaolinite quarry (site 1) is composed of a variety of mineralogical constituents, basically of sedimentary type. This site was chosen because it is composed of elements of different sizes, and the presence of dark and bright constituents such as boulders and fine particles, clays and silt. The composing rocks of site 1 are chert (dark constituents), limestone (bright constituents), sandstone and silt (fine particles) (Fig 2.19). Sandstone and kaolinite deposits are within the Jurassic sandstone complex (Fig 2.4) which includes large lenses of white kaolinite, which was quarried in the past. Kaolinite is a clay formed as a result of hydrothermal alteration. Plant fossils indicate a continental-lacustrine paleo-environment. The kaolinite mines have been closed and the landscape is well rehabilitated. High abundances of kaolinite are found in the fine fraction (silt). In the field fine particles appear as a substrate for the coarser fraction.

Main composing end-members of the site are: silt rich in clays, cherts rich in iron oxides, sandstones and limestones. Rocks and boulders of the same type may have various sizes from a

few centimeters up to 40-50 centimeters. Some of the rocks are coated with finer particles (clays and iron oxides), and most of them are weathered (patina or desert varnish).

2.5.1.1 Samples description

Samples that appear in mixtures were collected in the field and are shown on Fig. 2.19. Thin sections of the samples were prepared in order to define sample composing minerals, to identify them and to estimate their proportion in the sample.

Chert is a microcrystalline silicon dioxide (SiO_2) rich in iron oxides (Fig. 2.19 a, c). As chert nodules or concretions grow within the sediment mass, they can incorporate significant amounts of the surrounding sediment as inclusions. These inclusions can impart a distinctive color to the chert. Main composing minerals of chert are: quartz, iron oxides, clay. In black chert, iron oxides of goethite type are prevailing; in red chert, it is hematite, producing its red color (fig 2.15, 2.16, 2.19). Cherts with prevailing goethite are usually weathered red cherts, as hematite transforms into goethite during the weathering process.

In addition to iron oxides and quartz, high amounts of kaolinite clays were observed in the sample. Kaolinite concentration was higher in the red chert.

Proportions of composing minerals in red chert (accuracy 88% estimated by cross validation method) are:

Iron oxides ~ 30%; Quartz ~ 30%; Clay~30 %; Calcite ~10%

Proportions of composing minerals in black chert (accuracy 80%) are:

Iron oxides – 25%; Quartz – 40%; Clay ~ 20% ; Calcite ~10%

The proportion of composing minerals was estimated by classification of thin section images using the ENVI software (Visual ITT) (Fig. 2.13, 2.14). The supervised classification was applied (Support Vector Machine algorithm) (Chang and Lin, 2001). First the end-member minerals were selected manually on the image, then the image was classified, and proportion for each end-member was estimated. The degree of misclassification was assessed by cross-validation method. This requires to select known minerals on the image and to compare with classification result, this way the % accuracy can be defined.

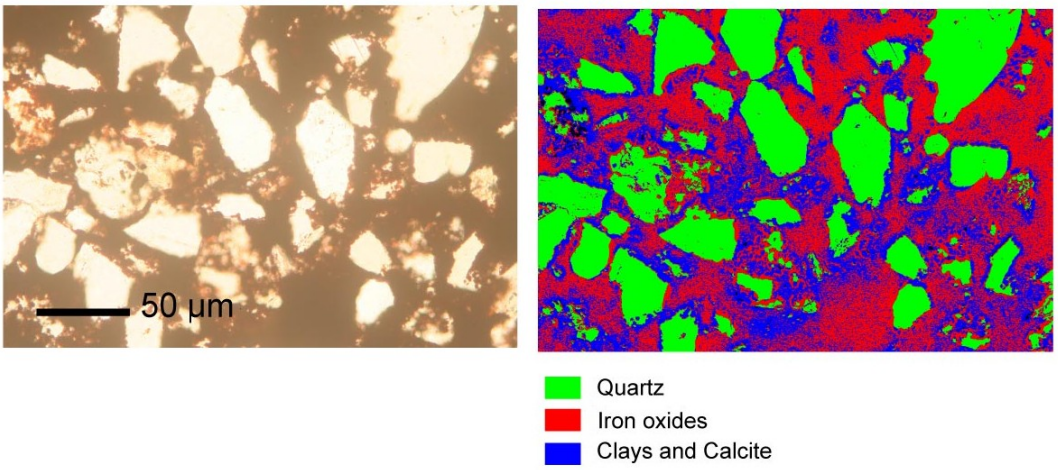

Figure 2.13 – Thin section of red chert in plain polarized light and classification result.

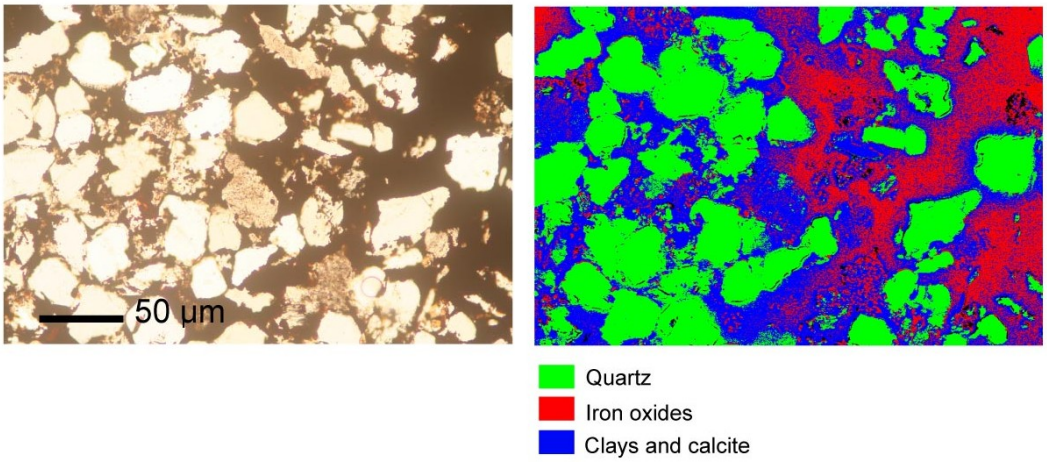

Figure 2.14 – Thin section of black chert in plain polarized light (left) and classification result.

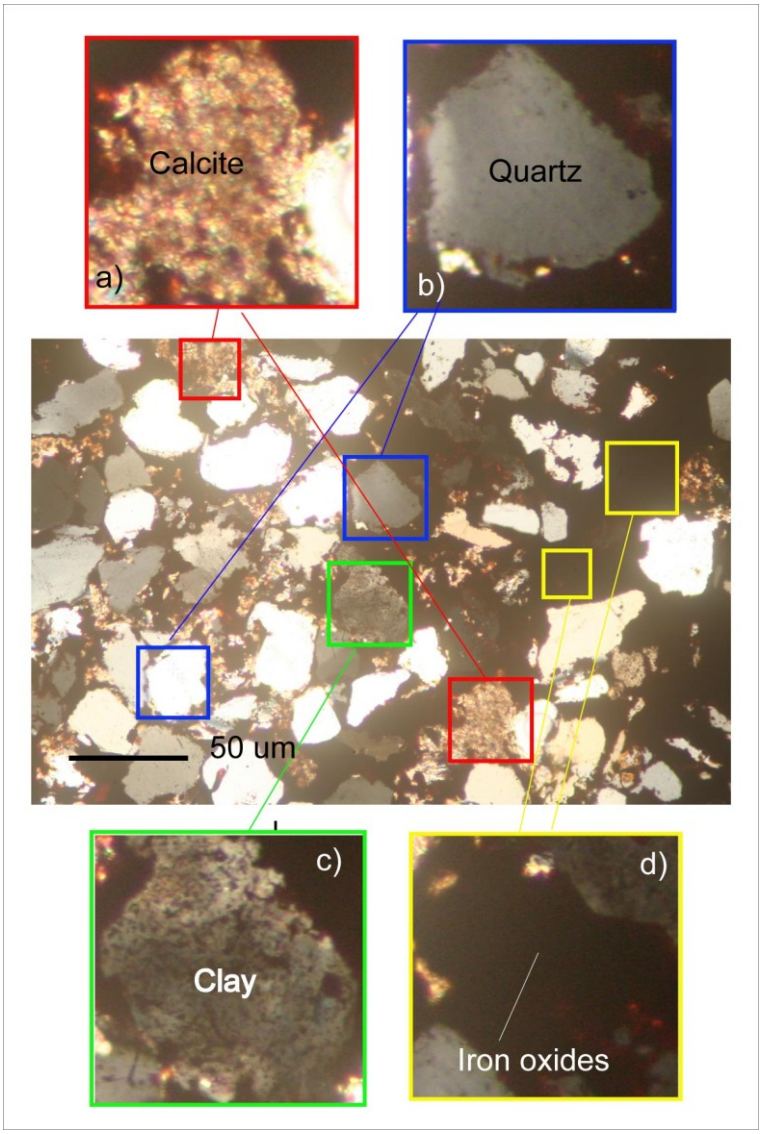

Figure 2.15 – Thin section of black chert in cross-polarized light, zoom on composing minerals.

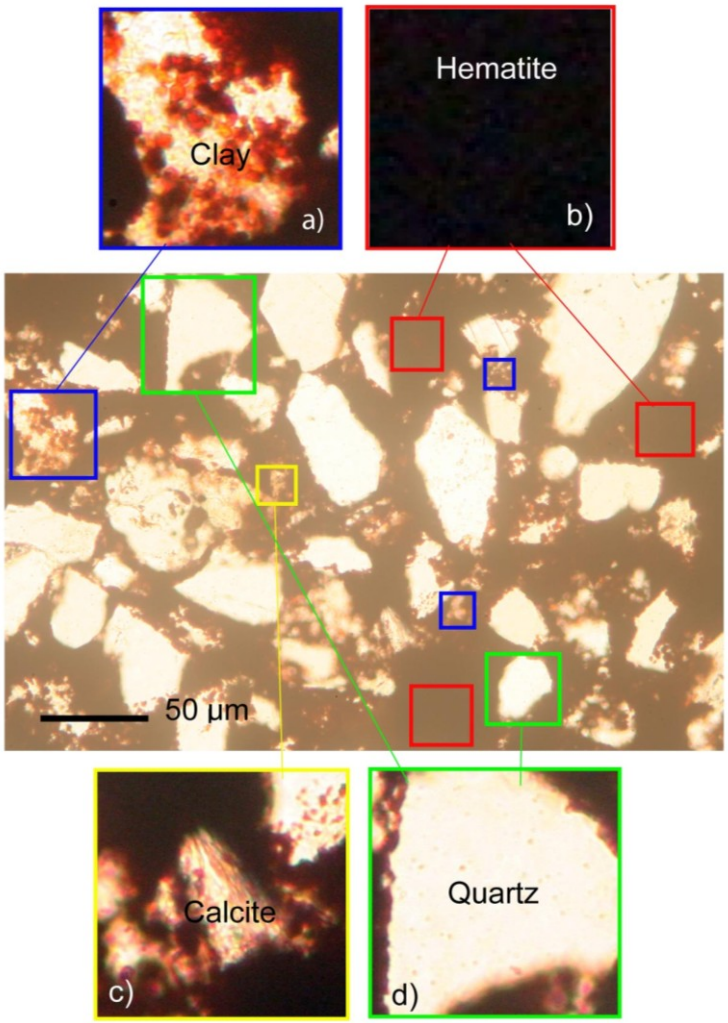

Figure 2.16 – Thin section of red chert in cross-polarized light, zoom on composing minerals.

Limestone - composed of sedimentary minerals formed by chemical precipitation through the evaporation of solutions rich in calcium bicarbonate or by extraction through the action of marine and freshwater organisms (Fig. 2.19 d). The main composing minerals are calcite and clays. In limestones calcite is the main composing mineral and forms 95% of the rock, while clays are result of weathering appear in the rock and constitute about 5% (Fig. 2.17). The size distribution of calcite minerals is difficult to define, it looks homogeneous in the thin section, and it is homogeneously spread in the rock.

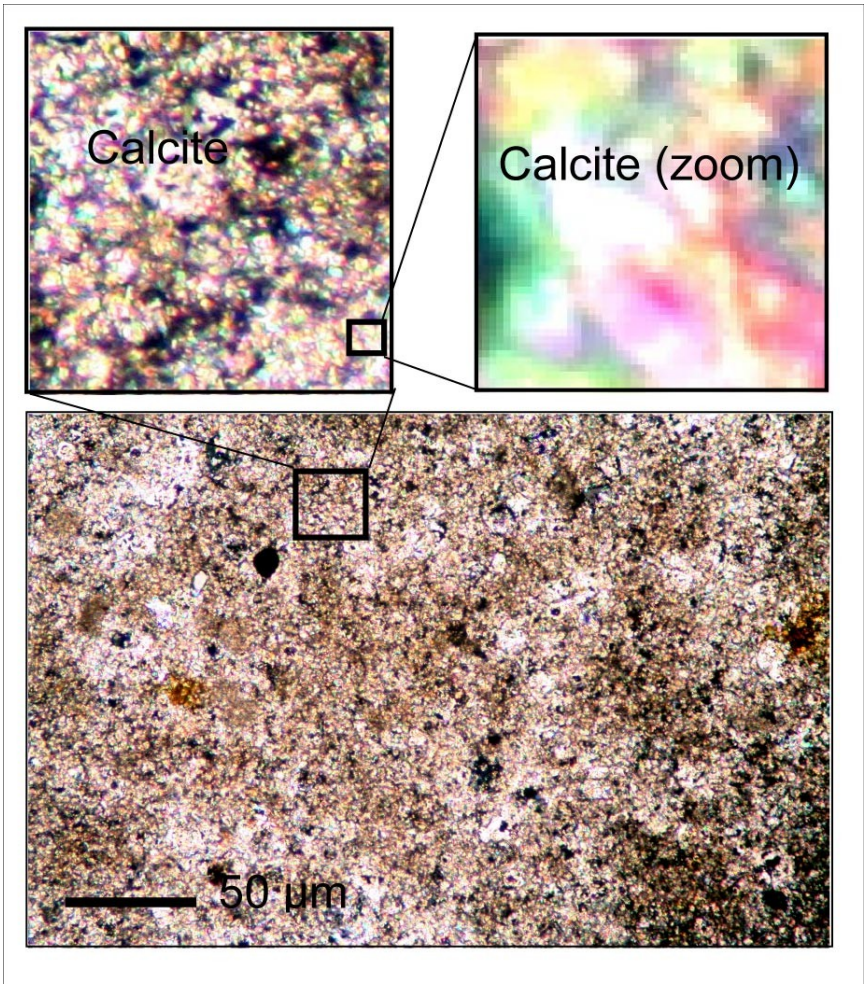

Figure 2.17 – Thin section of limestone in cross-polarized light.

Sandstone – clastic sedimentary rock with sand size grains. Composed of minerals: quartz, feldspars, calcite and clays (Fig. 2.18, 2.19, b). The coarse grains are quartz that can be observed in the thin section. Clays are result of weathering and can be found in small quantities. Iron oxides are composing sandstone, supposing mostly of goethite type, due to the dark-brown color. However, in sandstone the quantity of iron oxides is lower compared to chert.

Estimated proportions of composing minerals in sandstone (accuracy 80%) are:

Iron oxides ~ 20%; Quartz – 50% ; Clays ~10; Calcite ~ 20%

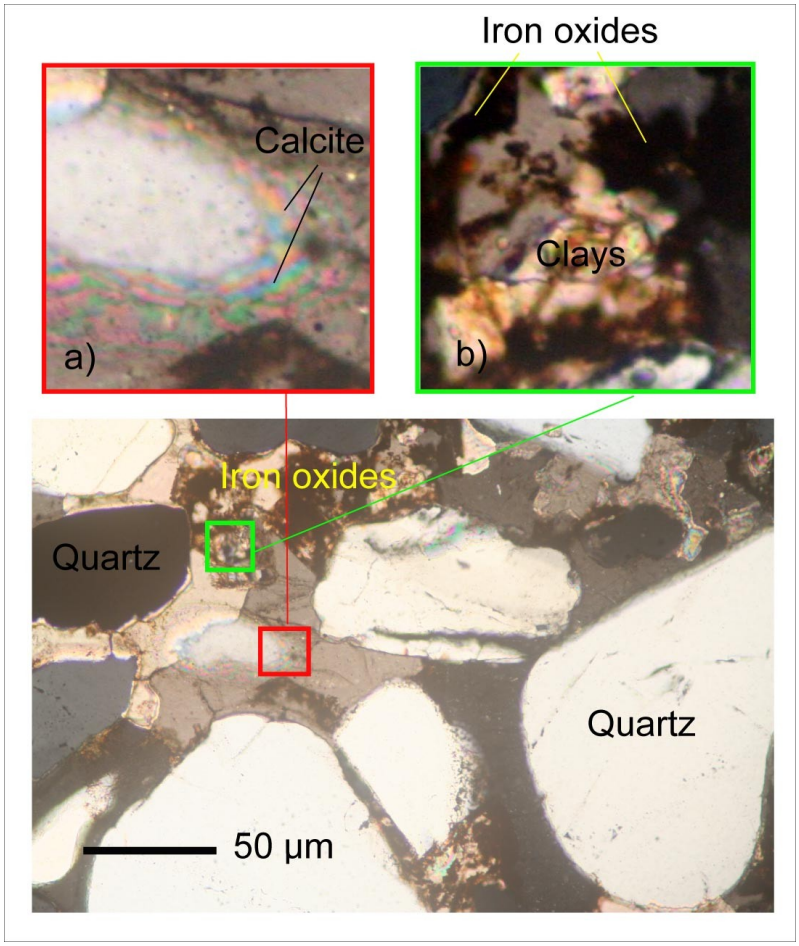

Figure 2.18 – Thin section of sandstone, zoom on composing minerals.

Silt is composed of fine particles of quartz with some amount of clays, mostly of montmorillonite type, and small amounts of iron oxides (hematite) (Fig.2.19 e). Exact grain size of silt was not established, but generally grain size of silt is finer than sand, and coarser than dust. In the field silt appear as down most layer and may contain dust particles and sometimes organic matter, products of weathering. The color of silt was relatively bright compared to other rocks.

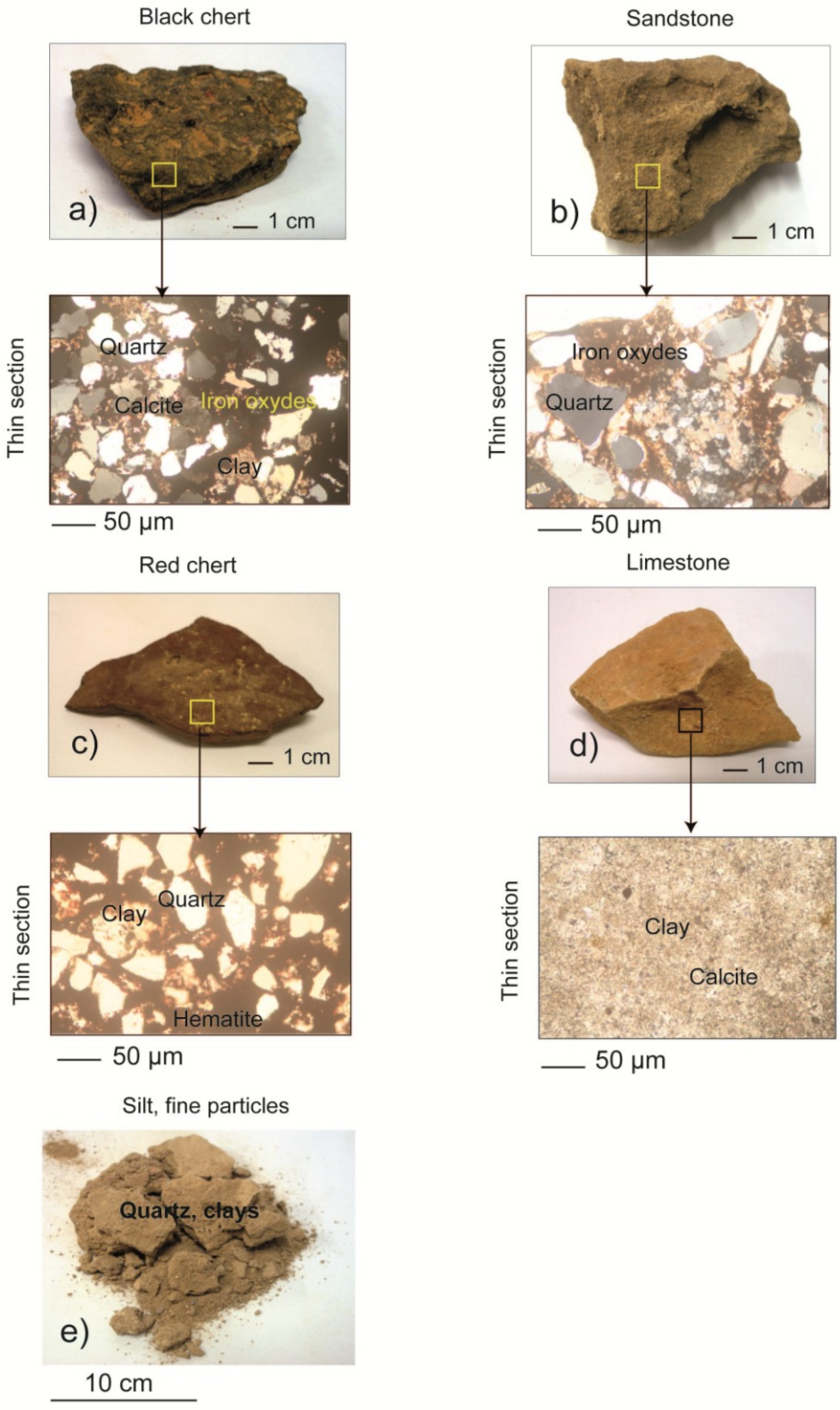

Figure 2.19 – Samples from site 1 and their thin sections.

2.5.1.2 Spectral properties of the samples

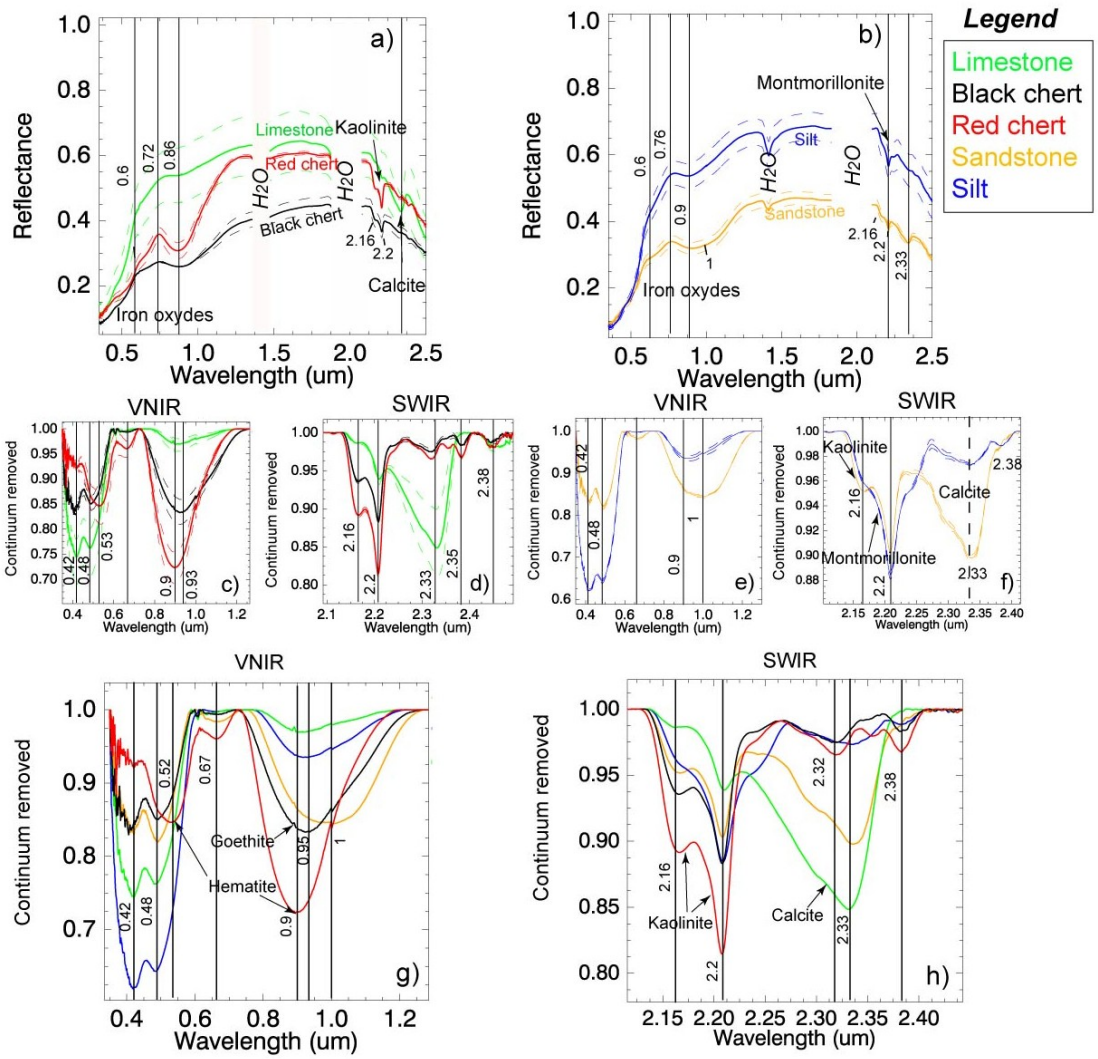

Figure 2.20 – Spectra of the samples from site 1: a, b) full range of spectra; c,e) VNIR continuum removed; d, f) SWIR continuum removed, mean spectra +/- std shown with a dashed lines; g, h) comparison of composing end-members absorption in continuum removed.

Black chert

Black chert is a dark constituent. Spectrum of black chert has low albedo, especially in the visible, reflectance values do not exceed 30%. Reflectance increases towards the NIR, reaches 40%, and then decreases to the end of the SWIR (Fig. 2.20). In the VIS, peaks at 0.6 μm and 0.72 μm can be observed, these peaks are resulting from electronic processes of iron oxides (Hunt, 1977). The spectral slope between 0.4 μm and 1 μm is low. Specific absorptions in the VIS are related to electronic processes in iron oxides, which mean strong absorption features. For example, spectral absorption features that are observed in continuum removed mode at 0.42 μm,

0.48 μm (Fig. 2.21 g). These two minima are considered to be due to Fe-O charge transfer band (Hunt, 1977). Another strong absorption feature with a minimum at 0.95 μm is also caused by iron oxides, in this case goethite (FeO(OH)) (Hunt, 1977). In the SWIR the absorption of kaolinite [$Al_4(Si_4O_{10})(OH)_8$] is well pronounced and appears as a doublet at 2.16 and 2.2 μm. This absorption results from combination bands, the fundamental stretch of Al-OH bending (Hunt, 1977). Absorption at 2.32, 2.35, and 2.38 μm are related to calcite ($CaCO_3$) (Fig. 2.20 h) These absorptions are weak, since there is a small quantity of calcite in the sample. By this, calcite ($CaCO_3$) in cherts can be distinguished from calcite in limestone. Limestone is composed mainly of calcite, its quantity is high, as a result the absorption is much stronger and appears as a deep single band at 2.33 μm (Fig. 2.20 d). In chert calcite absorption appears as a weak double band at 2.32- 2.35 and absorption at 2.38 μm (Fig 2.20 d).

Red chert

Red chert composition is very similar to that of black chert, with the main difference that red chert is less weathered, and contains mainly hematite, that gives to red chert its red color. Spectrum of red chert has relatively low albedo in the VIS, then reflectance increases towards the NIR, with the steep slope between 0.9 and 1.4 μm.

Peaks in the visible at 0.6 μm and 0.72 μm result from iron oxides charge transfer (Fig. 2.20 a), the maximum reflectance occurs at these wavelengths, with a maximum at 0.72 μm, causing the red color of the rock. The absorptions in the VIS, observed in continuum removed mode, at 0.52 μm, 0.62 μm and 0.9 μm, can also be attributed to the hematite (Hunt, 1977). The 0.9 μm absorption of hematite has an asymmetric shape and a minimum shifted towards shorter wavelengths (Fig. 2.20 c). The absorption minimum produces the general difference from goethite. Another difference from goethite is the absorption at 0.52 μm, in the case when goethite composes the rock this absorption is not observed. In the SWIR the absorption of kaolinite can be observed as a doublet at 2.16 μm and 2.2 μm (Fig. 2.20 d). It is relatively deep compared to that of black chert, meaning that the sample contains higher amounts of kaolinite. A double absorption at 2.32 and 2.38 μm is related to calcite, and is due to small amounts of calcite in the sample.

Spectra of red and black chert are shown on figure 2.20. Iron oxides of different types cause absorption at different positions in the visible, these absorptions appear to be due to electronic

processes. Black chert has characteristic absorption features at 0.4, 0.48 and 0.9 μm, red chert has absorptions at 0.53, 0.65 and 0.93 μm. A shift of 0.03 μm in absorption minima between 0.9 and 1 μm is a good indicator that enables to differentiate between goethite and hematite. Absorptions at 2.18 and 2.2 μm are caused by kaolinite. In red chert, kaolinite amount is higher than in black chert, as a result absorption is deeper.

Limestone

Spectrum of limestone has a relatively high albedo in VIS-NIR-SWIR, values reach 50-60%. Limestone is a bright material, most of the radiation is reflected from its surface (Fig. 2.20 a). Standard deviation is rather high and can be explained by heterogeneous composition of the sample, different roughness and the presence of patina, resulting in up to 20% variation in reflectance (Fig. 2.20 a) and differences in absorption depth.

Weak absorptions in the VIS are related to free iron oxides in the sample, which appear as a coating layer on the sample's surface. Weak absorptions of iron oxides are observed at 0.42 μm, 0.48 μm and 0.9 μm in continuum removed mode. In the SWIR very weak double absorption of kaolinite at 2.16-2.2 μm is due to a small amount of kaolinite. A very strong absorption at 2.33 μm is related to calcite ($CaCO_3$) and is attributed to the $3\nu_3$ overtone (Hunt, 1977). Calcite is the main composing mineral of limestone. This absorption is very deep and wide with an asymmetric shape, and a center (minimum) shifted to longer wavelengths (Fig. 2.20 d). However depth of this absorption may also vary as a result of sample non-homogeneity, up to 10%.

Sandstone

The spectrum of sandstone has a relatively low albedo across the VIS-NIR-SWIR range. In the VIS, reflectance is the lowest and does not exceed 40%; in the NIR, values are higher and can reach 45%, then reflectance again decreases towards the SWIR. Sandstone is a relatively dark rock and contains iron oxides, which are opaque and absorbing most of the light. Absorptions in the VIS are mainly caused by iron oxides; their peaks are well expressed at 0.6 μm and 0.76 μm. In continuum removed mode, absorptions due to iron oxides appear as a double absorption at 0.42 μm and 0.48 μm. Absorption of iron centered at 1 μm is strong and is symmetric in shape. This absorption is unique to sandstone (in our samples) and enables to identify sandstone from

other end-members. In the SWIR absorption of kaolinite at 2.16-2.2 μm can be observed, some kaolinite is present within a rock and probably may appear as coating. Absorption at 2.33 μm is deep and strong and is related to calcite, as there is a relatively high amount of calcite in the sample (Fig. 2.20 f).

Silt

The spectrum of silt has a high reflectance in the VIS-NIR and SWIR, the color of silt is bright and its grain size is fine, causing multiple scattering effects (Fig. 2.20 b). The color of silt is darker compared to limestone, but because of multiple scattering, its reflectance is higher compared to that of limestone. Variation in average reflectance between the various measurements can be observed and can be attributed to package of the particles. If the particles are well packed, they will produce a smoother surface, while if they are not, a rougher surface will result. In this case the shadowing effect will increase and will cause albedo to decrease. Absorptions in the VIS result from free iron oxides, which appear as fine particles and mainly are composed of goethite (the absorption minimum is located at 0.92 μm). However, iron oxide absorption at 0.92 μm is not very strong compared to other spectra (Fig. 2.20 e, g). The spectral slope of silt between 0.4 and 0.7 μm is the highest compared to other end-members. In the SWIR the single absorption band at 2.2 μm appears as a result of montmorillonite (Al-OH bond, Hunt, 1977). Montmorillonite clay appears as free particles in the silt, and is a result of weathering. Absorption at 2.33 μm is not very strong and is due to small amounts of calcite.

2.5.2 Site 4: Gypsite quarry

The site location on the map is shown on figure 2.21. A flat area was chosen for spectral measurements, as shown on the picture, this area is also easy to pick on the hyperspectral images. In comparison to other sites, the gypsite quarry is composed of homogeneously spread end-members, which are varieties of gypsum rocks, in contrast to other sites, which may contain different kinds of rocks in one scene. The most abundant end-member of the mixtures is gypsite. Most of the scenes of this site are composed of gypsite of various sizes and a fine fraction, with a similar composition as the rocks.

2.5.2.1 Site description

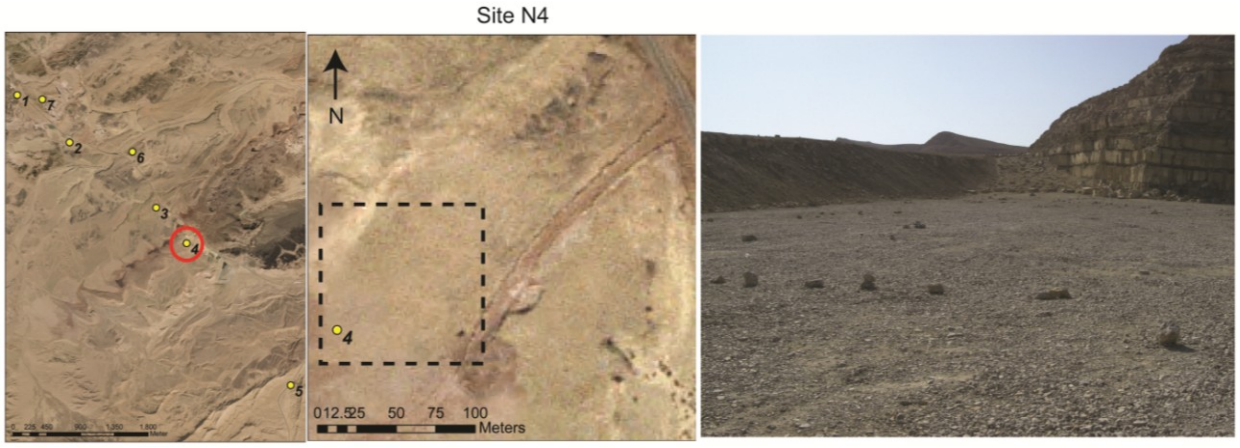

Figure 2.21 – site N4 locations, aerial photographs (left) and picture acquired from the site (right).

The gypsum quarry site is a part of the Upper Triassic rock sequence. The Triassic rock sequence exposed at the Makhtesh includes an upper unit of about 150 meters of gypsum with thin inter-layers of dark shale, limestone and dolomite (Fig. 2.22) (Plakht, 1999).

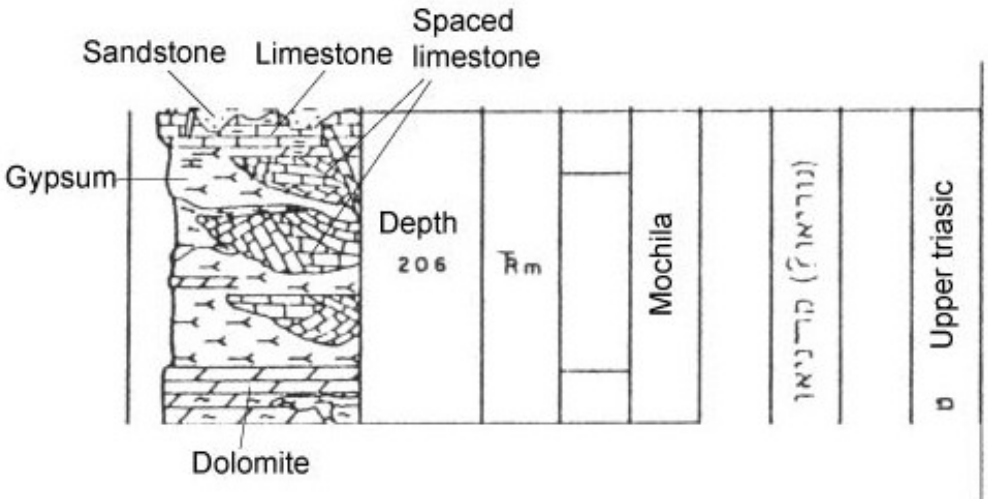

Figure 2.22 – A stratigraphic log of site 4, upper Triassic section (Israel geological survey, 1996).

2.5.2.2 Samples description

Gypsite - A variety of gypsum consisting of dirt and sand; found as a deposit in arid regions, overlying gypsum (also known as gypsum earth). Site 4 is mostly composed of this type of rock, sometimes rare pure gypsum is found in the field, and in very small quantities (Fig. 2.24). The main composing minerals of gypsite are gypsum, quartz and clays (Fig. 2.23).

The proportions of minerals in the sample (accuracy classification – 95%):

Gypsum – 75%, Quartz – 25%

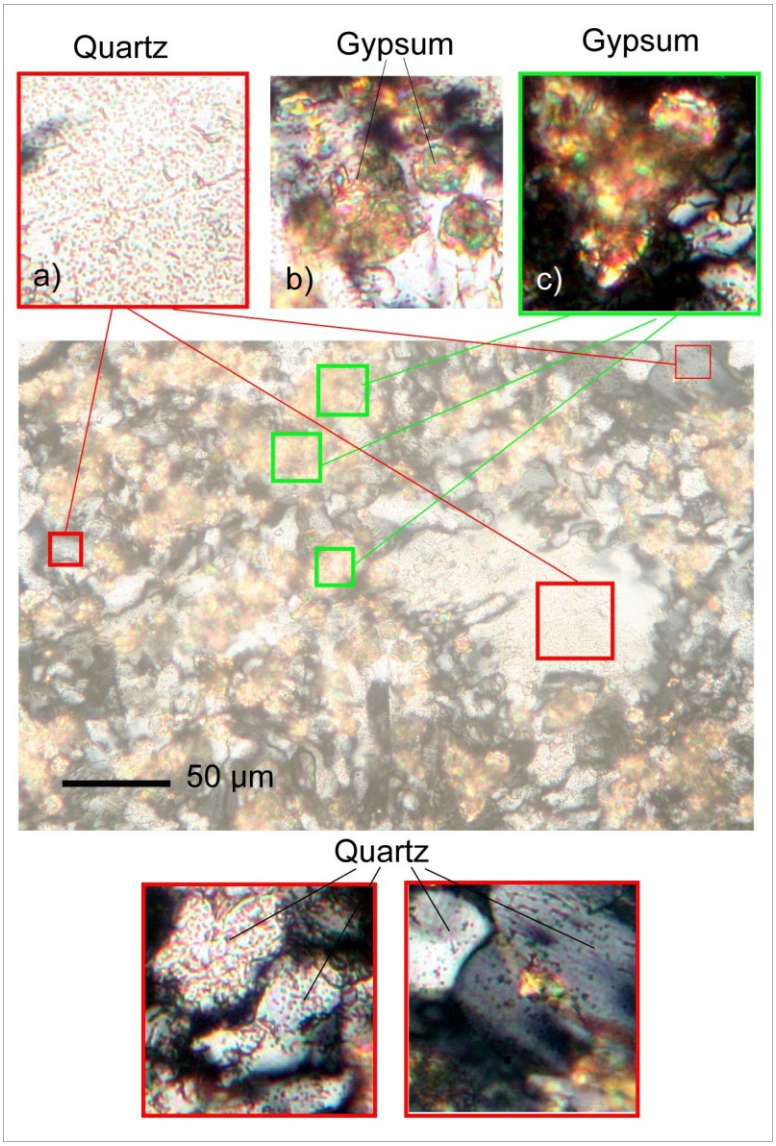

Figure 2.23 – Thin section of gypsite in cross-polarized light, zoom on composing minerals.

Gypsum – hydrated calcium sulfate $CaSO_4.2(H_2O)$. Gypsum is one of the most common minerals in sedimentary environments. It is a major rock forming mineral that produces massive beds, usually from precipitation out of highly saline waters. In site 4, pure gypsum is rare, and appears in small quantities.

Limestone – in site 4 it is mainly composed of dolomite and there are some clays**.**

Silt – fine particles, which were formed as a result of weathering of gypsite and gypsum rocks. Silt color is relatively dark, matching the color of composing rocks. The composing minerals of silt are the same as for rocks from which it was formed. It is composed of minerals of quartz, small amount of gypsum and montmorillonite clay.

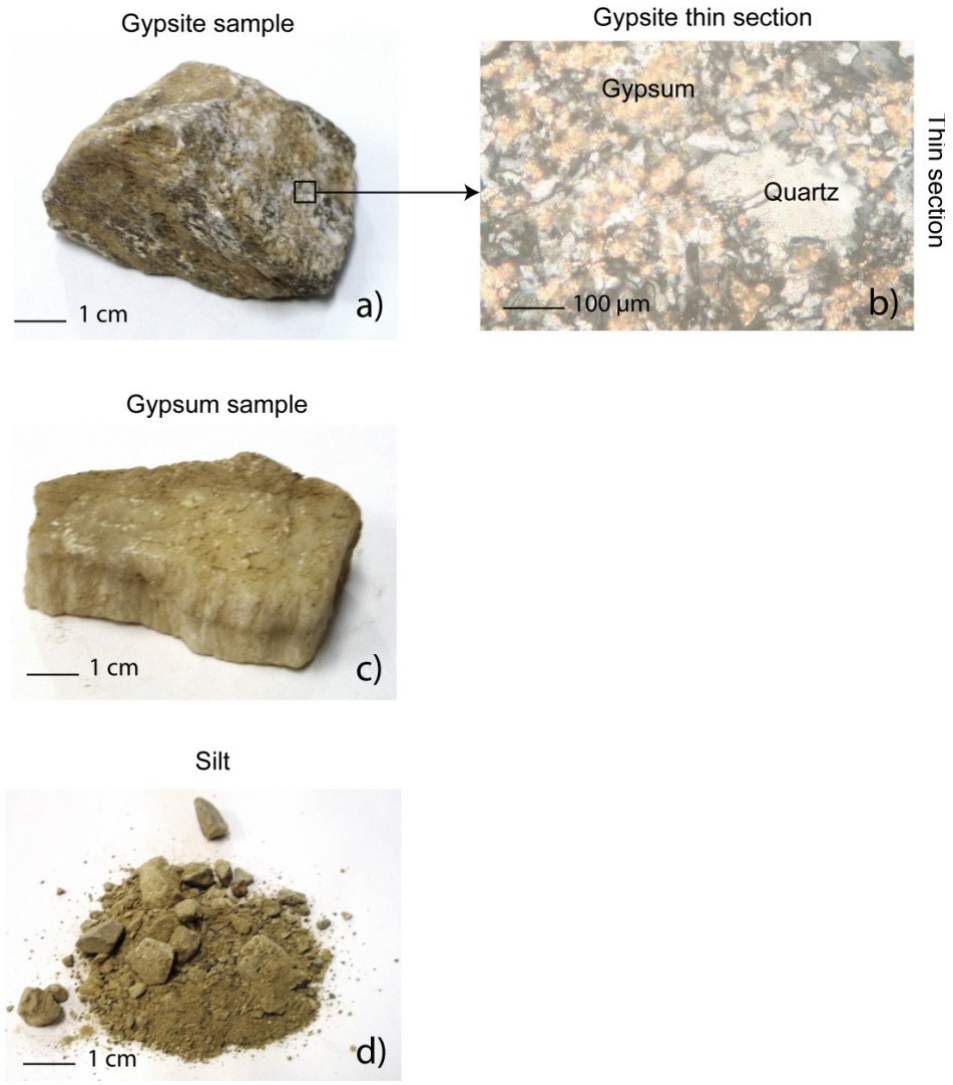

Figure 2.24 – Samples from site N 4: a) gypsite, b) thin section of gypsite, c) gypsum, d) silt.

2.5.2.3 Spectral properties of the samples

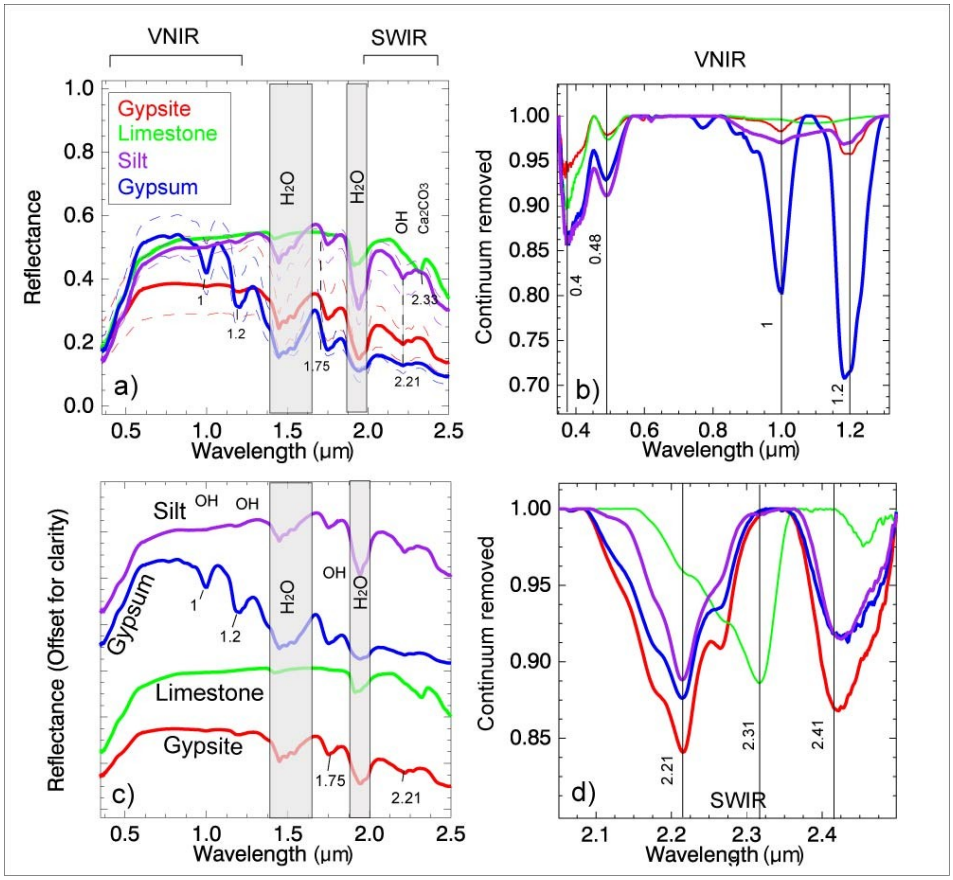

Figure 2.25 – Spectra of the samples collected at site N 4: a) reflectance spectra in full range, minimum and maximum spectral variations are shown with dashed lines; b) VNIR continuum removed; c) spectra shown in offset; d) continuum removed of the SWIR.

Gypsite is composed of gypsum ($CaSO_4.2H_2O$) and quartz. Spectrally gypsite is similar to gypsum, it has the same specific absorptions as gypsum, but these absorptions are weaker (Fig. 2.25). The majority of the bands in the near-infrared can be assigned to water vibrations (ν_1 and ν_2 the OH stretching modes, and ν_2 the H-O-H bending mode) (Hunt, 1977). In gypsum, H_2O absorptions are well pronounced: at 1 µm, 1.2 µm and 1.75 µm (Fig. 2.25 b). In the SWIR, two specific absorptions typical for gypsum at 2.21-2.41 µm are caused by a combination of stretching fundamental ν_3 with the first overtone of the 22.22 µm libration (Fig. 2.25 d). In the visible, the gypsite spectrum is relatively flat, weak absorptions are observed at 1 and 1.2 µm, resulting from the overtone or combination of the internal vibrations of the OH. The absorption at 2.21 µm has an asymmetric shape (Fig. 2.25 d).

Dolomite spectrum is flat in the visible, with a characteristic high albedo across all spectral regions in the VIS-NIR-SWIR. In the SWIR, the well pronounced absorption of dolomite is observed at 2.31 μm (Fig. 2.25 d). The absorption of dolomite is located at 2.31 μm, while absorption of calcite is located at 2.33 μm, this shift of absorption minima enables to differentiate between the two.

Silt spectrum has relatively high albedo (Fig. 2.25 a), multiple scattering from the grains increases the albedo, because silt is mainly composed of fine particles. Absorptions features of silt are corresponding to that of gypsite, however they are much weaker than in the original rock. These absorptions are located at 1, 1.2, 1.75, 2.21 and 2.41 μm. The causes of these absorptions are the same as were described for gypsite.

2.5.3 Site 6 – Kaolinite quarry with high chert content.

2.5.3.1 Site description

Location of the site on the map is shown on figure 2.26. This site is characterized by a high content of dark constituents, mainly boulders of cherts, as it can be seen on the picture (Fig. 2.26). Site 6 is similar to site 1 and also belongs to the Jurassic sequence. The measured area is relatively flat, and the site can be easily located on the hyperspectral images. Mixtures at this site are mainly mixtures of two major constituents: bright silt (fine particles) and dark, coarse boulders of cherts. However, in general, the size distribution of cherts varies from small to very course boulders at different locations. The special interest of the mixtures of this site comes from highly contrasted end-members, dark and bright constituents, represented by chert and silt. As was mentioned in the introduction, from laboratory observations of mixtures with opaque and non-opaque minerals, opaque constituents tend to absorb radiation out of the proportions of their abundances. This feature is also related to the presence of iron oxides in the mixtures, which tend to mask the absorptions of other constituents of the mixtures. This effect in macro scale is observed. This site in most of the cases represents the dual mixtures, where only two end-members are present.

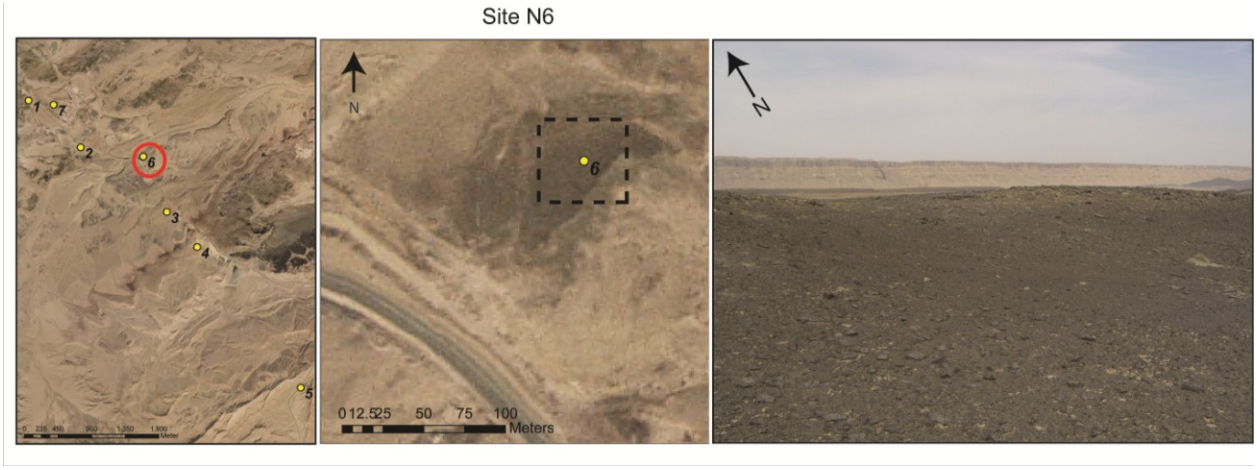

Figure 2.26 – Site N 6 location on aerial photographs and a picture from the site.

2.5.3.2 Samples description

Chert - On this site, both black and red cherts are present, and are similar to that that was described for site 1 (Fig. 2.19 a, c). Red cherts are composed of hematite and black cherts are more weathered and are mainly composed of goethite. Sometimes visually chert composition is difficult to define, for this spectral or laboratory analysis is required. Bright chert was also found on the site, a chert that has a low amount of iron oxides compared to other cherts and therefore a brighter color. Bright chert is something intermediate between chert and sandstone.

Sandstone – clastic sedimentary rock with sand size grains. Common minerals: quartz, feldspars, calcite and clays (Fig. 2.27). In sandstone the quantity of iron oxides is significantly lower compared to chert.

Silt is here composed of fine particles of quartz and kaolinite clays (Fig. 2.27), and small amounts of free iron oxides (hematite). Silt at this site has bright color, and produces high contrast compared with chert.

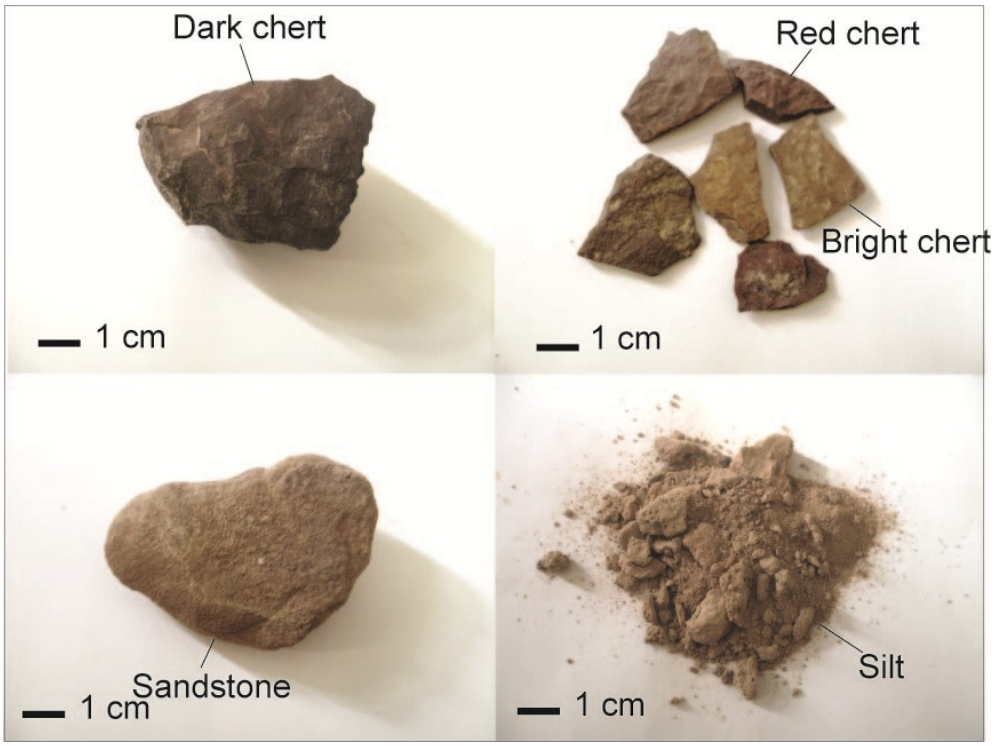

Figure 2.27- Samples from site 6.

2.5.3.3 Spectral properties of the samples

For most of the mixtures measured at this site, the main composing end-members were silt and chert, this are dual mixtures composed only of two principal end-members, in some cases sandstones appeared in small quantities. *Chert* of three types was identified on the site: **dark cherts** rich in goethite **red cherts** with higher hematite content and **bright chert** with low content of iron oxides. Spectra of cherts are shown on the fig. 2.28. Dark chert has a lower albedo in VIS-NIR-SWIR compared to the spectrum of red chert. In red chert a red peak at 0.7 is observed, and is higher compared to dark chert.

Special attention should be paid to spectrally similar end-members, in this site such end-members are red chert and sandstone. Their spectra look quite similar in the visible, though main differences can be observed in the SWIR. In such case un-mixing algorithm may misestimate abundances of these materials. It is important to use full spectral range to be able to identify these end-members.

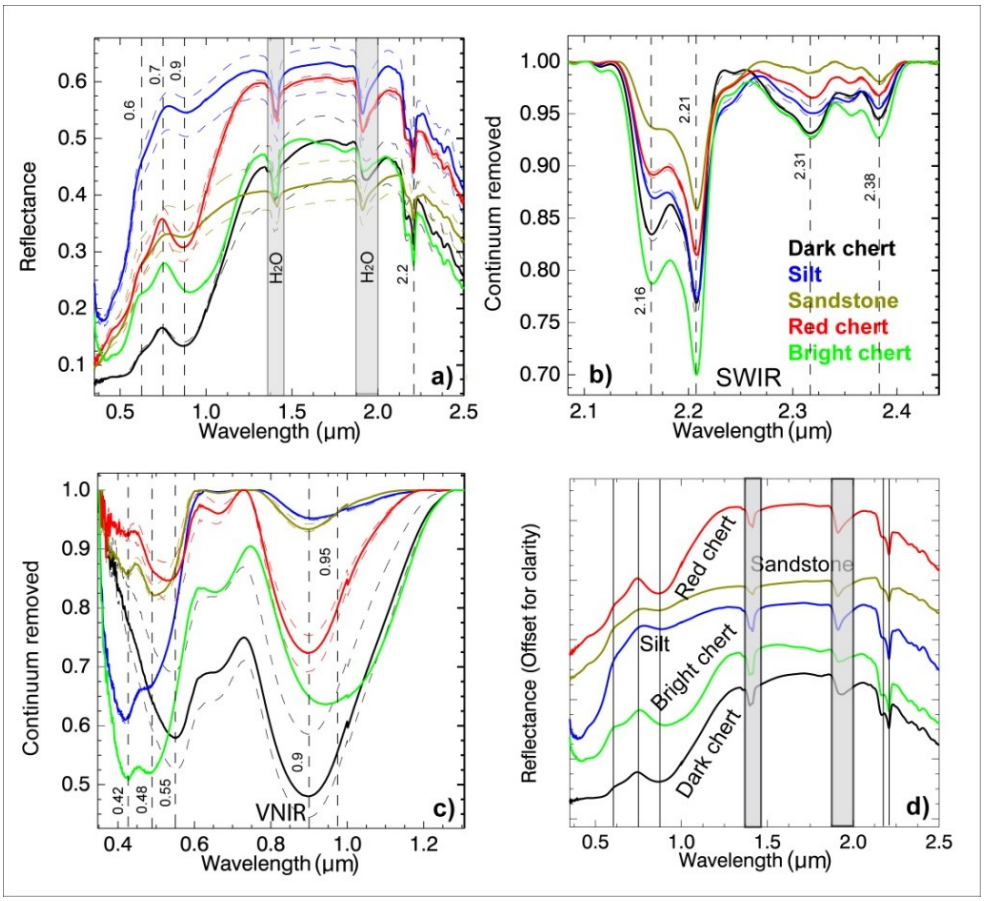

Figure 2.28 – Spectra of the samples from site 6: a) spectra in full range, average spectra +/- std is shown with dashed line; b) SWIR continuum removed; c) VNIR continuum removed; d) spectra shown with an offset .

Cherts have well pronounced absorption of iron oxides with a minimum at 0.9 µm. A double absorption in the SWIR at 2.16-2.21 µm is corresponding to kaolinite (Fig. 2.28 b). Absorption with a minimum at 2.31 µm corresponds to dolomite (Fig. 2.28 b). Dolomite is present in all observed samples, however the highest dolomite content is present in chert. Another type of chert is bright chert, which has a brighter color than other cherts, and contains lower quantities of hematite compared to red chert. The absorption corresponding to iron oxides has a minimum at 0.95 µm that corresponds to goethite. In the SWIR, this chert has a deeper kaolinite absorption at 2.16-2.21 µm, and a dolomite absorption at 2.31 µm.

The spectrum of **silt** has a high albedo compared to other constituents across the entire spectral range, caused by multiple scattering effects from fine grains. The absorption of iron oxides is observed in the VIS with a minimum at 0.9 µm, this absorption is relatively weak compared to other end-members and is mainly caused by free iron oxides particles. In the SWIR, absorption

of kaolinite is found at 2.16-2.21 µm (Fig. 2.28 b) as well as absorption of dolomite at 2.31 and 2.38 µm.

Sandstone spectrum is relatively flat, absorption features are not very strong (Fig. 2.28 a). In the visible, absorption of iron oxides is weak and has a minimum at 0.9 µm. Absorptions in the SWIR are weaker than in other constituents. Absorptions of kaolinite can be observed at 2.16 and 2.21 µm. Absorptions at 2.31 and 2.38 µm correspond to dolomite.

2.5.4 Site 7: Kaolinite quarry

2.5.4.1 Site description

Site number 7 is a kaolinite quarry located not far from site 1. This site, similar to site 1, also belongs to the Jurassic rock sequence (Fig. 2.4). The site location is shown on Figure 2.29. At this site, kaolinite clays are very abundant in the fine fraction, and they are characterized by a very bright color. On the site are frequent rocks of red (hematite) cherts and bright sandstones. On this site mixtures of bright and dark constituents were selected. On the site there are bright and dark boulders of various sizes and proportions, sometimes of very coarse size (conglomerates) which was not the case for other sites. Kaolinite clays coated significantly part of the rocks, which visually interfered with rocks identification in some cases.

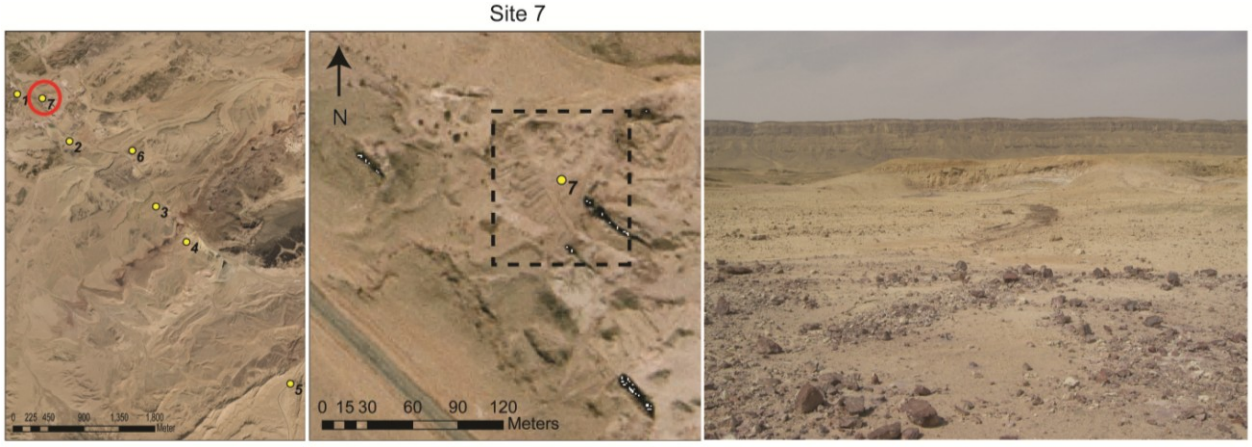

Figure 2.29 – Site N 7 location on aerial photograph and image taken in the field.

2.5.4.2 Samples description

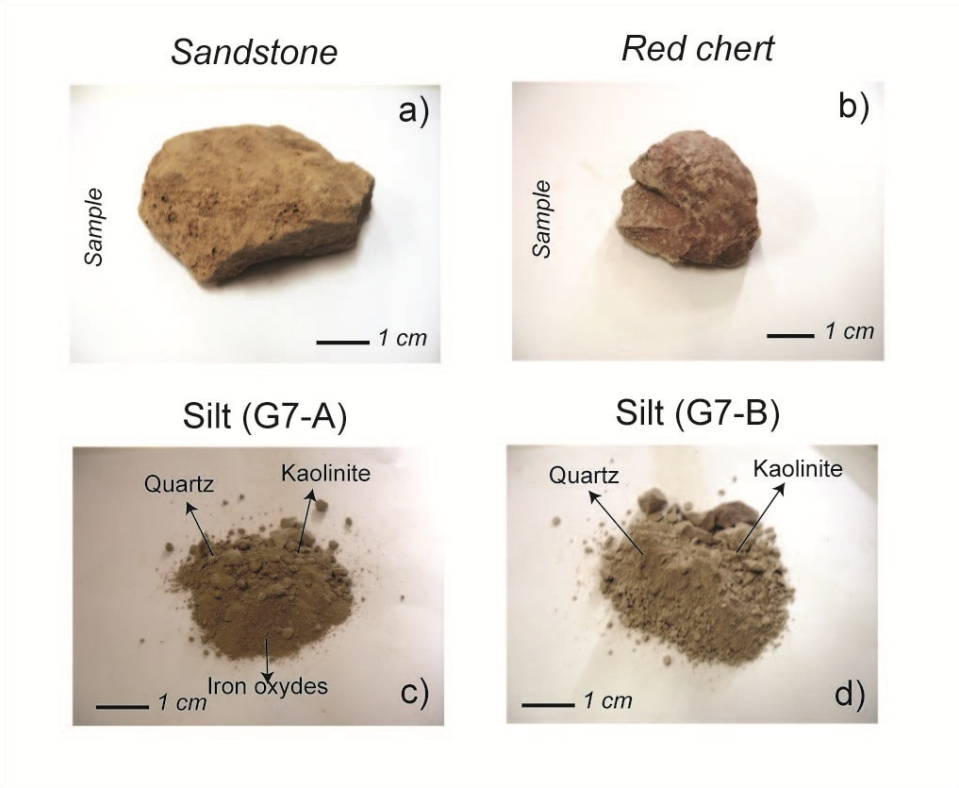

Figure 2.30 – Samples from site 7.

Red chert – Same rock type as was described for site 1 and 6. The main composing minerals of chert are: quartz, iron oxides (hematite), kaolinite clays and small amounts of calcite. High hematite content is the main cause for red color of the rock (Fig. 2.30 b). In contrast to other sites red chert in this site was less weathered.

Sandstone - Clastic sedimentary rock with sand size grains of quartz. Composing minerals are quartz, iron oxides and kaolinite clays. Sandstone of this site has no calcite compared to other sandstones found in the field.

Silt – Two types of silt were defined in this site (Fig. 2.30 c). One type (from group A) is darker than the other one. It is composed of fine particles of quartz with some amounts of clays mainly of kaolinite type, and small amounts of iron oxides (hematite). Silt from group B has a brighter color and is composed mainly of quartz and high amounts of kaolinite. The bright color is a result of the absence of iron oxides.

2.5.4.3 Spectral properties of the samples

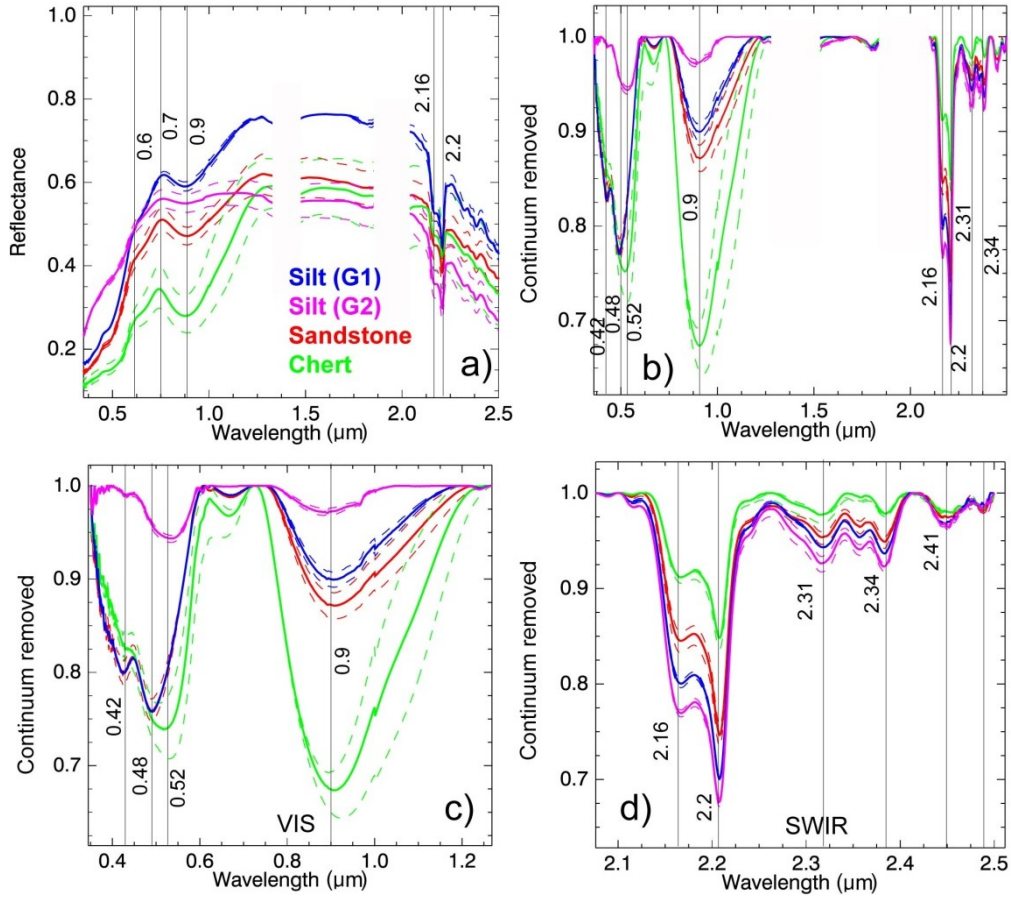

Figure 2.31 – Spectra of the samples from site 7: a) full range spectra, average spectra +/- std are shown with dashed lines; b) full range continuum removed; c) VNIR continuum removed; d) SWIR continuum removed.

Spectrum of chert has low albedo in the visible, strong absorptions of iron oxides at 0.9 μm (Fig. 2.31). Iron oxides in chert are of hematite type, absorption is asymmetric with a minimum at 0.9 μm. Absorptions of kaolinite at 2.16-2.21 μm is observed, though not very strong (Fig. 2.31 d). Absorptions at 2.31 and 2.34 μm indicate small amounts of dolomite.

Sandstone has a relatively high albedo, compared with chert. A weak absorption of iron oxides is observed with a minimum at 0.9 μm, due to hematite (Fig. 2.31 a, c). Kaolinite absorption in the SWIR, at 2.16-2.2 μm, is relatively strong. Absorptions of dolomite at 2.31 and 2.34 μm are also present in the spectrum.

The spectrum of **silt** (group A) is very similar to that of sandstone, but with a higher reflectance, because of scattering from the grains (smaller grain size). Absorption of iron oxides at 0.9 μm is not very strong, but absorption of kaolinite at 2.16-2.2 μm is stronger than in other end-members.

Silt from group B is brighter and contains almost no iron oxides, absorption at 0.9 μm is weak. However the absorption of kaolinite at 2.16-2.21 μm is well pronounced, indicating high kaolinite content. A weak absorption of dolomite is present in the spectra.

2.5.5 Summary of field groups

Four sites were selected for field mixture analysis: these are sites number 1, 4, 6, 7, which finally were classified into eight general groups of mixtures. Mixtures were classified into different groups due to their parameters, such as composition, number of end-members, element size distribution, spectral contrast. Table 2-2 summarizes these parameters for each group. The groups are presented according to the logic from the simplest cases with smaller number of end-members to more complicated ones with increasing number of end-members and parameters. They will be presented following this sequence in the results chapter.

Table 2-2 – Summary of measured sites and field data parameters.

Site-Group	N end-members	Contrast	El. Size	Description
4-A	1	-	Medium	Scenes with a single end-member, rocks of gypsite. Slightly different element size
4-B	2	Low	Medium	Mixtures of two end-members, rocks of gypsite and fine particles (silt).
6-A	2	High	Small-Medium	Two-component mixtures with high contrast end-members dark cherts rich in iron oxides and fine particles of silt.
7-B	3	Low	Coarse	Mixtures of low-contrast constituents, cherts, sandstones and silt.
1-A	3	High	Small	Mixtures with high abundance of fine fraction and small quantity of dark weathered cherts.
1-B	3	High	Coarse	Mixtures with high contrast constituents, coarse boulders of cherts –dark constituents, limestones- bright constituents and silt – fine particles.
1-D	4	High	Coarse	Mixtures with high contrast end-members of cherts and sandstones, small and coarse elements sizes.
1-F	3	High	Medium	Mixtures of red chert rich in hematite, non-weathered constituent and silt- fine particles at the background.

To facilate naming of the groups in the text they will appear as site-group short name, as, for example, 4-A, 4 is the name of the site, A is the name of the group.

Group 4-A and B consist of scenes with small number of constituents of low contrast. In these groups such parameters as composition and illumination effects can be studied. In the field reflectance may be influenced by shadow and other illumination effects which may add non-linearity in the mixture.

Group 6-A consist of mixtures with two highly contrasted end-members, one of which is opaque and rich in iron oxides (chert) and another one more neutral (silt) composed of quartz and clays. In this group, non-linear compositional effects can be studied. From case to case, there also are different distributions of element sizes which might influence the spectral reflectance.

In group 7-B, there are more constituents but they have low spectral contrast and are spectrally similar. This case can be compared to the previous one with high spectral contrast mixtures. The ability of un-mixing algorithms to separate spectrally similar end-members will also be tested.

Mixtures of site 1 are the complicated ones since they are composed of a higher number of end-members. Group 1-A is composed of dark constituents of small sizes and bright fine particles (silt). Here the influence of elements of small sizes on spectral reflectance can be observed. Group 1-B is composed of more sophisticated cases, which have three end-members, dark and bright, and of relatively coarse sizes. In group 1-D element size distribution vary from scene to scene. The last group of field mixtures, group 1-F represents cases with highly spectrally contrasted end-members, hematite rich cherts and silt. The interest of this group is to show an influence of hematite on absorption features in mixtures with bright constituent and masking effect of strong hematite absorptions.

2.5.6 Spectral variations of the samples

2.5.6.1 Patina and fresh rock

Spectral measurements of the samples in the laboratory were acquired while sample field condition remained preserved. This is important particularly to represent field end-members in a more precise way. However, significant differences between the acquired spectra of patined and fresh rocks can be observed. Figure 2.32 shows spectra of patined and fresh rocks. Absorption depths are more pronounced in case of fresh rocks than in the weathered ones. Patina covers a rock as a result of chemical (oxidation) and physical weathering. Therefore the spectrum of patina is less absorbing compared to the spectrum of fresh rock. Since absorption features of rocks are caused by their composing minerals, if the minerals are weathered, the absorption will

be less pronounced. A fresh rock of black chert has a higher reflectance, the absorptions of iron oxides and kaolinite are stronger. The spectrum of a fresh sandstone has a higher reflectance and a stronger absorption depth compared to the patined rock. The spectrum of a fresh red chert has also stronger absorptions than the rock covered by patina. As a consequence, if the spectrum of fresh rock is used for un-mixing, it will result in an overestimation of the corresponding end-members, in case the patined rocks compose the mixture.

2.5.6.2 Lattice orientation effect

All minerals are constructed of crystal lattice. In case of anisotropic minerals, light interaction with the mineral lattice is different along different crystallographic directions. As a result spectra of single mineral will be different depending on mineral orientation. It was found that reflectance measured from a mineral at different orientation angles may vary by up to 10% in reflectance level and several percents in absorption depths. This observation was produced at microscopic scale from single mineral reflectance (Carmina and Carrère, 2009; Dyar, 2005). Hence, considering the fact that a rock is composed of many minerals, lattice effect may influence at a bigger scale, where not just a single mineral, but several hundreds of minerals are observed at the same time (sample scale).

To check this phenomenon a series of measurements were produced in the laboratory. Homogeneous area of exposed fresh sample was fixated on a sample holder, in such a way that the same area was exposed for measurement. The sample surface roughness was minimal; however it was not polished to avoid specular reflectance. An ASD probe was fixated over the sample holder, and while the probe remained at a fixed position, the sample was rotated every 30° and its spectrum recorded. This way the same region was measured each time, with only its orientation changed. Our measurements showed that rotating the sample influenced the average reflectance and absorption depths of the spectra (Fig. 2.33). Reflectance may vary by up to 10% because of orientation effects of the sample. Absorptions depths may vary up to 2-3% with different orientation of the sample. Because sample roughness was very small, we suppose that this effect results from mineral orientation. In cases when the surface of the sample is rough, the orientation effect might be weaker, and the spectra will be influenced by the sample surface roughness. Spectra might be sensitive to micro-roughness. Considering the wavelength range of observation, there should be an influence of grain size smaller than 1 mm. However in our case

this effect is homogeneous over the measured sample area, what is changing while the sample is rotated is mainly orientation.

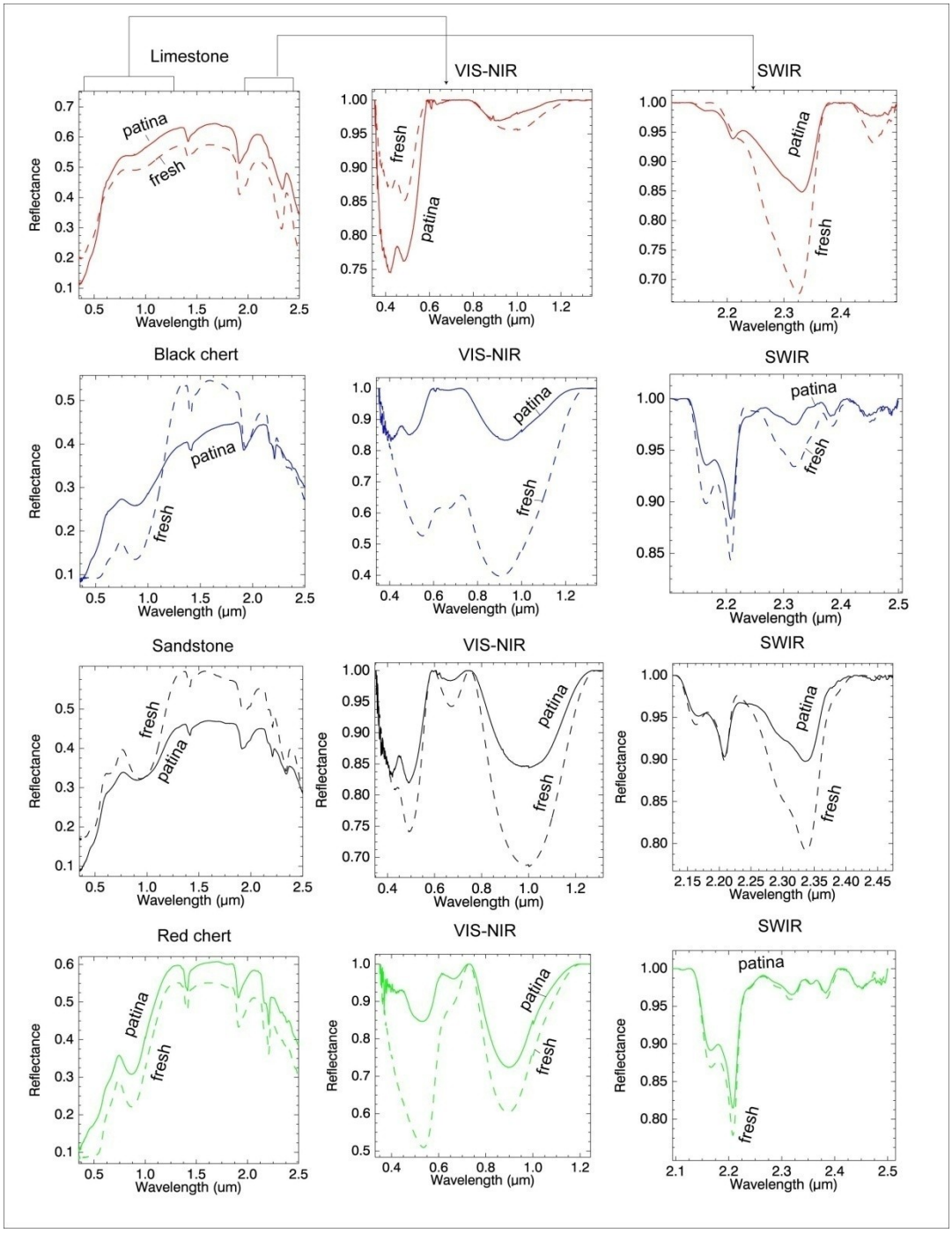

Figure 2.32 – Comparison of spectra of patina and fresh rock of the samples, measured in the laboratory with the ASD.

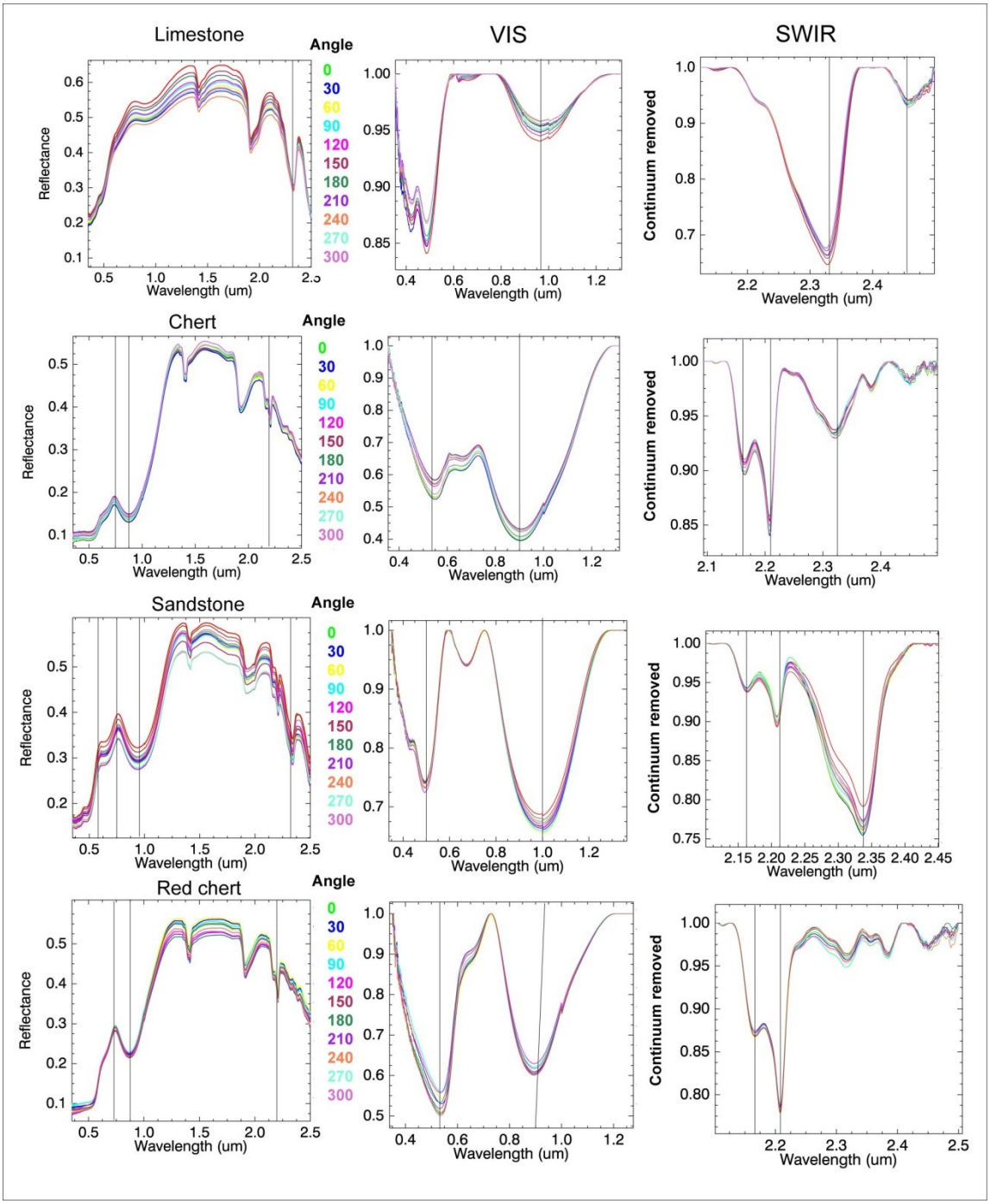

Figure 2.33 – Spectra of the samples measured in the laboratory with an ASD, samples were rotated every 30°.

In this chapter the study area, measured sites and their composing samples were introduced. The methods, which were applied in this work for data analysis were described. The next chapter will present the main findings and results.

Chapter III

3 Results

Results of the field scenarios are presented, starting from the simplest cases with smaller number of end-members to more complicated ones, with larger number of end-members and parameters. The main parameters of the mixtures are: number of end-members, type of end-members, element size distribution and shadow coverage. Each of these parameters influences the spectral signature of a mixture. If there is an areal combination of end-members in the field, linear model and field spectra should correspond, and linear un-mixing will predict correct abundances of end-members. If there are non-linear effects in the field, they will be appear as differences and their origin will be investigated, since field mixtures are macro-mixtures, which are expected to represent the sub-pixel scale.

3.1 Site 4 - Group A – scenes with a single end-member and different element sizes.

The first group of scenes was selected from site 4, the gypsite quarry; this group of scenes is composed of a single end-member (Fig. 3.1). In the field, scenes consist of boulders and gravels of different shapes, of medium, but not very coarse size. The main composing end-member of these scenes is gypsite. In contrast to spectra acquired in the laboratory of pure gypsite samples, in the field it is expected to observe differences, mainly attributed to changes in size and to shadow. The end-members have a rocky structure, so in the field, in these type of mixtures, boulders and rocks, as usual, produce shadow, that has an influence on the spectral signature.

3.1.1 Cases presentation

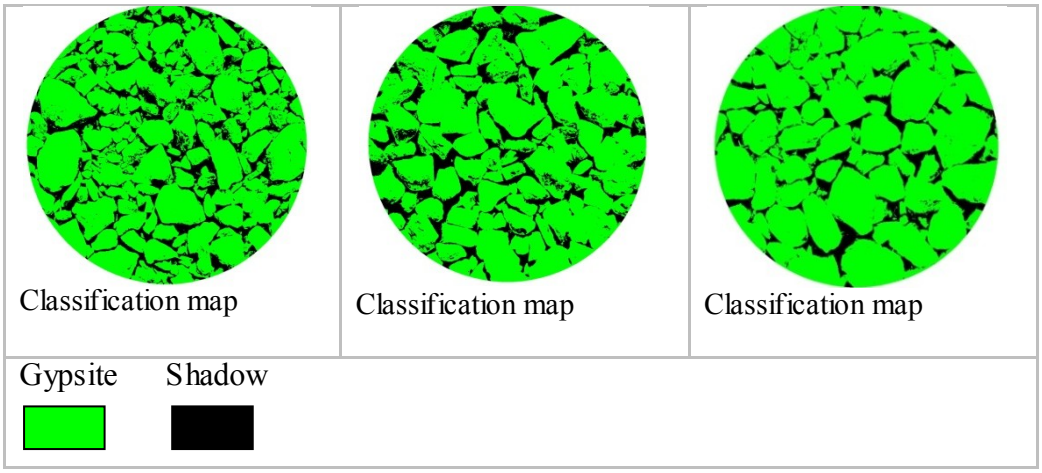

Figure 3.1 – Field scenes and classification maps, site 4 group A, diameter of each scene is 35 cm.

Table 3-1 – End-member abundances, site 4, group A.

ID	Gypsite %	Shadow %	Accuracy %
2075	81	19	99.3
2077	79	21	99.1
2078	86	14	99.9

Field scenes of this group are presented on figure 3.1, all scenes are composed of a single end-member - gypsite, the element size and shadow coverage is not constant from case to case, and there are some differences in classification result (Table 3-1).

Case **2077** has the highest percent of of shadow (21%), and for case **2078**, the shadow coverage is the lowest (14%). According to the visual aspect, scene **2075** has smaller gravels of gypsite than scenes **2077** and **2078**.

3.1.2 Spectral characteristics

Spectra of field scenes are shown on figure 3.2, showing spectral properties of the mixtures: reflectance and spectral shape, absorption positions and depth. The standard deviation of the spectra is less than 1%, thus noise effect should be minimal (Fig. 3.2.(b)). Mixtures of this group are composed of the single end-member - gypsite, despite that, spectral difference between the

scenes can be observed. Changes in spectral signatures are mostly attributed to changes in element size and shadow. The main differences appear in the VIS-NIR continuum, and less in the SWIR. Differences are not very strong, less than 1%. The highest reflectance is attributed to the mixture 2077, the lowest to 2078.

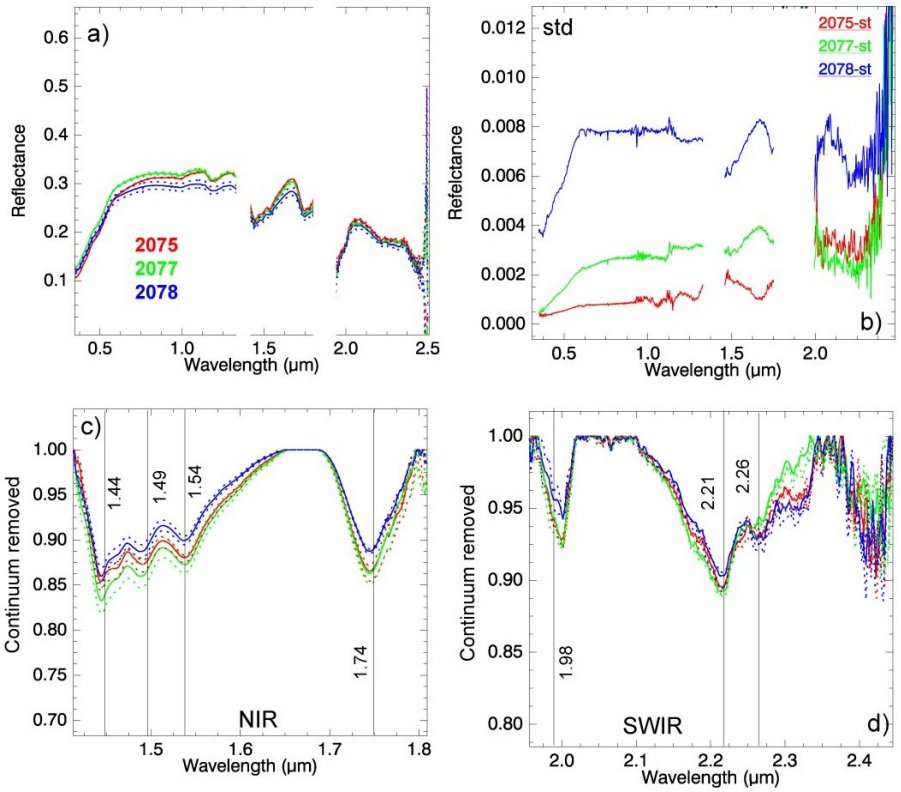

Figure 3.2 – Field spectra of mixtures, site 4, group A: a) full spectral range; b) standard deviation; c) VNIR continuum removed; d) SWIR continuum removed.

Changes in absorption depths are not very high, but they reach several percents (2-3%). In the VIS-NIR differences are higher than in the SWIR.

To achieve the better interpretation of the factors that influence spectra at the field, field spectra were compared to the pure spectrum of gypsite, which we picked in the field, and was measured afterwards with an ASD FieldSpec in the laboratory (gypsite mineralogical composition is described in section 2.5.2.2).

In general, field spectra of all the mixtures have lower albedo than the average gypsite spectrum (Fig. 3.3). Absorption in the VNIR at 1 μm of the field spectra is deeper compared to the

spectrum of the sample measured in the laboratory. Absorptions in the NIR are more pronounced for gypsite measured in the laboratory than for the field spectra.

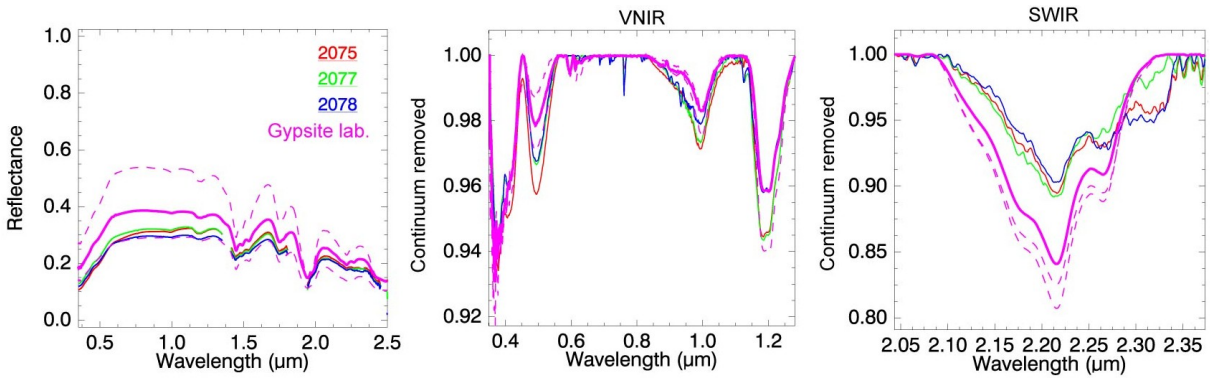

Figure 3.3 – Laboratory spectrum of gypsite and field spectrum.

Absorption in the SWIR is deeper for the laboratory spectrum. These absorptions are caused by H_2O vibrational processes. Difference between laboratory spectra of gypsite and field measurements are due to shadow effect, element structure and different measurement conditions.

3.1.3 Difference analysis (DA)

Differences between field cases and pure gypsite sample measured in the laboratory are shown on fig. 3.4. The highest differences values show at the beginning of the VIS, then the difference decreases towards the SWIR.

The differences between cases 2075-2077 and 2075-2078 have similar shapes (Fig. 3.4 right), with negative values in the beginning of the VIS and values which are close to 0 in the SWIR. Spectral difference results from non-homogeneous rock sizes and shadow effect. Case 2075 has smaller element size than the other cases, while in cases 2077 and 2078 rock size distribution is quite similar. From this result we can conclude that shadow has a higher influence in the beginning of the VIS. Because field spectra were compared to laboratory spectrum of gypsite, where shadow is absent and therefore reflectance is higher in the VIS than in the field, this resulted in a higher normalized difference in the VIS. Probably this is also a result of different measurement conditions, e.g. laboratory and field (Fig. 3.4 left). Normalized difference is lower in the SWIR, values are closer to 0, and consequently the SWIR was less influenced by shadow

and changes in element size. Element size has an indirect influence on shadow, as for coarser boulder shadow will be bigger.

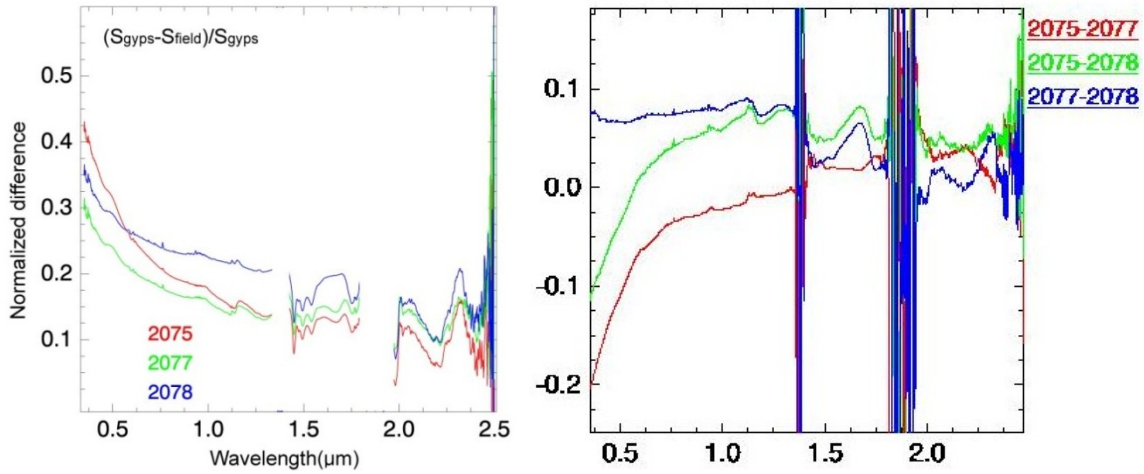

Figure 3.4 – Normalized difference between spectrum of gypsite and field spectra (left) , normalized difference between cases (right).

Observation of this group of mixtures showed that different size distribution of mixture elements and shadow effect may cause differences in spectral signature. In the observed group composition of the mixtures was similar between the cases, so the main spectral differences were attributed to shadow and element size. Comparison to the laboratory spectra of gypsite showed that spectra of the field cases have lower reflectance intensity and less pronounced absorptions. Laboratory spectra used do not take into account shadow effects, a usual phenomenon for field cases, where the sun is the illumination source. Interspectral changes between the observed mixtures were mainly identified in the VIS and less in the NIR and SWIR. This result points on important environmental factor that should be encountered in field mixtures analysis.

3.2 Site 4, group B - mixtures of two end-members with low spectral contrast (rocks and fine particles).

This group of scenes is composed of boulders of gypsite and a background of fine particles (silt), a two-component mixture. The end-members in this group have low spectral contrast, their color is quite similar, as well as their mineralogical composition; however the main difference between the end-members is their structure, and for the selected scenarios, their content in rock versus fine particles of silt.

Cases **2079** and **2080** are presented on figure 3.5, each scene is accompanied with the classification result.

	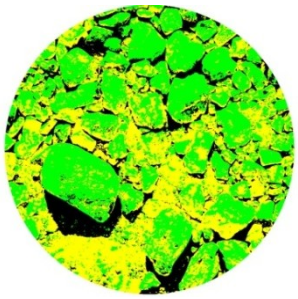
2079	Medium-coarse boulder size
	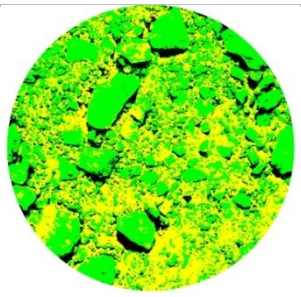
2080	Medium, coarse and small

Figure 3.5 – Field scenes and classification maps of mixtures of group B, site 4, scene diameter is 35 cm.

3.2.1 Cases presentation

Case **2079** is composed mainly of rocks of gypsite, which covers a significant part of the scene (44%), the elements size is coarse and medium coarse (4-10 cm.). The scene contains amount of fine particles of silt in the background (40%). Shadow covers about 16% of the scene (Table 3-2).

For case **2080,** the amount of fine particles is higher than in the previous case, and reaches 50%, there are also rocks of gypsite, which proportion is 38%, element size of gypsite vary from small to medium (0.5-1 to 5-9 cm).

Table 3-2 – End-member abundances of mixtures site 4, group B.

	2079	2080
Gypsite %	44	38
Silt %	40	50
Shadow %	16	12
Accuracy %	95	95

Spectra of mixtures are shown on fig. 3.6: full spectral range (a), continuum removed spectra in the VIS-NIR (b) and SWIR (c). Standard deviation is less than 1% for all mixtures (3.6 d), meaning that spectra were not influenced by noise or atmospheric instability.

Spectrum of case **2080** has a higher reflectance compared to case **2079**, the difference is smaller in the VIS and bigger in the SWIR. This difference could be explained by the difference in element sizes, or proportion of silt and rock in the mixtures, leading to higher scattering for the case having the highest proportion of silt. In case **2080** there are more fine particles and gravels of small size than in case **2079**. Consequently, absorptions in the NIR are deeper in case **2079**, for which the proportion of rocks is bigger. In the SWIR absorptions are in the same range for both cases.

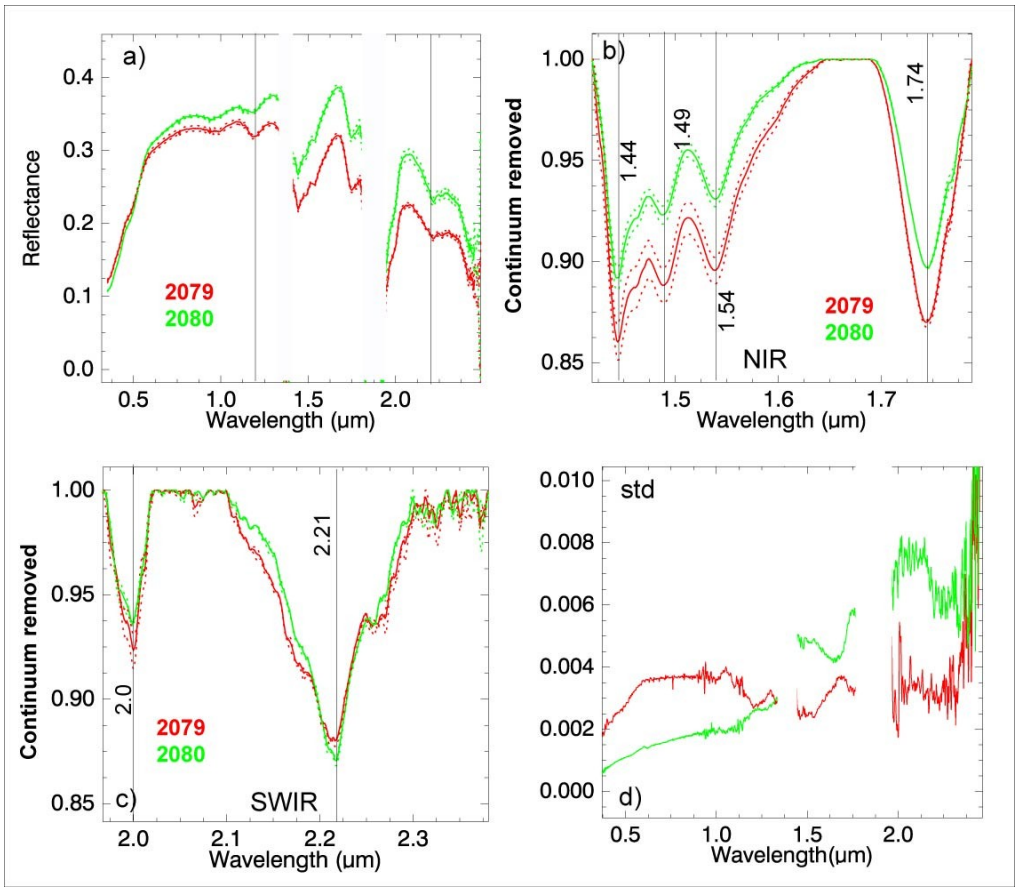

Figure 3.6 – Field spectra of scenes group B, site 4: a) full spectral range; b) VNIR continuum removed; c) SWIR continuum removed; d) standard deviation.

3.2.2 Linear modeling

Linear modeling for the observed group showed, that the average modeled spectrum is higher than the field spectrum (Fig. 3.7). In cases 2079 and 2080 field spectra correspond to the values of the lower level of modeled spectra. Absorptions in the visible at 1 μm and 1.2 μm are deeper in the field spectra compared to the model. In case 2079 predicted and measured absorption depths are close to each other. Absorption at 2.21 μm appears in the same range with the average modeled spectra in cases 2079 and 2080. The reason, probably, is shadow effect that lowered the field reflectance spectrum, and was not accounted for in the model. Consequently the field spectrum has a lower reflectance than the modeled average.

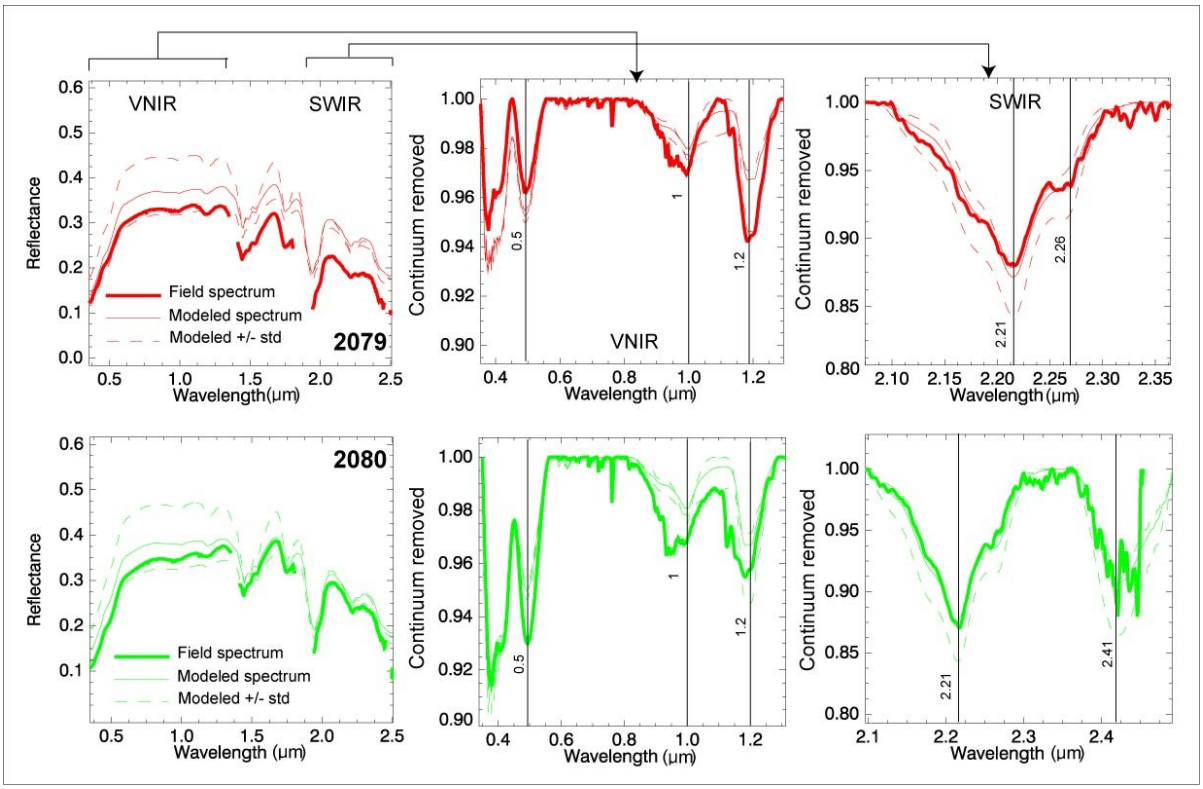

Figure 3.7 – Modeled and field spectra of mixtures, standard deviation of modeled spectra (due to samples heterogeniety) is shown with dashed line.

Formulas used for linear modeling (*Sp* means spectrum):

$$\textbf{2079} = (0.44 * Sp_{gypsite}) + (0.4 * Sp_{silt})$$

$$\textbf{2080} = (0.38 * Sp_{gypsite}) + (0.5 * Sp_{silt})$$

3.2.3 Difference analysis (DA)

Normalized difference between field and modeled spectra are shown on Fig. 3.8. Differences are low, values are close to 0 in the VIS in cases 2079 and 2080. This means that linear model prediction and field spectra matched to each other. Though for case 2079 the linear model predicted a higher reflectance in the SWIR, this scene is composed of coarser boulders. A negative difference in the SWIR was obtained for case 2079, because the linear model overestimated the reflectance in the SWIR.

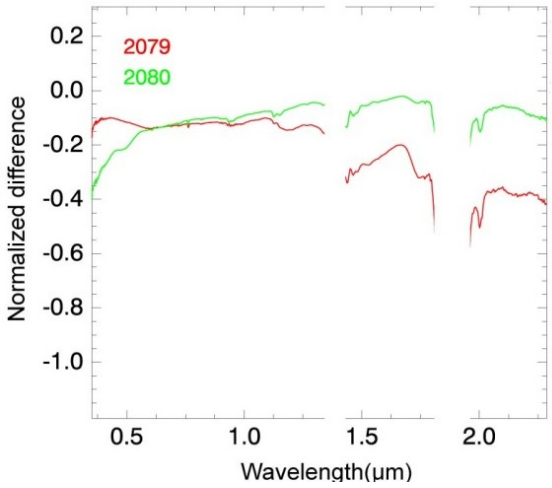

Figure 3.8 – Normalized difference between modeled and field mixtures.

The main conclusion for this group of mixtures is that end-member structure (fine particles or rocks) in a mixture has a strong influence on field reflectance spectra, even when their mineralogical composition is similar. In mixture with higher silt content, the reflectance intensity is higher, due to multiple scattering. In the mixture with a higher proportion of rocks, absorptions are more pronounced, and reflectance intensity is lower. Thus for rocky structure the element size (of gravels and rocks) is important, this factor mainly adds variations to the reflectance levels. Simple linear model does not take into account the size of the rocky elements, therefore inconsistencies between modeled and field spectra are to be expected.

3.3 Site 6 - Group A- Two-component mixtures of highly contrasted end-members.

Mixtures with highly contrasted end-members are mixtures of dark and bright constituents. First, simple cases of two component mixtures will be presented. The dark constituent in our case is chert, which shows high iron oxides content. The masking effect of iron oxides with respect to more neutral silt will be tested in a natural field environment, since this effect has been proven to have a strong influence in mixtures of powders, as observed at micro-scale in empirical studies (see chapter 1 p.19).

For this group, are presented mixtures that are combinations of a dark constituent (dark chert), containing a high amount of iron oxides (see chapter 2, paragraph 2.7.3) on a bright substrate (silt) composed of quartz (spectrally neutral) mixed with clays. Hematite and goethite (iron oxides) content in cherts may vary from rock to rock as a result of different weathering level. If

difference in chert composition can be easily accessed from their spectral signature, they are not always visually distinguishable on digital photographs. However, from spectra, differences between cherts are distinguishable, since these differences are resulting from goethite and hematite content, that have specific absorption features. In current group of mixtures, all types of cherts were classified to one class of dark cherts.

3.3.1 Cases presentation

	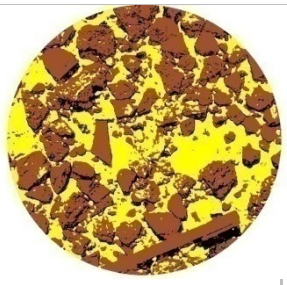	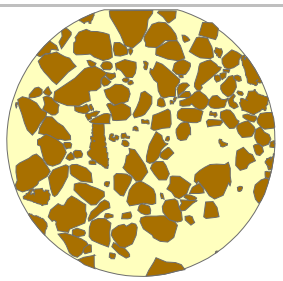	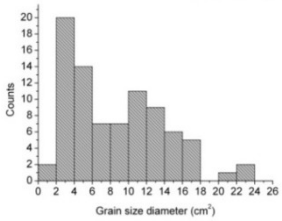
2184	Classification map	Chert	Element size distribution
	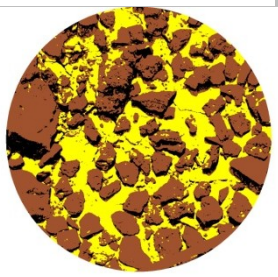	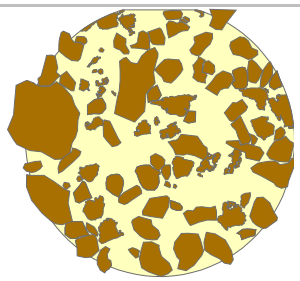	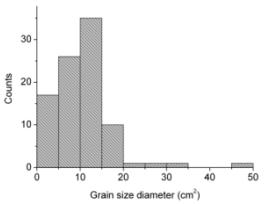
2185	Classification map	Chert	Element size distribution
	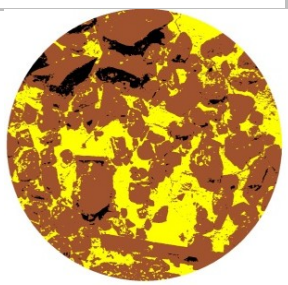	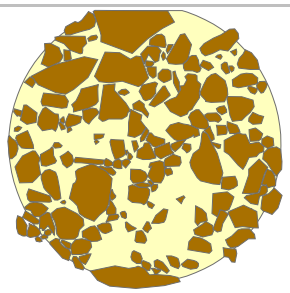	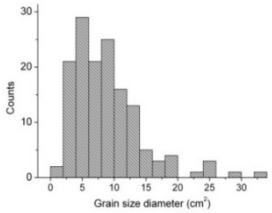
2187	Classification map	Chert	Element size

			distribution
	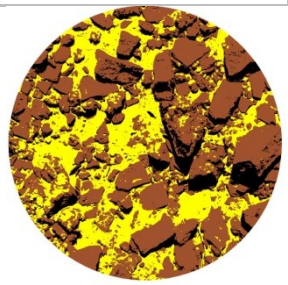	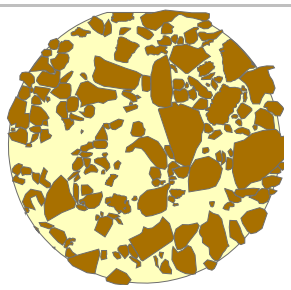	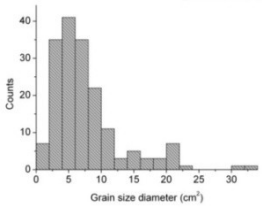
2188	Classification map	Chert	Element size distribution
		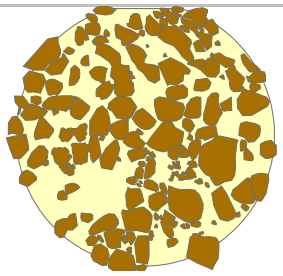	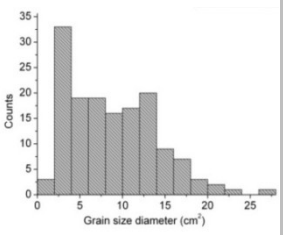
2189	Classification map	Chert	Element size distribution
	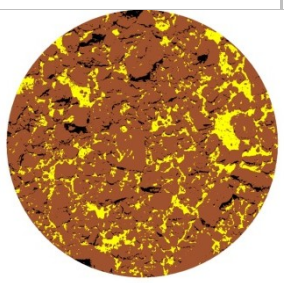	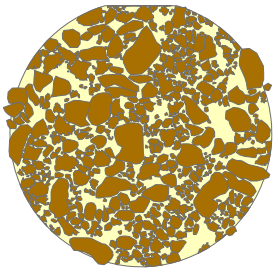	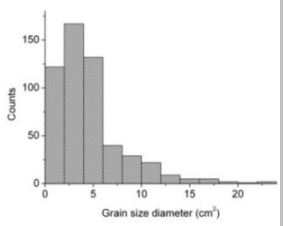
2190	Classification map	Chert	Element size distribution
Chert	Silt	Shadow	

Figure 3.9 – Field mixtures, classification maps and element size distribution of mixtures of site 6, groupA.

The proportion of chert in this group of mixtures varies from case to case, from low in cases 2185 and 2188 to high in cases 2187, 2189 and 2190 (Table 3-3).

Table 3-3 – End-member abundances, mixtures of site 6, group A.

ID	Silt%	Shadow%	Chert%	Classification Accuracy%
2184	34.98	12.50	52.52	99.00
2185	37.68	15.52	55.20	96.00
2187	36.24	5.19	58.56	99.00
2188	31.68	17.47	50.85	98.00
2189	29.99	12.64	57.36	98.00
2190	25.04	5.50	69.45	98.00

Estimates of % coverage have to take into account abundance of all the constituents including shadow, and accuracy of the classification is high. Size distribution plot for each scene is provided in figure 3.9, full statistics on element size can be found in annex.

In case **2184** abundance of chert is high, 52.5 %, element size is about 8 cm^2 in average, this is not a very coarse size compared to other cases. A high standard deviation of element size points to the variability of boulder sizes, which vary from small gravels to large boulders. Silt abundance is about 35%. Classification results and size distribution plots are shown on figure 3.9.

In case **2185** abundance of black chert is 55.2 %, silt, 38 %. In this mixture, elements of cherts are coarser, with an average size of 10 cm^2, which is coarser than in the previous case. The maximum boulder size is found in this scene and reaches 45.35 cm^2. The scene and its classification map are shown on figure 3.9.

In case **2187** there is a high amount of cherts (59%), the silt abundance amounts to 36%.The element size of cherts is 9 cm^2 in average, with coarse elements present, but a higher quantity of small elements. The standard deviation of element size is 7.73 cm^2.

In case **2188** the chert content is 51%, silt, 32%. The average element size of chert is 7.6 cm^2, which is the smallest average compared to others, and the standard deviation is 6.13. There are smaller variations in element size, meaning that elements are about the same size, which can be visually observed on the picture.

Case **2189** is composed of chert (57%), and silt (30%). Theboulder size of cherts is about 9 cm^2 in average, the standard deviation is 8.24, meaning that there are size variations in this scene.

In case **2190** chert almost covers the entire field of view (70%), while proportion of silt is about 25%. However, element size for chert is smaller, 4.6 cm^2 in average, the standard deviation of element size is the lowest 3.65 compared to other cases, meaning that size distribution is quite homogeneous.

3.3.2 Spectral characteristics

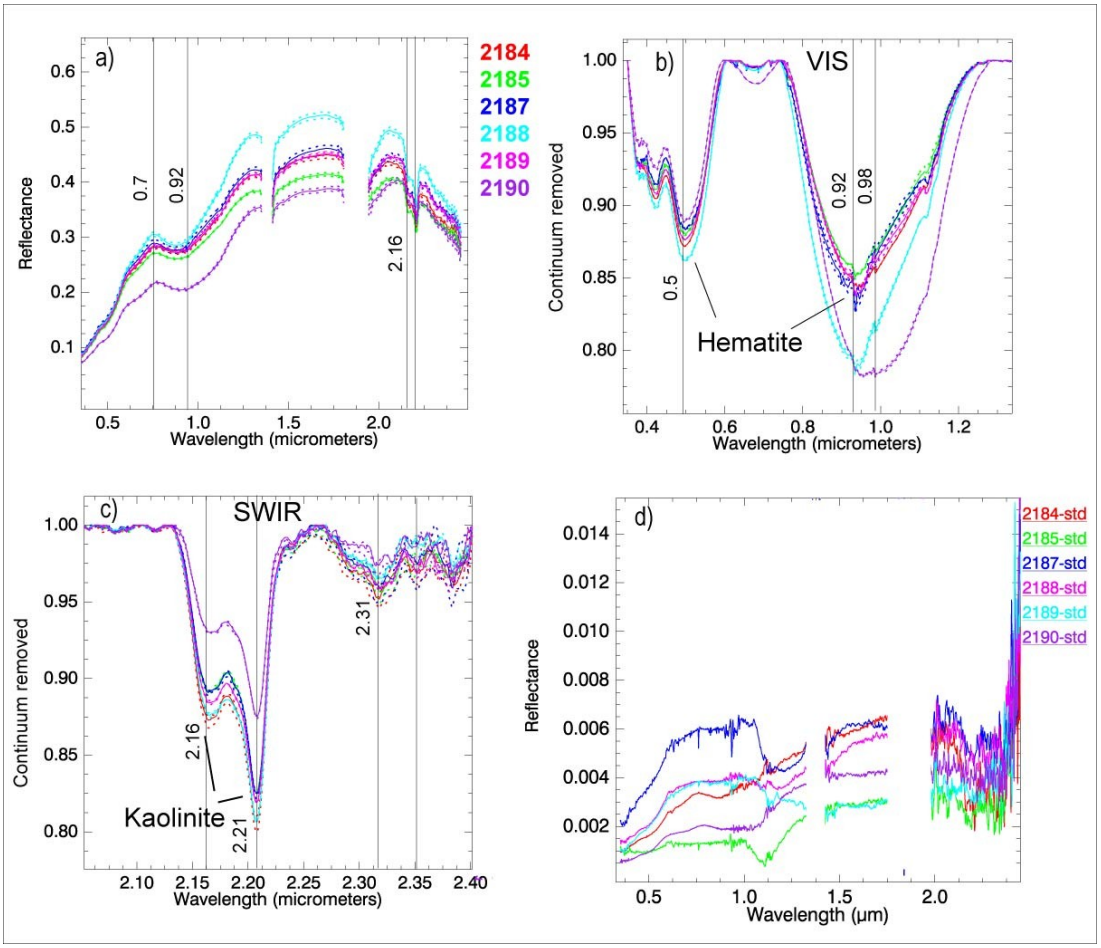

Figure 3.10 – Field spectra of mixtures, group A, site 6: a) spectra of the scenes; b) VNIR continuum removed; c) SWIR continuum removed; d) standard deviation of field spectra .

Spectra of group A are shown on Fig. 3.10, full spectral range (a), continuum removed VNIR (b), continuum removed SWIR (c), and standard deviation of field measurements (d): the values of are low, less than 0.1%, spectra become noisier at the end of the SWIR.

From the observed mixtures, the highest reflectance level belongs to case **2188**. In this case silt abundance is relatively high (51%), and chert content is relatively low (32%), compared to other

mixtures. Absorption of hematite is located at 0.92 μm, with a negative asymmetry, and is well pronounced. Element size of cherts is relatively small, many small gravels can be observed in the scene, the average size 7.6, ±6.13 cm^2. The lowest reflectance was acquired for case **2090**. In this case chert is a dominant end-member, it almost covers the entire field of view (70%), while the amount of silt is about 25%. Absorption of iron oxides, around 0.96 μm, is the deepest in this case. Cherts in this scene are rich in iron oxides of goethite type, as shown by the absorption minimum, located at 0.96 μm. In case **2188** absorption of iron oxides has a minimum at 0.95 μm, which is well pronounced and is asymmetric; the minimum is shifted toward shorter wavelengths, which indicates hematite (Fig. 3.10 b). The absorption feature at 0.4-0.6 μm is also asymmetric, with a minimum at 0.5 μm which is also an indicator of hematite. In cases **2184**, **2185**, **2187** and **2189,** the depths of iron oxides absorptions are in the same range. These mixtures have approximately similar proportion of chert.

The double absorption of kaolinite at 2.16-2.2 μm has the same strength in all cases excepting case **2190**. Absorption at 2.2 μm is relatively weak in case **2190** compared to other scenes; this mixture contains less silt, therefore less kaolinite. Absorption of dolomite at 2.31 μm originates from dolomite in cherts, so in mixtures with higher chert content it becomes deeper; however this absorption is not very pronounced for all observed cases.

Table 3-4 – Absorption features of field scenes, site 6, group A.

Case ID	Min wvl 0.44-0.61	Min wvl 0.73-0.99	Abs area 0.95	Abs area 2.2	Asymmetry 0.95	Abs. depth			
						0.42	0.48	0.95	2.2
2184	0.497	0.942	0.043	0.010	-0.011	0.095	0.118	0.156	0.162
2185	0.498	0.934	0.040	0.009	-0.011	0.089	0.110	0.146	0.142
2187	0.499	0.935	0.043	0.009	-0.009	0.085	0.106	0.160	0.141
2188	0.498	0.935	0.058	0.010	-0.012	0.100	0.127	0.208	0.157
2189	0.498	0.935	0.043	0.009	-0.012	0.091	0.114	0.158	0.147
2190	0.498	0.960	0.067	0.006	-0.017	0.074	0.100	0.217	0.098

3.3.3 Linear mixing (direct modeling)

Direct modeling is a linear (areal) combination of end-members using abundances which were derived from classification maps. In observed group only fractions of the two end-members were taken into account, excluding evaluation of shadowing and other non-linear effects (shadow was

identified as a separate end-member). Spectra of end-members used for modeling are shown on figure 3.11, full spectral range and continuum removed of VIS and SWIR.

The resulting modeled spectrum was compared to the field spectrum, as shown on fig. 3.12. Linear model shows good results for predicted cases. The albedo levels correspond well to the field mixtures, however for most of the cases the model predicts a higher albedo than what was measured in the field. The estimation of spectral shape in the VIS is better than in the NIR. In the NIR, the model predicted higher slopes for cases 2184, 2185, 2187, 2189 and 2190. The difference between model and field spectra is lower in cases 2184, 2185 and 2187, while in cases 2189 and 2190 the difference is higher. Absorptions in the visible related to iron oxides are overestimated in all cases except 2188, for which the model predicted a deeper absorption of hematite with a minimum at 0.90 µm (Fig. 3.12). However, in the field, the absorption has a minimum at 0.94 µm which corresponds to goethite. In the SWIR absorption of kaolinite was overestimated in cases 2185, 2187, 2189 and 2190. Cases 2189 and 2190 are mixtures with dominant chert content, field reflectance of these mixtures is lower than was estimated by linear modeling. In these cases, dark constituents influenced more, than the range of their abundances. Absorptions of iron oxides in modeled spectra are more influenced by hematite (left asymmetry), their depth is slightly overestimated.

In case 2188, model prediction is close to the field data spectral shape and reflectances are very similar. Absorption in the VIS corresponds well but a small shift toward longer wavelengths is observed. In the SWIR a very good fit for the kaolinite absorptions is observed. In this case the content in chert is lower than in other cases.

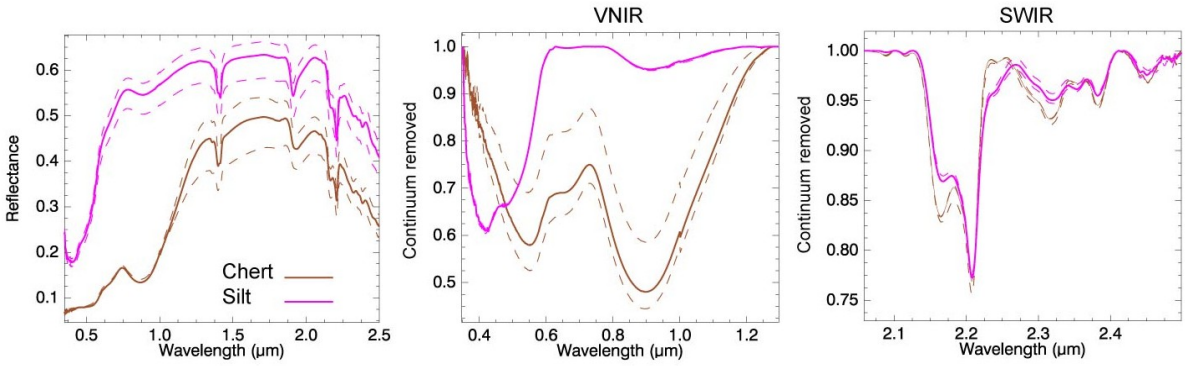

Figure 3.11 – Spectra of end-members used for model , +/- std is shown with dashed lines.

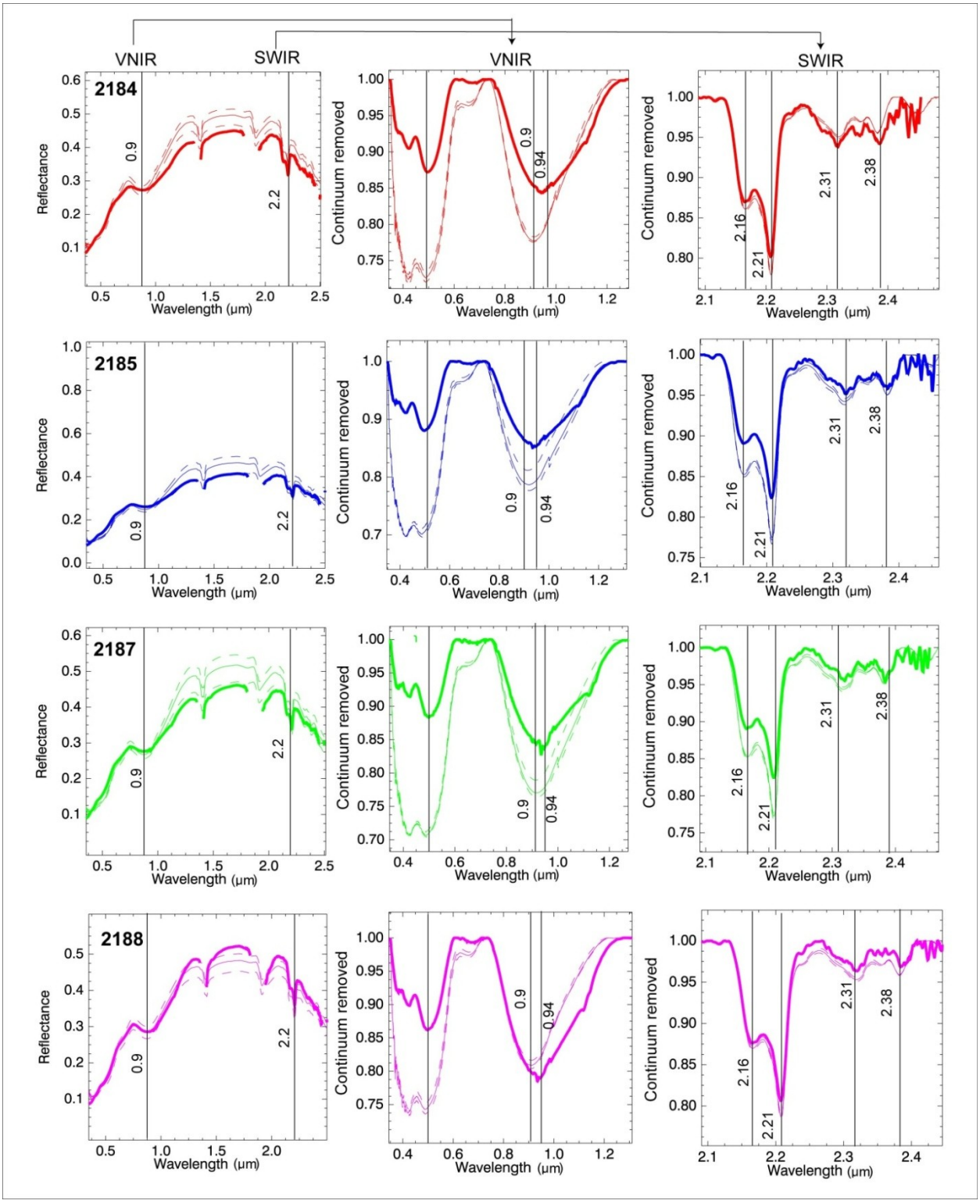
VNIR
SWIR
VNIR
SWIR
2184
2185
2187
2188
Reflectance
Continuum removed
Wavelength (μm)
0.9
2.2
0.94
2.16
2.21
2.31
2.38

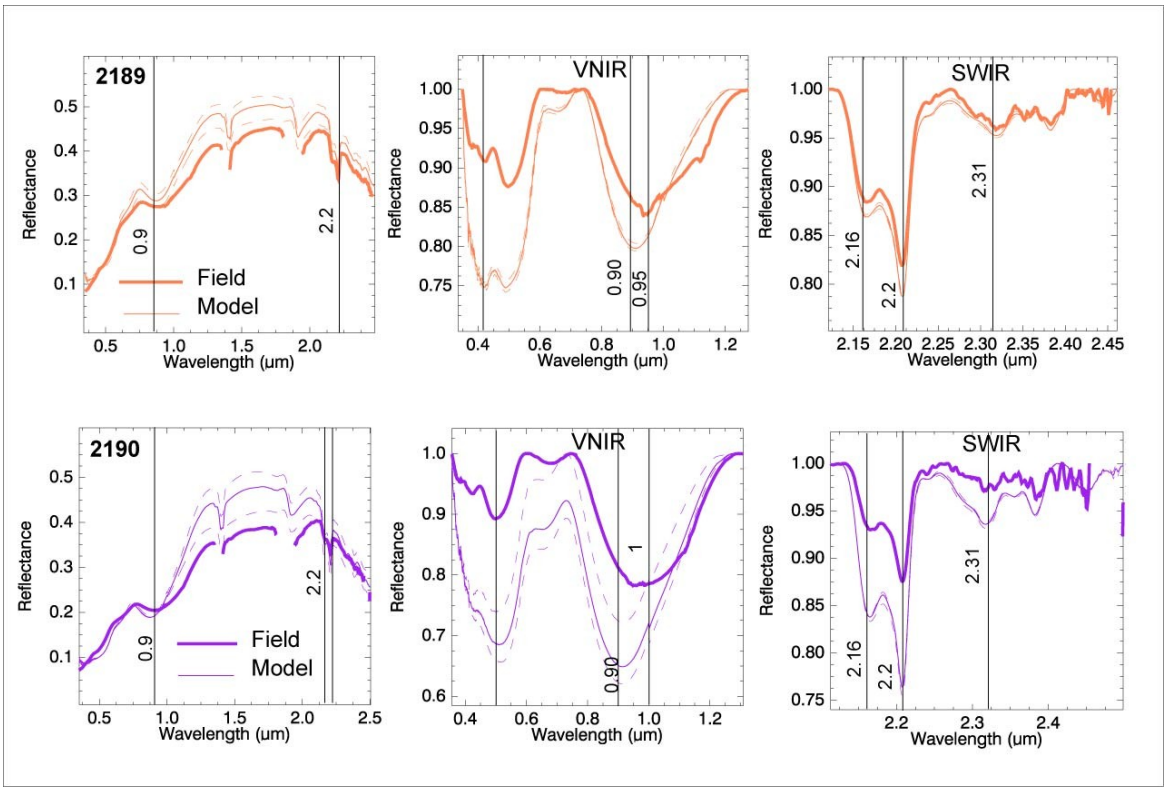

Figure 3.12 – Modeled spectra compared to the field spectra, dashed lines show modeled spectra +/- std, mixtures of group A, site 6.

Formulas for linear mixing (direct modeling):

2184 = *(0.3498 * Sp $_{Silt}$) + (0.5252 * Sp $_{Chert}$)*

2185 = *(0.3768 * Sp $_{Silt}$) + (0.5520 * Sp $_{Chert}$)*

2187 = *(0.3624 * Sp $_{Silt}$) + (0.5856 * Sp $_{Chert}$)*

2188 = *(0.3168 * Sp $_{Silt}$) + (0.5085 * Sp $_{Chert}$)*

2189 = *(0.2999 * Sp $_{Silt}$) + (0.5736 * Sp $_{Chert}$)*

2190 = *(0.2504 * Sp $_{Silt}$) + (0.6945 * Sp $_{Chert}$)*

3.3.4 Difference Analysis (DA)

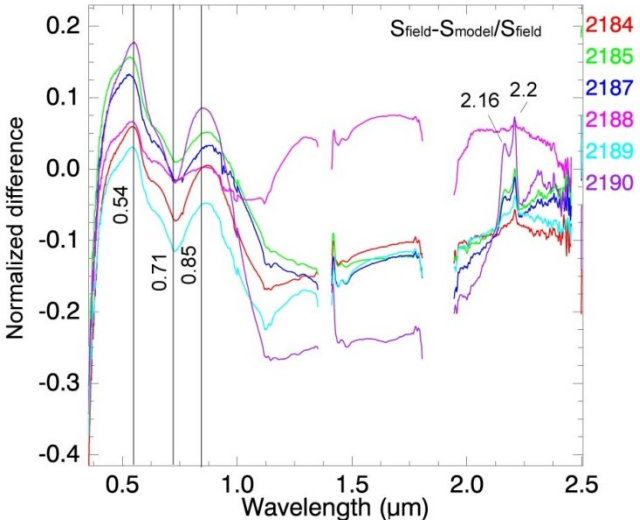

Figure 3.13 – Normalized difference between field and modeled spectra.

Difference between modeled and field spectra is shown on fig. 3.13. The difference is positive in the VIS and negative in the NIR. In the SWIR, the difference is relatively low, and its values are close to 0. The peaks or trough at 0.54, 0.71 and 0.85µm result from differences in the predicted content in iron oxides: estimation of the type of iron oxide and of their quantity did not match. Difference in the NIR is negative in all cases except case 2188, for which prediction by the linear model in the NIR was higher than what was observed in the field. Slopes of modeled spectra in the NIR are higher than in the field. Continuum and slopes of mixture spectra in the NIR are lower than linear model prediction. Supposedly, chert lowered reflectance more than its proportion would indicate. This effect is highlighted in case 2190, where chert covers almost the entire scene. As a result, reflectance is low. In the ND spectrum, negative values in the NIR indicate the highest difference between the model and field spectrum. Differences in iron absorption position between model and field spectra could be due to the fact that the sample of chert collected in the field was rich in hematite and was not representative of the field general situation, since for example in goethite absorption was observed in the field for cases 2189 and 2190.

3.3.5 Spectral un-mixing- inverse modeling

Spectra of end-members were used as inputs to the un-mixing algorithms. The resulting proportions were compared to that estimated from the pictures. Both linear and non-linear un-mixing were applied, the result is shown on figure 3.14.

Linear and non-linear un-mixing predicted both constituents, chert and silt, however linear un-mixing predicted result that matches better field abundances. Non-linear algorithm slightly overestimated silt content in the mixtures, and estimated less chert. In this case, the non-linear algorithm was less effective than the linear. Variations related to samples heterogeneity are not very high, and do not overcome 10% in abundance prediction.

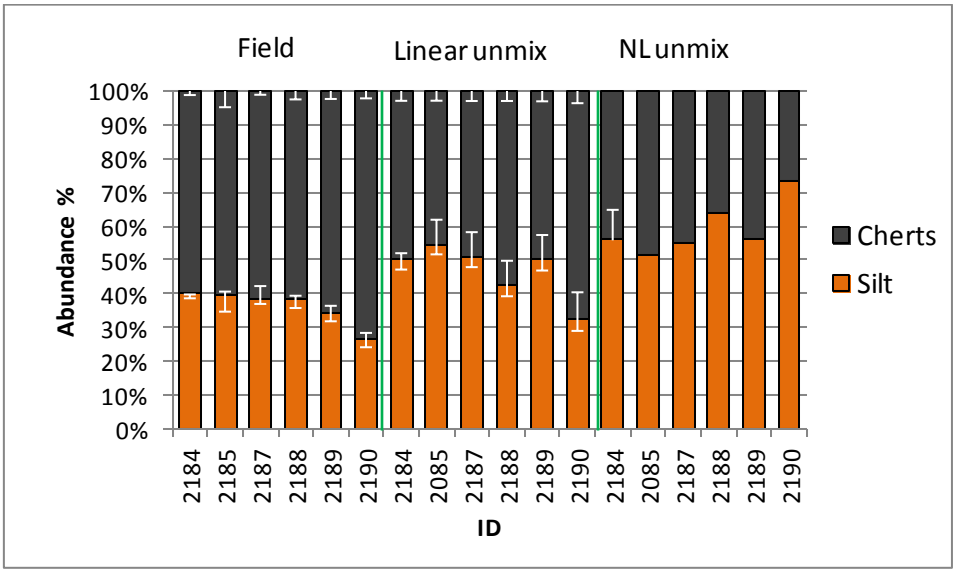

Figure 3.14- un-mixing result of group A, site 6: linear and non-linear un-mixing, compared to the field abundances.

Table 3- 5 – RMSE, of un-mixing result.

Linear un-mixing					
2184	**2085**	**2187**	**2188**	**2189**	**2190**
0.0089	0.0115	0.0126	0.0101	0.0136	0.0236
Non-linear un-mixing					
2184	**2085**	**2187**	**2188**	**2189**	**2190**
0.0086	0.0085	0.0099	0.012	0.0112	0.021

The RMSE is lower for non-linear un-mixing result, however predicted abundances are closer in linear un-mixing.

Observation of this group of mixtures showed that a linear model can be used to represent these field mixtures, however different measurement conditions, samples heterogeneity, element size and shadow introduced non-linear effects into the spectra. In the cases where these factors are minimal, the linear model gave the best fit. Difference analysis pointed to spectral regions where the main differences between linear model and field spectra were observed. Difference in reflectance intensity was observed in the SWIR, while differences that could be attributed to composition were found mainly in the VIS and related to iron oxides content. Iron oxides absorption was overestimated in some cases and asymmetric due to hematite, while in the field more goethite was observed. This effect may be caused by chert heterogeneity in the field and non-conformity between laboratory chert sample and field chert. In general, the linear model was good enough for direct modeling and inverse modeling (un-mixing), since it showed better predictions than a non-linear method.

3.4 Site 7, group B - mixtures of low-contrast constituents.

This group of mixtures is located in the kaolinite quarry (Site 7); these scenes are composed of fine fractions of kaolinite-rich silt, bright boulders of sandstones and some cherts, mostly coated with fine particles. Mixtures of this group are mixtures of bright constituents, therefore there is a low contrast between the end-members, rocks and fine fraction are approximately of similar color, however low quantity of weathered cherts are still present. Manual classification was applied for this group, because automatic classification was not effective to separate end-members from each other, due to coating by fine particles (Fig. 3.15). The dominant composers of the mixtures are sandstones, which are also coated with fine particles. Cherts do not appear here in high abundance as they were in the previous groups, therefore iron oxides are a minor fraction.

3.4.1 Cases presentation

<table>
<tr><td>  </td><td>Cherts
 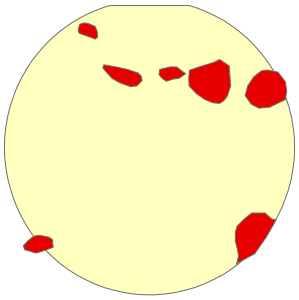 </td><td>Sandstones
 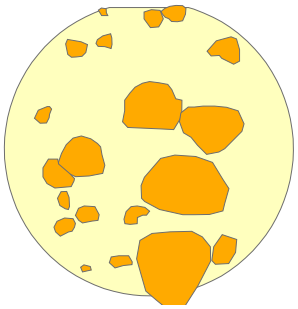 </td></tr>
<tr><td>2205</td><td>Element size distribution (cm)
 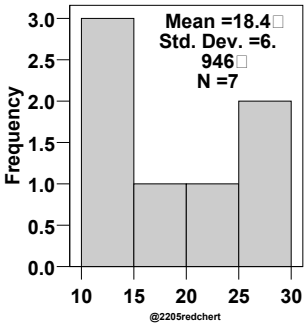
</td><td>Element size distribution (cm)
 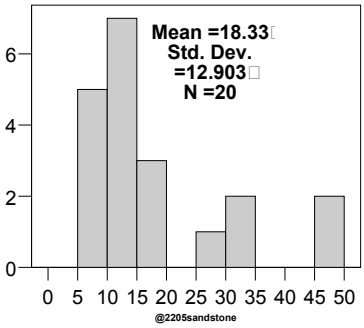
</td></tr>
<tr><td>  </td><td></td><td>Sandstones
 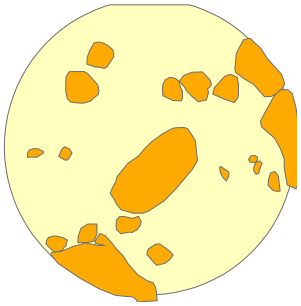 </td></tr>
<tr><td>2206</td><td></td><td>Element size distribution (cm)
 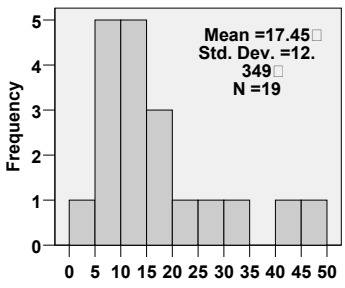
</td></tr>
</table>

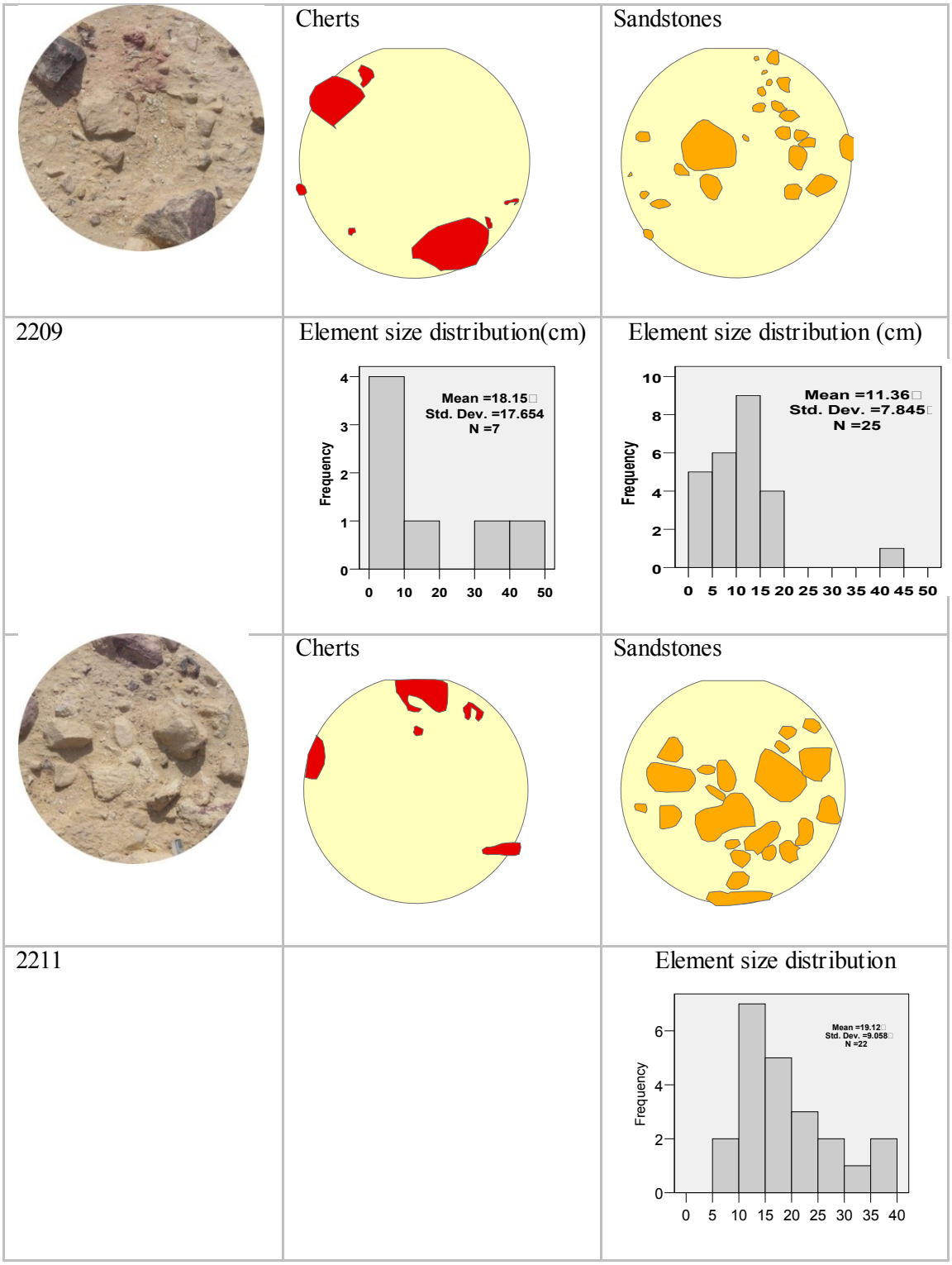

Figure 3.15 – Field cases and classification maps of site 7, group B.

Table 3-6 – End-member abundances of group B, site 7.

	Chert %	Sandstone %	Silt %	Classification accuracy %
2205	7.58	28.16	64.27	95.00
2206		24.31	75.69	95.00
2209	11.9	13.41	74.69	95.00
2211	6.21	27.82	65.97	95.00

End-member proportions derived from classification are shown in table 3-6.

Case **2205** is mostly composed of silt (64.27%) and sandstones (28.16%), chert content is low (7.58%). Element size of sandstones is medium-coarse – the average size is 18.3 cm^2, standard deviation is high (12 cm^2), meaning that in the field there are small and coarse elements.

Case **2206** is mostly covered by silt (76 %), silt covers also sandstones as a thin layer, sandstone proportion in the mixtures is 24%. The element size for sandstone is coarse (17.45 cm^2), the maximum element size is 48 cm^2.

Case **2209** is composed of sandstones (13.4%), cherts (11.9%) and the dominant end-members is silt (75 %). Sandstones are of relatively small size, 11 cm^2 in average. Elements of chert are relatively coarse (18 cm^2).

Case **2211** is composed of sandstones, with a relatively high content (28%), element size of which is medium-coarse (19 cm^2); as can be observed in the picture, sandstones are coated with silt, the dominant end-member in this mixture is silt (66%).

The highest abundance of sandstone is for cases 2205 and 2211, while for cases 2206 and 2209 the dominant fraction is silt.

3.4.2 Spectral characteristics

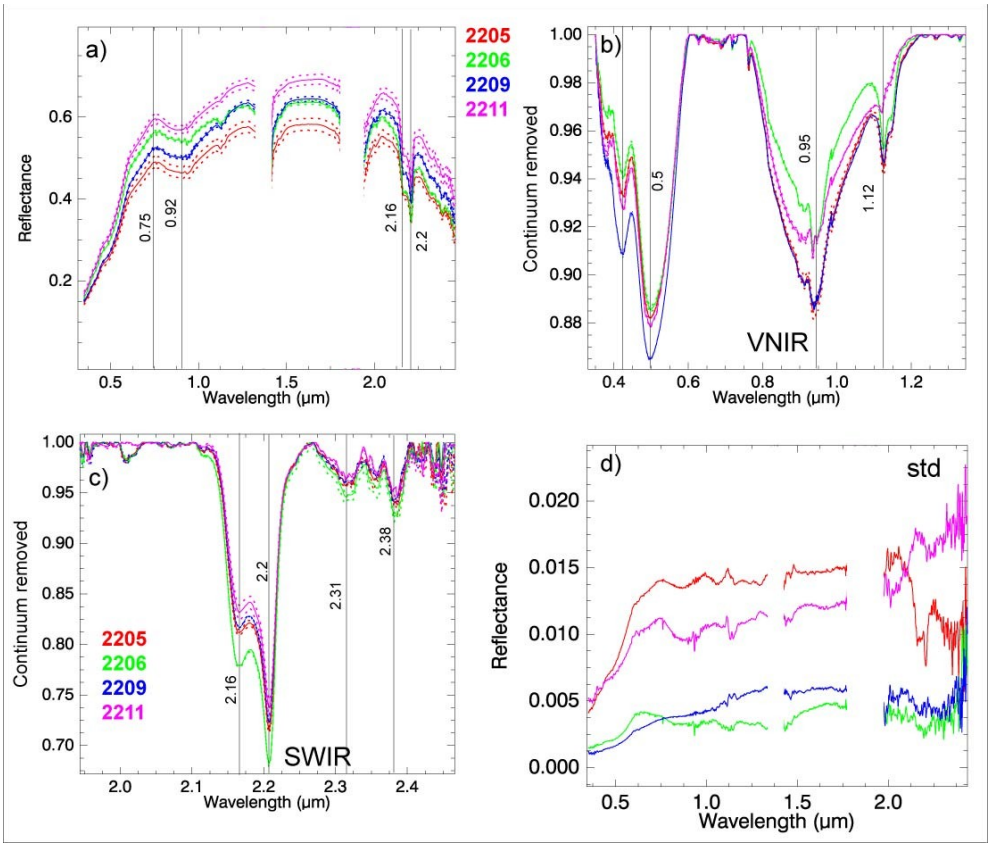

Figure 3.16 – Field spectra of group B, site 7.

Field spectra of the group are shown on fig, 3.16, full spectral range (a) and absorptions in continuum removed (b, c). Standard deviation of field measurements is shown on fig. 3.16 (d). For most of the cases, the standard deviation is less than 1 %, except for case 2205, where it is about 1.5%.

Cases 2211 and 2206 have the highest albedo (Fig. 3.16). These mixtures are bright, composed of silt and sandstones, and red cherts are almost absent. Even though red cherts are not contributing to these mixtures, absorption of iron oxides is observed (with a minimum at 0.95 µm), corresponding to hematite. This means that iron oxides are present in silt as free particles and in sandstones. However, compared to other cases (composed by cherts), this absorption is significantly weaker. Double absorption at 2.16-2.2 µm is caused by kaolinite, silt has a high kaolinite content (as free particles). As a result this absorption is deeper in the cases where silt abundance is higher, as this is expected from the spectra of samples. In case 2205 albedo is relatively low, this mixture contains cherts and sandstones, and boulders of composing

constituents are coarse. Absorption of hematite at 0.95 µm is well pronounced. Kaolinite absorption in the SWIR is deep for all mixtures of the group (Fig. 3.16 c), it reaches about 30%, due to very high kaolinite content.

Table 3-7 – Absorption features of field spectra, site 7, group B.

ID	Min wvl 0.7-1.2	Assymetry 0.95	Abs area 0.9	Abs area 2.2	Depth 0.42	Depth 0.48	Depth 0.9	Depth 2.21
2205	0.936	-0.002	0.025	0.016	0.066	0.105	0.116	0.275
2206	0.936	-0.001	0.017	0.019	0.057	0.1	0.089	0.308
2209	0.94	0.001	0.026	0.016	0.091	0.123	0.114	0.268
2211	0.935	0	0.02	0.015	0.07	0.108	0.092	0.253

3.4.3 Linear mixing-direct modeling

Modeled mixtures were computed from spectra of the end-members collected in the field using linear (areal) proportions derived from classification maps. Spectra of end-members used for modeling are shown on figure 3.17. Field mixtures spectra have lower albedo than modeled mixtures in all cases, except mixture 2211. Linear model precisely predicted absorption of iron oxides at 0.9 µm in cases 2205 and 2209, the depth and the shape of absorption is well fitted. These mixtures have relatively small amounts of cherts. Absorptions of kaolinite in the SWIR were estimated correctly with modeling.

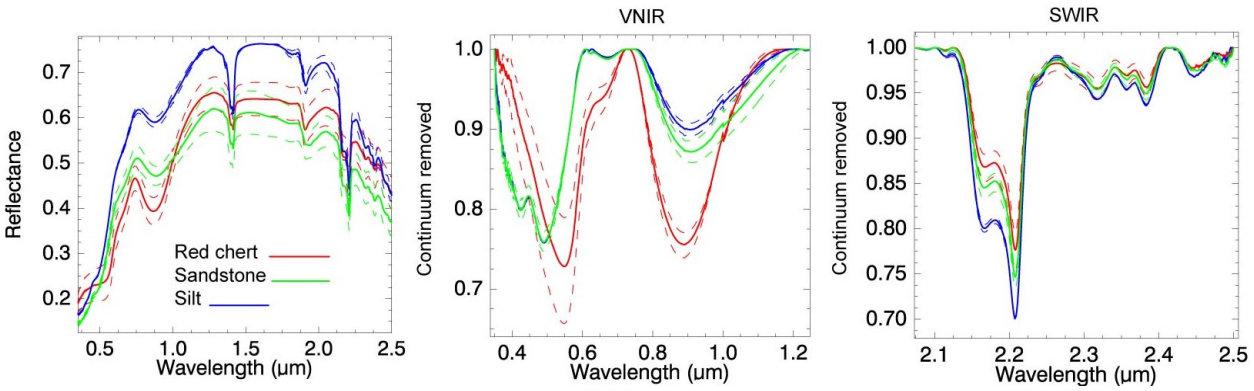

Figure 3.17 – Spectra of end-members used for model, +/- std spectra are shown with dashed lines.

Formulas used for direct modeling:

2205 = *(0.075 * Sp $_{Chert}$) + (0.28 * Sp $_{Sandstone}$) + (0.64 * Sp $_{Silt}$)*

2208 = *(0.243 * Sp $_{Sandstone}$) + (0.76 * Sp $_{Silt}$)*

2209 = *(0.119 * Sp $_{Chert}$) + (0.13 * Sp $_{Sandstone}$) + (0.75 * Sp $_{Silt}$)*

2211 = *(0.062 * Sp $_{Chert}$) + (0.278 * Sp $_{Sandstone}$) + (0.65 * Sp $_{Silt}$)*

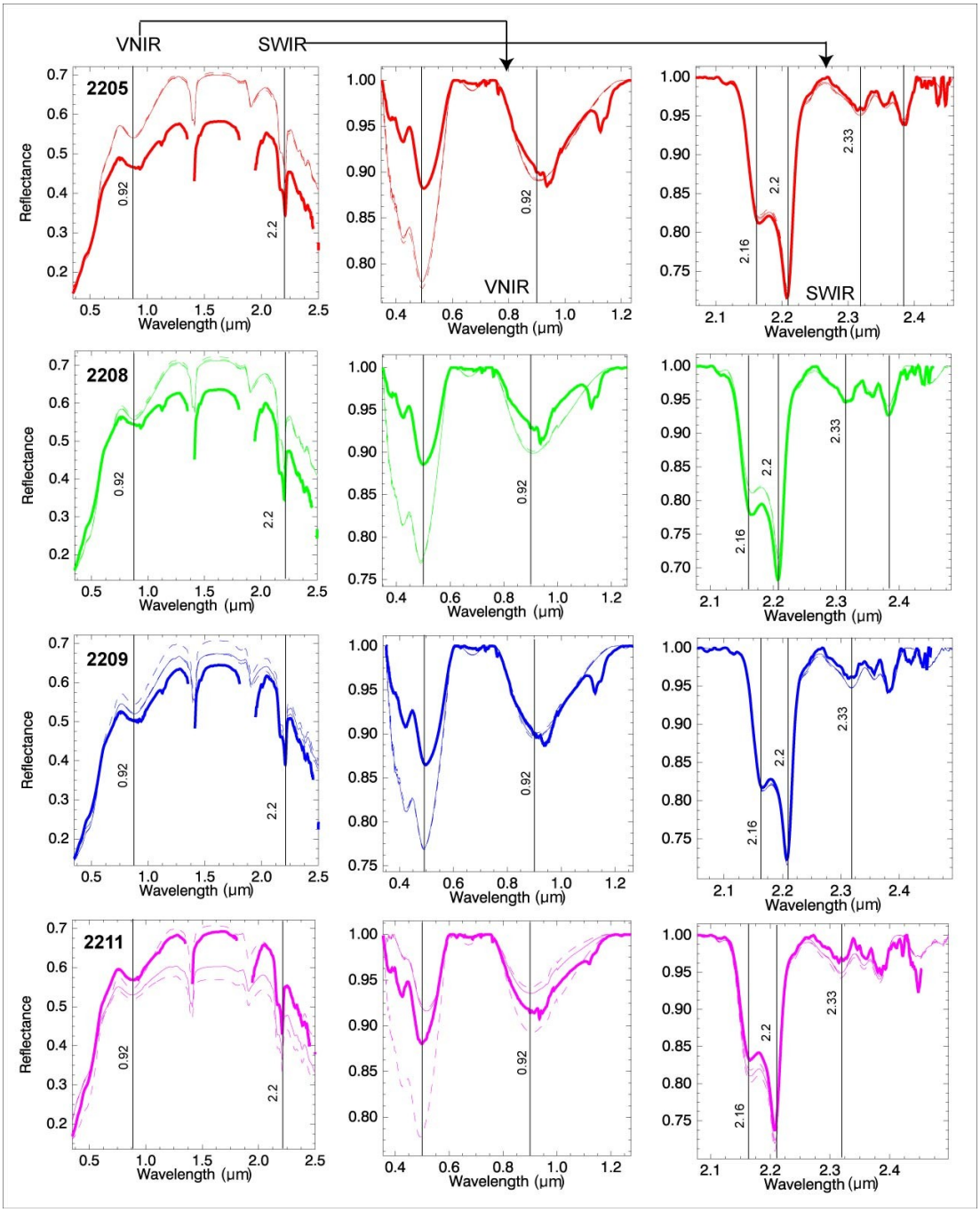

Figure 3.18 – Modeled spectra and field spectra, group B, site 7.

3.4.4 Difference analysis (DA)

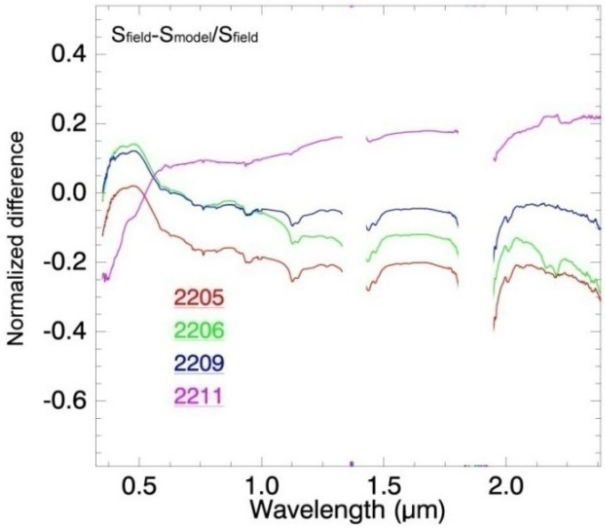

Figure 3.19 – Difference spectra between field and modeled spectra, formula is shown.

The normalized difference between modeled and field spectra is shown on fig. 3.19. For most of the cases the difference was negative, which means that reflectance in the field was lower than the model prediction. Only in case 2211 is the difference positive, which means that the field reflectance spectrum was higher than the average model prediction, as can be observed on figure 3.18. The difference closest to 0 was obtained for case 2209, for which the model prediction was close to the field spectrum. In cases 2205, 2209 and 2213, the difference between model and field spectra is higher in the beginning of the visible and lower in the NIR and SWIR. This result can be due to shadow, which lowered the reflectance in the SWIR and was not accounted for by the linear model.

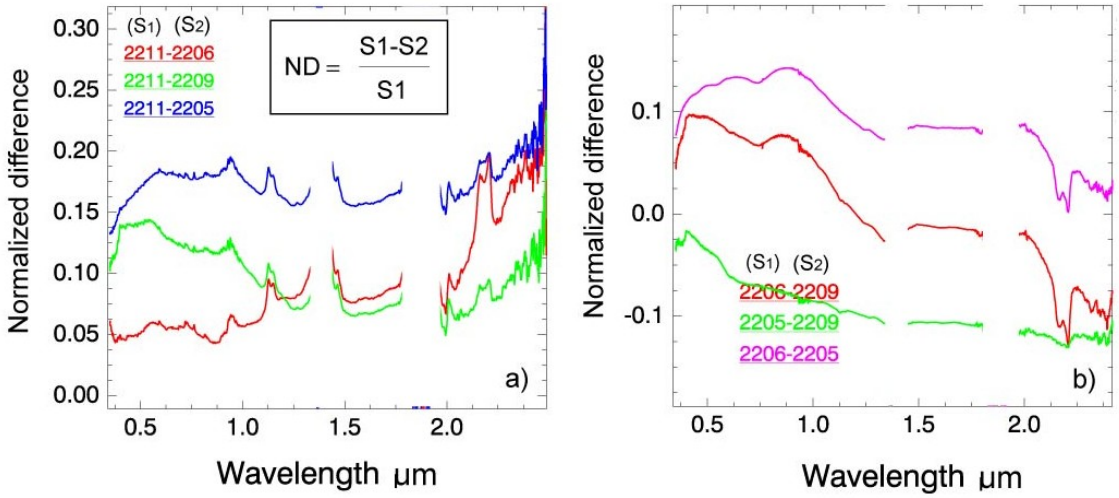

Figure 3.20 – Difference spectra of field cases: two types of shapes were defined.

If we calculate differences between field mixtures (Fig. 3.20), two groups of ND can be defined, based on their shapes (a, b). In group (a) the difference in the VIS and SWIR is equal, or in the SWIR the difference is higher than in the VIS. In this case, the differences are resulting from abundances of bright end-members (silt and sandstones). Cases 2211 and 2206 are both relatively bright; therefore their difference is small in the VIS (5%), and increasing towards the SWIR. The main reason for this is the difference in mineral composition, mixture 2206 has higher kaolinite content than 2211; this mineral has a specific absorption in the SWIR at 2.16-2.2 µm. It also has a higher abundance of fine particles. Additionally, case 2206 is mainly composed of fine silt while case 2211 is composed mostly of sandstones. In group (b) the differences between cases 2205 and 2206, and case 2206 and 2209 are higher in the visible part of the spectrum and then decrease towards the SWIR. This shape indicates a difference in contrast materials content in the mixtures, such as cherts and silt. Mixtures with higher chert content and mixtures without chert could explain this difference in shape.

Supposedly, mixtures of non-contrasted bright end-members (like sandstone and silt) have lower variations in the visible than mixtures where bright and dark end-members are mixed. In other words, if we look at mixtures that contain bright and dark end-members, and will change proportions of their constituents, we will observe most of the changes in the VIS. However, if we change mixtures proportions of non-contrasted end-members (like silt and sandstones), we will see changes generally in the NIR and the SWIR. Iron oxides have a strong influence in the VIS and NIR, therefore the continuum of a mixture with high iron oxides content will be more

influenced in the VIS-NIR than in the SWIR. If the end-member is mainly composed of kaolinite, as kaolinite has a specific absorption in the SWIR at 2.16-2.2 µm, the continuum of this end-member will be lower in the SWIR, where strong absorptions are located. However continuum has a complex behavior, which depends not only on absorption depths, but also on scattering.

3.4.5 Spectral un-mixing - inverse modeling

Spectral un-mixing results from linear and non-linear models are compared to the field fractions (Fig. 3.21). Results of linear un-mixing and fractions acquired from nonlinear prediction are very close. In both cases sandstone fraction was overestimated, and silt was underestimated. In the field, silt is a dominant fraction, but the un-mixing algorithm was not able to differentiate between silt and sandstone and to predict their abundances in correct proportions.

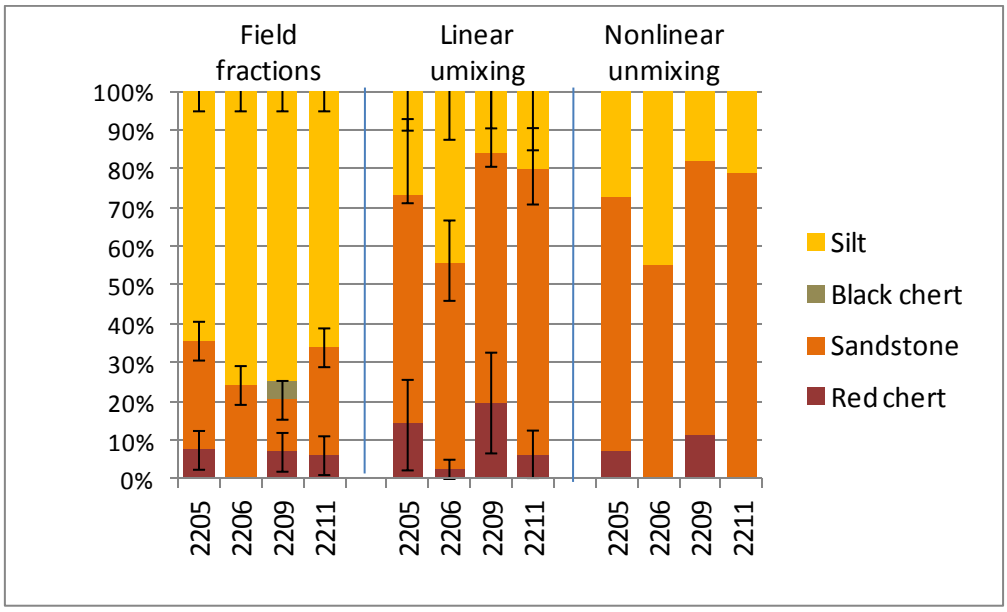

Figure 3.21 – Un-mixing result ofsite 7, group B.

Despite that, prediction of chert was close in both cases, small abundance of red chert was correctly predicted with a linear un-mixing, with a slight overestimation. There is no significant improvement of un-mixing results by non-linear transformation, however RMSE is lower in the second case.

Variations resulted from end-members heterogeneity are high and reach up to 20% in prediction result in case 2205. In other cases it varies between 10-15% from case to case.

Table 3-8- RMSE of un-mixing, site 7, group B.

Linear un-mixing				Non-linear un-mixing			
2205	**2206**	**2209**	**2211**	**2205**	**2206**	**2209**	**2211**
0.0165	0.0221	0.0192	0.0132	0.0124	0.0144	0.0137	0.0113

For this group of mixtures linear model well estimated absorption depths of the constituents, though reflectance intensity varied in part of the cases, probably due to illumination effects. In this type of mixtures, composed of non-contrast constituents such as sandstones and silt, linear model can be used for direct modeling. However such spectrally similar end-members caused to un-mixing algorpthm to misestimate their fractions. That's why special attention in mixture analysis should be paid to spectrally similar end-members. Coating by fine particles may overlay the major constituents and therefore mask their spectral characteristics, in these cases a non-linear method should be applied.

3.5 Site 1 – Group A: mixtures with high abundance of fine fraction.

This group of scenes contains mixtures for which the dominant fraction is fine particles (silt). Other constituents of the mixtures are chert and limestone and appear in small proportions and have small element sizes. Cases presentation and end-member classification maps are shown on fig. 3.22.

 2045	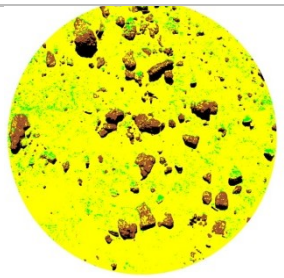 Classification map	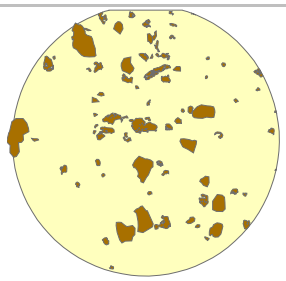 Black chert	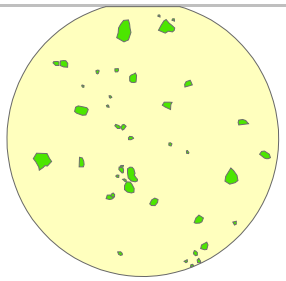 Limestone
		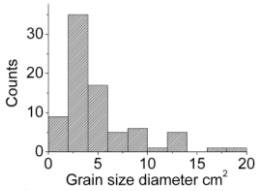 Element size distribution (cm)	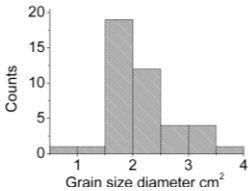 Element size distribution (cm)
 2047	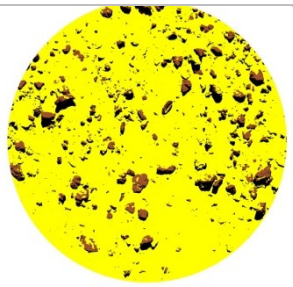 Classification map	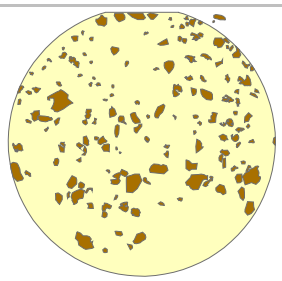 Black Chert	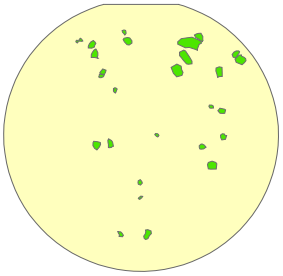 Limestone
		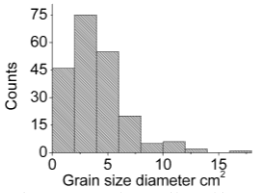 Element size distribution (cm)	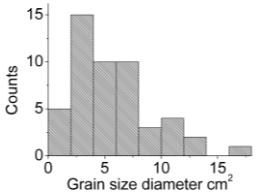 Element size distribution (cm)
 2048	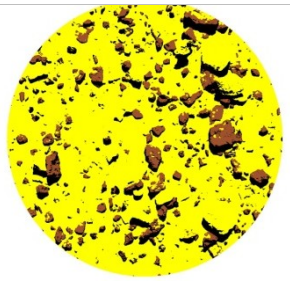 Classification map	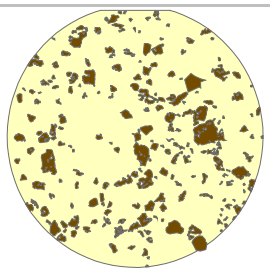 Black chert	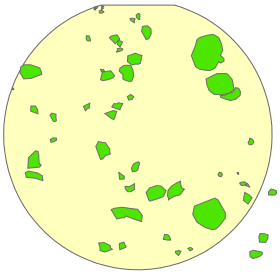 Limestone

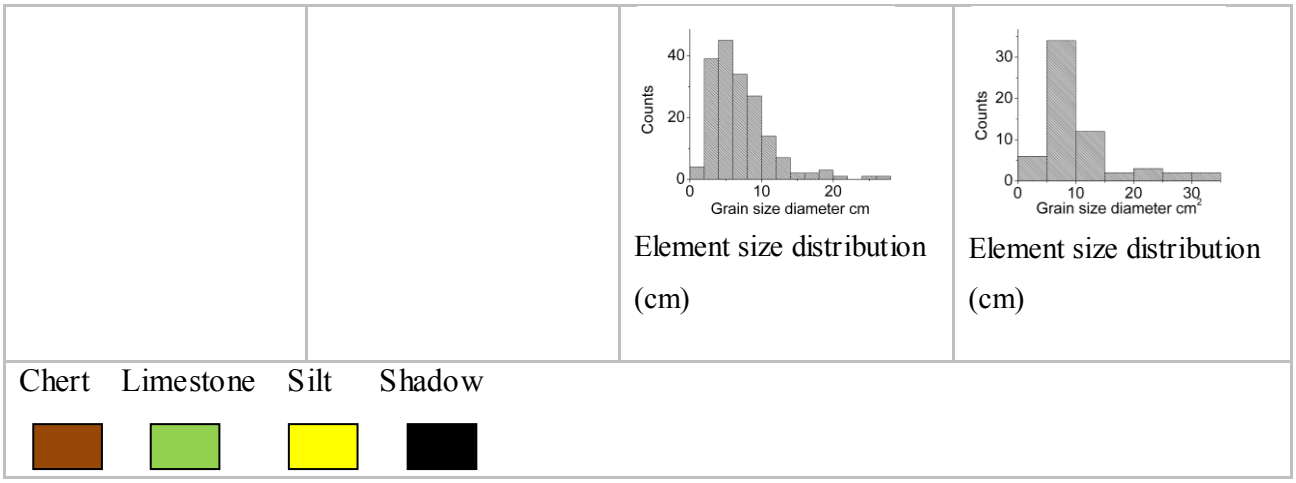

Figure 3.22 – Field mixtures and end-members classification maps of group A, site 1.

3.5.1 Cases presentation

Case **2045** is composed of silt (83%), with a small abundance of black chert (7.6%) and limestones (4%). The size distribution is not normal, there is a small quantity of coarser boulders and a higher quantity of small boulders, skewness is 1.74. The mean size of black chert is 5 cm^2, with a majority in the 2-5 cm^2 range. Limestones are less numerous than black chert, with a mean grain size smaller than 2 cm^2. Size distribution of limestones is more normal, with a skewness of 0.85. The maximum boulder size is coarser for cherts than for limestones.

Case **2047** is characterized by a higher abundance of black chert (10%) than in the previous case; however the mean size is the same as in the first case. The quantity of limestone is lower than in the previous case with only 2% (Table 3-9).

Case **2048** contains more black chert (13%) than cases 2045 and 2047 and limestone (7%). Limestone average size is coarser, the mean value being 5.7 cm^2. Distribution of cherts and limestone is not normal, skewness values are higher than 1, because there are coarser boulders in the mixture than finer ones. Since there are some shadows in the field, their proportion in the mixtures was estimated, in order to take its influence on mixture spectra into account.

Table 3-9 – End-member abundances of mixtures group A, site 1.

Case N	Black chert abundance %	Silt %	Shadow %	Limestone %	Classification
					Accuracy %
2045	7.6	83.2	5.2	4..0	92
2047	10.0	68	8.7	2.0	95
2048	13.0	68	12.0	7.0	93

3.5.2 Spectral characteristics

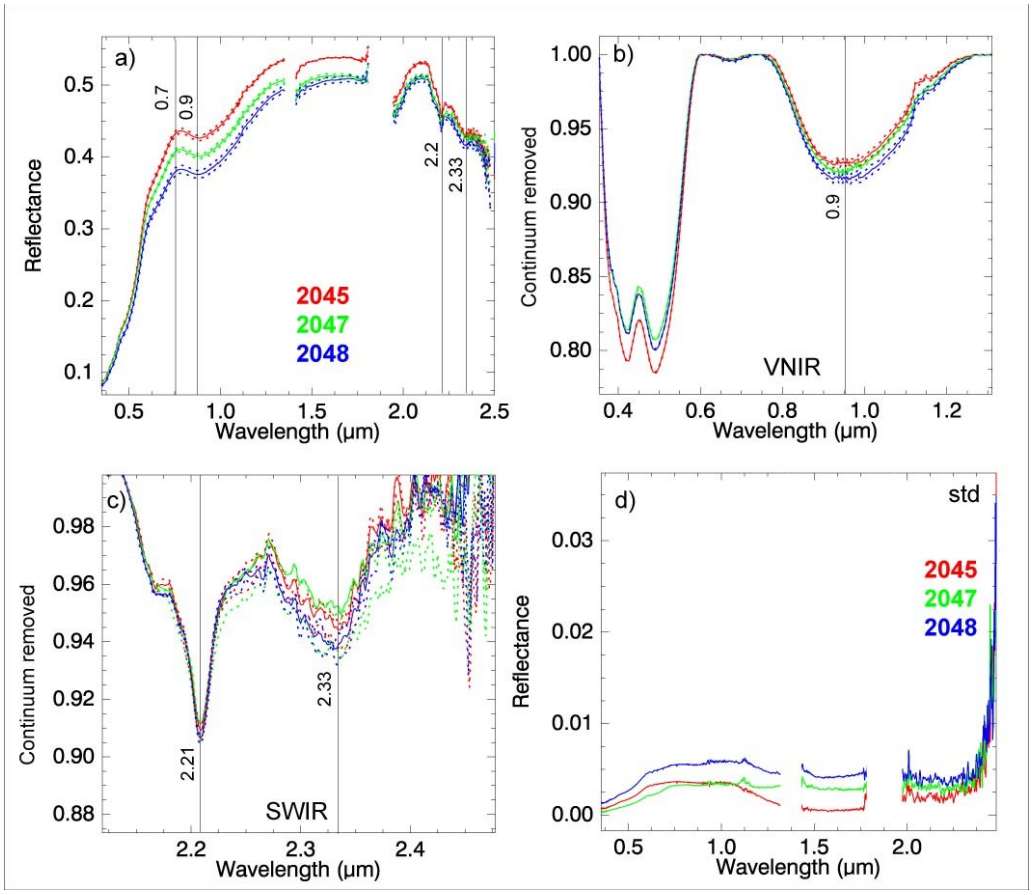

Figure 3.23 – Spectra of field mixtures of group A, site 1: a) full range spectra; b) VNIR continuum removed; c) SWIR continuum removed; d) standard deviation.

Spectra of the mixtures are shown on fig. 3.23; the standard deviation is not high and does not reach 1% (Fig. 3.23 d).

Mixture 2045 has the highest silt content; as a result its level of reflectance is higher compared to the other cases (Fig. 3.23 a). Silt is a bright material of fine grain size; as a result, due to multiple scattering, its reflectance is increased. Presence of black chert is expected to decrease reflectance (dark component), as in case 2048 which has the highest chert content and the lowest reflectance. The absorption around 0.95 µm is deeper for cases with a high amount of iron oxides, since a higher black chert content is supposed to increase this absorption because of its high concentration in iron oxides. The absorption of iron oxides is the deepest in case 2048 (Fig. 3.23 b). Absorptions of kaolinite at 2.16-2.2 µm have the same depth in all cases, and did not change with different constituents abundances (Fig. 3.23 c). Absorption at 2.33 µm of calcite becomes deeper with increasing limestone content. In cases 2045 and 2048 it is deeper than in case 2047. The depth of the absorption around 0.95 µm is about 18% in continuum removed mode for observed mixtures; the depth of the calcite absorption is 4% in continuum removed mode for observed mixtures. The 5% increase in chert content in the mixture caused an increase of 1% in absorption depth at 0.95 µm. An increase of 5% in limestone content also caused a 1% deepening of the absorption at 2.33 µm. With increasing abundances of these end-members, the depths of their specific absorptions raised equally. Table 3-10 summarizes values of specific absorption of the observed mixtures.

Table 3-10 – Absorption features of the field mixtures, group A, site 1.

Case N	Min wvl 0.73-0.99	Abs area 0.95	Abs area 2.2	Abs area 2.33	Assymetry 0.95	Absorption depth				
						0.4	0.48	0.95	2.2	2.33
2045	0.927	0.938	0.112	0.14	-0.0023	0.1951	0.2156	0.0730	0.0701	0.0527
2047	0.944	1.037	0.107	0.1	-0.0041	0.1773	0.1931	0.0791	0.0667	0.0400
2048	0.945	1.143	0.108	0.13	-0.0085	0.1769	0.1996	0.0833	0.0679	0.0489

In this group absorption minimum between 0.73 and 0.99 µm is characterized by a small shift to shorter wavelengths. In case 2045, this shift is well observed, the absorption minimum is located

at 0.927 μm (Table 3-10), and consequently this mixture contains hematite. The area of iron oxides absorption around 1 μm is weak (0.938), since chert abundance is very low in this case. However, absorption of montmorillonite at 2.2 μm is deeper in case 2045; here the relative abundance of fine particles (silt) is high. In cases 2047 and 2048, the montmorillonite absorption is weaker. Mixture 2048 has the highest amount of black chert in the group, and as a result iron oxides absorption is the deepest and has the biggest area.

3.5.3 Linear mixing – direct modeling

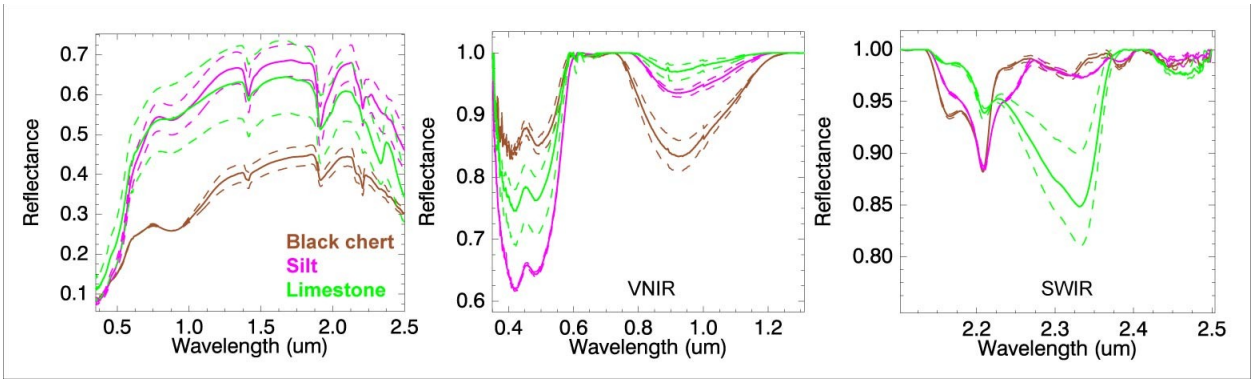

Figure 3.24 – Spectra of end-members used for model, +/- std is shown with dashed lines.

Formulas for calculation of linear model:

2045 = *(0.076 * Sp $_{B.chert}$) + (0.832 * Sp $_{Silt}$) + (0.04 * Sp $_{Limestone}$)*

2047 = *(0.01 * Sp $_{B.chert}$) + (0.68 * Sp $_{Silt}$) + (0.02 * Sp $_{Limestone}$)*

2048 = *(0.013 * Sp $_{B.chert}$) + (0.68 * Sp $_{Silt}$) + (0.07 * Sp $_{Limestone}$)*

Spectra of end-members used for modeling are shown of fig. 3.24, dashed lines indicate on samples heterogeneity due to patina, roughness and coatings.

The result of linear modeling is presented on the figure 3.25. It shows that in cases 2045 and 2048 spectra from the field have a lower reflectance compared to the modeled spectra (Fig. 3.25). The lower standard deviation of the model is closer to the field spectra than the average. In case 2047 the field spectrum fits well to the modeled linear mixture. In this mixture the amount of limestone is very low (2%), compared to mixtures 2045 and 2047, where the amount of limestone is higher. In cases 2045 and 2048 the linear model predicted a higher reflectance, although in the field limestone did not increase the reflectance to the level that was predicted. Limestone affected in a weak manner the reflectance and the shape of the mixture spectrum, but strongly affected the absorption at 2.33 μm. Absorptions of iron oxides are well represented by linear model, both their shape and their depths. These are the cases where iron oxides content was not very high, chert abundance was minor.

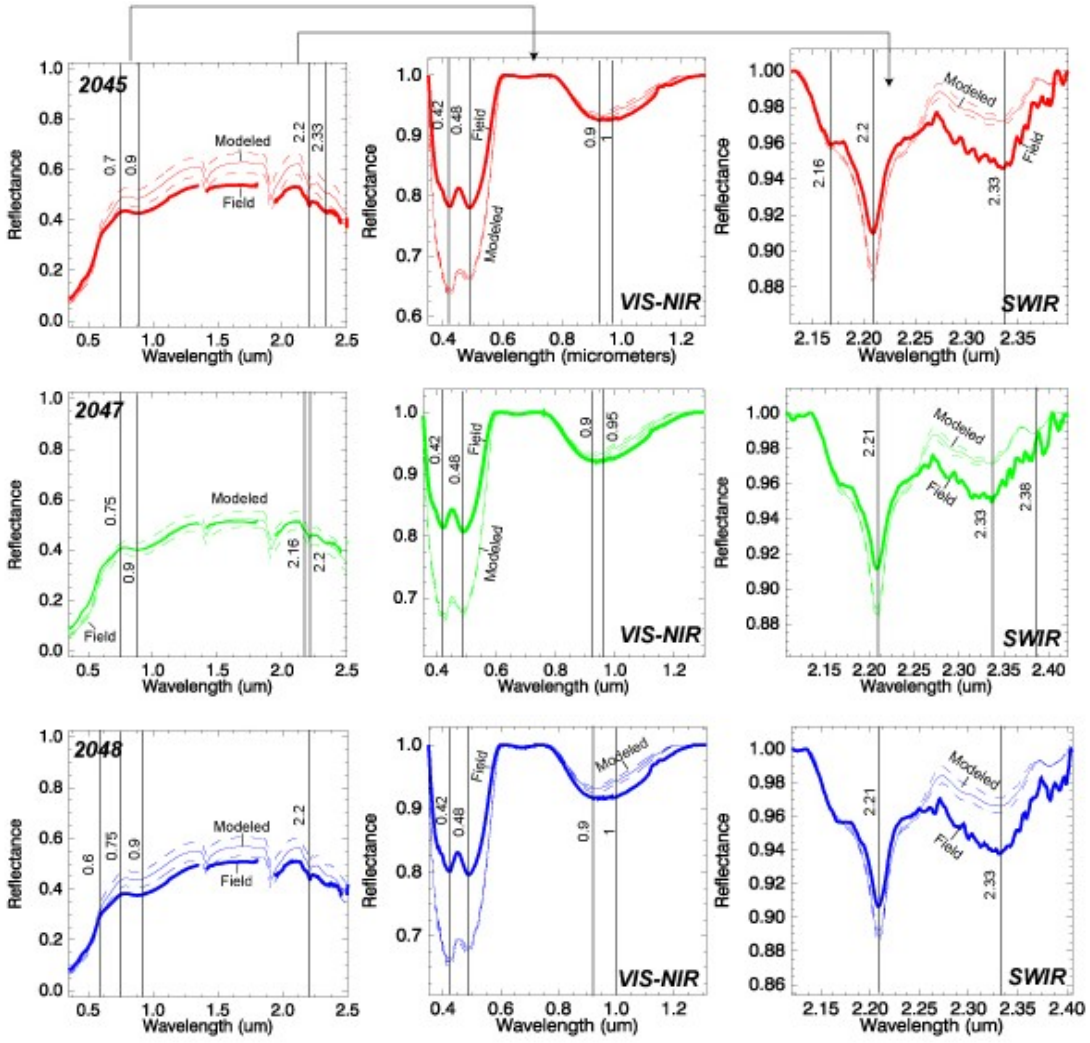

Figure 3.25 – Field spectra and modeled spectra of mixtures of group A, site 1, model std (due to sample heterogeniety) is shown with dashed lines.

3.5.4 Difference analysis (DA)

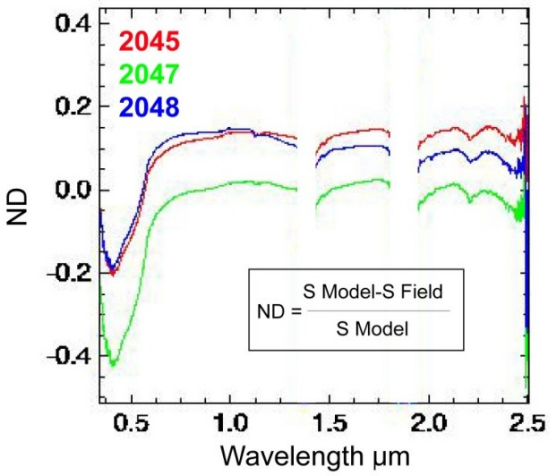

Figure 3.26 – Normalized difference between modeled and field spectra.

Difference between modeled and measured spectra is closer to 0 for case 2047 (Fig. 3.26). In cases 2045 and 2048 the difference is higher in the NIR and the SWIR. The shape of the difference spectra is quite homogeneous from the middle of the VIS, and remains on the same level till the end of the SWIR. A high negative feature is observed in the beginning of the VIS between 0.4 µm and 0.5 µm; it points to a higher reflectance in this range for the measured spectra compared to the modeled ones. The feature at 2.33 µm is under-estimated by the model.

Spectral difference was also calculated between spectra of field mixtures (Fig. 3.27).

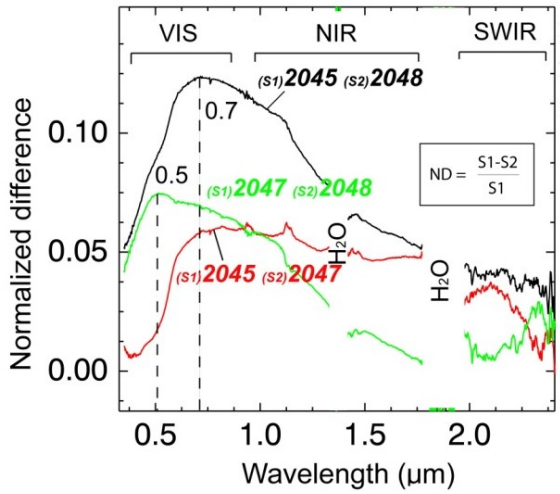

Figure 3.27 – Normalized difference between field spectra.

The difference between mixtures 2045 and 2048 is high, with the higher values in the VIS than in the NIR and the lowest in the SWIR. These mixtures contain different amounts of chert a dark constituent, therefore the maximum difference in reflectance is observed in the visible, where chert absorbs maximum radiation. From this observation it can be concluded that dark constituent had a higher influence in the VIS than in other spectral range. However the difference between cases 2045 and 2047 has a more homogeneous shape in the VIS-NIR-SWIR. In these mixtures there is no big difference in contrasted constituents. The difference between cases 2047 and 2048 is higher in the visible, as a result of the difference in chert content.

3.5.5 Spectral un-mixing

Figure 3.28 demonstrates abundances of the end-members of field mixtures, linear un-mixing results of the full spectral range, linear un-mixing results for the visible part of the spectra and non-linear un-mixing results for the full spectral range. Limestone content was overestimated by linear un-mixing over the full range, while silt amount was under-estimated. When visible range was used for un-mixing, silt content was totally replaced by limestone. The reason for this is that spectra of silt and limestone in the visible are very similar, there is no specific absorptions in the VIS. Only in the NIR and SWIR can differences be observed. Non-linear un-mixing improved the result for limestone and silt prediction, however limestone amount was still overestimated and black chert was slightly overestimated. Chert abundance was well estimated by linear un-mixing, both with full spectra and the VIS.

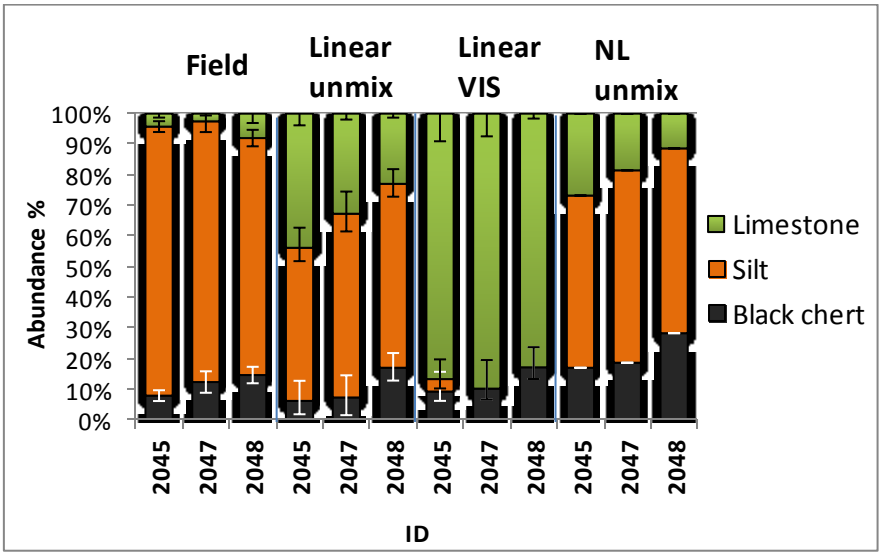

Figure 3.28 – Un-mixing results compared to the field abundances, group A site 1.

Error bars on un-mixing results represent variations resulting from using standard deviation spectra of end-members as an input for un-mixing. From the result we can observe that spectrum of the same end-member used for un-mixing of the same mixture can add up to 10% variation on un-mixing results. This depends on how spectra of the same end-member can vary. In case of non-linear un-mixing, end-member variation was not calculated since the spectrum of the end-member is transformed using non-linear fitting depending on how it appears in the mixture. In the visible, spectral variation is more important and the standard deviations are higher. Therefore when only the visible part of the spectra is used for un-mixing, errors will be higher than if the full spectral range is used.

Table 3-11 – RMSE of un-mixing results.

Linear un-mix all spectra			Linear un-mix VIS			Non-linear un-mixing		
2045	**2047**	**2048**	**2045**	**2047**	**2048**	**2045**	**2047**	**2048**
0.0121	0.0163	0.0159	0.033	0.0036	0.0028	0.0110	0.012	0.0116

This group of mixtures composed of silt as a dominant end-member and minor fraction of chert and limestones. Chert and limestones in these cases were of relatively small size. Linear model was effective in the prediction of the spectra. Reflectance intensity, spectral shape and absorption features were correctly estimated. Iron oxides absorptions were well predicted and limestone absorption features were correctly estimated, with differences that are not significant. Linear un-mixing overestimated limestone content, which could be explained by spectrally similar end-members that cannot be correctly resolved by current un-mixing techniques. In this group of mixtures where the dark component (chert) is a minor fraction and its size relatively small, its abundance was not overestimated despite the fact that it was expected that the dark constituent should have a higher spectral influence than indicated by its proportions.

3.6 Site 1 – Group B- Mixtures of highly contrasted constituents.

This group of mixtures is composed of three end-members: black chert, limestone and silt. In these cases the most abundant constituents are limestones and black cherts and silt fraction is minor. The element size of the constituents is relatively coarse, compared to previous group of mixtures. Cases presentation, classification maps with end member abundances and their size distribution plots are shown in fig 3.29. Full statistical data table of element size distribution for each group can be found in the annex.

	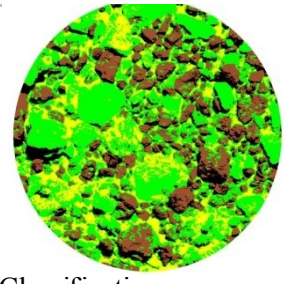 Classification map	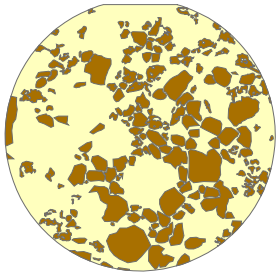 Black chert	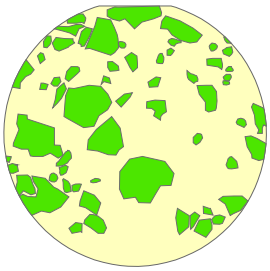 Limestone
2049		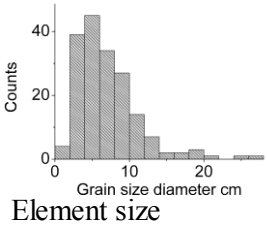 Element size distribution (cm)	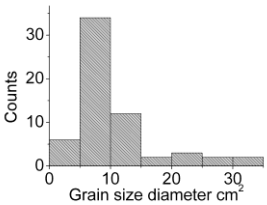 Element size distribution (cm)
	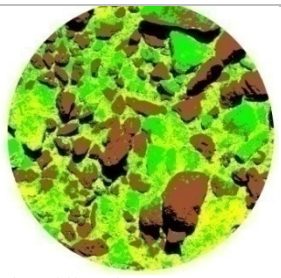 Classification map	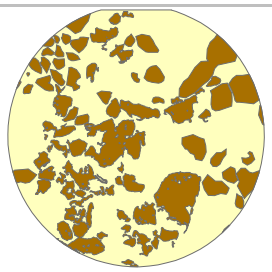 Black chert	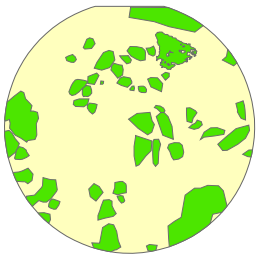 Limestone
2050		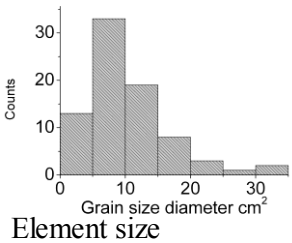 Element size distribution (cm)	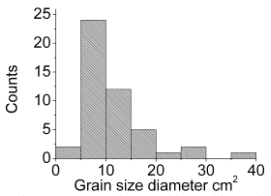 Element size distribution (cm)
	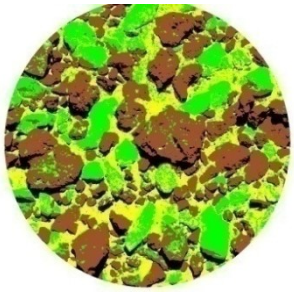 Classification map	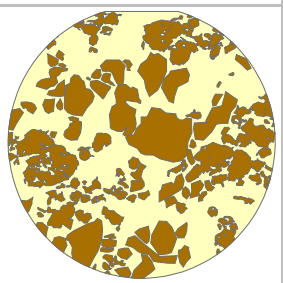 Black chert	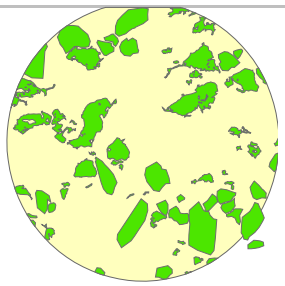 Limestone

2051		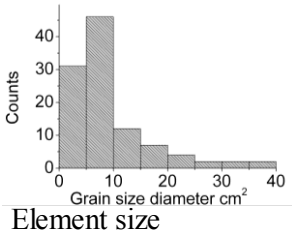 Element size distribution (cm)	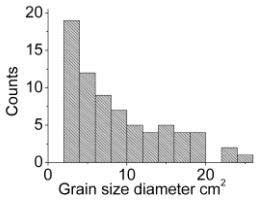 Element size distribution (cm)
	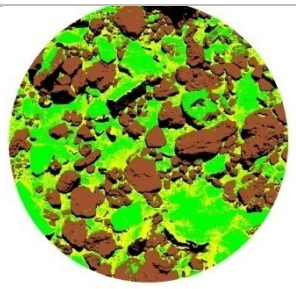 Classification map	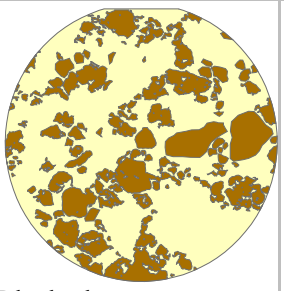 Black chert	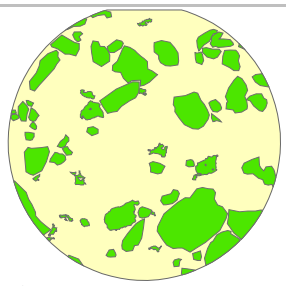 Limestone
2052		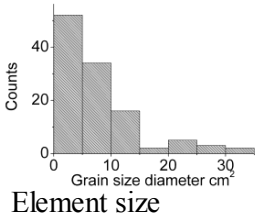 Element size distribution (cm)	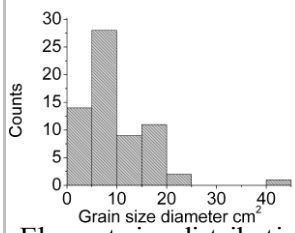 Element size distribution (cm)
	 Classification map	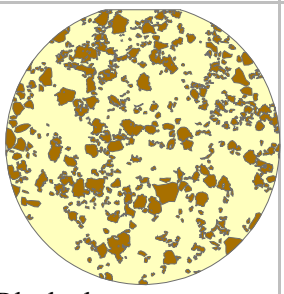 Black chert	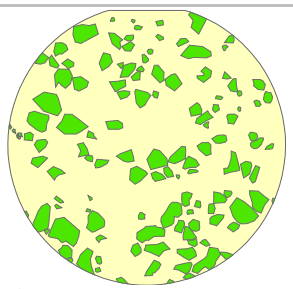 Limestone
2053		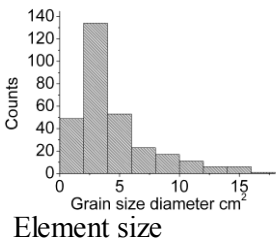 Element size distribution (cm)	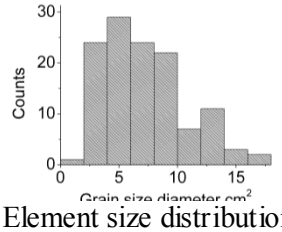 Element size distribution (cm)

Figure 3.29 – Field mixtures and end-member classification maps, site 1 group B.

3.6.1 Cases presentation

Case **2049** – The dominant end-member is black chert (**40%**), with an average size of 7 cm^2, and a standard deviation of 4 cm^2 (relatively high); the maximum boulder size is 26 cm^2. The distribution of size is not normal (skewness is higher than 1.5), the number of coarse boulders is higher than fines. It can be observed from the picture that relatively to other scenes, boulder sizes of cherts are smaller and their quantity is higher. Limestone abundance is **27%**, boulder size is relatively coarse, in average 10.5 cm^2, with a maximum size of 34.2 cm^2. The abundance of silt is **26%** (Table. 3.12).

Case **2050** is composed of black chert (**33%**), size of chert in average is 10 cm^2, maximum boulder size is 33 cm^2, that is coarser that in the previous case. Limestone constitutes **29%,** the boulder size is relatively coarse, 11 cm^2 in average, with a maximum at 37 cm^2. The silt constitutes **26%** from the mixture.

Case **2051** is composed of **42%** of chert, the average chert size is 9.3 cm^2, with a maximum at 38.3 cm^2. Limestone constitutes **32%** of the mixture and **24%** is silt. Limestone boulder size is relatively coarse, in average 8.8 cm^2; the maximum element size reaches 25 cm^2.

Case **2052** is composed at **36%** of black chert, the average element size of black chert is 7.8 cm^2, with a maximum at 30 cm^2, **29%** of limestones, which element size is 9.9 cm^2 in average, with a maximum of 41.3 cm^2. Silt constitutes **19%** of the mixture.

Case **2053** is composed of the same end-members, but their size is relatively small compared to other scenarios, the average size of chert is 4.5 cm^2, the average size of limestone is 7 cm^2. Black chert abundance is **27%**, abundance of limestone is **34%,** and silt constitutes **20%**.

Table 3-12 – End-member abundances of the field mixtures, site 1 group B.

Id	Black chert %	Limestone %	Silt %	Shadow %	Accuracy %
2049	33	27	29	11	92
2050	32	29	26	13	80

2051	42	22	24	12	90
2052	36	29	19	16	85
2053	27	34	20	19	80

3.6.2 Spectral characteristics

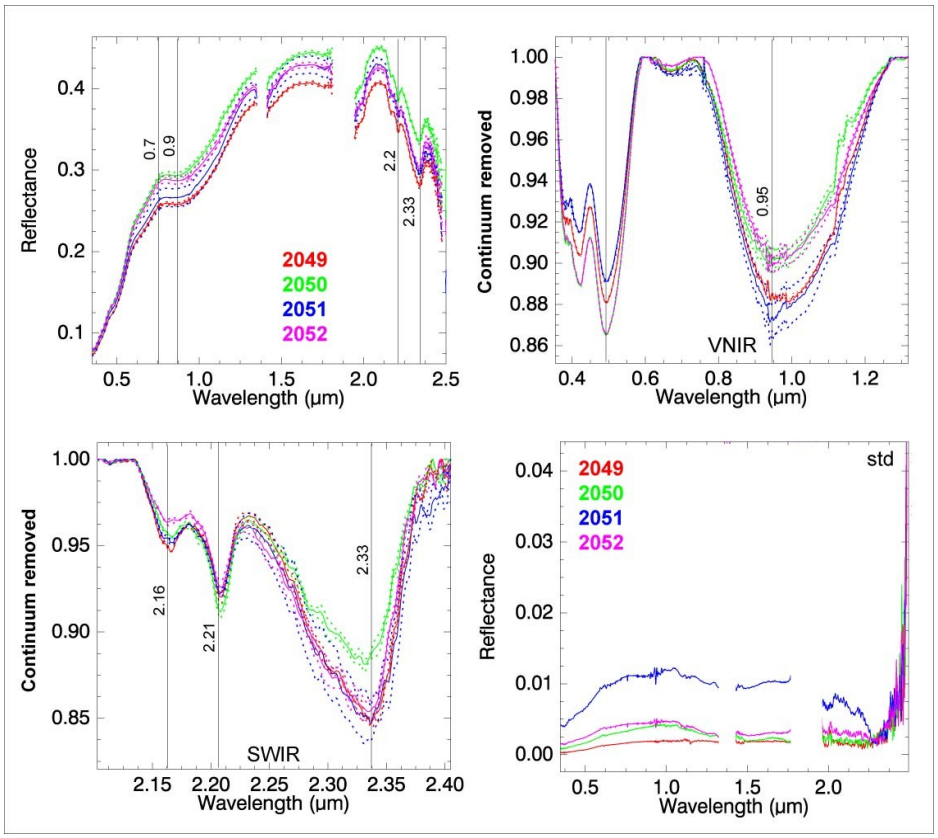

Figure 3.30 – Field spectra of the mixtures of site 1, group B: a)full spectral range; b) VNIR continuum removed; c) SWIR continuum removed; d) a standard deviation of field measurements.

Among all of the cases from the group the highest albedo belongs to mixture 2053. In this mixture, all end-members element size is relatively small. Case 2053 has approximately similar abundances of end-members as cases 2050 and 2052, but with a finer element size. This is the main reason for increase in its reflectance in the VIS, NIR and in the SWIR. In this group of mixtures the lowest albedo is observed for mixtures 2049 and 2051. In these mixtures the amount of black chert is higher, and element size is coarser than in cases 2050 and 2052.

In the continuum removed mode in the VIS cases 2049, 2051 and 2053 have similar absorption depth of iron oxides around 0.95 μm (Fig. 3.30 b). In cases 2050 and 2052 absorption of iron oxides is less pronounced; in these cases chert content is lower. In the SWIR clay absorption at 2.16-2.2 μm looks to be of the same depth in all cases. The absorption of calcite at 2.33 μm is stronger in cases 2049 and 2051 and weaker in cases 2050 and 2053 (Fig. 3.30 c). The reason is the amount of limestone in the mixture. Abundance of calcite was supposed to be high in case 2050. Probably some of the sandstone in the scene was confused with limestone. The absorption at 2.33 μm is weaker compared to other scenes.

In cases 2049 and 2053, the minimum wavelength of iron oxides absorption between 0.73 and 0.99 is shifted towards longer wavelength and is located at 0.98 μm, due to higher goethite content. In cases 2050, 2051 and 2052, the minimum of this absorption is shifted to shorter wavelengths (0.94 μm) and have a negative asymmetry. This indicates a higher amount of hematite (Table 3-13). The area of the absorption at 0.95 μm increases proportionally to increasing chert content in the mixtures. The biggest absorption area (1.856) is observed in case 2051 and the smallest (1.405) is observed in case 2050. The absorption area at 2.33 μm is the highest in case 2049, for which the abundance of calcite is higher.

Table 3-13 – Absorption features of spectra, mixtures of site 1, group B.

ID	Min wvl 0.73-0.99	Abs area 0.95	Abs area 2.2	Abs area 2.33	Asymmetry 0.95	0.4	0.48	0.95	2.2	2.33
2049	0.989	1.731	0.102	0.51	0.009	0.091	0.115	0.117	0.057	0.146
2050	0.94	1.405	0.107	0.36	-0.027	0.104	0.131	0.098	0.064	0.118
2051	0.94	1.856	0.089	0.45	-0.036	0.082	0.105	0.128	0.055	0.135
2052	0.935	1.413	0.076	0.46	-0.048	0.105	0.131	0.1	0.054	0.139
2053	0.986	1.768	0.072	0.34	0.001	0.104	0.131	0.122	0.055	0.106

3.6.3 Linear mixing – direct modeling.

Modeled and field spectra are shown on figure 3.31, differences between predicted and field spectra can be observed. The highest difference in reflectance spectra appears in case **2049** (Fig. 3.31). This mixture is composed of black chert, limestone and silt. Absorption of iron oxides at 0.92 μm is under-estimated by the model. The minimum of the absorption in the modeled spectrum is located at 0.92 μm, while in the field the minimum is located closer to 1 μm, that

corresponds more to sandstone. The absorption of calcite at 2.33 μm is deep and indicates to a high content in limestone. In this case both iron oxides absorptions and calcite absorptions estimated from the linear model did not correspond to the absorptions of the field spectrum. In the picture part of the limestone looks dark, and sometimes may be confused with sandstone in classification.

In case **2050**, absorptions of iron oxides around 0.95 μm and absorption of calcite at 2.33 μm were underestimated by linear model (Fig. 3.31). The minimum of iron oxides absorption in the field spectrum is located around 1 μm. In the modeled spectrum the minimum is closer to 0.95 μm, which corresponds to hematite.

In case **2051**, the linear model also underestimated all absorption depths (Fig. 3.31). Absorption of iron oxides at 0.95 μm is under-estimated and its minimum is shifted closer to 0.92 μm. In the modeled spectrum this absorption is asymmetric, which is corresponding to hematite. In the field this absorption was symmetric. In this case absorption of calcite at 2.33 μm has the highest difference with the modeled spectra. In cases **2052** and **2053** the same features are observed: reflectance of field spectrum is lower than modeled. Absorption of iron oxides in the VIS are under-estimated similarly to the previous cases, absorption of calcite at 2.33 μm is also under-estimated. However, the absorption of kaolinite in the SWIR is in the same range (Fig. 3.31).

Differences between linear model prediction and field spectra appear both in albedo parameters and absorption depths and shapes. And there are several possible explanations for these differences, between field and modeled spectra. First, the end-members used for the mixtures do not exactly correspond to those in the field. Although end-members were collected in the field, some rocks in the field may have different roughness, coatings, composition. The concentration of specific minerals in the field and in the sample may be different, this is not always visually detectable, however in the field heterogeneity may be very significant. As a result the linear model will have a difficulty to predict the correct spectrum, using spectra of the specific end-members.

The second problem can be some misidentification of end-members. For example, limestone may be visually confused with sandstone; as a result differences between modeled and field spectra will appear. Classification based on RGB images is not very precise; however we tried to take this into account. Another possible reason for differences is measurement conditions: the modeled spectrum is calculated using spectra acquired in the laboratory from the end-members collected in the field, while field spectrum is acquired directly from mixtures in the field, with

specific sun illumination, angle of measurement, shadow may also reduce the reflectance. Supposing element size has an influence on reflectance spectra of field mixtures, which is not encountered by simple linear model.

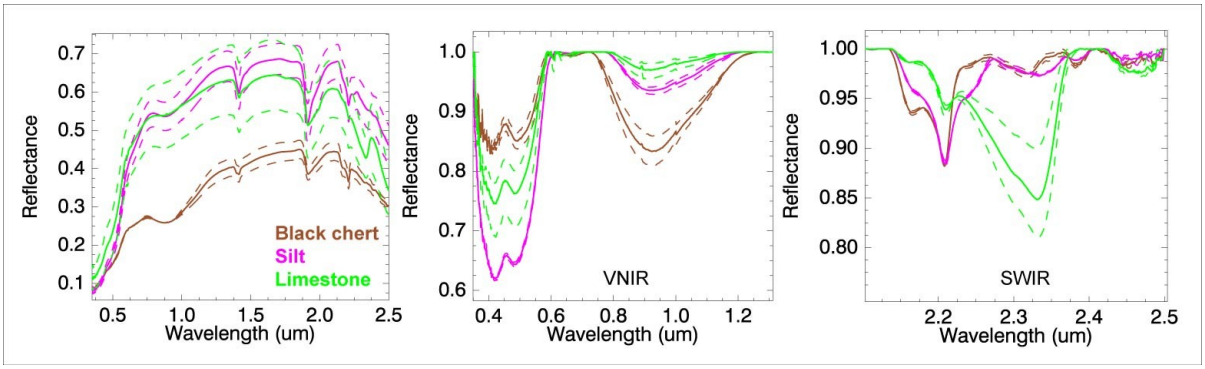

Figure 3. 31 – End-members spectra of mixtures, site 1, group B.

Formulas for linear modeling:

$$\mathbf{2049} = (0.33 * Sp_{B.chert}) + (0.27 * Sp_{Limestone}) + (0.29 * Sp_{Silt})$$

$$\mathbf{2050} = (0.32 * Sp_{B.chert}) + (0.29 * Sp_{Limestone}) + (0.26 * Sp_{Silt})$$

$$\mathbf{2051} = (0.42 * Sp_{B.chert}) + (0.22 * Sp_{Limestone}) + (0.24 * Sp_{Silt})$$

$$\mathbf{2052} = (0.36 * Sp_{B.chert}) + (0.29 * Sp_{Limestone}) + (0.19 * Sp_{Silt})$$

$$\mathbf{2053} = (0.27 * Sp_{B.chert}) + (0.34 * Sp_{Limestone}) + (0.20 * Sp_{Silt})$$

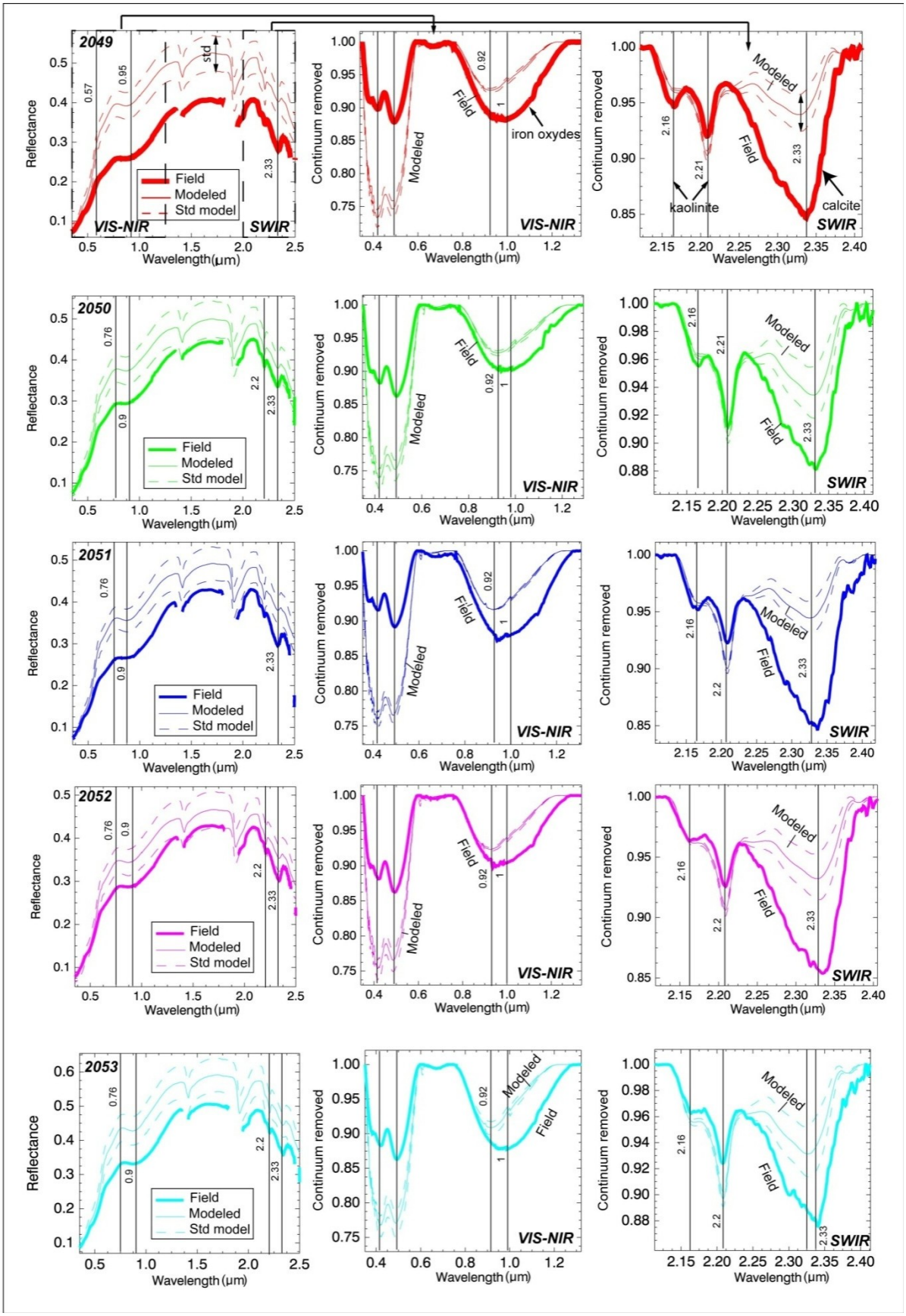

Figure 3.32 - Modeled and field spectra, mixtures of group B, site 1.

3.6.4 Difference analysis (DA)

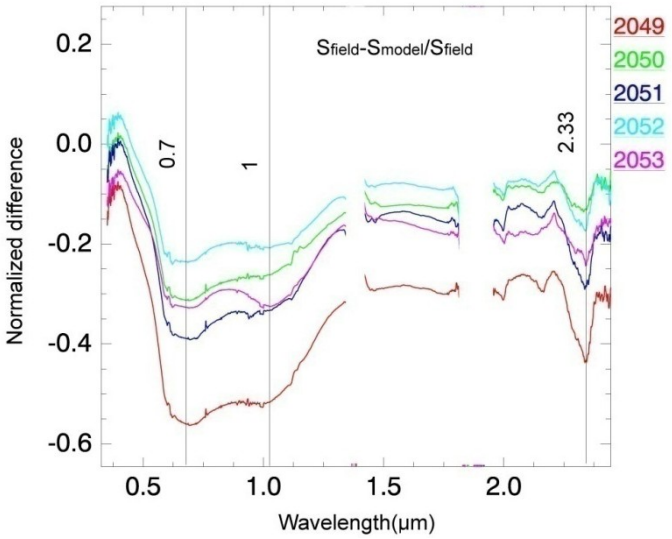

Figure 3.33 – Normalized difference of field and modeled spectra.

Normalized difference between field and modeled spectra are shown on fig 3.32. Negative values for the difference are due to a higher reflectance for the field than for the modeled spectrum. The highest difference is observed in the VIS, while in the NIR and SWIR values are closer to 0. In the SWIR, the difference for the calcite absorption results from an underestimation of limestone content. Non-linear effects are higher in the VIS, due to the presence of a dark end-member and iron oxides.

3.6.5 Spectral un-mixing

End-member proportions derived from un-mixing are shown on fig. 3.34. Better results were obtained for the full spectral range, than for the visible part of spectra alone. When only the visible was used, un-mixing totally misestimated silt and replaced it by limestone. Also errors are lower when the full spectral range is used. Variation of limestone spectra (standard deviation) can cause up to 15% difference in limestone content prediction if only the visible range is used, and it is about 5% when the full range is considered. Therefore it is important to use full spectral range to achieve more truthful results.

Estimations of linear and non-linear models are very close, therefore it is hard to define which model gave better prediction. Non-linear un-mixing better predicted silt content, but under-

estimated limestone content, and slightly over-estimated chert abundance (Fig. 3.34). Error bars are lower for linear un-mixing of the full spectral range, than for non-linear un-mixing.

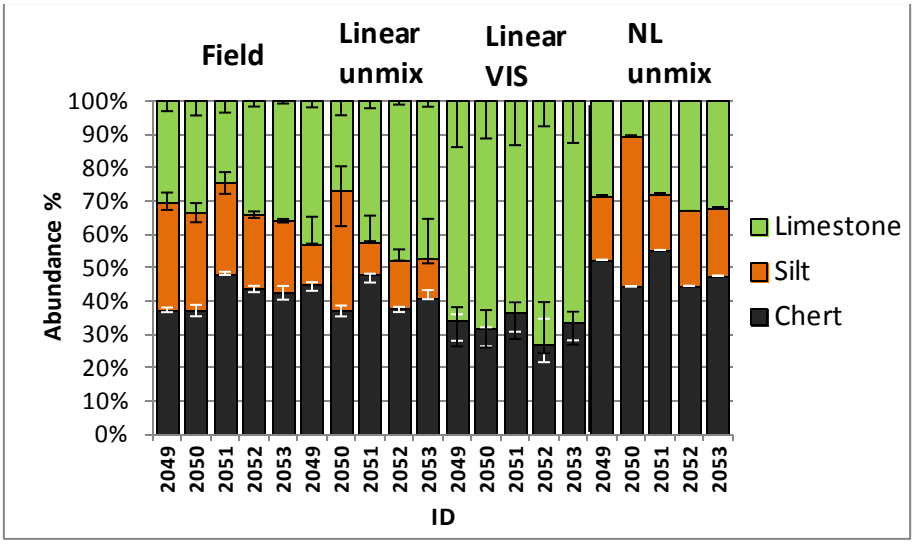

Figure 3.34 – Un-mixing result compared to the field abundances.

Variations in fraction prediction due to end-member heterogeneity vary up to 10% in case of silt and limestone, however are lower in case of chert. In the VIS these variations are higher.

RMS are lower for non-linear un-mixing than for linear even if RMS of linear un-mixing of the VIS are the lowest, the result of this un-mixing is not correct, as silt was totally misestimated.

Table 3-14 – RMSE of un-mixing result.

Linear un-mixing all specta					Linear un-mixing VIS				
2049	**2050**	**2051**	**2052**	**2053**	**2049**	**2050**	**2051**	**2052**	**2053**
0.0138	0.0158	0.015	0.0135	0.0126	0.0051	0.0042	0.0057	0.0048	0.0052
Non-linear un-mixing									
2049	**2050**	**2051**	**2052**	**2053**					
0.0109	0.011	0.0123	0.0099	0.0089					

Observation of this group showed that field spectra of the mixtures were not represented in a best way by linear modeling (using a direct model). Absorptions of the most mixture spectra were underestimated, and reflectance levels in the field were lower comparative to the field spectra. What is common for all these cases is that the element size of chert was rather coarse and the end-members showed a high spectral contrast. This is the main reason for non-linear effects in these cases. Also, shadow may add non-linear effects to the picture. However, in such cases when there is non-conformity between end-members of a mixture or there is a high heterogeneity

of the end-members, a non-linear model should minimize these differences (to force laboratory spectra to fit to the field spectra). Therefore we expected an improved result from non-linear un-mixing compared to linear. Here non-linear un-mixing was more effective and gave a better prediction of the dark constituent, but the problematic of separation of spectrally similar end-members still remained. Silt and limestones content was not correctly estimated.

3.7 Site 1 - Group D – high contrast end-members, large boulders.

This group of mixtures is composed of cherts with size distribution varying from very coarse to small gravels, of limestones (coarse boulders) and sandstones. In these mixtures, the effect of element size can be studied, since there are different size distributions for each case, as well as compositional effect, of the end-members which contain high amounts of iron oxides.

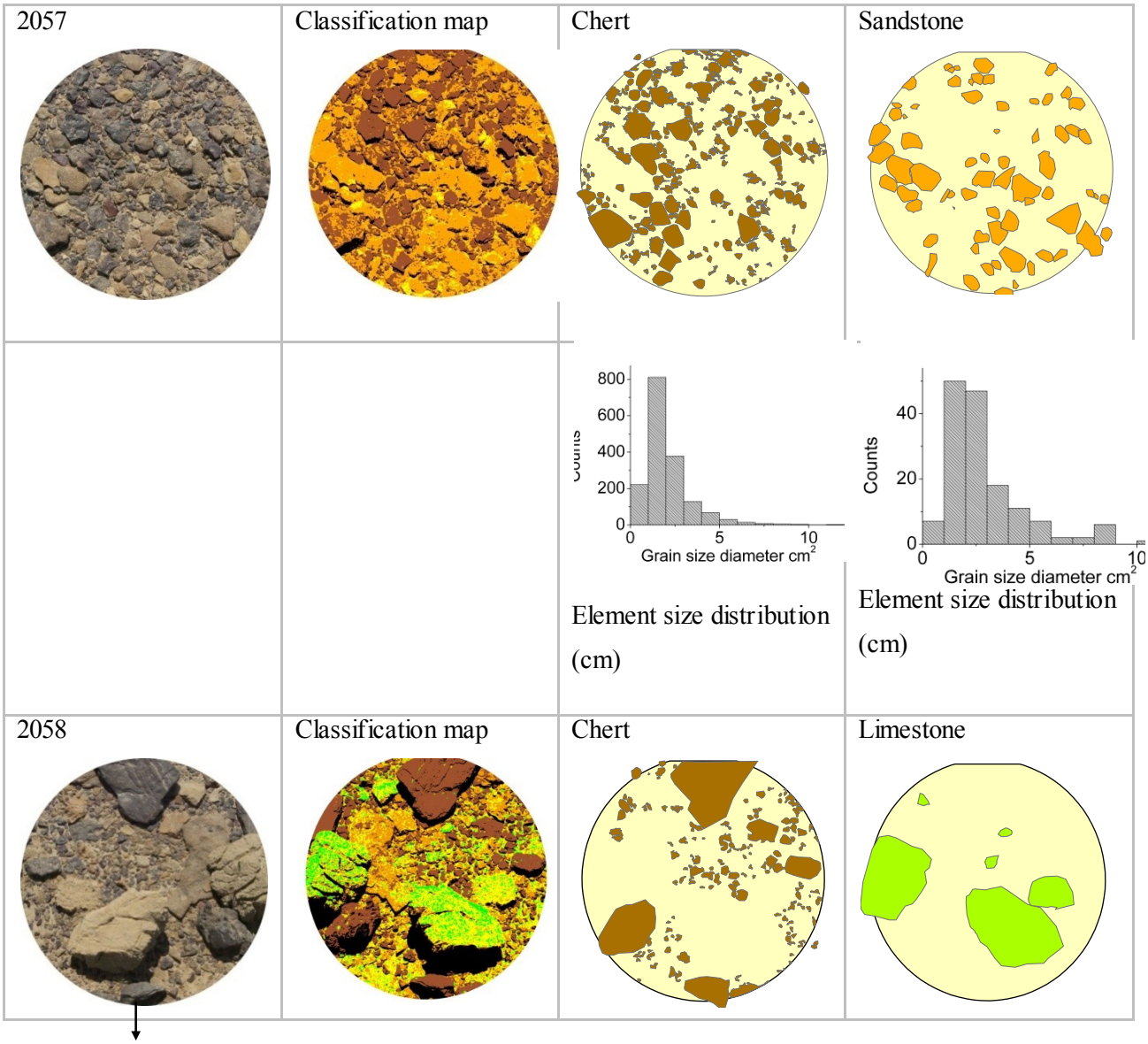

Sandstone 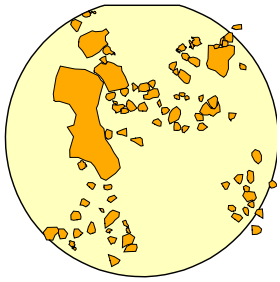	Element size distribution (cm) 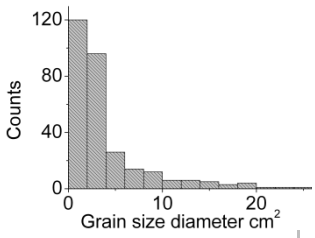	Element size distribution 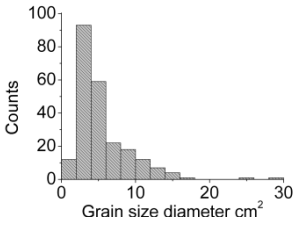	Very coarse boulders.
	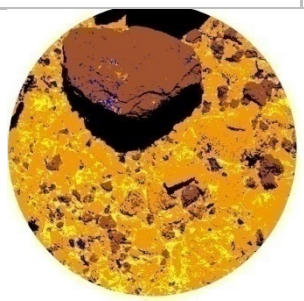 Classification map	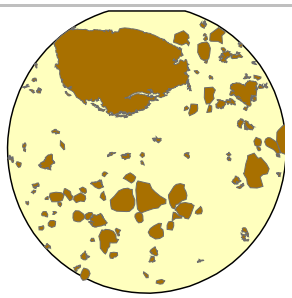 Chert	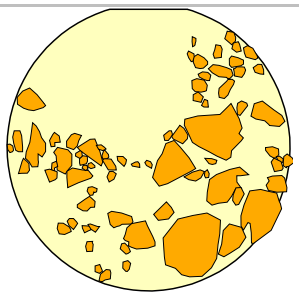 Sandstone
2059		Element size distribution (cm) 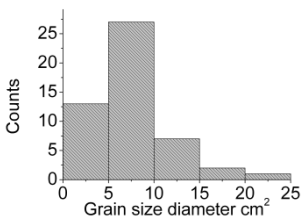	Element size distribution (cm) 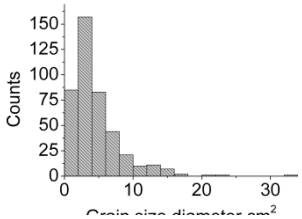
	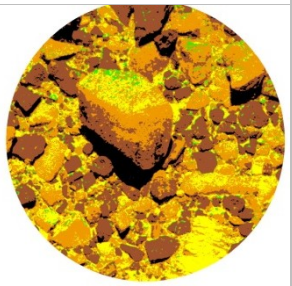 Classification map	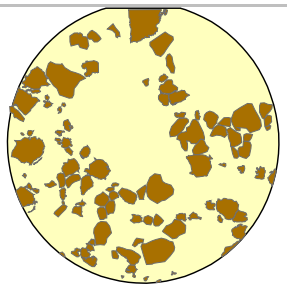 Chert	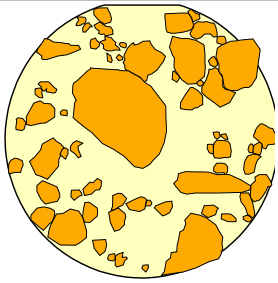 Sandstone
2060		Element size distribution	Element size distribution

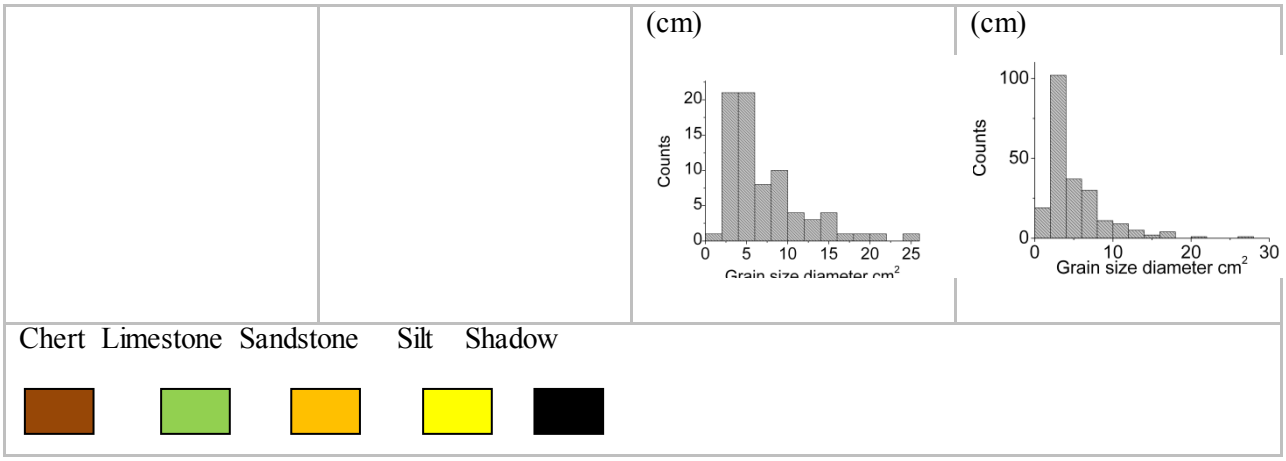

Figure 3.35 – Field cases of mixtures and end-member classification maps, Site 1 group D.

3.7.1 Cases presentation

Table 3-15 – End-member abundances of mixtures from group D, site 1.

Case N	Black chert	Silt	Sandstone	Shadow	Limestone	Classification Accuracy %
2057	40.7	4.3	45.9	9.1		87
2058	25.0	18.0	14.0	15.0	28.0	90
2059	24.1	8.6	53.5	13.8		95
2060	34.0	16.0	40.8	9.2		80

Case **2057** is composed of cherts (40.7%), sandstone (45%) and silt (4.3%). In this mixture mean grain size of cherts in average is 5 cm^2 and sandstones is 10 cm^2.

Case **2058** is composed of black chert (25%), sandstone (14%), silt (18%) and limestone (28%) (Table 3-15). Boulder size of most species of black chert is relatively coarse, 5 cm^2 in average, several large boulders can be observed (Fig. 3.34). Maximum size of chert reaches 50 cm^2. Several coarse boulders of limestones are noticeable in the scene (Fig. 3.34); sandstones boulder size is relatively smaller compared to other end-members, in average 8 cm^2.

Case **2059** is composed of the black chert (20.7%), sandstone (53%), red chert (3.4%) and silt (8.6%). Large boulders of black chert and many boulders of medium size are observed in the scene. Sandstone size is also coarse, 9 cm^2 in average (Fig. 3.34).

Case **2060** is composed of the black chert (15%), red chert (19%), silt (16%), sandstone (38%) and small amount of limestone (2.6%). In this case very large boulders of sandstone are present and cherts have a medium size of 7cm^2.

3.7.2 Spectral characteristics

Spectra of field mixtures are shown on fig. 3.35. The standard deviation (d) is relatively low for all the mixtures and does not overcome 1%, only in case 2060 standard deviation is higher and reaches 1.5%. The highest reflectance is observed in case 2059. In this case boulder size is relatively fine with a single coarse boulder of chert. Features of iron oxides are characteristic for all spectra of this group, red peaks appear at 0.6 μm and 0.7 μm, and well pronounced absorption of iron oxides at 1 μm. Absorption at 1 μm is deeper in case 2057, this mixture contains a higher amount of sandstones than the other cases. The shape of this absorption is quite symmetric, (Table 3-16). Absorption of calcite with a minimum at 2.33 μm is the deepest in case 2058, a case with higher amounts of limestone compared to others. This absorption is sensitive to changing calcite content and its depth changes significantly when calcite content is increased or reduced. Absorptions of kaolinite at 2.16 - 2.2 μm are less sensitive to changing amounts of end-members and remained stable in all cases.

Table 3-16 – Absorption features of spectra of mixtures of group D, site 1.

ID	Min wvl 0.73-1	Area % 0.95	abs area 2.2	Abs area 2.33	Assymetry 0.95	0.95	2.2	2.33
2057	0.988	2.905	0.138	13%	0.013	0.194	0.082	0.046
2058	0.986	2.321	0.141	36%	0.004	0.159	0.077	0.110
2059	0.987	2.308	0.125	15%	-0.013	0.158	0.078	0.052
2060	0.986	2.668	0.127	22%	-0.017	0.178	0.074	0.077

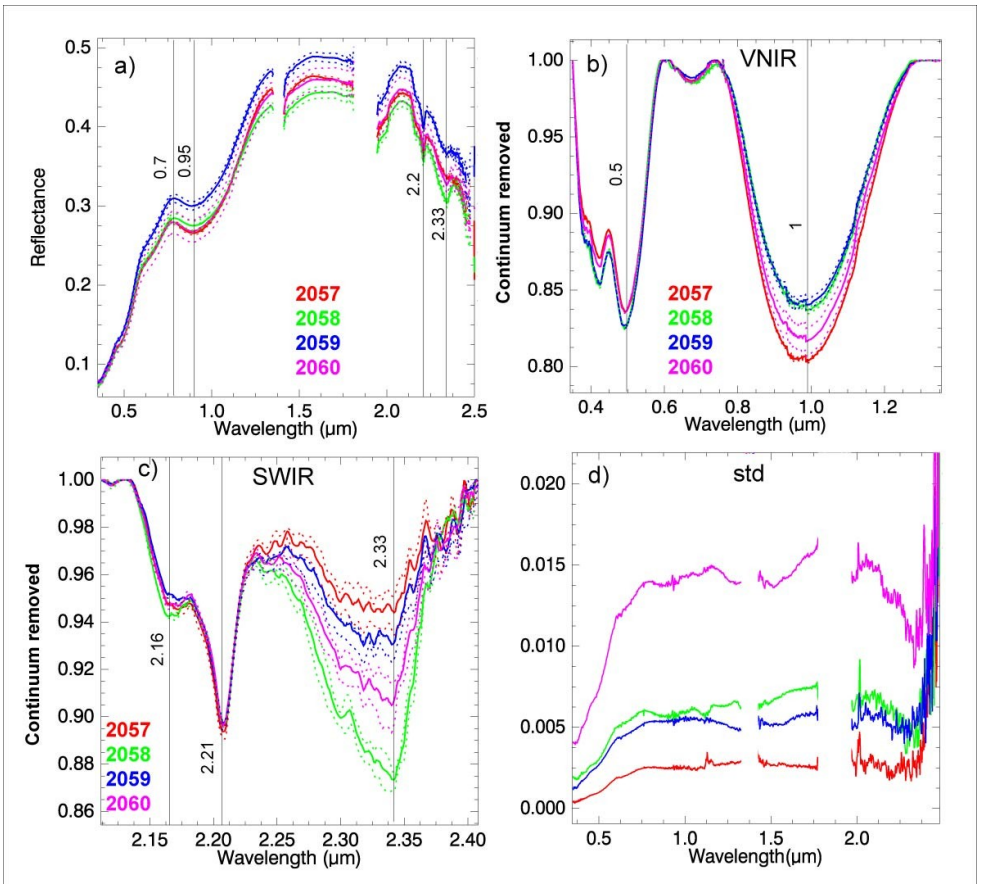

Figure 3.36 – Field spectra of mixtures of group D, site 1: a) full spectral range; b) VNIR continuum removed; c) SWIR continuum removed; d) standard deviation.

3.7.3 Linear mixing (direct modeling)

Spectra of end-members used for linear direct and inverse modeling are shown on figure 3.36, the dashed lines show spectra acquired from the same end-member due to its heterogeneity: patina, roughness etc. There are spectrally similar end-members silt and limestone, their shapes look similar, this can be an issue for un-mixing algorithms, and main differences between these spectra are in absorption positions.

From the result of direct modeling (Fig. 3.38) is observed, that in cases 2058 and 2060 reflectance of the field spectra is lower than the modeled spectra. In case 2059 reflectance of modeled spectra is higher than the field spectrum, these are albedo parameters. Spectral shape is well estimated by linear model for all observed mixtures, however its intensity was not always correctly estimated.

Absorption depths in the VNIR are in the same range; however modeled spectra predicted higher hematite content (Fig. 3.38). In the field spectrum the absorption minimum is observed at 1 μm, which corresponds more to sandstone. In the SWIR absorptions of kaolinite at 2.16-2.2 μm are overestimated for cases 2059 and 2060. Absorptions of calcite at 2.33 μm are under-estimated for cases 2058 and 2060, while these mixtures contain a high amount of limestone. In case 2059 absorption of calcite is in the predicted range. Calcite absorption was underestimated in cases 2058 and 2060; these cases are composed of large boulders of limestone and sandstone. From here it can be supposed that boulder size influence on spectra of the mixtures at macro-scale, and as a result may add non-linear effects: in cases where large boulders were present in the mixture, the absorption features are deeper than they are predicted by a linear combination of end-members.

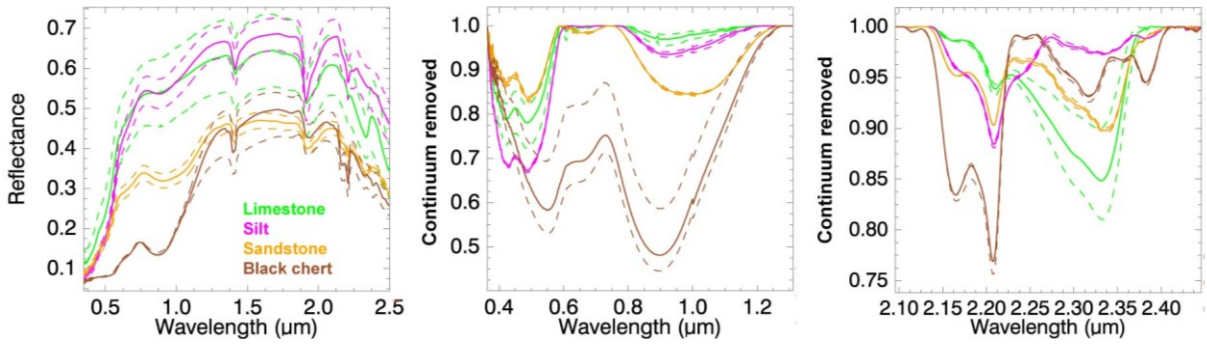

Figure 3.37 – Spectra of end-members used for model, +/- std spectra are shown with dashed lines.

Formulas for calculation of linear mixtures:

2057 = *(0.407 * Sp $_{B.chert}$) + (0.043 * Sp $_{Silt}$) + (0.459 * Sp $_{Sandstone}$)*

2058 = *(0.25 * Sp $_{B.chert}$) + (0.18 * Sp $_{Silt}$) + (0.014 * Sp $_{Sandstone}$) + (0.28 * Sp $_{Limestone}$)*

2059 = *(0.241 * Sp $_{B.chert}$) + (0.086 * Sp $_{Silt}$) + (0.535 * Sp $_{Sandstone}$)*

2060 = *(0.34 * Sp $_{B.chert}$) + (0.16 * Sp $_{Silt}$) + (0.408 * Sp $_{Sandstone}$)*

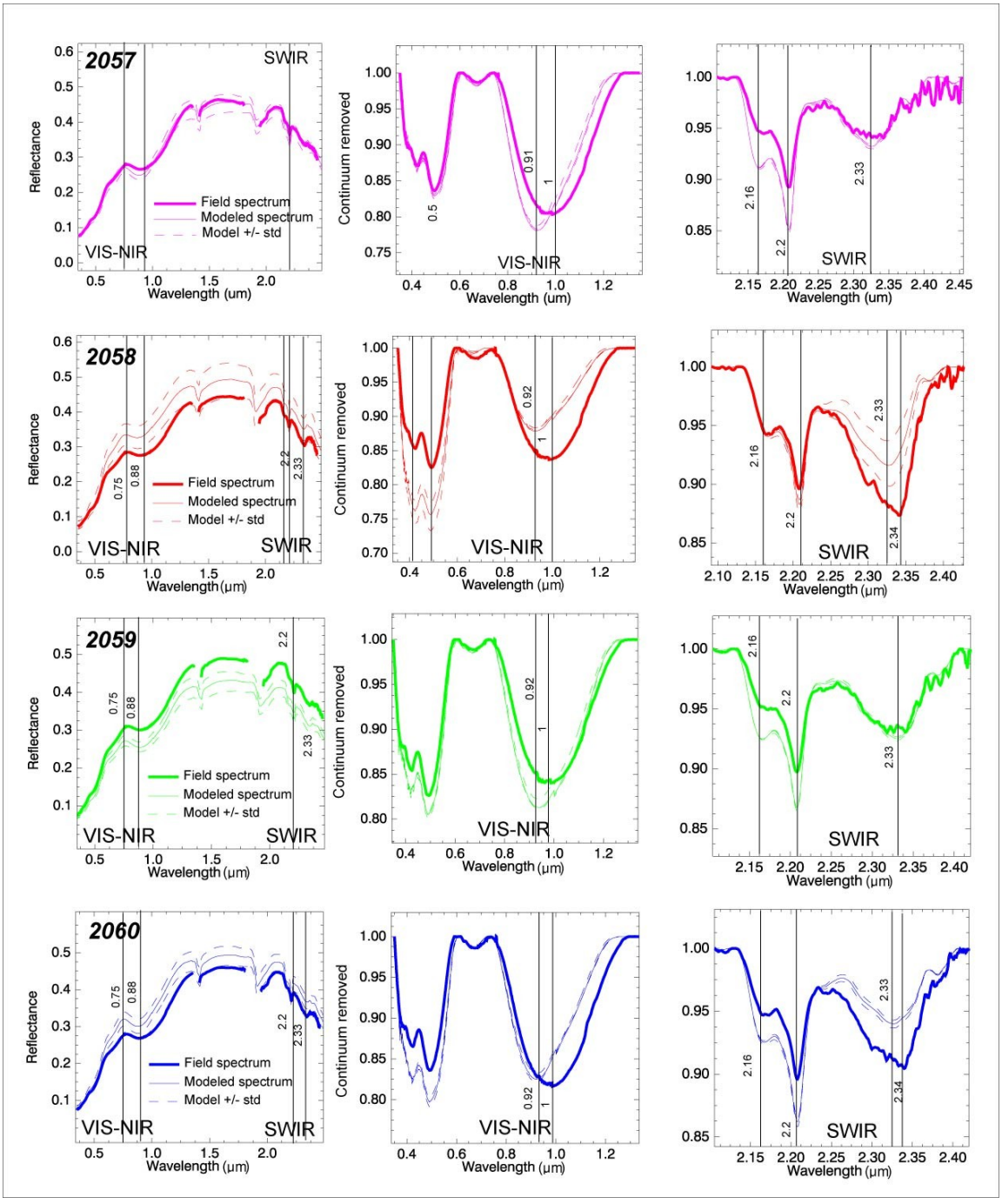

Figure 3.38 – Field and modeled spectra of mixtures of group D, site 1.

3.7.4 Differences analysis

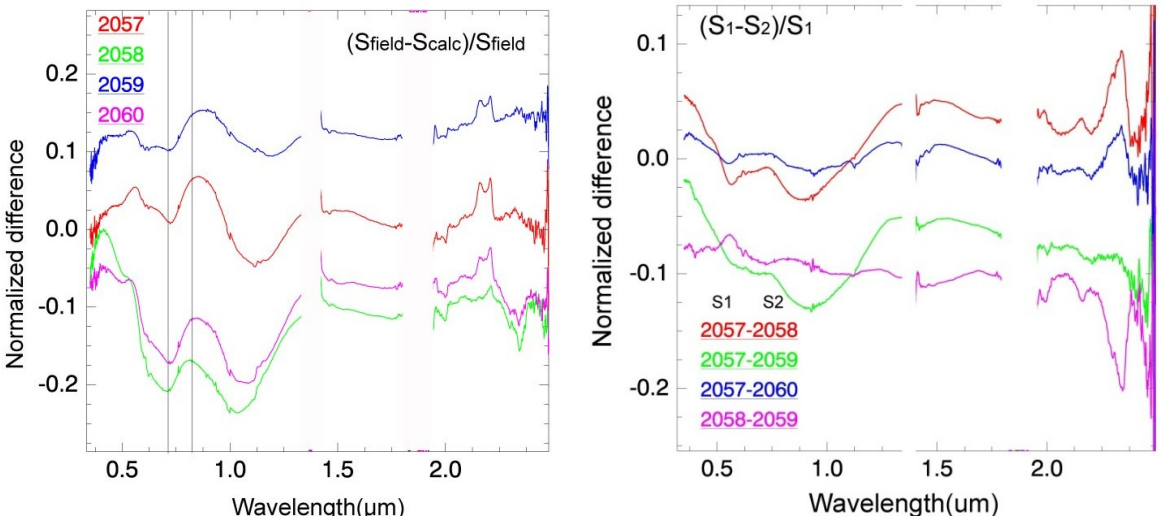

Figure 3.39 – Normalized difference of field spectra, two spectral shapes can be defined (left, right).

Normalized difference between field and model spectra of mixtures are shown on fig. 3.39. DA enables to find the origin of the differences between spectra at different wavelengths. There are differences both in reflectance levels and in absorption positions and depths. Negative values were obtained for mixtures 2058 and 2060, with similar shape for the spectra. Maximum difference is observed in the VNIR, however in the SWIR the difference is closer to 0. Spectral features at 0.7, 0.85 and 1 µm are related to iron oxides, which were underestimated by the linear model. In case 2059 the shape of the difference looks quite homogeneous in the VIS-NIR-SWIR and has positive values. In case 2057 the difference is close to 0, with differences in absorption features in the VIS related to iron oxides.

If we observe normalized difference between the cases (Fig. 3.39), the high negative difference is observed in cases 2057 and 2059. In case 2059 chert appears as a single boulder, while in case 2057 chert element size is smaller and its fraction is composed of many gravels. This is the main reason for difference in albedo. Due to different element sizes, in case 2059 absorption corresponding to chert are more pronounced than in case 2057.

3.7.5 Spectral un-mixing (inverse model)

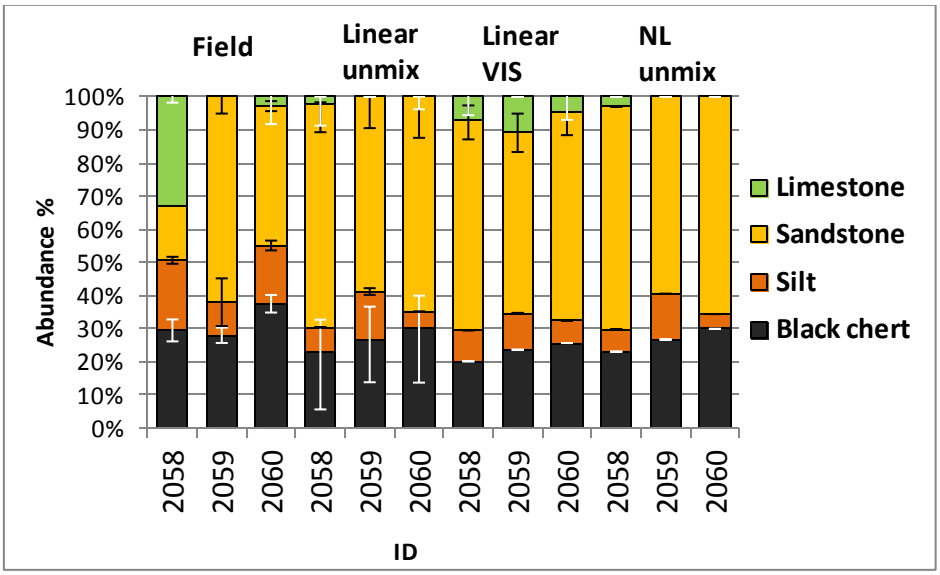

Figure 3.40– Un-mixing result compared to field abundances, group D site 1.

In this group of mixtures linear and non-linear un-mixing showed analogous results. Black chert abundance was estimated correctly both by linear and non-linear models, silt was slightly underestimated and sandstone was overestimated. Limestone content was better predicted when only the visible range was used, but almost ignored if using the full spectral range. Black chert content was well estimated by all methods. Error bars of black chert are higher in case of linear un-mixing of full spectra. Variations due to sample heterogeneity are strong in the case of black chert, up to 20% in case 2058. In other cases these variations are less significant, meaning that samples were quite homogeneous over the scenes. RMS are lower for un-mixing of the visible only (Table 3-17). In this case limestone content was better predicted (Fig. 3.40).

Table 3-17 – RMSE of un-mixing.

Linear un-mixing all spectra			Linear un-mixing VIS			Non-linear un-mixing		
2058	**2059**	**2060**	**2058**	**2059**	**2060**	**2058**	**2059**	**2060**
0.006	0.0074	0.0066	0.0025	0.0026	0.0023	0.006	0.0074	0.0066

For this group of mixtures linear (direct) model fitted well the absorption depths of iron oxides and the general shape of the spectra. However, the absorption of calcite in the SWIR was underestimated in the cases where coarse boulders of sandstones appeared. This proves that element size of field end-members has an important influence on mixture spectra. The linear model used for construction of the mixture spectra did not take into account this effect. Therefore

the inverse models, linear and non-linear, were not completely accurate in identifying some of the end-members. These were spectrally similar end-members: limestone and silt. However model better predicted chert and silt content.

3.8 Site 1 - Group F – Background of red chert and silt.

In this group of mixtures red chert figure as a main composing end-member, silt is present in minor amounts. Boulder size of chert is medium, about 5 cm in average. In this group iron oxides of hematite type are the main component, which composes red cherts. Its behavior in mixture with silt will be studied.

	 Classification map	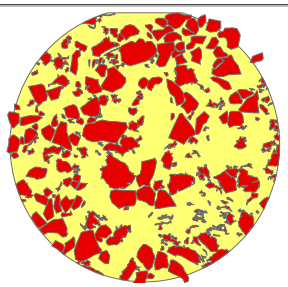 Red chert	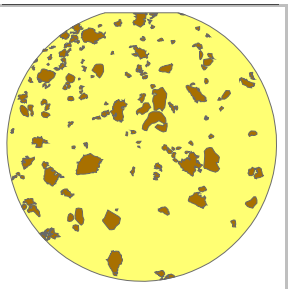 Black chert
2065		Element size distribution (cm) 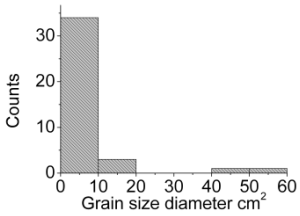	Element size distribution(cm) 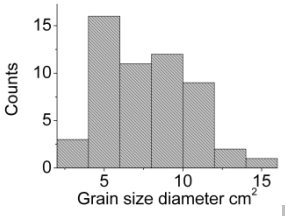
	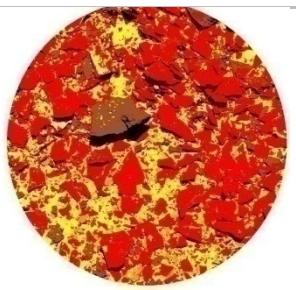 Classification map	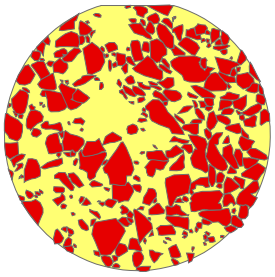 Red chert	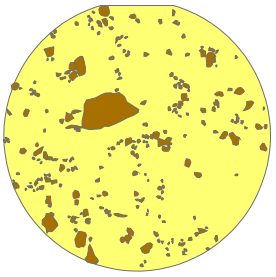 Black chert

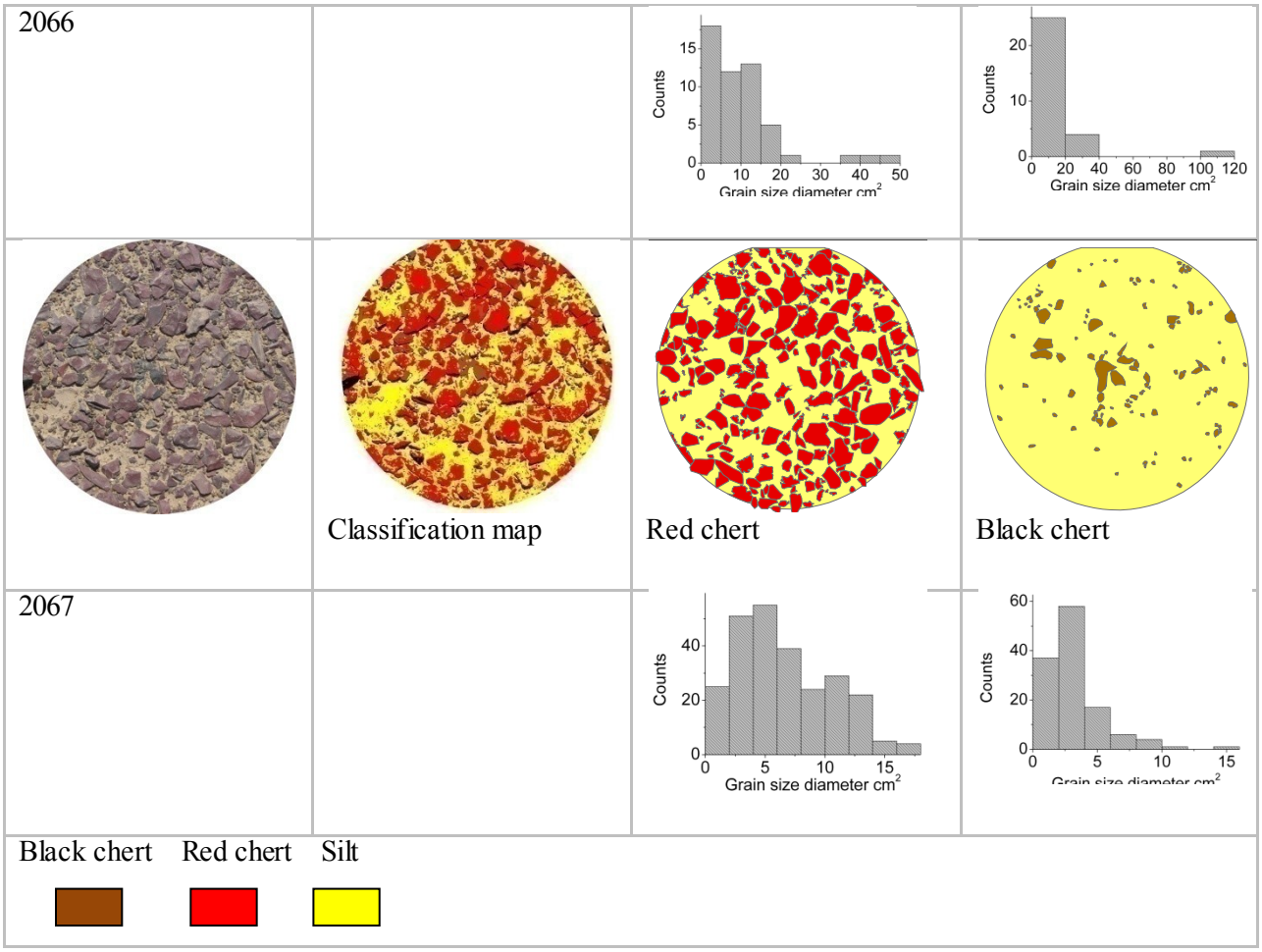

Figure 3.41 – Field cases and end-member classification maps, mixtures of group F, site 1.

3.8.1 Cases presentation

Table 3-18 – End-member abundances of field mixtures of group F, site 1.

Case N	Black chert	Silt	Red chert	Shadow	Accuracy %
2065	11.6	36.7	41.2	10.5	98.0
2066	10.4	26.3	54.8	8.5	94.0
2067	5.4	46.5	39.9	8.2	93.0

Case **2065** has a high amount of red chert (41%), silt (20%), small amount of black chert (12%) and sandstone (17%). Average size of red chert is 6.2 cm^2, and black chert, 4.2 cm^2.

Case **2066** is composed by a high amount of red chert (55%), black chert contributes 10%, silt 20% and sandstone 6%. Red chert mean size is 6.6 cm^2.

Case **2067** shows a high amount of red chert (40%), with a mean size for chert of 6.6 cm^2 and silt (43%), a small amount of black chert (5.4%) and sandstone (3.7%).

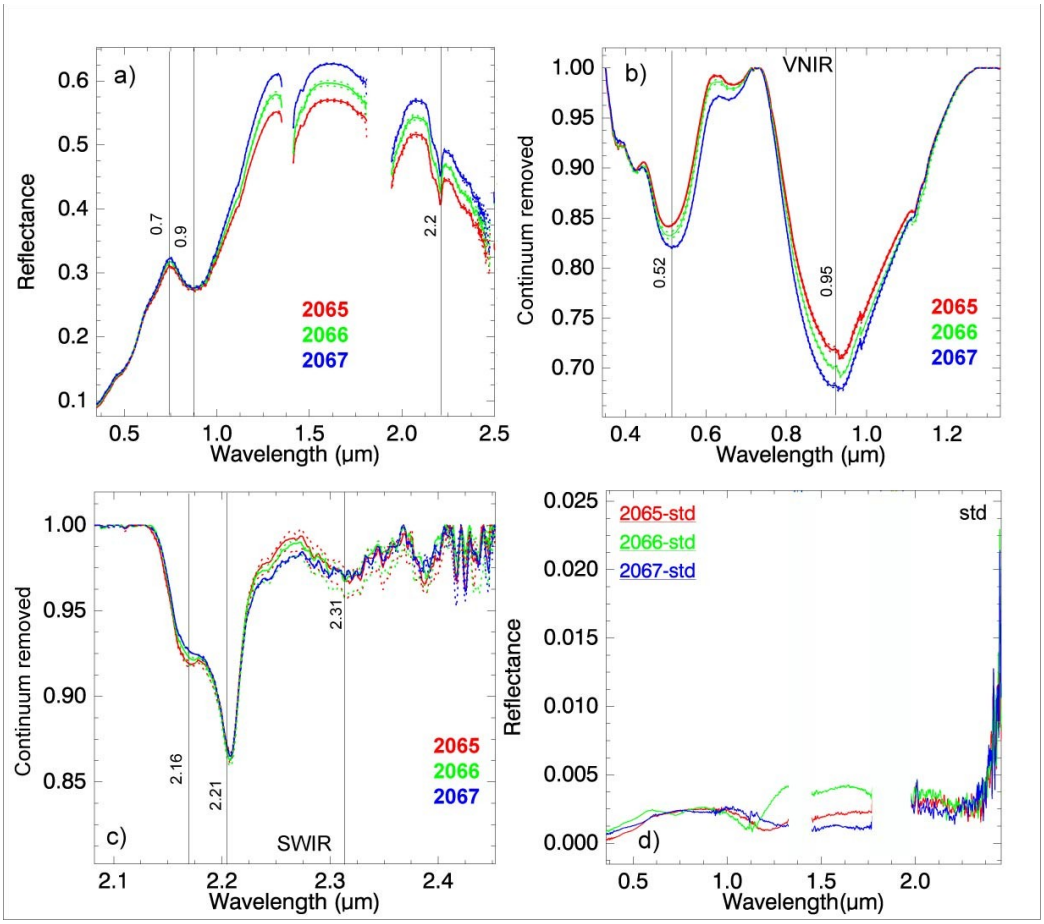

Figure 3.42 – Field spectra of mixtures of group F, site 1: a) full range of spectra; b) VNIR continuum removed; c) SWIR continuum removed; d) standard deviation of field measurements.

Spectra of field mixtures are shown on fig. 3.42, standard deviation is less than 1% for all field spectra.

Spectra of observed groups are strongly influenced by iron oxides in the VIS. The spectral shape of the mixtures has a low albedo in the VIS. Then albedo drastically increases in the NIR and becomes low again in the SWIR. This shape of spectra is also attributed to red chert. Maximum albedo is observed in case 2067. It is interesting to point out that in the VIS, the albedo is similar for all mixtures, but the main differences are observed in the NIR and in the SWIR.

A spectral peak at 0.74 μm (red peak) is caused by hematite and absorptions at 0.5 and 0.88 μm are produced by hematite and goethite (Fig 3.42). The absorption at 0.88 μm is asymmetric (negative asymmetry from table 3-19), shifted to shorter wavelengths with a minimum around

0.93 μm and is caused by hematite. Absorption areas are relatively strong which indicates high iron oxides content (Table 3.19). Absorption of kaolinite at 2.16-2.2 μm is well pronounced, and is mainly caused by kaolinite found in cherts. Absorption of dolomite, observed at 2.31-2.38 μm, is not very strong, and is caused by small amounts of dolomite from the red chert.

Table 3-19 – Absorption features of mixtures, group F, site 1.

Wavelength	Min wvl 0.44-0.61	Min wvl 0.73-0.99	Area % 0.95	abs area 2.16-2.2	Abs area 2.33	Asymmetry 0.95	Depth 0.95	Depth 2.2	Depth 2.33
2065-field	0.507	0.935	3.951	0.231	7%	-0.116	0.283	0.110	0.024
2066-field	0.514	0.935	4.204	0.230	7%	-0.114	0.301	0.113	0.023
2067-field	0.517	0.931	4.390	0.226	6%	-0.121	0.313	0.111	0.025

3.8.2 Linear mixing (direct model)

Reflectance of modeled spectra compared to the field spectra is higher in the VIS than in the SWIR in all cases of the group (Fig. 3.44). Spectra of the field mixtures are "darker" than it was predicted by the model. As was noticed in the field spectra in the VIS, spectra of all cases were similar, while differences were observed in the NIR-SWIR, nevertheless scenes were different. The linear model estimated higher albedo for the VIS and higher variations of this albedo for the different cases. Absorption depths in the VNIR around 1 μm is deeper in the field mixtures compared to the model. In the field spectra, absorption at 0.5 μm has an asymmetric shape which corresponds to hematite. There is a higher hematite content in the field than was estimated by the modeled spectra, and absorption of hematite is deeper in the field spectra. As can be observed on fig. 3.43, absorption of hematite of the chert sample is about of the same depth as in the field mixtures, however in the field (additionally to red chert) there are other end-members composing the mixture: silt and black chert. Thus, in the mixture spectra hematite absorption is as deep as for 100% of red chert content. In other words, absorption of hematite is stronger than the range predicted by the linear model. An explanation for this is that the concentration of hematite in the field was higher than in the sample (relative abundance of hematite in chert), therefore a non-consistency between the linear model and the field spectrum. However, in the SWIR the absorption of kaolinite and the absorption of calcite fit well in model and field spectra and appear

in the predicted range (Fig. 3.44). This means that the abundance of kaolinite is correctly estimated by the linear model.

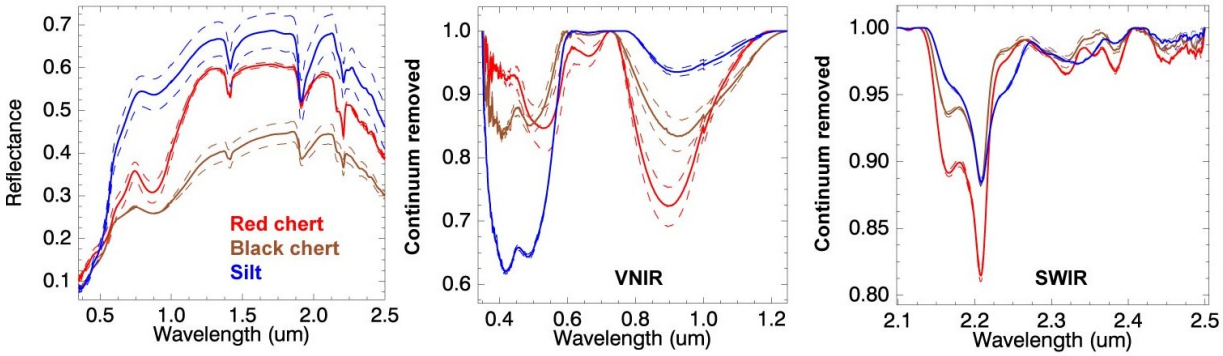

Figure 3.43 – Spectra of end-members used for model, +/- std shown with dashed lines.

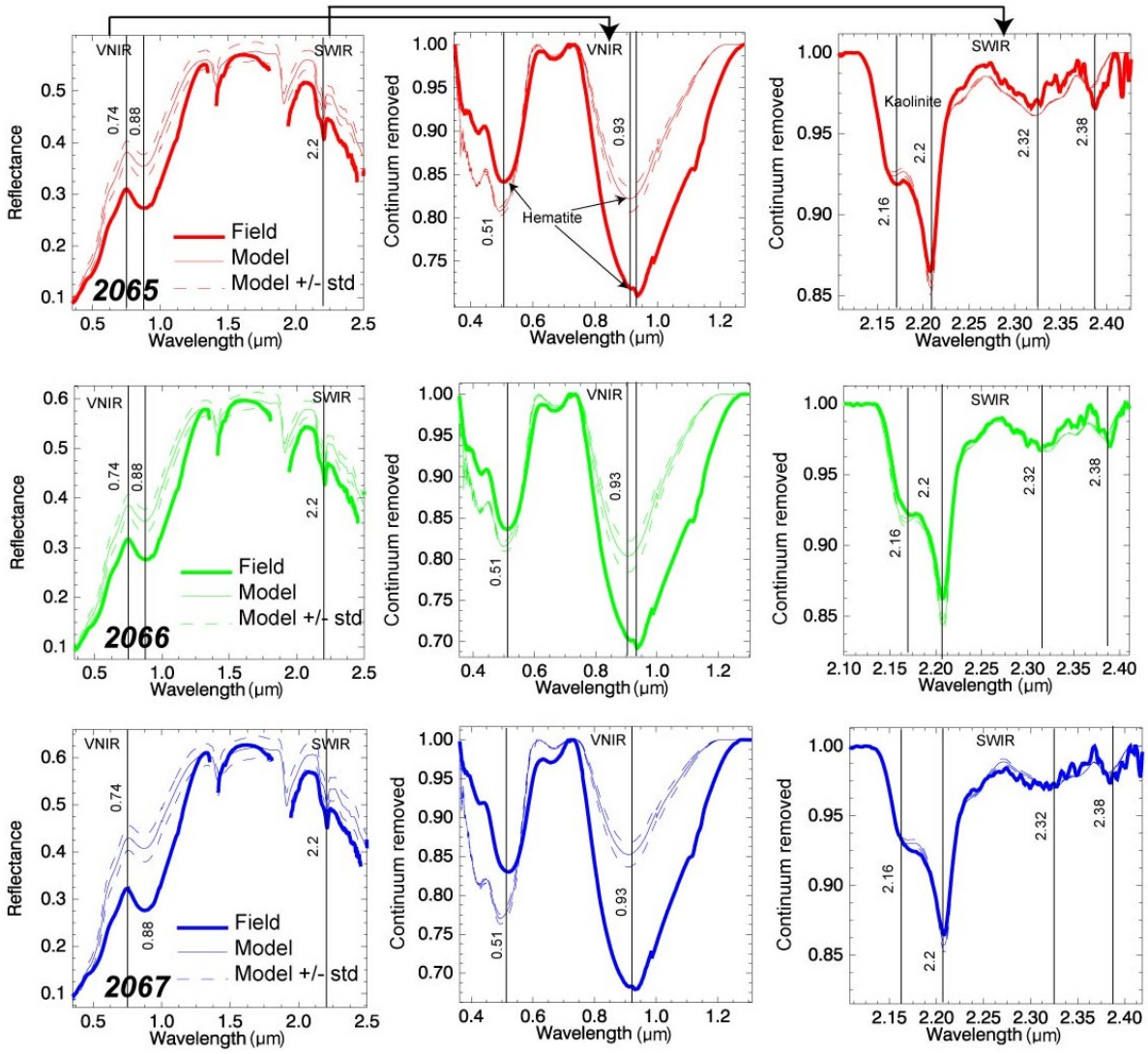

Figure 3.44- Modeled and field spectra of mixtures, group F, site 1.

Formulas for calculation of linear model:

$$\textbf{2065} = (0.11 * Sp_{B.chert}) + (0.367 * Sp_{Silt}) + (0.412 * Sp_{R.chert})$$

$$\textbf{2066} = (0.104 * Sp_{B.chert}) + (0.263 * Sp_{Silt}) + (0.548 * Sp_{R.chert})$$

$$\textbf{2067} = (0.054 * Sp_{B.chert}) + (0.465 * Sp_{Silt}) + (0.399 * Sp_{R.chert})$$

3.8.3 Difference analysis

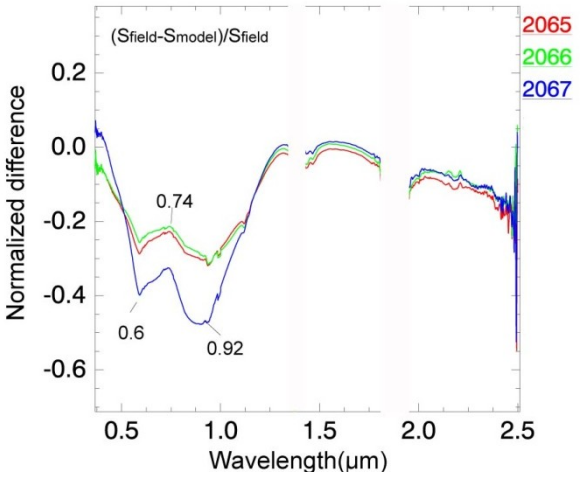

Figure 3.45 – Normalized difference between field and modeled spectra.

Normalized difference between modeled and field spectra indicates differences in albedos and absorption features. Differences between linear model and the cases are higher in the VIS and in the NIR, than in the SWIR where the values are closer to 0. ND spectra of all cases have similar shapes in the VIS, with two peaks at 0.6 and 0.92 μm, these peaks are related to iron oxides. The linear model underestimated the impact of iron oxides compared to the field spectra. In the SWIR difference values are closer to 0, which indicates small differences.

If we observe the normalized difference between field mixtures (Fig. 3.45) we will find that most of the differences are located in the SWIR, while in the VIS values are close to 0. The most exceptional difference is between cases 2065 and 2067, which have the highest values in the SWIR. In these cases end-member abundance was similar, thus the main difference was in boulder sizes. Therefore a non-linear effect was observed in the SWIR, with a difference reaching 10%.

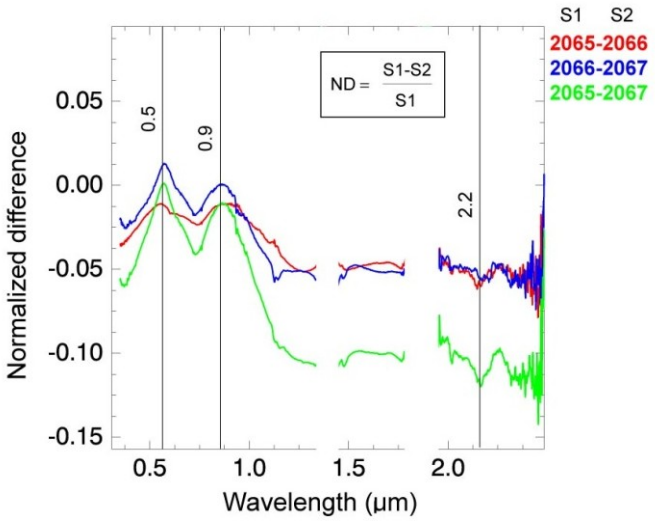

Figure 3.46 – Normalized difference of field spectra.

In mixtures containing high abundance of iron oxides, most of the radiation in this region is absorbed by iron oxides (charge transfer). However in the SWIR the radiation is more reflected and therefore can be multiply scattered. Non linear effects related to composition appear at absorptions positions and depth, non-linear effects related to element size influence mostly the continuum, especially in the SWIR, in this group of mixtures. In mixtures that are composed of contrasted end-members, the VIS spectral range is sensitive to changes in abundance of the constituents, and will be more exposed to non-linear behavior.

3.8.4 Spectral un-mixing (inverse model)

This group of mixtures has a high content of red chert and silt content is lower. Linear un-mixing based on full spectral range showed a dominant proportion of red chert though ignoring other end-members: silt and sandstone. Based only on the visible range black chert abundances prediction was higher. Non-linear un-mixing showed the best result, it detected silt, showed correct red chert abundance, but over-estimated black chert. Non-linear un-mixing was more effective than the linear model, but estimation of spectrally similar end-members was not very precise.

In the case when only the visible range is used for un-mixing, results can vary up to 30% for red chert and up to 15% for black chert. If the full spectral range is used the variations are lower, up to 18% for red chert. These are huge errors that derive from sample heterogeneity and non

conformiety between end-member sample and field constituents. It was observed in direct linear model that linear combination didn't fit absorption depths. Non-linear un-mixing gave better prediction in this group. Silt was not detected by linear un-mixing, non-linear un-mixing detected silt but its content was underestimated. Here can be observed the problem of separation of spectrally similar end-members, cherts Non-linear un-mixing showed lower RMS compared to the linear one (Table 3-20).

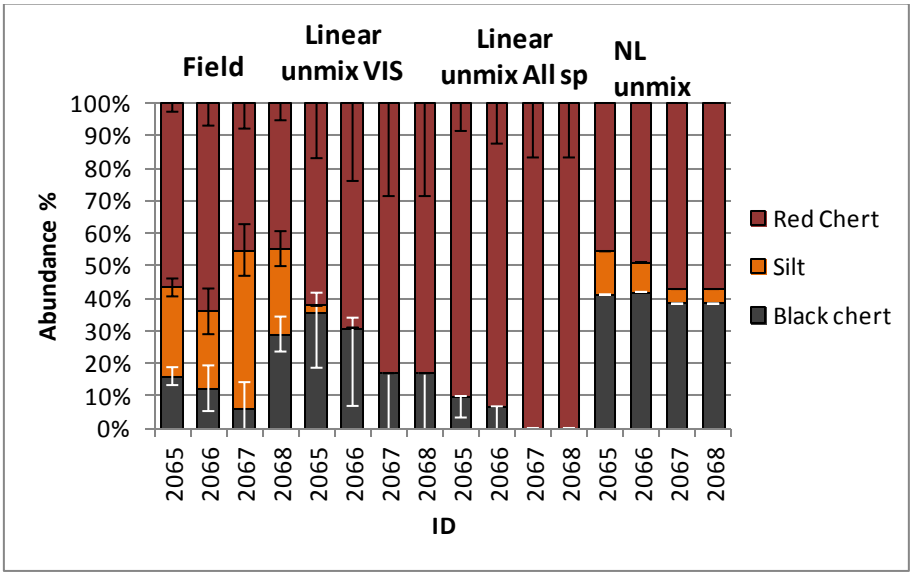

Figure 3.47 – Un-mixing result compared to the field abundances, group F, site 1.

Table 3-20 – RMSE of un-mixing.

Linear un-mixing all spectra				Linear un-mixing VIS			
2065	**2066**	**2067**	**2068**	**2065**	**2066**	**2067**	**2068**
0.0251	0.0324	0.0472	0.0472	0.0078	0.0092	0.0102	0.0102
Non-linear un-mixing							
2065	**2066**	**2067**	**2068**				
0.0157	0.0164	0.0169	0.0169				

In this group of cases, absorption of hematite was highly overestimated by the simple linear model. However, the general shape of the spectra was well predicted. Field spectra show strong absorptions of hematite. The discrepancy probably results from a difference in composition (hematite content) between the sample collected in the field and the other elements present in the

field of view of the instrument which had probably a higher hematite content. Iron oxides have very strong absorptions that mask spectrally neutral constituents. In our case it is difficult to conclude if this was the reason for the overestimation of iron oxides absorptions. More observations are needed. However the non-linear effects which appeared in this group of mixture may be attributed also to environmental factors and effect of element size distribution. Based on our observations, mixtures at macro-scale are influenced by different factors: composition of constituents, size of elements, shadow effect. A simple linear model does not take into account all these factors, and linear un-mixing results in errors.

3.9 Summary field scenes

From the study of field mixtures, we learned that at macro scale mixture behavior might be variable. Therefore scale factor is important in mixture analysis especially when we deal with airborne data. Observation of different field scenarios enabled to better understand what is going on in the case of natural outcrops, with real environmental factors. Since a large amount of previous studies was mainly related to microscopic mixtures, some field empirical study was necessary to understand mixture behavior of macro-scale. However, it was difficult from these preliminary observations to find some generic rules equally relevant for all cases, since mixtures are complex, and from case to case there can be different results.

Table 3.21 – Summary of field results, macro mixtures.

Site-Group	N end-members	Contrast	Element size	Linearity in direct modeling		Un-mixing result	Supposed causes of non-linearity
				Reflectance features	Absorptions features		
4-A	1	Low	Medium	Linear	Linear		Shadow
4-B	2	Low	Medium	Non-linear	Linear		Element size
6-A	2	High	Small-Medium	Linear	Non-linear	Linear	Composition, shadow
7-B	3	Low	Coarse	Non-linear	Linear	Linear	Shadow, composition
1-A	3	High	Small	Linear	Linear	Linear	-
1-B	3	High	Coarse	Non-linear	Non-linear	Non-linear	Element size, composition, shadow
1-D	3,4	High	Coarse	Linear	Non-linear	Non-linear	Element size, composition
1-F	3	High	Medium	Linear	Non-linear	Non-linear	Composition

Table 3.21 summarizes the main results acquired from the observation of the field scenarios. Examination of part of the cases showed that these cases can be well modeled with a simple direct linear model. These are generally mixtures of low-contrast constituents, with a small number of end-members and medium (not extremely small or large) element sizes. For inverse modeling, the un-mixing of spectrally similar end-members was challenging, therefore high errors in content prediction were obtained.

Mixtures of endmembers with high spectral contrast tend to non-linearity (based on direct modeling), while mixtures with low contrast are closer to linear. High spectral contrast endmember mixtures with coarse element size show non-linearity in absorption depths and reflectance. The non-linearity in absorption depths is usually related to composition of the constituents, such as for group 1-F which contained red cherts rich in hematite. In this group, iron oxides were significantly overestimated relatively to their observed abundance. This phenomenon has already been observed for mixtures of powders, where absorptions of magnetite masked the reflectance of spectrally neutral plagioclase (Adams, 1974). Thus, discrepancies in mixtures spectra relatively to modeled spectra may be the result also of heterogeneity between end-members (represented by selected samples) and mixture constituents in the field.

All mixtures exhibited non-linearity in the scenes where elements were coarse, probably also due to shadow, which caused scattering of radiation. Shadow is an environmental effect that is usually present in the field in natural scenes. Our results showed that shadow is a major cause of non-conformity in reflectance intensity of the mixtures. Shadow tended to decrease reflectance intensity of the field cases, but had a lower influence on absorption features. The influence of shadow is wavelength dependant and in some cases we observed higher errors in the visible than in NIR and SWIR. However it was not possible to separately quantify the influence of each parameter such as shadow, element size or patina, etc. To enable this, simulations should be produced. These simulations should take into account one parameter at a time; this will allow separating one factor from another and precisely evaluating their influence on the spectra.

The number of end-members is an important issue in mixture analysis. For more complex mixtures with a higher number of end-members, the result of un-mixing was worse. With decreasing number of end-members, non-linear un-mixing (inverse modeling) gave better prediction results than a simple linear model. Mixtures with low-contrast end-members were in some cases composed of spectrally similar end-members. In these cases, spectral un-mixing results were less accurate. The magnitude of errors was each time different, and it is difficult

based on current results to define the overall influence of the errors coming from different sources. The errors coming from the heterogeneity of the samples have quite a strong influence on un-mixing results, since at the field scale, different factors such as patina, coating and weathering are present. In the un-mixing results, their magnitude is shown for each end-member. In some cases were samples heterogeneity was high the magnitude of the error reached up to 20%. However in most of the cases, this error did not exceed 5-10%.

3.10 Mixtures of powders

Results from the field, which correspond to macro-scale observations, were described in the previous sections. Since scale factor in mixture analysis was not widely studied before, it was interesting to observe macro-mixtures in the field and at some point to compare them to micro-mixtures. As was described in the theoretical overview, powders of minerals were widely used to calibrate macro-mixtures in different studies, even though at the scale of airborne image mixtures have a macroscopic behavior. And accordingly the level of uncertainties deriving from scale change factors was not estimated. To observe this phenomenon we produced powder mixtures with equivalent proportion of minerals as were in macro-mixtures from the field, and compared their spectra. This analysis enables to see how different/similar can be microscopic mixtures of minerals from the macroscopic mixtures were samples are not just powders, but gravels or rocks and boulders.

To achieve powders, rocks were grounded to fine powders, and then were sieved with sieves into the groups with grain sizes of 100-500 μm, 500 μm-0.7 mm, and 0.7-1 mm. Afterwards all constituents were mixed together in one powdered mixture, according to proportional abundance of the constituents corresponding to proportions calculated from the pictures for selected mixtures.

3.10.1 Powders of site 1

For site 1, group B, were selected cases 2049, 2050, 2051 and 2052. These cases are presented in section 3.6. The constituents of these mixtures are: black chert, silt and limestone. Proportion of each composing end-member is shown in table 3-22. Proportions of minerals in the powders

were prepared equivalent to that of sample end-members in the field. Spectra of field mixtures of group B from site 1 and powder spectra are shown on fig. 3.49.

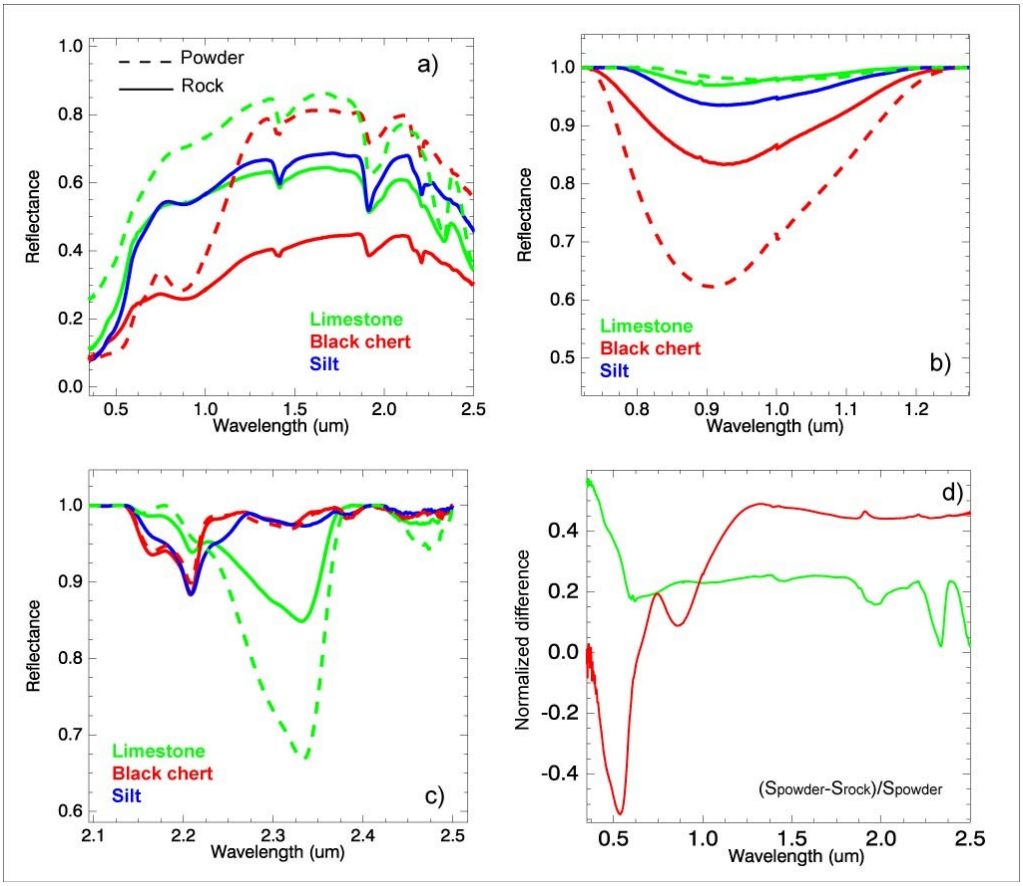

Figure 3.48 – Spectra of powdered samples (100-500 µm) compared to rocks samples.

Table 3-22 – end-member abundance in mixtures, group B, site 1.

Id	Black chert %	Limestone %	Silt %	Shadow %	Accuracy %
2049	33	27	29	11	92
2050	32	29	26	13	80
2051	42	22	24	12	90
2052	36	29	19	16	85

Spectra of powdered (100-500 µm) and rock samples of chert and limestone acquired with ASD in the laboratory are shown on figure 3.48. Differences between rock and powder are noticeable.

Reflectance is higher for powdered samples of limestone and chert. In chert, the slope in the NIR is higher compared to the spectrum of rock, and reflectance remains high till the end of the SWIR. In the VIS reflectance is low, because of absorptions of iron oxides. For chert, absorption of iron oxides is deeper in powdered sample and is more influenced by hematite; in the bulk rock, the absorption is more influenced by goethite. For the limestone powder, the absorption of calcite is deeper, than in the bulk rock.

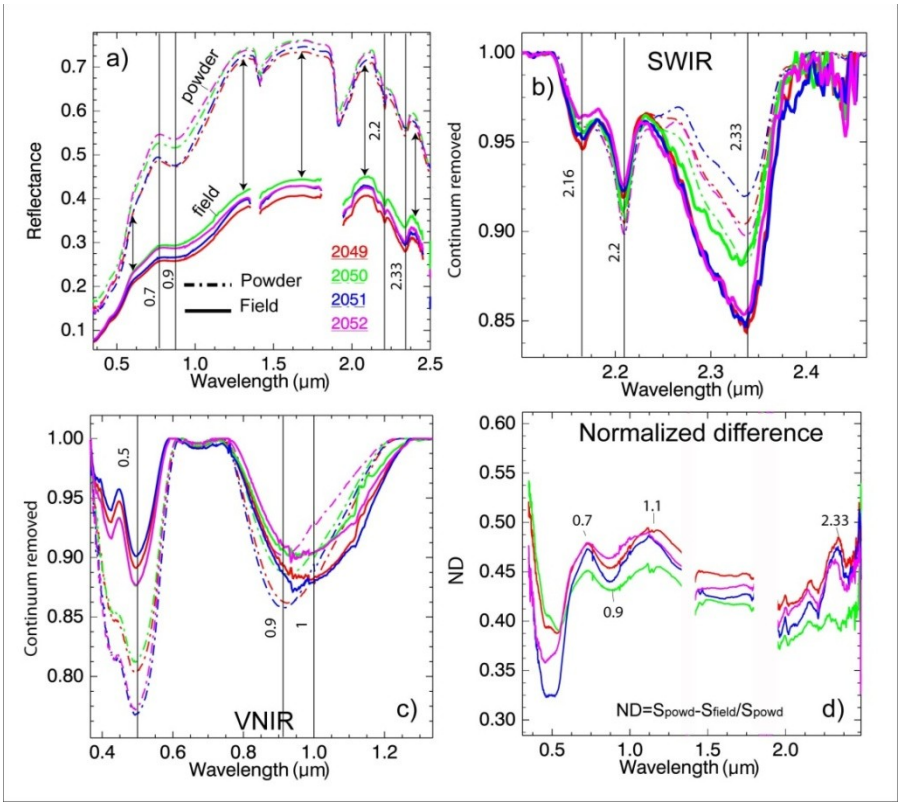

Figure 3.49 – Spectra of powder mixtures (grain sizes 100-500 µm) and field spectra of mixtures with corresponding abundances (a, b, c), normalized difference between powder and field spectra (d).

Powder reflectance is significantly higher than reflectance from the field mixtures and their spectral shapes are different. Differences between field reflectance and reflectance of powders reach 40-50% due to volume scattering (Fig. 3.49.d). The scattering is higher when grain size is smaller, accordingly it is higher for powders. The smallest difference is observed in the VIS (between 0.48 µm and 0.6 µm), where iron oxides specific absorptions are located. Therefore the light is less scattered in this wavelength range, most of the light being absorbed by iron oxides. Then differences increase towards the end of the VIS, and in the NIR, the difference reaches a maximum at 1.1 µm, and in the SWIR still remains high (Fig 3.49 b).

Absorptions in powders in the VNIR are mainly caused by hematite, the absorption around 1 μm is asymmetric, with a minimum shifted to 0.9-0.92 μm. For the mixtures in the field, iron oxides absorption has a minimum around 1 μm, which is corresponding to goethite. This result is due to surface alteration; in the field, black cherts were altered/weathered and coated with crust, and powders were prepared from bulk rock, not only from the crust, thus containing fresh and altered minerals. However, depths of iron oxides absorptions are in the same range in powders and field spectra. Absorption depths of kaolinite at 2.2 μm in the SWIR are in the same range for powders and field spectra. Absorption of calcite at 2.33 μm is more pronounced in field mixtures, than in powders.

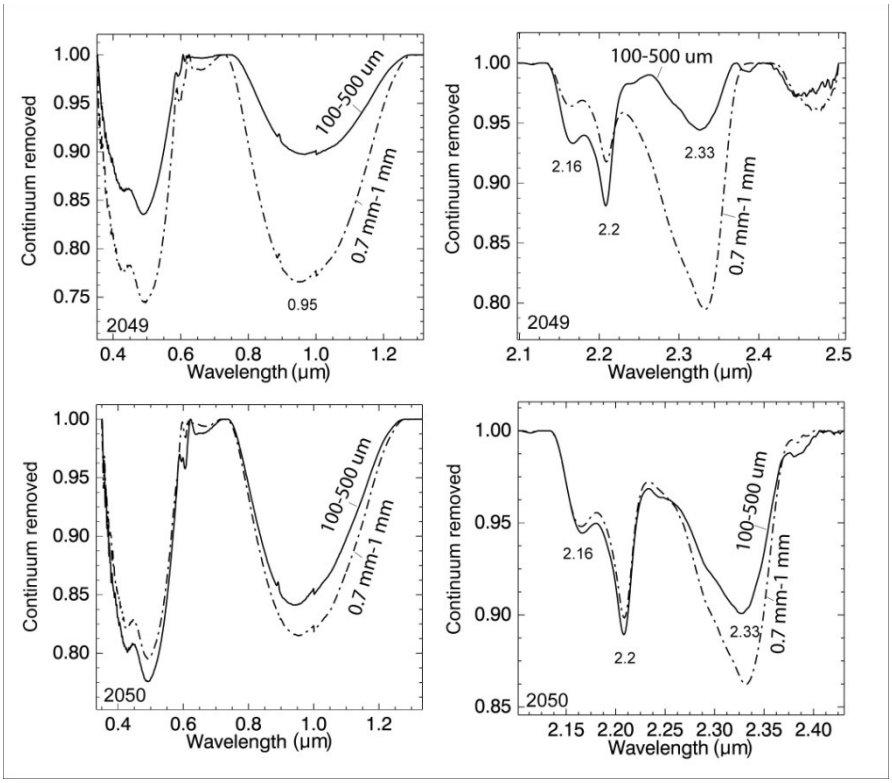

Figure 3.50 – Spectra of powders (100-500 and 0.7-1mm grain size).

It is known from the theory that grain size of the powder must have an equivalent grain size to that of minerals in the rock in order to be comparable. However, in some cases, grain size of minerals in a sample may vary or be difficult to define. For example, grain size of calcite in limestone from site 1 was difficult to define, because in the thin section the sample looked homogeneous. Our results showed that a 100-500 μm grain size for calcite in the powder was not big enough to form a mixture with corresponding absorption depths as those was observed in the

field spectra. Powders with the similar abundances but different grain sizes of minerals have different spectra. An example is shown for mixtures of cases 2049 and 2050, with spectra of powders with different grain sizes of 100-500 μm and 0.7-1mm shown on figure 3.50.

Powders of coarser grain size have much deeper absorptions than powders of finer grain size, however since proportions were equal, this result was to be expected. In case 2049 spectra and absorption depths of two powders are more dissimilar than in case 2050. However, it is expected that differences should be in the same range. Probably this is the result of different grain size distribution of the mixtures. Although the grain size of the mixtures varies in the 100-500 μm range, there can be higher amounts of coarser grains (exact distribution analysis was not estimated). Microscopic mixtures are very sensitive to grain size variations, and small changes in grain size distribution cause big differences in spectral response and absorption depths. This effect at microscopic scale is known (Clark, 1999). Therefore, using spectra of powdered minerals as end-members for macro mixtures is not very correct. Minerals which compose a rock in the field or fine particles may have various size distributions. And microscopic mixtures cannot be directly compared with the macro-mixtures and/or airborne data.

3.10.2 Powders from site 6.

Site 6 is composed of two main end-members, silt and cherts, a dual mixture. Field cases 2189, 2190, 2198 and 2199 were selected, with the proportion of the end-members as shown in table 3-23. Powdered mixtures with the same proportion of end-members were constructed.

Table 3-23 – End-member abundances of mixtures of site 6.

ID	Silt%	Shadow%	Chert%	Classification Accuracy%
2189	29.99	12.64	57.36	98.00
2190	25.04	5.50	69.45	98.00
2198	46.50	8.52	45.00	98.00
2199	60.00	4.00	36.00	98.00

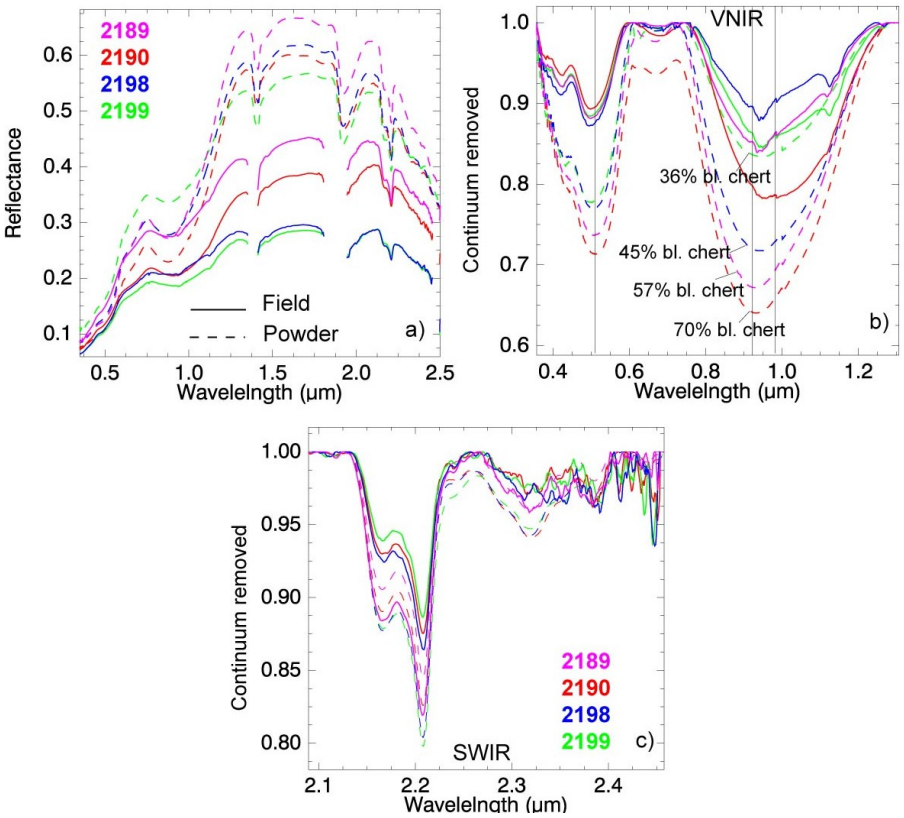

Figure 3.51 – Spectra of powders (500-0.7µm grain size) compared to the field spectra with corresponding abundances.

Another example is shown on fig. 3.51. Powders of coarser grain sizes, 500µm-0.7mm, were compared to the field mixtures with the same abundance for the constituents. It can be observed that spectra of powders are different from the field mixtures. In mixtures of powders the reflectance is higher, especially in NIR and SWIR. Absorption of iron oxides is deeper in spectra of powders, absorptions in the SWIR are also deeper in powders. Again, proportional abundances were similar, but grain size was critical in formation of absorption depths. Moreover, when we produce powders we destroy the sample and its structure. In our case cherts from site 6 were weathered from outside and rock interiors contained more hematite, while outer layer contained more goethite. When powder is produced this effect is destroyed. As was observed in our result absorption of iron oxides of powders corresponds to hematite.

3.11 Correlation analysis

The aim of this analysis is to find which spectral parameters correspond to specific end-members using correlation analysis, which helps to examine relationship between physical/chemical

properties of material and spectra. Mixture composition, elements size, roughness, abundances of end-members will be correlated to specific spectral features. Each end-member is responsible for some spectral feature in the mixture spectrum, and influence specific part of the spectral region. For example, composition of the end-members influence absorptions (position, strength), while element size will affect the general spectral shape (continuum). Absorption features were characterized with parameters such as minimum wavelength, absorption area, symmetry/asymmetry, absorption depth. Continuum and shape were characterized by average reflectance levels and spectral slopes.

Mixtures (35 cases) of site 1 and site 6 were selected for correlation analysis, since they are composed of similar end-members: black chert, silt and limestone and sandstone. Specific absorptions of spectra of these mixtures are similar (similar composition), therefore the same specific absorptions can be examined each time.

3.11.1 Absorption features

Correlation coefficients were calculated between the abundance of the end-members and absorption features, and result is presented in the table 3.24. The table shows correlation coefficients (R) for each parameter with respect to end-member abundance, high correlation coefficients are marked with green.

Table 3.24 - Correlation coefficients (R) between spectral features and end-member abundances.

End-member	Min wvl 0.44-0.61	Min wvl 0.73-0.99	Abs area 0.95	Abs area 2.2	Asymmetry 0.95	0.4 Depth	0.48 Depth	0.95 Depth	2.2 Depth	2.33 Depth
Black chert	-0.14	0.20	-0.14	**-0.41**	0.27	**-0.42**	**-0.69**	-0.19	**-0.45**	**0.55**
Silt	-0.12	**-0.52**	**-0.45**	-0.08	0.04	**0.67**	**0.60**	**-0.40**	-0.11	-0.08
Red Chert	**0.82**	**-0.70**	**0.86**	**0.82**	**-0.59**	**-0.79**	-0.22	**0.86**	**0.82**	-0.63
Sandstone	-0.79	**0.74**	-0.76	**-0.76**	0.64	**0.70**	0.30	-0.77	-0.74	0.33
Shadow	-0.27	0.06	-0.13	-0.17	-0.16	0.15	0.13	-0.13	-0.14	0.08
Limestone	0.30	0.17	-0.05	-0.42	-0.18	-0.62	-0.66	-0.06	-0.58	0.86

High positive correlation (0.82) between red chert and minimum wavelength between 0.44 and 0.61 μm indicates hematite, with a minimum is closer to the shorter wavelengths when there is more hematite in a mixture. The absorption area at 0.95 μm positively correlated to red chert content (0.86), with higher chert content the absorption is deeper. The absorption area at 2.2 μm, is caused by kaolinite, also positively correlated to red chert. With higher red chert content, the absorption feature at 0.95 μm was shifted towards shorter wavelength and becomes more pronounced, a high negative (-0.7) correlation was found between red chert content and minimum wavelength between 0.7 and 1 μm. This is also related to hematite, the minimum is shifted to the longer wavelength in case when there is more goethite in the sample.

In black chert there was no significant correlation to specific absorptions, because black chert is weathered, and the iron oxides absorption is less pronounced. Weak positive correlation 0.3 is observed with minimum wavelength of iron oxides absorption, in black chert this absorption is shifted to the longer wavelength and is related to goethite.

In sandstone the correlation between minimum wavelength of iron oxides absorption and sandstone abundance is high 0.74, in sandstone this absorption minimum is located around 1 μm. A high correlation can be observed with the asymmetry of this absorption, it means that with higher sandstone content the absorption is more symmetric. A medium positive correlation (0.33) between sandstone and absorption at 2.33 μm indicates that there is calcite in sandstones. This result reinforces all previous observations in the field.

The absorption area at 2.33 μm positively correlated to calcite content which is highly concentrated in limestone. It negatively correlated to other absorptions, which indicates the lack of influence of limestone on other absorptions.

Shadow did not correlate to any specific absorption. Only a weak correlation is found with absorptions at the beginning of the VIS, at 0.4 and 0.48 μm, however these are not specific absorptions, but features more related to continuum. It is expected that shadow influence more on continuum of the spectra and less on absorption features, since shadow is featureless.

3.11.2 Albedo parameters

Correlation coefficients were estimated for albedo parameters of mixtures spectra, and the end-members. Table 3-25 shows correlation coefficients between average albedos of VIS-NIR-

SWIR, represented by boundaries of 0.61-0.73 µm, 1.42-1.79 µm and 2.03-2.15 µm and spectral slopes at 0.35-0.78 µm and 0.89-1.3 µm and end-member abundances.

Table 3-25 – Correlation coefficients between albedo properties and end-member abundances.

	Average reflectance level				Spectral slope	
	0.61-0.73	**1.42-1.79**	**2.03-2.15**		**0.35-0.78**	**0.89-1.3**
Black chert	**-0.40**	**-0.39**	**-0.38**		**-0.41**	**-0.21**
Silt	**0.86**	0.37	0.49		**0.85**	-0.20
Red Chert	**0.40**	**0.73**	**0.69**		0.08	**0.83**
Sandstone	-0.53	**-0.73**	**-0.71**		-0.22	-0.78
Shadow	-0.34	-0.45	-0.44		-0.24	-0.25

Each end-member should influence specific parts of the spectra. Black chert is a dark material, therefore it lowers the reflectance intensity, and as a result a negative correlation is observed with spectra in the VIS-NIR-SWIR and the spectral slopes (Table 3-25).

Silt has a high positive correlation with spectral region in the beginning of the VIS (0.61-0.73 µm). Slope at 0.35-0.78 µm is higher with a higher silt content (R=0.85). Silt is a bright end-member and is composed of fine particles and therefore increases scattering and reflectance of the mixtures. It has a greater influence in the VIS, and less in NIR and SWIR. There is a positive correlation between the amount of silt and reflectance slope in the VIS, but a lower correlation in the NIR. This result from scattering being a function of grain size: at shorter wavelengths scattering is higher than at longer wavelengths.

Red chert has a higher correlation with spectra in the NIR and SWIR (R=0.7), this correlation is positive, which means that chert increases reflectance in these regions. However in the beginning of the VIS (R=0.4), its influence is lower. Sandstone has a negative correlation with reflectance levels and slopes of mixture spectra, it means that sandstone is a dark constituent, relatively to others and decreases reflectance levels.

Shadow negatively correlated with reflectance levels and spectral slopes, it lowers reflectance in the VIS-NIR and the SWIR. A higher correlation was observed in the NIR and SWIR (R=-0.45).

Shadow is not a constituent, but it reduces radiation level (reflectance) coming from all of the constituents. From the observations shadow does not influence significantly absorption features, but the influence on albedo is noticeable.

Such an analysis enabled us to decompose spectra of mixtures into parameters and to show how different constituents can have an influence on each spectral parameter.

3.11.3 Element size

Influence of element size on reflectance spectra of the mixtures was also examined with regression analysis on the example of cherts. Size parameters of cherts were selected: number of boulders, average size, standard deviation, skewness, minumun size, maximum and median. These features were correlated to spectral characteristics: absorption depths at 0.42, 0.48 and 0.95 μm, reflectance mean level and slopes of mixtures spectra. The result is shown in table 3-26. For smaller elements multiple scattering is expected to raise the reflectance, for coarser elements reflectance will decrease, and absorptions will be more pronounced.

Table 3-26 – Element size statistics versus albedo spectral properties, R-correlation coefficients are shown (sites 1 and 6).

	Abs. depths			Refl. Mean			Slope	
Size	**0.4**	**0.48**	**0.95**	**0.61-0.73**	**1.42-1.79**	**2.03-2.15**	**0.35-0.78**	**0.89-1.3**
N total	-0.16	-0.16	0.19	-0.17	-0.04	-0.06	-0.17	0.09
Mean	0.03	-0.19	**-0.36**	-0.11	**-0.31**	-0.27	-0.08	**-0.38**
STD	0.00	-0.06	-0.15	-0.29	**-0.31**	-0.29	-0.22	-0.22
Skewness	-0.12	0.11	0.34	-0.21	0.05	0.01	-0.19	0.28
Minimum	0.02	0.04	-0.16	-0.15	-0.15	-0.11	-0.09	-0.14
Median	0.04	-0.23	-0.41	-0.03	-0.29	-0.25	-0.03	**-0.42**
Maximum	-0.10	-0.09	0.02	**-0.39**	**-0.31**	**-0.31**	**-0.33**	-0.11

Element size of cherts correlated (medium negative correlation) with mean reflectance levels in the VIS, between 1.42 and 1.79 μm and in the SWIR 2.03 and 2.15 μm. Spectral slope in the NIR at 0.89 and 1.3 μm also negatively correlated to mean chert element size. With increasing element size of chert, reflectance is lower and the slope is lower, and inversely, the smaller the chert element size is, the higher is reflectance and the steeper the slope in the NIR. The highest correlation was obtained for maximum size of the elements and reflectance, large boulders of

cherts decreased reflectance. There is an influence of element sizes on absorption depths, but not very strong.

Chert is a dark constituent therefore its influence on spectra of a mixture is negative, high chert content decreases reflectance. A negative correlation showed that with increasing element size of cherts albedo is lower, and for finer size of cherts reflectance increases (scattering increases). However, correlation coefficients (R) are not very high, but low and medium. Element size influences spectral parameters, but not in such a significant manner, as relative abundance do. The influence of each constituent that compose the mixture should be taken into account, since each of the constituents may have an influence on a specific region of the spectrum. Chert is only one parameter, but there are other constituents: silt, sandstone, limestone. Element size is a property of a constituent and it is responsible for scattering, which changes with increasing or decreasing size of mixture elements. At macro-scale, this effect is not accounted for in linear un-mixing (model), because it was supposed that boulder size is a part of an areal contribution of end-members. From our results it was observed that at macro-scale, the size of the mixture (macro) elements also plays an important role.

Chapter IV

4. Conclusions

The main objective of this work was to perform empirical study of macroscopic mineral mixtures at the field scale, to observe mixtures of natural scenes in real environments. Most of empirical studies of mineral mixtures are based on microscopic simulated measurements in a laboratory, and there is a lack of observations of mixtures in the field, from natural outcrops. For this purpose, in our study, spectra were collected at the field with an ASD FieldSpec spectrometer at Makhtesh Ramon, Israel, a vegetation-free area, rich in exposed mineral mixtures. Mixtures with different constituents properties were selected: high and low contrast of end-members, proportions of constituents and various element sizes. All the mixtures were classified into groups according to their properties. Spectra of mixtures were modeled using direct linear modeling from spectra of end-members collected in the field. Difference analysis (DA) enabled to compare modeled and field spectra at different wavelengths. Linear and non-linear un-mixing was applied to the observed scenes.

4.1 Non-linearity

It was supposed that spectra of field mixtures should be a linear combination (in areal proportion) of end-members. Our observations showed that in some of the mixtures, absorption depths of modeled spectra and field spectra well corresponded to each other. These cases are usually composed of end-members which element size is not very coarse and when samples picked in the field correspond well with mixture end-members, by their composition, weathering rate, coating, etc. For example, at site 6, where there are dual mixtures of dark and bright constituents, chert and silt, for these mixtures absorption depth of iron oxides appeared in the same range in modeled and field spectra. Black chert was weathered in these cases, and its specific absorptions are weaker than in non-weathered/fresh chert. In high-contrast mixtures like in group 1-B, were boulder size of chert was coarse, linear model under-estimated the influence of chert on mixture spectrum, and in the field iron specific absorptions were stronger than model prediction. In mixtures with low-contrast end-members, as in group 7-A, linear modeling was close in prediction of both albedo levels and absorption depths.

A general conclusion for field mixtures is that in some cases linear combination of end-members corresponded to the field mixtures, but in some cases it did not. There could be several reasons for non-linear effects in the mixtures:

1. Shadow reduces reflectance levels; it was found in our study that shadow reduces spectral reflectance all across the VIS-NIR-SWIR spectral range. Negative correlation was found between shadow coverage and reflectance. The linear model does not take into account shadow; however in the field it obviously influences reflectance. Shadow is a function of illumination and element size, and with coarser elements, the shadow is supposed to increase.
2. Measurements conditions: in the field and in the laboratory, measurement conditions were different. In the field spectra are influenced by atmospheric effects, viewing angle (BRDF) and light source, which is different from an artificial light source. Therefore spectra coming from different sources already include some differences.
3. Linear mixture model does not take into account boulder size of the constituents, only areal contribution (proportion). It was found that element size of chert correlated with reflectance levels and spectral slopes of the field mixtures. As boulder size was bigger reflectance decreased and slope became less steep. At the field scale, boulder size is an important factor that is usually not taken into account by linear modeling and linear un-mixing algorithms. At microscopic scale element size has different dimensions, than at macro-scale, therefore cannot be directly compared. At macro-scale, elements of a mixture may vary from fine particles to boulders. At microscopic scale spectra is sensitive to grain size, scattering effect is stronger. At macro-scale, the size of the macro-constituents is also important, however scattering effect of macro-constituents will be less influenced by elements, such as rocks and boulders.
4. Rocks in the field are not homogeneous, they may vary in surface roughness, coatings, weathering rate. As a result, spectra of the same sample might show variations. As was observed from spectra of a fresh and patined rock, there were significant differences between the spectra. In weathered samples, specific absorptions are weaker, and spectral shape is different. In our case it was observed in the field that rocks were covered by patina, and patined samples were used for analysis. In cases where field access is limited, *a priori* knowledge about mixture constituents is partial, weathering can be a factor of large uncertainties.
5. There might be non-linear contribution of some of the end-members. For example, some of the constituents influence more one specific part of a spectrum than others. When we

produce linear mixture modeling we suppose that the influence of each constituent on the mixture is equal over the whole spectral range and is proportional to its appearance in a mixture. Our results showed that some end-members influenced spectral reflectance more than their simple areal proportion. It was found, for example, that in mixtures containing high amounts of red chert, spectra in the VIS was highly influenced by iron oxides, and less by other constituents. Actually, the influence of other constituents was particularly hidden in the VIS, where the absorption effect of iron oxides was very strong and masked features of other constituents. In all of the observed cases, calcite absorption of the field spectra did not correspond to the modeled spectra. In the field, the absorption of calcite was deeper than in the calculated spectra, even when end-member proportions were corresponding.

Difference analysis enables to perform comparative study of the spectra. Difference spectrum contains information about differences in shape and intensity. As mixtures are more dissimilar their difference will be bigger, and vice versa. It was found that in some of the cases ND had high values in the visible and lower difference in the SWIR. In these cases mixtures were composed of contrasted end-members. A high difference in the VIS originated from non-equal proportions of bright and dark constituents. Therefore spectra of mixtures with high spectral contrast end-members show more differences in the VIS. In mixtures with low spectral contrast constituents, difference in the VIS was less pronounced, major differences were observed in NIR and SWIR, and were derived from compositional differences and element sizes in the mixtures. Difference spectra with similar shapes, but different intensity were also observed in the mixtures with similar proportion of constituents, but different element sizes.

Mixtures of powders were compared to the field mixtures with corresponding proportion of composing minerals. Due to scattering effect between powder grains, reflectance of powders was higher than reflectance from the field mixtures with equivalent proportions of end-members. However, absorption depths of powders and field mixtures were the same, for powders which grain size did not overcome 500 μm. Element size in powders influences not only reflectance levels, but also absorptions. It is very important to find an optimum grain size of powder to be able to represent macro-sample or mixture; however in some cases it is quite difficult. It is usually considered that grain size of powder should match the grain size of minerals composing the rock. However, in some cases a mineral in a rock may have various sizes or its size is difficult to define. As was found from our observations, a grain size of 100-500 μm was good enough to represent chert absorptions in mixture; however in the case of limestone this grain size was not enough to represent calcite absorptions. Spectra of powders are different from field

spectra, therefore their reflectance levels (albedo) cannot be compared. Also at micro-scale physical and environmental factors are different, therefore macro and micro scenes cannot be directly compared.

With the help of a correlation analysis, each property of a mixture spectrum was related to a specific end-member and its property. Some end-members had more influence on specific spectral features, and some on others. Cherts-dark constituents, exhibited albedo reducing property in all spectral region, from VIS to SWIR. Absorption depths and absorptions positions also corresponded to end-member abundances.

Mixture properties at different scales are different: at microscopic scale spectra are very sensitive to grain size distribution of constituents. As grain size is smaller, scattering effect increases, as a result reflectance will increase. At macro scale if constituents are rocks or boulders, spectra are less sensitive to element size variations, but their influence on the spectra still remains important.

Therefore it is not correct to make direct comparison of macroscopic mixtures with powders, if in the field mixtures are not powders, even if their mineral proportions are similar. Our results showed that mixtures of powders and field mixtures with equivalent composition and abundance of constituents have different spectral shapes, even if some absorptions may be in the same range. Powders produced from fresh rock do not take into account the effects of weathering, patina, coatings that is very usual in the field. Therefore it is not correct to calibrate image spectra to powders, but more correct to calibrate macro-mixtures from images to field data.

4.2 Un-mixing

Linear un-mixing is a common method to produce un-mixing of macro-mixtures. However our results showed that the linear un-mixing method is not efficient in some cases, and gave false results and high prediction errors. Our results showed that using the full spectral range is more efficient than just the visible, but in some cases, the visible range can be enough to predict correct abundances. Some end-members might have similar spectra in the visible; in these cases it is impossible to differentiate between them. Therefore it is recommended to use the full VIS-NIR-SWIR spectral range. Non-linear un-mixing improved un-mixing results in part of the cases. However it was not fully effective, as prediction of some end-members was successful, but some were misestimated. This method is effective in cases where spectra of end-members are not fully corresponding to the spectra of the field constituents. Sometimes non-linear effects may change

spectral response of the end-members: patina, coatings, shadow, etc. Spectral response of the same end-member might vary as a function of different factors. Our results showed that using spectra of the same sample may add/remove up to 30% of predicted end-member abundance in some of the cases. The visible range is more sensitive to these variations. Therefore a non-linear algorithm might improve un-mixing results by changing (fitting) the spectrum of end-member according to the mixture from the field and then to produce un-mixing.

According to our results there was no significant problem for un-mixing of a dark end-member from high contrast end-members. The best un-mixing results were obtained in dual mixtures of contrasted constituents silt and chert. The smaller was the number of end-members, the better was the un-mixing result. The worst result was in the cases where spectra of composing end-members resembled each other (spectrally similar end-members), such as red chert and sandstone. However, the technique used in this work might be improved furthermore.

A non-linear fit of end-member's spectra may be useful for un-mixing of macro-mixtures, since they are influenced by non-linear effects and correspond to pixels of airborne images. This is why usually non-linear effects are not taken into account by conventional linear un-mixing algorithms. Non linear effects might appear if spectra from spectral libraries are taken as end-members for un-mixing. Thus, such effects as patina, coatings, roughness, shadows will be ignored, and will add errors to un-mixing.

4.3 Future prospective

This study was one of the studies that referenced to scale-factor in mixture analysis and observed natural field scenarios at macro-scale. This study is important since mixed pixels of airborne images are macro-mixtures. We only studied a limited number of cases and this is only a start for this type of research. In the future it is highly recommended to observe more natural situations, scenes, in different types of surfaces: regolith-like, outcrops, soils etc. It is required to perform simulations at macro-scale, with controlled proportions of constituents and element sizes, similarly to empirical observations in the laboratory, but at macro-scale, preferably in field conditions. These simulations will enable to separate the influence of abundance from the influence of element size, shadows, and other elements. Such technique might be applied on hyperspectral images to learn mixture behavior at sub-pixel scale. For this purpose, the exact knowledge of pixel location will be required, and pixel area should be divided into sub-areas.

Since, usually planetary surfaces are composed of mixture of elements and not of one unique material, more attention should be paid to mixture analysis at macro-scale.

In un-mixing technique special attention should be paid to spectrally similar end-members, which provide the highest errors in un-mixing results. The number of end-members is an issue for today un-mixing algorithms. With higher number of end-members, un-mixing accuracy is reduced. Non-linear algorithms are required for more precise un-mixing of macro-scale mixtures, linear algorithms do not account for many important effects that appear in the field, and result in misclassification of some end-members. Therefore non-linear algorithms have a high potential to improve un-mixing results, if they account for end-member non-homogeneity in the field and other non-linear effects, like shadows, coatings, or element sizes.

Physical models have a high potential in SMA; in some cases they can give a very good interpretation of mixture properties. But as for empirical modeling these models have been only applied on powdered mixtures measured in laboratory conditions. Logically it is expected to test physical models (Hapke, Shkuratov, etc) on natural field scenarios, to obtain more truthful results for further applications of these models on spaceborne data. Field tests will enable to evaluate the ability of these techniques to analyze mixtures in real environments, and to estimate the magnitude of error of their results.

Scale factor in mixture analysis is also an important issue, as spectral characteristics might be different at different scales. For example, at macro-scale some mixture properties that exist at micro-scale may be non-relevant. A masking effect of iron was observed in microscopic mixtures, because the spectrum of these minerals is "strong" and may mask other constituents. Therefore, it would be difficult to find minor fractions of “weak constituents”, if iron masked their features. Another effect is mineral orientation, which is observed at micro-scale, but at field scale might not be relevant. Spectral mixture analysis does not have a unique solution, this subject is as complex as mixing complexity of materials in nature.

5. Bibliography

Adams, J.B., Filice, A.L., (1967). Spectral reflectance 0.4-2.0 microns of silicate rock powders. JGR, vol. 72, 5705-5715

Adams, J. B.,and T. B. McCord, (1971). Alteration of lunar optical properties: Age and composition effects. Science

Adams J.,B., (1974). Visible and near-infrared diffuse reflectance spectra of pyroxenes as applied to remote sensing of solid objects in the solar system, J.G.R., vol 79, NO. 32, pp. 4829-4836.

Adams, J. B., Smith, M. O., and Johnson, P. E. (1986). Spectral mixture modeling — A newanalysis of rock and soil types at the Viking Lander-1 site. Journal of Geophysical Research, Solid Earth and Planets, 91, 8098−8112.

Adams, J. B., and Gillespie, A. R. (2006). Remote sensing of landscapes with spectral images: A physical modeling approach. Cambridge, UK: Cambridge University Press 362 pp.

Adler-Golden, S.M., Matthew, M.W. Bernstein, L.S. Levine, R.Y. Berk, A. Richtsmeier, S.C. Acharya, P.K. Anderson, G.P. Felde, G. Gardner, J. Hoke, M. Jeong, L.S. Pukall, B. Ratkowski A. and Burke H.K. (1999). Atmospheric Correction for Short-wave Spectral Imagery Based on MODTRAN4. Summaries of the Eighth Annual JPL EarthScience Workshop, Vol. I.

Alan R. Gillespie, (1992). Spectral mixture analysis of multispectral thermal infrared images. Remote Sensing of Environment, Volume 42, Issue 2, November 1992, Pages 137-145

Arvidson, R.E., Gooding, J.L., Moore, H.J. (1989). The Martian surface as imaged, sampled and analyzed by the Viking landers. Rev. Geophys., 27, 39-60.

ASD (1999). Analytic Spectral Devices, Inc. technical guide, third ed. Boulder, Colorado.

Atkinson, P. M., and Tatnall, A. R. L. (1997). Neural networks in remote sensing — Introduction. International Journal of Remote Sensing, 18, 699−709.

Atkinson, P. M., Cutler, M. E. J., and Lewis, H. (1997). Mapping sub-pixel proportional land cover with AVHRR imagery. International Journal of Remote Sensing, 18, 917−935.

Barnard, E., and Casasent, D., (1989). A comparison between criterion functions for linear lassifiers, with an application to neural nets. IEEE Transactions on Systems, Man, and cybernetics, 19, 1030–1041.

Baldridge, A. M., and J. D. Farmer, (2004). Mars remote-sensing analog studies in the Badwater Basin, Death Valley, California. J.G.R., 109, E12006, doi:10.1029/2004JE002315.

Ballew, G., (1975). A method for converting Landsat I MSS data to reflectance by means of ground calibration sites. Stanford Remote Sensing Laboratory Technical Report 75-5, Stanford, CA.

Bartholomeus, H., Kooistra, L., Stevens, A., van Leeuwen, M., van Wesemael, B., Ben-Dor, E., Tychon,B., (2011). Soil organic carbon mapping of partially vegetated agricultural fields with imaging spectroscopy. Int. J. Applied Earth Observation and Geoinformation, 13, 61-88.

Bateson, C. A., Asner, G. P., and Wessman, C. A. (2000). Endmember bundles: A new approach to incorporating endmember variability into spectral mixture analysis. IEEE transactions on geoscience and remote sensing, 38, 1083−1094.

Bedini, E. (2009). Mapping lithology of the Sarfartoq carbonatite complex, southern West Greenland, using HyMap imaging spectrometer data. Remote Sensing of Environment, 113, 1208−1219.

Ben-Dor, E., Karnieli, A., Anker, Y., Mazor, E. (2009). "Machtesh Ramon Guide for field trip", 6th EARSel IS SIG Workshop, Field trip.

Bernard-Michel, C., Douté, S., Fauvel, M., Gardes, L., Girard, S., (2009). Retrieval of Mars surface physical properties from OMEGA hyperspectral images using regularized sliced inverse regression. J.G.R., 114, E06005, doi:10.1029/2008JE003171.

Bioucas-Dias, J. M., and Nascimento, J. M. P. (2008). Hyperspectral subspace identification. IEEE Transactions on Geoscience and Remote Sensing, 46, 2435−2445.

Bioucas-Dias, J.M., Figueiredo, M.A.T., (2010). Alternating direction algorithms for constrained sparse regression: application to hyperspectral unmixing. Hyperspectral image and signal processing: evolution in remote sensing, Whispers 2010

Boardman, J. W., and Kruse, F. A., (1994). Automated spectral analysis: A geological example using AVIRIS data, northern Grapevine Mountains, Nevada, in Proceedings, Tenth Thematic Conference, Geologic Remote Sensing, 9-12 May 1994, San Antonio, Texas, p. I-407 - I-418.

Boardman, J.W., Kruse, F.A.,Green, R.O., (1995). Mapping target signatures via partial un-mixing of AVIRIS data. In: Proceeding of the fifth JPL airborne earth science workshop, JPL publication, 95(1), 23-26.

Borel , C.C., Gerstl, S.A.W., (1994). Nonlinear spectral mixing models for vegetative and soil surfaces. Rem. Sen. Of Env., Vol. 47, pp.403-416

Borel, C.C., Gerstl, S.A.(1994). Nonlinear spectral mixing models for vegetative and soil surfaces. Remote Sensing of Environment, 47, 403–416.

Bovolo, F., Bruzzone, L., Carlin, L., (2010). A Novel Technique for Subpixel Image Classification Based on Support Vector Machine. Image Processing, IEEE Transactions on Image processing, Volume: 19 Issue:11

Broadwater, J., Banerjee, A., (2009). A comparison of kernel functions for intimate mixture models. Proc. WHISPERS'09, Grenoble, France, Aug. 2009, 1-4.

Broadwater, J., Banerjee, A.,(2010). A generalized kernel for areal and intimate mixtures. IEEE Trans. 978-I-4244-8907-7/10.

Broadwater, J., Chellapa, R., Banerjee, A., Burlina, P., (2007). Kernel fully constraned least squares abundance estimates. Proc. IEEE Int. Geosc. Remote Sens. Symp. (IGARSS 2007), Barcelona, Spain, July 2007, 4041-4044.

Brown, M., Gunn, S. R., and Lewis, H. G. (1999). Support vector machines for optimal classification and spectral unmixing. Ecological Modelling, 120, 167−179.

Bryant, R.G. (1996). Validated linear mixture modeling of Landsat TM data for mapping evaporate minerals on a playa surface: methods and applications. Int. J. Remote Sens. 17:315-330.

Burns, R.G. (1970). Crystal field spectra and evidence of cation orderingin olivine minerals, American Mineralogist 5, 5, 1608-1632.

Burns, R.G. (1993). Mineralogical applications of crystal field theory. Cmbridge University Press, second edition.

Cahill, J.T.S., Lucey, P.G., Wieczorek, M.A., (2009). Compositional variations of the lunar crust : results from radiative transfer modeling of central peak spectra. J.G.R., 114, E09001, doi :10.1029/2008JE003282.

Cahill, J.T., Lucey, P.G., (2007). Radiative transfer modeling of lunar highlands spectral classes and relationship to lunar samples. J.G.R., 112, E10007, doi:10.1029/2006JE002868.

Carmina E., Carrère, V, (2009). Influence of mineral (preferred) orientation on composition mapping: observed in IR range of transmission spectra. IEEE whispers workshop 2009.

Carpenter, G. A., Gopal, S., Macomber, S., Martens, S., and Woodstock, C. E. (1999). A neural network method for mixture estimation for vegetation mapping. R.S.E., 70, 138−152.

Chabrillat, S., Pinet, P. C., Ceuleneer, G., Johnson, P. E., and Mustard, J. F. (2000). Ronda peridotite massif: methodology for its geological mapping and lithological discrimination from airborne hyperspectral data. International Journal of Remote Sensing, 21, 2363−2388.

Chang, C.C. and C.-J. Lin, (2001). "LIBSVM: a library for support vector machines."

Chen, Q., Wang, L., Westland, S., (2008). A perceptual study of linear models of spectral reflectance. Proc. IEEE 2008 Int. Conf. Computer Science and Software Engineering, doi:10.1109/CSSE.2008.1038.

Chen, X., and Vierling, L. (2006). Spectral mixture analysis of hyperspectral data acquired using a tethered balloon. Remote Sensing of Environment, 103, 338−350.

Chen, X., Vierling, L. (2006). Spectral mixture analysis of hyperspectral data acquired using a tethered balloon. Remote Sensing of Environment, 103, 338–350.

Chevrel, S.D., Pinet, P.C., Head, J.W. (1999). Gruithuisen domes region:a candidate for an extended non-mare volcanism unit on the Moon. J.G.R 104, 16515–16529, 1999.

Clark, R. N. (1983). Spectral properties of mixtures of montmorillonite and dark carbon grains: Implications for remote sensing of minerals containing chemically and physically adsorbed water, J.G.R., 88, 10,635– 10,644.

Clark, R. N. and Kierein, K. S. (1988). Reflectance spectra of mixtures as a function of grain size and viewing geometry: Implications for remote sensing. Icarus (in press).

Clark, R. N., and T. L. Roush (1984). Reflectance Spectroscopy: Quantitative Analysis Techniques for Remote Sensing Applications. J.G.R., 89(B7), 6329–6340.

Clark, R.N., (1999). Chapter 1: "Spectroscopy of rocks and minerals, and principles of spectroscopy, in manual of remote sensing", Volume 3, Remote sensing for the Earth Sciences, p 3-58.

Clark, R.N., Swayze, G.A., Wise, R., Livo, K.E., Hoefen, T.M., Kokaly, S.J., Sultley, R.F. (2007). The U.S. Geological Survey, Digital spectral library Speclib06a. U.S. Geological Survey Open File Report DLR-IB, Wessling, Germany, pp. 93-592.

Clenet, H., Pinet, P., Daydou, Y., Heuripeau, F., Rosemberg, C., Baratoux, D., Cheverl, S., (2011). A new systematic approach using the Modified Gaussian Model: Insight for the characterization of chemical composition of olivines, pyroxenes and olivine-pyroxene mixtures. Icarus, 213, 404-422.

Cloutis, E.A., Bell III, J.F., (2004). Mafin silicate mapping on Mars : effects of palagonitic material, multiple mafic silicates, and spectral resolution. Icarus, 172, 233-254.

Collins, E. F., Roberts, D. A., and Borel, C. C. (2001). Spectral mixture analysis of simulated thermal infrared spectrometry data: An initial temperature estimate bounded TESSMA search approach. IEEE Transactions on Geoscience and Remote Sensing, 39,1435−1446.

Combe, J.-Ph., LeMoue´ lic, S., Sotin,C., Gendrin,A., Mustard,J.F., LeDeit,L., Launeau, P.,Bibring,J.-P.,Gondet,B.,Langevin,Y.,Pinet,P.,andtheOMEGAScienceteam, (2008). Analysis of OMEGA/Mars Express data hyperspectral data using a Multiple-End member Linear Spectral Un mixing Model (MELSUM): Methodology and first results.PlanetaryandSpaceScience56,951–975, doi:10.1016/ j.pss.2007.12.007.

Cooper, C.D., and Mustard J.F., (2002). Spectroscopy of loose and cemented sulfate-bearing soils: Implications for duricrust on Mars, Icarus, 158, 42-55, doi: 10.1006/icar.2002.6874.

Dalton, J.B., (2007). Linear mixture modeling of Europa's non-ice material based on cryogenic laboratory spectroscopy. G.R.L., 34, L21205, doi:10.1029/2007GL031497.

Denevi, B.W., Lucey, P.G., Sherman, S.B., (2008). Radiative transfer modeling of near-infrared spectra of lunar mare soils: theory and measurement. J.G.R., vol. 113, E02003, doi:10.1029/2007JE002929.

Dennison, P. E., and Roberts, D. A. (2003a). Endmember selection for multiple endmember spectral mixture analysis using endmember average RMSE. Remote Sensing of Environment, 87, 123−135.

Dennison, P. E., Charoensiri, K., Roberts, D. A., Peterson, S. H., and Green, R. O. (2006). Wildfire temperature and land cover modeling using hyperspectral data. Remote Sensing of Environment, 100, 212−222.

Dennison, P.E., Halligan, K.Q., Roberts, D.A., (2004). A comparison of error metrics and constraints for multiple endmember spectral mixture analysis and spectral angle mapper. R.S.E., 93, 359-367.

Dennison, P.E., Roberts, D.A., (2003). Endmember selection for multiple endmember spectral mixture analysis using endmember average RMSE. R.S.E., 87, 123-135.

Dyar, M.D., Gunter,S.R., Sutton,S.R., Lanzarotti, A.(2005). Broad spectrum characterization of returned samples: orientation constraints of small samples on X-ray and other spectroscopies. Lunar and Planetary Science XXXVI.

Eastes, John W. (1989). Spectral properties of halite-rich mineral mixtures: Implications for middle infrared remote sensing of highly saline environments. Remote Sensing of Environment Volume 27, Issue 3, Pages 289-303

Eckmann, T. C., Roberts, D. A., and Still, C. J. (2008). Using multiple endmember spectral mixture analysis to retrieve subpixel fire properties from MODIS. Remote Sensing of Environment, 112, 3773−3783.

Eckmann, T. C., Roberts, D. A., and Still, C. J. (2008). Using multiple endmember spectral mixture analysis to retrieve subpixel fire properties from MODIS. Remote Sensing of Environment, 112, 3773−3783.

Eckmann, T. C., Roberts, D. A., and Still, C. J. (2009). Estimating subpixel fire sizes and temperatures from ASTER using multiple endmember spectral mixture analysis. International Journal of Remote Sensing, 30, 5851−5864.

Elmore, A. J., Mustard, J. F., Manning, S. J., and Lobell, D. B. (2000). Quantifying vegetation change in semiarid environments: Precision and accuracy of spectral mixture analysis and the normalized difference vegetation index. R.S.E., 73, 87−102.

Elmore, A. J., Mustard, J. F., Manning, S. J., and Lobell, D. B. (2000). Quantifying vegetation change in semiarid environments: Precision and accuracy of Spectral Mixture Analysis and the Normalized Difference Vegetation Index. Remote Sensing of Environment, 73, 86–102.

Elvidge, C.D. (1989). Vegetation reflectance features in AVIRIS data. Proc. 6th Thematic Conf. on Remote Sensing for Exploration Geology.

Farrand, W.H., Bell III, J.F., Johnson, J.R., Squyres, S.W., Soderblom, J., Ming, D.W., (2006). Spectral variability among rocks in visible and near-infrared multispectral Pancam data collected at Gusev crater: examinations using spectral mixture analysis and related techniques. J.G.R., vol. 111, E02S15, doi:10.1029/2005JE002495.

Feldman, W.C. (2002). Global distribution of neutrons from Mars: Results from Mars Odyssey. Science, 297, 75-78.

Fitzgerald, G. J., Pinter, P. J., Hunsaker, D. J., and Clarke, T. R. (2005). Multiple shadow fractions in spectral mixture analysis of a cotton canopy. Remote Sensing of Environment, 97, 526−539.

Fonti, S., Montanaro, S., Politi, R., Blanco, A., Marra, A.C., Marzo, G.A., Orofino, V., (2010). Infrared reflectance spectra of particulate mixtures. J.G.R., vol. 115, E06003, doi:10.1029/2009JE003461.

Franke, J., Roberts, D.A., Halligan, K., Menz, G. (2009). Hierarchical multiple endmember spectral mixture analysis (MESMA) of hyperspectral imagery for urban environments. R.S.E., 113, 1712-1723.

Gaffey,M. J., L. Lebofsky,M. Nelson, and T. Jones (1993), Asteroid surface composition from Earth-based reflectance spectroscopy, in Remote Geochemical Analysis: Elemental and Mineralogical Composition, edited by C. M. Pieters and P. A. J. Englert, pp. 437– 453, Cambridge Univ. Press, New York.

Gao, B.-C., A. F. H. Goetz, and W. J. Wiscombe, (1993). Cirrus cloud detection from airborne imaging spectrometer data using the 1.38-mm water vapor band. Geophys. Res. Lett., **20,** 301–304.

Garcia-Haro, F. J. Gilabert, M. A. Melia, J. (1999). Extraction of endmembers from spectral mixtures. Remote Sens. Environ., 68:237-253.

Gendrin, A., and Erard S. (2003). A new tool to investigate infrared spectra,based on wavelet filtering: Application to Hawaii. Proc. Lunar Planet. Sci. Conf. 34th, 1376.

Gillespie, A. R.. Smith, Ni. O., Adams, 1'. B.. and Willis,S. C. (1990). Spectral mixture analysis of multispectral thermal infrared images. In Proc., 2nd Thermal IR Multi-spectral Scanner (TIMS) Workshop, 90-55, Jet Propulsion Laboratory, Pasadena, CA, pp. 5'i'- T4

Goldberg, M., (1970). The lithostratigraphy of the Arad Group (Jurassic) in the northern Negev, Geological Survey of Israel, Report MM/ 3/70, 136 pp (in Hebrew, with English abstract).

Goodwin, N., Coops, N.C., Stone, C., (2005). Assessing plantation canopy condition from airborne imagery using spectral mixture analysis and fractional abundance. Int. J. Appl. Earth Observation and Geoinformation, 7, 11-28.

Green, A. A., Berman, M., Switzer, B., and Craig, M. D., (1988). A transformation for ordering multispectral data in terms of image quality with implications for noise removal. IEEE Transactions on Geoscience and Remote Sensing, v. 26, no. 1, p. 65 - 74.

Green, A.A., Berman, M., Switzer, P., Craig, M.D. (1988). A transformation for ordering multispectral data in terms of image quality with implications for noise removal. IEEE Transactions on Geosciences and Remote Sensing, 26, 65-74.

Green, R. O., Eastwood, M. L., Sarture, C. M., Chrien, T. G., Aronsson, M., Chippendale, B. J., et al. (1998). Imaging spectroscopy and the Airborne Visible/Infrared Imaging Spectrometer (AVIRIS). Remote Sensing of Environment, 65, 227−248.

Guilfoyle, K. J., Althouse, M. L., and Chang, C. -I. (2001). A quantitative and comparative analysis of linear and nonlinear spectral mixture models using radial basis function neural networks. IEEE Transactions on Geoscience and Remote Sensing, 39, 2314−2318.

Hapke, B. (1981). Bi-directional reflectance spectroscopy, 1, Theory. J. G. R., 86, 3.039–3.054.

Hapke, B. and Wells, E., (1981). Bi-directional reflectance spectroscopy, 2, Experiments and Observations. J.G.R. 86, pp. 3.055–3.060.

Hapke, B. (1984). Bi-directional reflectance spectroscopy, 3, Correction for macroscopic Roughness. Icarus, 59, 41–59.

Hapke, B., (1981). Biderectional reflectance spectroscopy: 1. Theory. J.G.R., 86,3039-3054.

Hapke, B., (1986). Bi-directional reflectance spectroscopy, 4, The extinction coefficient and the opposition effect. Icarus, 67, 264–287.

Harloff, J., Arnold, G.: Near-infrared reflectance spectroscopy of bulk analog materials for planetary crust. Planetary and Space Science, 49, 2, (2001), S. 191-211

Harsanyi, J.C., (1993). Detection and Classification of Subpixel Spectral Signatures in Hyperspectral Image equences, Ph.D. Dissertation, University of Maryland, Baltimore County, 116 pp.

Heinz, D. C., and Chang, C. I. (2001). Fully constrained least squares linear spectral mixture analysismethod formaterial quantification in hyperspectral imagery. IEEE Transactions on Geoscience and Remote Sensing, 39, 529−545.

Hochberg, E.J., Atkinson, M.J., (2003). Capabilities of remote sensors to classify coral, algae, and sand as pure and mixed spectra. R.S.E., 85, 174-189.

Hunt, G., (1977). Spectral signatures of particulate minerals in the visible and near-infrared, Geophysics, vol. 42, NO 3, p. 501-513

Hunt, G., Salisbury, J., (1971). Visible and near-infrared spectra of minerals and rocks: II. Carbonates. Modern Geology,2, 23-30.

Johnson, J.R., Christensen, R.R., Lucey, P.G., (2002). Dust coatings on basaltic rocks and implications for thermal infrared spectroscopy of Mars. JGR vol 107

Johnson, P. E., M. O. Smith, and J. B. Adams (1992). Simple Algorithms for Remote Determination of Mineral Abundances and Particle Sizes From Reflectance Spectra, J.G.R., 97(E2), 2649–2657, doi:10.1029/91JE02504.

Johnson, P. E., M. O. Smith, S. Taylor-George, and J. B. Adams (1983). A semiempirical method for analysis of the reflectance spectra of binary mineral mixtures., J. G. R., 88(B4), 3557–3561, doi:10.1029/JB088iB04p03557.

Johnson, P.E., (1983). A semiempirical method for analysis of the reflectance spectra of binary mineral mixtures. J.G.R., vol.88, NO B4 pp. 3557-3561

Johnson, P.E., Smith M.O., Adams, J.B. (1985). Quantitative analysis of planetary reflectance spectra with principal component analysis. J.G.R., Vol 90, 805-810.

Johnson, P.E., Smith, M.O.,Adams, J.B.,(1992). Simple algorithms for remote determination of mineral abundances and particle sizes from reflectance spectra. J.G.R., vol. 97, NO E2, pp 2649-2657

Johnson, T. V., F. P. Fanale, (1973). Optical properties of carbonaceous chondrites and their relationship to asteroids. J. G.R. 78, 8507-8518.

Ju, J., Kolackzyk, E.D., Gopal, S., (2003). Gaussian mixture discriminant analysis and sub-pixel land cover characterization in remote sensing. R.S.E., 84, 550-560.

Kerekes,J.P., 2009. Optical sensor technology, The SAGE handbook of remote sensing, Ch. 7,

Keshava, N., and Mustard, J. F. (2002). Spectral unmixing. IEEE Signal Processing, 19, 44−57.

Kirkpatrick, S., Jr., C. G., Vecchi, M., (1983). Optimization by simulated annealing. Science, 220.

Kruse, F. A., Kierein-Young, K. S., Boardman, J. W., (1990). Mineral mapping at Cuprite, Nevada with a 63 channel imaging spectrometer. Photogrammetric Engineering and Remote Sensing, v. 56, no. 1, pp. 83-92.

Kuosmanen, V.V., Laitinen, L.J., (2008). Quantitative mineral assessment of Apatite, Calcite/Dolomite, and Phlogopite powder mixtures by using VSWIR reflectance. IEEE Trans. Geosc. and Remote Sens., 46(6), 1774-1782.

Kwan, C., Ayhan, B., Chen, G., Jing Wang, Baohong Ji, Chein-I Chang (2006). A novel approach for spectral unmixing, classification and concentration estimation of chemical and biological agents. IEEE Transactions on Geoscience and Remote Sensing, Volume 44, Issue 2.

Lawrence, S.J., Lucey, P.G., (2007). Radiative transfer mixing models of meteoritic assemblages. J.G.R., 112, doi:10.1029/2006JE002765.

Le Bras A. and Erard S. (2003). Reflectance of regolith analogs in the mid-infrared: effects of grain size. *Planet. Space Sci.* **51**, 281-294.

Li, L., (2008). Partial least squares methods for spectrally estimating lunar soil FeO abundance: A stratified approach to revealing nonlinear effect and qualitative interpretation. J.G.R., 113, doi:10.1029/2008JE003213.

Li, L., and Mustard, J. F. (2003). Highland contamination in lunar mare soils: Improved mapping with multiple endmember spectral mixture analysis (MESMA). Journal of Geophysical Research, Planets, 108(5053).

Li, L., Ustin, S. L., and Lay, M. (2005). Application of multiple endmember spectral mixture analysis (MESMA) to AVIRIS imagery for coastal salt marsh mapping: a case study in China Camp, CA, USA. International Journal of Remote Sensing, 26, 5193−5207.

Lillesand, T.M., Kiefer, R.W., Chipman, J.W., (2004). *Remote Sensing and Image Interpretation*. 5th ed. (pp.491-610). New York: John Wiley and Sons.

Longhi, I., Sgavetti, M., Meli, S., Pompilio, L., (2004). Complex spectra interactions of different minerals and textures in Mars terrestrial analogues: Some examples. Planetary and Space Science, 52, 141-147.

Lucey, P.G., (2006). Radiative transfer modeling of the effect of mineralogy on some empirical methods for estimating iron concentration from multispectral imaging of the Moon. J.G.R., 111, doi:10.1029/2005JE002661.

Lumme, K., Bowell, E. (1981). Radiative transfer in the surfaces of atmosphereless bodies I. Theory. Astron. In press.

Lyon, J.P., (1965). Analysis of rocks by spectral infrared emission (8 to 25 Microns). Econ. Geol. 60, 717–736.

Mathews, J.D., Doherty, J.F., Wen, C.-H., Briczinski, S.J.,Janches, D., Meisel, D.D., (2003). An update of UHF radar meteor observations and associated signal processing techniques at Arecibo Observatory. Journal of Atmospheric and Solar Terrestrial Physics 65, 1139–1149

Mazor, E., (2005). Machtesh Ramon - a geological window, Enviro. Sci. and Ener. Res., Weizmann Institute of science Pub., Rehovot, Israel, p.18.

McGwire, K., Minor, T., and Fenstermaker, L. (1999). Hyperspectral mixture modeling for quantifying sparse vegetation cover in arid environments. Remote Sensing of Moroz, L. Arnold, G. (1999). Influence of neutral components on relative band contrasts in reflectance spectra of intimate mixtures: Implications for remote sensing:1. Nonlinear mixing modeling. J. G. R., Vol 104, pp 109-14, 121.

Mercier, G., Hubert-Moy, L., Houet, T., and Gouery, P. (2005). Estimation and monitoring of bare soil/vegetation ratio with SPOT VEGETATION and HRVIR. IEEE Transactions on Geoscience and Remote Sensing, 43, 348−354.

Minitti, M. E., J. F. Mustard, and M. J. Rutherford (2002). Effects of glass content and oxidation on the spectra of SNC-like basalts: Applications to Mars remote sensing. J. Geophys. Res., 107(E5), 5030, doi:10.1029/2001JE001518.

Moersch, J.E., Christensen, P.R. (1995). Thermal emission from particulate surfaces: A comparison of scattering models with measured spectra, J.G.R, VOL. 100, NO. E4, PP. 7465-7477, doi:10.1029/94JE03330

Moody, A.,S., Gopal, A.H. Strahler, (1996). Artificial neural network response to mixed pixels in coarse resolution satellite data. Rem. Sens. Env., Vol.58, pp. 329-343

Moroz, L. and Arnold, G (1999). Influence of neutral components on relative band contrasts in reflectance spectra of intimate mixtures: implications for remote sensing; Nonlinear mixing model. J. Geophys. Res. 104 , p. 14,109-14,122 .

Morton, D. C., DeFries, R. S., Shimabukuro, Y. E., Anderson, L. O., Espirito-Santo, F. D. B., Hansen, M., (2005). Rapid assessment of annual deforestaion in the Brazilian Amazon using MODIS data. Earth Interactions, 9(8).

Mustard, J. F., and Sunshine, J. M. (1999). Spectral analysis for Earth science investigations", in Manual of Remote Sensing, Volume 3, Remote Sensing for the Earth Sciences, edited by A. N. Rencz and R. A. Ryerson, pp. 251-306, John Wiley and Sons, Inc., New York.

Mustard, J. F., S. Erard, J. P. Bibring, J. W. Head, S. Hurtrez, Y. Langevin, C. M. Pieters, and C. J. Sotin, (1993). The surface of Syrtis Major: Composition of the volcanic substrate and mixing with altered dust and soil. J.G.R., 98, 3387-3400.

Mustard, J.F. and Sunshine J.M., (1995). Seeing through the dust: Martian crustal heterogeneity and links to the SNC meteorites. Science, 267, 1623-1626.

Mustard, J.F., and C.M. Pieters, (1989). Photometric phase functions of common geologic minerals and applications to quantitative analysis of mineral mixture reflectance spectra", J.G.R. 94, 13,619-13,634.

Mustard, J.F., and Pieters C.M. (1987). Quantitative abundance estimates from bidirectional reflectance measurements. in Proc. 17th Lunar Planet. Sci., Part 2, edited, pp. E617-E626, J.G.R.

Mustard, J.F., Hays, J.E. (1997). Effects of hyperfine particles on reflectance spectra from 0.3 to 25 μm. Icarus, 125, 145-163

Mustard, J.F., Pieters, C.M. (1989). Photometric phase functions of common geologic minerals and applications to quantitative analysis of mineral mixture reflectance spectra. J.G.R., Vol. 94, pp 13619-13634.

Mustard, J. F., and Pieters, C. M. (1987). Quantitative abundance estimates from bidirectional reflectance measurements. Journal of Geophysical Research, 92, 617–626.

Nascimento, J. M. P., and Bioucas-Dias, J. M. B. (2005). Does independent component analysis play a role in unmixing hyperspectral data? IEEE Transactions on Geoscience and Remote Sensing, 43, 175−187.

Nash, D. B., and J. E. Conel, (1973). Vitrification darkening of rock powders: Implications for optical properties of the lunar surface. The Moon 8, 346-364.

Nash, D. B., and Conel, J. E. (1974). Spectral reflectance systematics for mixtures of powdered hypersthene, labradorite, and ilmenite. J.G.R., 79, 1615−1621.

Nevo, E. (1963). The Jurassic strata of Makhtesh Ramon. Israel J. Earth Sci. 12

Okin, G. S., Roberts, D. A., Murray, B., and Okin, W. J. (2001). Practical limits on hyperspectral vegetation discrimination in arid and semiarid environments. Remote Sensing of Environment, 77, 212−225

Orofino, V. Politi, R. Blanco, A. Fonti, S. (2006). Diffuse reflectance of altered olivine grains: Remote sensing detection and implications for Mars studies Planetary and Space Science 54 784–793

Painter, T. H., Dozier, J., Roberts, D. A., Davis, R. E., and Green, R. O. (2003). Retrieval of subpixel snow-covered area and grain size from imaging spectrometer data. Remote Sensing of Environment, 85, 64−77.

Parente, M, Bishop, J.L., Bell III, J.F., (2009). Spectral unmixing for mineral identification in Pancam images of soils in Gusev crater, Mars. Icarus, 203, 421-436.

Peddle, D. R., Hall, F. G., and LeDrew, E. F. (1999). Spectral mixture analysis and geometricoptical reflectance modeling of boreal forest biophysical structure. Remote Sensing

Pieters, C. M. (1996). Plagioclase and maskelynite diagnostic features,Lunar Planet. Sci., XVII, abstract 1031.

Pieters, C. M., (2000). Space weathering on airless bodies: Resolving a mystery with lunar samples, Meteorit. Planet. Sci. 35, 1101-1107.

Pieters, C. M., J. W. Head III, L. Gaddis, B. Jolliff, and M. Duke, (2001). The charactear ndp ossibleo rigino f"Olivine Hill" in SouthP ole-Aitken Basin. Lunar Planet. Sci., XXXII 1810.

Pieters, C., T. McCord, S. Zisk, and J. Adams (1973). Lunar Black Spots and Nature of the Apollo 17 Landing Area1Publication 72, Planetary Astronomy Laboratory, Massachusetts Institute of Technology., J. G. R., 78(26), 5867-5875.

Placht, J. (1996). Mapping of Quaternary units in Maktesh Ramon, central Negev. Isr.J. Earth Sci.;45: 217-222.

Plakht, J., N. Patyk-Kara and Gorelikova, N.,(2000). Terrace pediments in Makhtesh Ramon, central Negev, Israel. Earth Surface Processes and Landforms 25: 29-30.

Plaza, A., Martinez, P., Perez, R., and Plaza, J. (2004). A quantitative and comparative analysis of endmember extraction algorithms from hyperspectral data. IEEE Transactions on Geoscience and Remote Sensing, 42, 650−663.

Pompilio, L., Sgavetti, M., Pedrazzi, G., (2007). Visible and near-infrared reflectance spectroscopy of pyroxene-bearing rocks: New constraints for understanding planetary surface compositions. J.G.R., 112, E01004, doi:10.1029/2006JE002737.

Poulet F., Erard, S., (2004). Nonlinear spectral mixing: quantitative analysis of laboratory mineral mixtures, J. G. R., Vol. 109, E02009,doi:10.1029/2003JE002179.

Poulet, F., Cuzzi, J.N., Cruikshank, D.P., Roush, T., Dalle Ore, C.M.,(2002). Comparison between the Shkuratov and Hapke Scatterign theories for solid planetary surfaces: application to the surface composition of two centaurs. Icarus 160, 313-324

Powell, R.L., Roberts, D.A., Dennison, P.E., Hess, L.L., (2007). Sub-pixel mapping of urban land cover using multiple endmember spectra mixture analysis: Manaus, Brazil. R.S.E., 106, 253-267.

Ray, T. W., Murray, B. C. (1996). Nonlinear spectral mixing in desert vegetation. Remote Sensing of Environment, 55, 59–64.

Rees, W.G. (2001). *Physical Principles of Remote Sensing*, second edition, Cambridge University Press.

Rendon, J. L. and Serna, C.J. (1981). IR spectra of powder hematite: Effect of particle size and shape: Clay Miner. 16, 375-381.

Ritter, G.X., Urcid, G., (2011). A lattice matrix method for hyperspectral image unmixing. Information Sciences, 181, 1787-1803.

Rivard, B., Feng, J., Gallie, A., Sanchez-Azofeifa, A., (2008). Continuous wavelets for the improved use of spectral libraries and hyperspectral data. R.S.E., 112, 2850-2862.

Roberts, D. A., Gardner, M., Church, R., Ustin, S., Scheer, G., and Green, R. O. (1998). Mapping Chaparral in the Santa Monica Mountains Using Multiple Endmember Spectral Mixture Models. Remote Sensing of Environment, 65, 267−279.

Roberts, D. A., Smith, M. O., and Adams, J. B. (1993). Green vegetation, nonphotosynthetic vegetation, and soils in AVIRIS data. Remote Sensing of Environment, 44, 255–269.

Roberts, D. A., Yamaguchi, Y., and Lyon, R. J. P. (1985). Calibration of Airborne Imaging Spectrometer Data to percent reflectance using field spectral measurements. In Proceedings, Nineteenth International Symposium on Remote Sensing of Environment, Ann Arbor, Michigan, October 21-25, 1985.

Robichaud, P.R., Lewis, S.A., Lacs, D.Y.M., Hudak, A.T., Kokaly, R.F., Zamudio, J.A., (2007). Postfire soil burn severity mapping with hyperspectral image unmixing. R.S.E., 108, 467-480.

Rogge, D.M., Rivard, B., Zhang, J., Sanchez, A., Harris, J., Feng, J., (2007). Integration of spatial-spectral information for the improved extraction of endmembers. R.S.E., 110, 287-303.

Roush, T.L. (1982). Effects of iron-silica gels on spectral reflectance. Lunar Plan. Sci. Conf. XIII, 661-662.

Schaepman, M.E., Ustin, S.L., Plaza, A.J., Painter, T.H., Verrelst, J., Liang, S., (2009). Earth system science related imaging spectroscopy – An assessment. R.S.E, 113, 5123-5137.

Shepard, M.K., Helfenstein, P., (2007). A test of the Hapke photometric model. J.G.R., 112, E03001, doi:10.1029/2005JE002625.

Shipman, H., Adams, J.B. (1987). Detectability of minerals on desert alluvial fans using reflectance spectra. J.G.R., 92: 10391-10402

Shkuratov, Y.G., Starukhina, L., Hoffman, H., and Arnold, G., (1999). A model of spectral albedo of particulate surfaces: Implications for optical properties of the Moon. Icarus, 137, 235-246

Singer, R.B. (1981). Near-infrared spectral reflectance of mineral mixtures: systematic combinations of pyroxenes, olivine and iron oxides". JGR vol 86, pp. 7967-7982

Singer, R.B., Roush, T.L. (1983). Spectral reflectance properties of particulate weathered coatings on rocks: laboratory modeling and applicability to Mars. Lunar Plan. Sci. Conf. XIV, 708-709.

Smith, D. J., McCarthy, D. P., and Luckman, B. H., (1994). Snow-avalanche impact pools in the Canadian Rocky Mountains. Arctic and Alpine Research, 26: 116-127.

Smith, M. O., Johnson, P. E., Adams, J. B.,(1985). Quantitative determination of mineral types and abundances from reflectance spectra using principal components analysis. J.G.R., Supplement (ISSN 0148-0227), vol. 90, Feb. 15, p. C797-C804.

Smith, M.O., Johnson, P.E., Adams, J.B., (1985). Quantitative determination of minereal types and abundances from reflectance spectra using principal components analysis. J.G.R., Vol. 90, pp C797-C804.

Somers, B., Asmern, G.P., Tits, L., Coppin P., (2011). Endmember variability in spectral mixture analysis: a review. R.S.E., 115, 1603-1616.

Somers, B., Cools, K., Delalieux, S., Stukens, J., Van der Zande, D., Verstraeten, W.W., Coppin, P., (2009). Nonlinear hyperspectral mixture analysis for tree cover estimates in orchards. R.S.E., 113, 1183-1193.

Song, C. H. (2005). Spectral mixture analysis for subpixel vegetation fractions in the urban environment: How to incorporate endmember variability? Remote Sensing of Environment, 95, 248−263.

Sonnetag, O., Chen, J. M., Roberts, D. A., Talbot, J., Halligan, K. Q., and Govind, A. (2007). Mapping tree and shrub leaf area indices in an ombrotrophic peatland through multiple endmember spectral unmixing. Remote Sensing of Environment, 109,342−360.

Sonnetag, O., Chen, J. M., Roberts, D. A., Talbot, J., Halligan, K. Q., and Govind, A. (2007). Mapping tree and shrub leaf area indices in an ombrotrophic peatland through multiple endmember spectral unmixing. Remote Sensing of Environment, 109, 342−360.

Sunshine, J.M., Pieters, C.M. (1991). Identification of modal abundances in spectra of natural and laboratory pyroxene mixtures: a key component for remote analysis of lunar basalts. Lunar and Plan. Sci. XXII, 1361-1362.

Sunshine, J.M., Pieters, C.M., Pratt, S.F. (1990). Deconvolution of mineral absorption bands: an improved approach. J.G.R., vol.95, NO B5, pp. 6955-6966

Sunshine, J.M., Pieters, C.M., Pratt, S.F., Mc Naron-Brown, K.S., (1999). Absorption band modeling in reflectance spectra: Availability of the Modified Gaussian Model.

Tompkins, S., Mustard, J. F., Pieters, C. M., and Forsyth, D. W. (1997). Optimization of End-members for spectral mixture analysis. Remote Sensing of Environment, 59, 472–489.

Ustin, S.L., D.A. Roberts, S. Jacquemoud, J. Pinzon, M. Gardner, G. Scheer, C.M. Castaneda, and A. Palacios. (1998). Estimating canopy water content of chaparral shrubs using optical methods. Remote Sensing of Environment 65:280-291.

Wald, A. E.,Salisbury, J. W. (1995). Thermal infrared directional emissivity of powdered quartz. J.G.R.. **100,** 24,665–24,675.

Wang, F. (1990). Fuzzy supervised classification of remote sensing images. IEEE Transactions on Geoscience and Remote Sensing, 28, 194−201.

Warell, J., Davidson, B.J.R., (2010). A Hapke model implementation for compositional analysis of VNIR spectra of Mercury. Icarus, 209, 164-178.

Weng, Q., and Hu, X. (2008). Medium spatial resolutionsatellite imagery for estimating and mapping urban impervious surfaces using LSMA and ANN. IEEE Transactions on Geoscience and Remote Sensing, 46, 2397−2406.

White,K., Drake, N. (1993). Mapping the distribution and abundance of gypsum in South-Central Tunisia from Landsat thematic mapper data. Geomophol. 37:309-325

Yan, B., Wang, R., Gan, F., Wang, C., (2010). Minerals mapping of the lunar surface with Clementine UVVIS/NIR data based on spectra unmixing method and Hapke model. Icarus, 208, 11-19.

Youngentob, K.N., Roberts, D.A., Held, A.A., Dennison, P.E., Jia, X., Lindenmayer, D.B., (2011). Mapping two Eucalyptus subgenera using multiple endmember spectral mixture analysis and continuum-removed imaging spectrometry data. R.S.E., 115, 1115-1128.

Zadeh, L. (1965). Fuzzy sets. Information and Control, 8: 338–353.

Zak, I. (1963). Remarks on the stratigraphy and tectonics of the Triassic of Makhtesh Ramon. Israel Journal of Earth Sciences 12: 87–89.

Zhang, J., Rivard, B., Sanchez-Azofeifa, A., (2005). Spectral unmixing of normalized reflectance data for the deconvolution of lichen and rock mixtures. R.S.E., 95, 57-66.

Annex

Table 3- 27 – Grain size statistics.

Site 1		Name	N total	Mean	Standard Deviation	Skewness	Minimum	Median	Maximum
		Black chert	80	4.8	3.7	1.7	0.5	3.6	18.1
	2045	Limestone	42	2.1	0.6	0.9	0.8	1.9	3.9
		Black chert	157	4.2	2.3	1.5	1.1	3.6	13.7
	2047	Limestone	28	4.5	2	1.2	1.7	4.3	10.8
		Black chert	210	4	2.5	1.9	1.3	3.4	17.8
A	***2048***	Limestone	50	5.7	3.4	1	1.1	4.95	17
		Black chert	180	6.9	4.2	1.7	1.8	6.15	26.2
	2049	Limestone	61	10.6	6.9	1.8	3.5	8.1	34.2
		Black chert	79	10.1	6.6	1.5	1.9	8.1	33.2
	2050	Limestone	47	11.2	6.8	1.9	2.5	9.4	37.1
		Black chert	106	9.3	7.5	1.9	2	6.85	38.3
	2051	Limestone	72	8.8	5.9	0.9	2	7.4	25.3
		Black chert	114	7.8	6.7	1.9	1.8	5.2	30.5
	2052	Limestone	65	9.9	6.9	1.9	2.2	7.1	41.3
		Black chert	300	4.4	3.2	1.6	0.3	3.1	16.7
B	***2053***	Limestone	123	7	3.5	0.8	1.9	6.8	17.8
		Black chert	1670	2	1.3	2.6	0.5	1.7	11.8
		Limestone	49	6.3	1.9	0	0.3	6.1	11.5
	2054	Sandstone	151	2.8	1.9	1.7	0.6	2.3	10.2
		Black chert	230	5.5	3.8	2.3	1	4.1	28.2
		Red chert	295	4	4.2	2.5	1.3	2.2	25.5
	2055	Sandstone	50	7.5	4.5	1.5	0	6.85	24.2
		Black chert	423	4.6	3.7	2.6	0.8	3.4	33.5
	2056	Sandstone	76	7	4.6	1.5	1.9	5.5	24.1
		Black chert	221	5.1	3.8	2.3	1.2	3.7	27.8
		Red chert	34	5.9	3.8	2.1	2.44	4.4	20.54
C	***2057***	Sandstone	68	9.9	4.6	0.7	1.1	9.1	21.5
		Black chert	138	5	6.1	5.2	1.3	3.4	50.7
	2058	Sandstone	89	7.9	10	4.4	2.1	5.4	64.4
		Black chert	108	5.3	7.1	6.9	1	3.4	68.7
	2059	Sandstone	72	9.4	6.7	2.5	3.4	7.4	39.7
		Black chert	117	7	4.7	1.2	1.2	6.1	22
D	***2060***	Sandstone	63	12	9.8	2.8	3.8	9.5	62.4
		Black chert	68	10.1	11.3	3.3	2.1	6.2	60.2
		Red chert	43	6.9	7.1	4.6	2.3	5.2	46.6
	2061	Sandstone	54	7.7	2.8	0.5	3.3	7.3	15.7
E	***2062***	Black chert	39	8.5	10.1	3.8	2.6	5.5	56.2

		Sandstone	30	13.8	18.4	4.3	4.7	7.9	103.3
	2063	Black chert	52	9.7	9.5	2.4	1.7	7	46.1
		Black chert	49	8.8	5.9	1.6	2.5	6.6	26.5
		Limestone	5	15.8	13.1	1.1	5.7	8.5	35.9
		Red chert	23	9.4	6.5	2	2.4	8.9	32
	2064	Sandstone	46	12.8	9.4	2.7	4.2	10.3	56.4
		Black chert	135	4.3	3	1.5	0	3.2	14.9
	2065	Red chert	233	6.2	4.4	1.3	1.2	5.1	25.7
		Black chert	255	2.7	2.3	7.1	0.8	2.2	29.7
	2066	Red chert	279	6.6	4.2	1.2	0.9	5.7	23
		Black chert	124	3.2	2.2	2.4	0.9	2.6	14.7
	2067	Red chert	254	6.6	3.9	0.6	1	5.8	17.6
		Black chert	148	5.6	5.8	2.7	1.1	3.4	38
F	***2068***	Red chert	192	6.1	5.2	2.1	1	4.4	31
Site 6									
	2184	Chert	84	8.57	7.03	5.38	0.72	1.19	23.91
	2185	Black chert	92	10.68	10.6	6.51	2.04	2.16	45.35
		Red chert	11	10.06	10.63	2.59	0.33	6.32	14.91
	2187	Chert	145	8.88	7.73	5.49	1.63	0.26	32.93
	2188	Chert	175	7.6	6.13	5.41	1.91	0.16	33.61
	2189	Chert	150	8.82	8.24	5.19	0.73	1.73	27.6
A	***2190***	Chert	536	4.6	3.65	3.57	1.97	0.13	23.58
	2194	Chert	175	6	4.22	6.71	4.41	0.07	58.1
	2196	Chert	136	5.92	4.86	4.03	1.43	0.48	22.87
	2198	Chert	259	5.33	4.34	4.54	3.62	0.09	38.22
B	***2199***	Chert	166	6.11	4.27	4.81	2.11	1.59	27.99
Site 7									
	2205	Sandstone	20	18.33	12.90	1.35	5.06	12.57	48.00
		Red chert	7	18.40	6.95	0.18	10.62	15.91	26.65
	2206	Sandstone	19	17.45	12.35	1.39	5.00	13.69	48.29
B	***2209***	Chert	7	18.15	17.65	1.27	5.74	8.65	48.61
		Sandstone	25	11.36	7.84	2.60	2.86	10.13	42.00
	2211	Chert	5	18.97	9.75	0.63	7.77	18.34	33.35
		Sandstone	22	19.12	9.06	1.07	8.73	17.22	39.62
	2220	Red chert	23.00	10.15	15.82	3.58	1.67	4.46	75.60
C	***2221***	Red chet	21.00	15.49	13.55	1.85	2.69	11.76	59.92
	2223	Red chert	62	14.90	11.98	2.92	3.16	11.82	67.21
		Sandstone	23	9.01	6.74	1.30	3.51	5.78	25.47

Impact des mélanges de minéraux à macro-échelle sur la réflectance spectrale de surfaces naturelles: étude empirique à partir de scénarios de terrain.

Les mélanges spectraux peuvent être enregistrés à différentes échelles: de microscopique (en laboratoire) au mètre (terrain) et au kilomètre (surfaces planétaires). Quand la roche est observée à l'échelle microscopique, les minéraux sont les composantes spectrales. A cette échelle, étant en contact intime les uns avec les autres, les minéraux produisent des mélanges intimes, qui ont un comportement non linéaire.

Le comportement de mélanges intimes a été principalement étudié à partir d'échantillons de poudre, qui permettent de produire des mélanges avec des proportions et des compositions connues. Cependant les mélanges de surfaces naturelles (macro-mélanges) sont moins bien connus. Dans des environnements naturels, les mélanges sont composés de différents types de roches dans des proportions et des tailles des éléments différentes. Les constituants peuvent varier de poussière avec des particules extrêmement fines à de gros blocs de roches qui sont des milieux continus.

Dans cette étude des mélanges spectraux macroscopiques ont été analysés, divers scénarios de surfaces naturelles ont été sélectionnés sur le terrain, leurs spectres ont été mesurés avec un spectromètre portable. Des échantillons (composantes de mélange) ont été recueillis sur le terrain et puis ont été analysés en laboratoire. Les modèles linéaires (direct et inverse) ont été appliqués, différents indices spectraux ont été calculés. Des données aéroportées à partir de trois différents capteurs ont été traitées.

Nos résultats ont montré que les mélanges de terrain ont un comportement complexe, qui parfois a été bien reproduite par le modèle linéaire, mais dans certains cas, il y avait non-conformité entre le modèle et les spectres terrain. Ces effets non-linéaires ont été causés par des facteurs comme la taille des éléments de constituants (rochers, graviers), d'ombre, l'hétérogénéité et la composition des échantillons. Ces effets ne sont généralement pas pris en compte par de simples modèles linéaires et par les algorithmes de démixage linéaires. Toutefois, à l'échelle du terrain ces facteurs sont naturels et apparaîtra en pixels mixtes d'images aéroportées.

Impact of mineral mixtures at macro-scale on surface spectral reflectance: empirical study of natural field scenarios.

Spectral mixtures can be registered at different scales: from microscopic (in the laboratory) to meter (field) and kilometer scale (planetary surfaces). The choice of mixture end-members is scale dependent: when a rock is observed at microscopic scale, single minerals are the end-members. At this scale, being in intimate contact with each other, minerals produce spectral intimate mixtures, which have non-linear behavior. The behavior of intimate mixtures mostly was studied from powdered samples, which enable to produce mixtures with known proportions and compositions. However mixtures of natural surfaces (macro-mixtures) are less known. In natural environments mixtures are composed from a diversity of rock types with various proportions and grain sizes.

In this study macroscopic spectral mixtures were analyzed, various scenarios of natural surfaces were selected in the field, their spectra were measured with a portable spectrometer. Samples (mixture endmembers) were collected in the field and were analyzed in the laboratory. Linear models (direct and inverse) were applied, different spectral indices were calculated. Airborne data from three different sensors were processed.

Our results showed that field mixtures have complex behavior, which sometimes was well reproduced by linear model, but in some cases there was nonconformity between the model and the field spectra due to the presence of non-linear effects. These nonlinear effects were caused by such factors as element size of mixture constituents (boulders, gravels), shadowing, heterogeneity and composition of the samples. These effects usually are not taken into account by simple linear models and linear un-mixing algorithms. However at the field scale these factors are natural and will appear in mixed pixel of airborne images.